Bioinspired Dinuclear Copper Complexes for Small Molecule Activation

Dissertation
zur Erlangung des
mathematisch-naturwissenschaftlichen Doktorgrades
„Doctor rerum naturalium“
der Georg-August-Universität Göttingen

im Promotionsprogramm Chemie
der Georg-August-University Göttingen School of Science (GAUSS)

vorgelegt von
Can-Jerome Spyra (geb. Güneş)
aus Hannover

Göttingen 2021

Betreuungsausschuss

Prof. Dr. Franc Meyer, Institut für Anorganische Chemie, Georg-August-Universität Göttingen

Prof. Dr. Inke Siewert, Institut für Anorganische Chemie, Georg-August-Universität Göttingen

Mitglieder der Prüfungskommission

Referent:

Prof. Dr. Franc Meyer, Institut für Anorganische Chemie, Georg-August-Universität Göttingen

Korreferentin:

Prof. Dr. Inke Siewert, Institut für Anorganische Chemie, Georg-August-Universität Göttingen

Weitere Mitglieder der Prüfungskommission:

Prof. Dr. Sven Schneider, Institut für Anorganische Chemie, Georg-August-Universität Göttingen

Prof. Dr. Ulf Diederichsen, Institut für Organische und Biomolekulare Chemie, Georg-August-Universität Göttingen

Jun. Prof. Anna Krawczuk, Institut für Anorganische Chemie, Georg-August-Universität Göttingen

Dr. Christian Sindlinger, Institut für Anorganische Chemie, Georg-August-Universität Göttingen

Tag der mündlichen Prüfung: 27.07.2021

Contents

1 General Introduction

During the last decades bioinorganic chemistry has established itself as an important interdisciplinary field of research, investigating the role of inorganic elements (especially metals) in biological systems.[1–5] Particularly, enzymes that coordinate transition metal ions in their active center, so-called metalloenzymes, receive a high level of attention, since they can carry out highly specific chemical reactions under mild conditions and participate in various physiological processes.[6,7] Therefore, investigation of active sites and mechanistic studies of metalloenzymes might be the key to design new economically and ecologically efficient catalysts. The role of metals in various medical fields, e.g. the origin of civilisatory diseases such as ALZHEIMER'S[8–10] or as potential drugs for anti-cancer therapy makes the research of those in biological systems highly particularly interesting.[11–13]

Hereby, metalloenzymes containing copper ions in their active center participate in a broad variety of reactions such as electron transfer (ET), binding, activation and reduction of oxygen, reduction of NO_2 and N_2O, and the activation of organic substrates.[14,15] This huge diversity of chemical reactions of the 3d transition metal copper in nature can be attributed to the early evolutionary biological availability and the accessible redox pair of Cu oxidation states +I and +II.[16–18]

In the following, exemplary copper-containing metalloenzymes which are divided in different types according to their active centers, reactivities and spectroscopical features are presented[19,20], as well as bioinorganic model systems to investigate reaction processes and structures of those. Emphasis is placed on dinuclear copper centers and the activation of small molecules, since this is the key topic of this work.

2 Copper Enzymes in Nature

2.1 Type I Example: Plastocyanin

Plastocyanin as an example for a type I copper protein can be found in biological domains, where fast electron transfer (ET) is required, such as in the photosystem I for photosynthesis.[21,22] The ability to enable fast ET reactions originates from the exceptional coordination geometry, which can be best described as a strongly distorted tetrahedron (Figure 1) and is often referred to as an 'entatic state'.[23,24] This unique geometry resembles a transition state which lowers the reorganization energy between the preferred tetrahedral or trigonal coordination geometry of the Cu^{I} ion and the square planar coordination sphere of the Cu^{II} ion and therefore enables fast shuttling between the Cu^{I}/Cu^{II} redox states.[14,23]

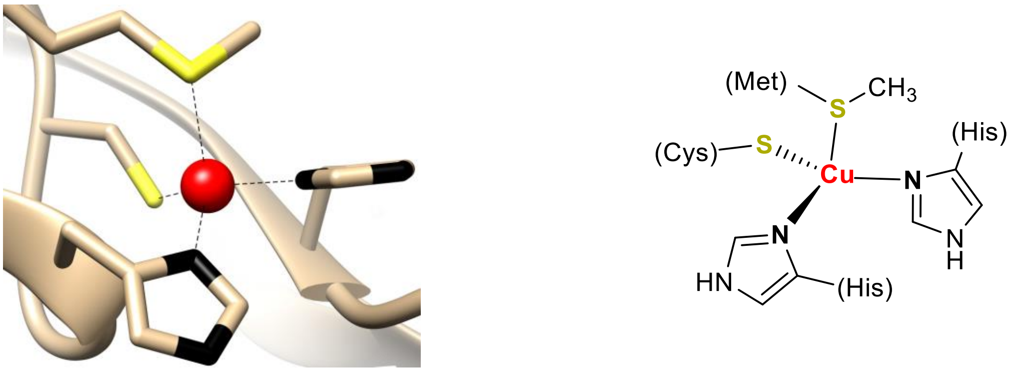

Figure 1. Active site of plastocyanin, illustrating the distorted tetrahedral {3+1} coordination geometry (PDB: 4R0O[25]).

The general coordination sphere of type I copper proteins includes two histidine and one cysteine ligand, whereby the intense absorption (600 nm, $\varepsilon \approx 5000\ M^{-1}\ cm^{-1}$), originating from a ligand to metal charge transfer (LMCT) between the thiolate of the cysteine and the Cu^{II} ion, is responsible for the name giving color of those 'blue copper proteins'.[24,26] The fourth coordinating ligand varies, depending on the specific enzyme, e.g. plastocyanin (methionine residue), stellacyanin (glutamine residue) and azurine (oxygen atom of an amide group of the peptide backbone).[27,28]

2.2 Type II Examples: Galactose Oxidase and Copper Nitrite Reductase

The enzyme galactose oxidase is an example of a type II copper protein and combines two $2e^-/2H^+$ processes; the oxidation of primary alcohols to aldehydes and the reduction of O_2 to H_2O_2.[29] The 'active' form of the enzyme exhibits a Cu^{II} center in a distorted square pyramidal coordination environment, which consists of two histidine ligands, a water molecule (respectively substrate) and a tyrosyl radical linked to a cysteine in the equatorial plane. The coordination sphere is completed by a tyrosine ligand in the axial position of the metal ion (Figure 2).[30]

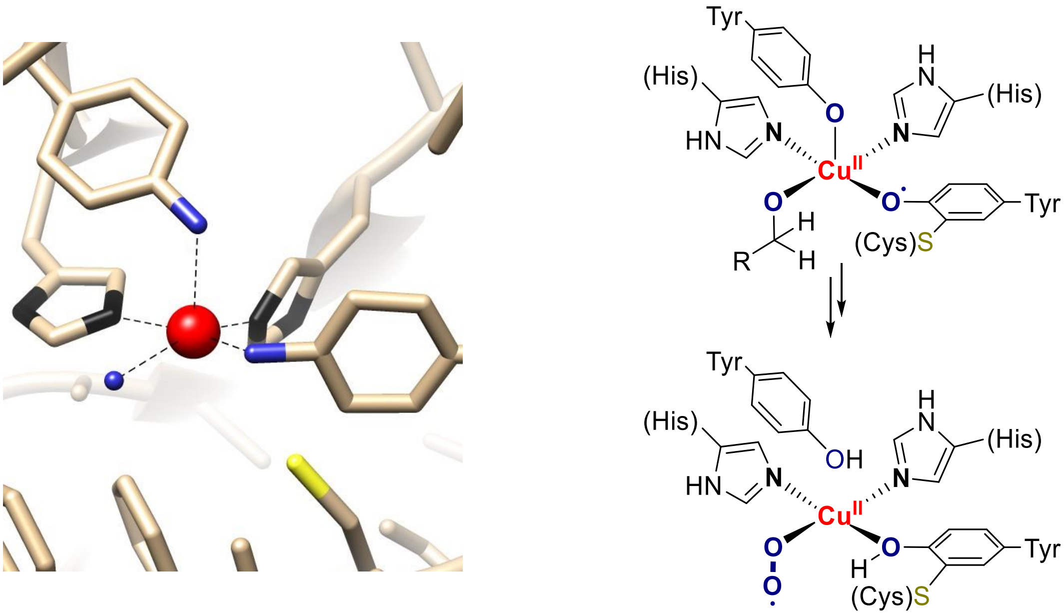

Figure 2. 'Inactive' (left) and 'active' (top right) form of Galactose Oxidase as well as the putative involved Cu/O_2 superoxo species (bottom right) during alcohol oxidation (PDB: 1GOG).[29–33]

Extensive enzymatic model studies and DFT calculations were conducted to elucidate the mechanism of galactose oxidase, marking the relevance of the Cu^{II} tyrosyl species, which is responsible for the alcohol oxidation via intramolecular proton coupled electron transfer (PCET).[34,35] The resulting Cu^{I} intermediate forms a putative superoxo species (Figure 2), which regenerates the 'active' form upon a second PCET process and subsequent release of H_2O_2.[31–33]

A further representative of type II copper active sites can be found within the copper containing nitrite reductase (CuNiR) enzyme, which occurs in plants and bacteria and is elementary for denitrification, i.e. the conversion of nitrate into N_2 and nitrogen oxides (NO, N_2O).[36,37] The active center of the CuNiR can be regarded as a combination of a type I and a type II center. Hereby the type I center provides electrons for the type II center, where substrate binding and reduction (Figure 3) occurs.[38,39] While the exact reaction sequence is still a matter of debate, a reduced type II Cu^{I} center with a coordinated nitrite can be regarded as the active intermediate for N–O cleavage.[40–43] After protonation of the bound nitrite and subsequent oxidation of the Cu^{I} site, nitric oxide is released.

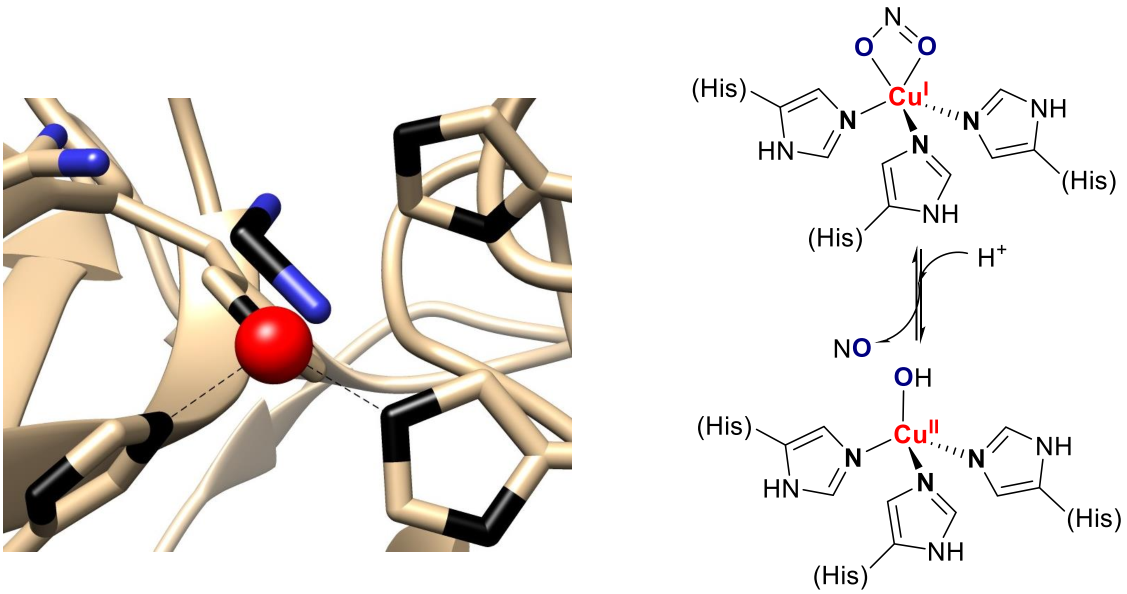

Figure 3. Type II active site in nitrite reductase (left), showing the nitrite anion bound to the copper(II) ion. (PDB:1SJM[39]) and on the right the reduced Cu^{I} nitrite intermediate responsible for NO cleavage. [40–43]

2.3 Type III Example: Hemocyanin

Type III copper proteins are able to bind molecular dioxygen and can either act as simple oxygen carriers or perform the oxidation and oxygenation of substrates.[44,45] The enzyme hemocyanin as an example of those proteins in molluscs and vertebrates can be regarded as an analog to hemoglobin in mammals and is required for O_2 transport in those organisms.[46] Enzymes like tyrosinase and catechol oxidase are not restricted to the transport of dioxygen but are also able to perform the oxidation of *ortho*-diphenols to the corresponding dichinones as well. Additionally, tyrosinase catalyzes the hydroxylation of monophenols to *ortho*-diphenols, a process that requires the activation of a C–H bond.[47] One characteristic common to all of those enzymes is the coordination of two copper ions by three histidine ligands each, forming the active site (Figure 4).

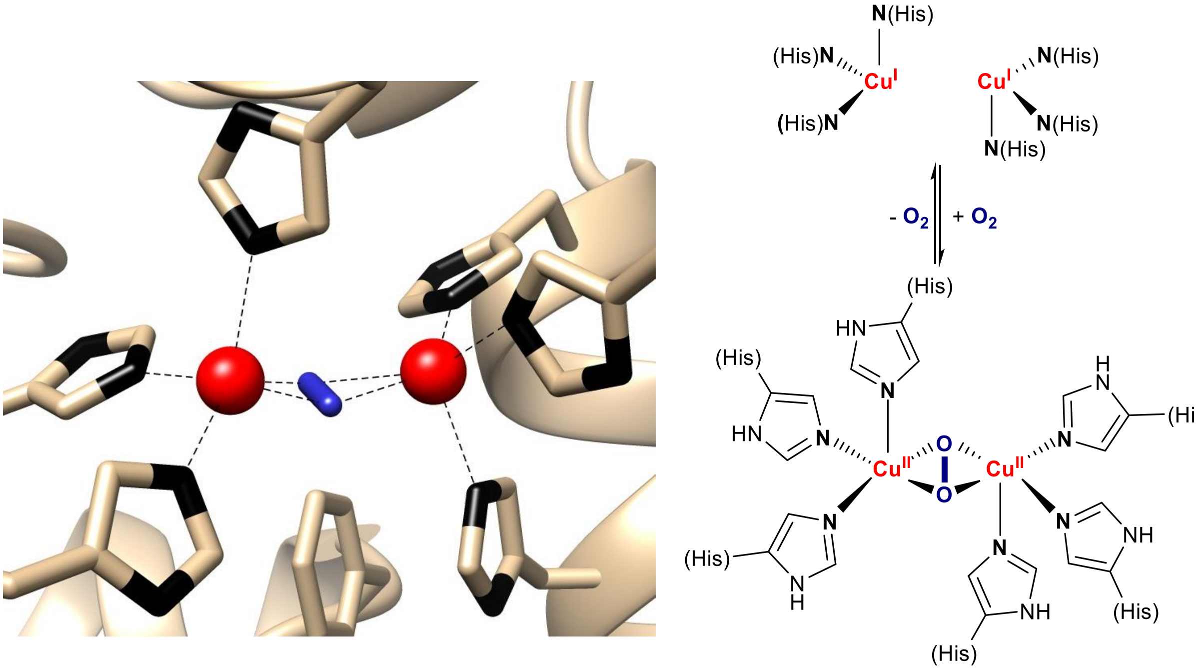

Figure 4. Active center of hemocyanin (left, PDB: 1OXY[48]), revealing a peroxo bridged binding motive and schematic representation of the reversible binding of dioxygen (right) within type III copper proteins.[47]

In the context of dicopper(II) active sites their magnetic properties are often investigated, since those might indicate structural properties and possible binding motifs of coordinated ligands. Two Cu^{II} ions that that are spanned by a bridging ligand (Figure 5), e.g., a peroxide, might have different magnetic ground states according to the extent of orbital overlap between metal ion and the bridging ligand.

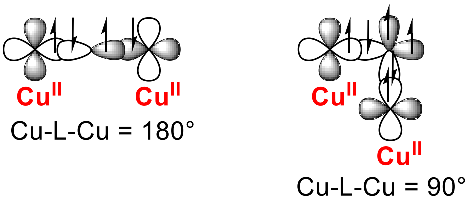

Figure 5. Possible magnetic coupling pathways for bridged dicopper(II) centers.[14]

A so called ‘superexchange’ pathway occurs when the Cu-L-Cu angle is 180°. In this situation the half-occupied d-orbital of the Cu^{II} overlaps with the filled valence orbital of the bridging ligand, leading to spin polarization of one of the electron spins and consecutively pairing. Overlap of the second Cu^{II} d-orbital with the remote polarized electron spin therefore leads to an antiferromagnetic coupling and an overall spin state of $S = 0$. However, if the magnetic orbitals of the two Cu^{II} ions overlap with orthogonal orbitals of the bridging ligand, thus Cu-L-Cu 90°, the exchange interactions of the electrons will lead to a ferromagnetic spin state with $S = 1$.[14]

Those features were also considered by Metz and Solomon to describe the binding and subsequent activation of dioxygen by hemocyanin (Scheme 1). Binding proceeds via oxidation of the Cu^{I} to Cu^{II} ions, which is accompanied by the reduction of O_2 to generate a bridging peroxide. The resulting μ-η^2:η^2-peroxo binding motive was first elucidated with the help of model complexes (see Section 3.2.1) and favors a singlet ($S = 0$) ground state due to strong antiferromagnetic coupling of the Cu^{II} ions.[49] As oxygen approaches the binuclear metal site, charge is continuously transferred from the Cu^{I} ions to orthogonal π* orbitals of oxygen.[50] As these proceeds, the resulting unpaired electrons of the copper ions are initially ferromagnetically coupled ($S = 1$) due to the nearly orthogonal overlap situation for the magnetic orbitals.[14]

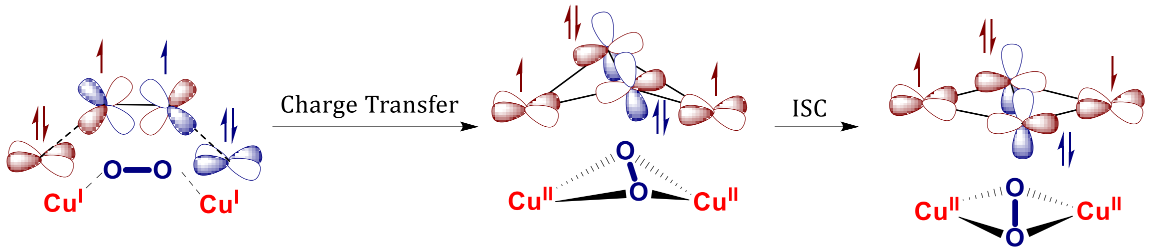

Scheme 1. Schematic representation of proposed steps for O_2 binding at the active center of Hemocyanin. S/T ISC= Singlet triplet intersystem crossing.[51,52]

The hereby formed butterfly structure experiences a decrease of its distortion, whereby orthogonality of the magnetic orbitals also decreases. Finally, this leads to a superexchange pathway between both copper ions, resulting in a singlet to triplet intersystem crossing (ISC), whereby the singlet state ($S = 0$) is highly stabilized.[50]

Based on this electronic structure, characteristic spectroscopic properties arise that can mainly attributed to interactions of the π* orbital in the Cu_2/O_2 plane with the $d_{x^2-y^2}$ orbitals of both copper ions.[49] The observed intensity of this π* to Cu^{II} charge transfer transitions around 350 nm ($\varepsilon \approx 20\,000$ M^{-1} cm^{-1}) and 550 nm ($\varepsilon \approx 1000$ M^{-1} cm^{-1}) reveals the magnitude of donor interactions between peroxide and Cu^{II} ion. Further, due to the strong antiferromagnetic coupling, the μ-η^2:η^2 binding mode leads to no EPR signal and relatively low O–O stretching vibrations in the resonance RAMAN spectrum, resulting from backbonding from the copper(II) ions into the π* orbital of the peroxide and therefore weakening the O–O bond.[14] Additional details concerning the electronical structure and spectroscopical features of Cu_2/O_2 binding motives will be discussed in Section 3.

2.4 Multicopper Oxidase Example: Laccase

Laccase as well as enzymes like caeruloplasmin, bilirubin- and ascorbate oxidases are multicopper oxidases (MCO).[14,53] Their active site (Figure 6) is composed of the previous described copper active sites I-III and contains a Cu cluster (combination of Type II and III) where the substrate is oxidized and oxygen is reduced to water and a type I copper center, which is responsible for electron transport.[54–57]

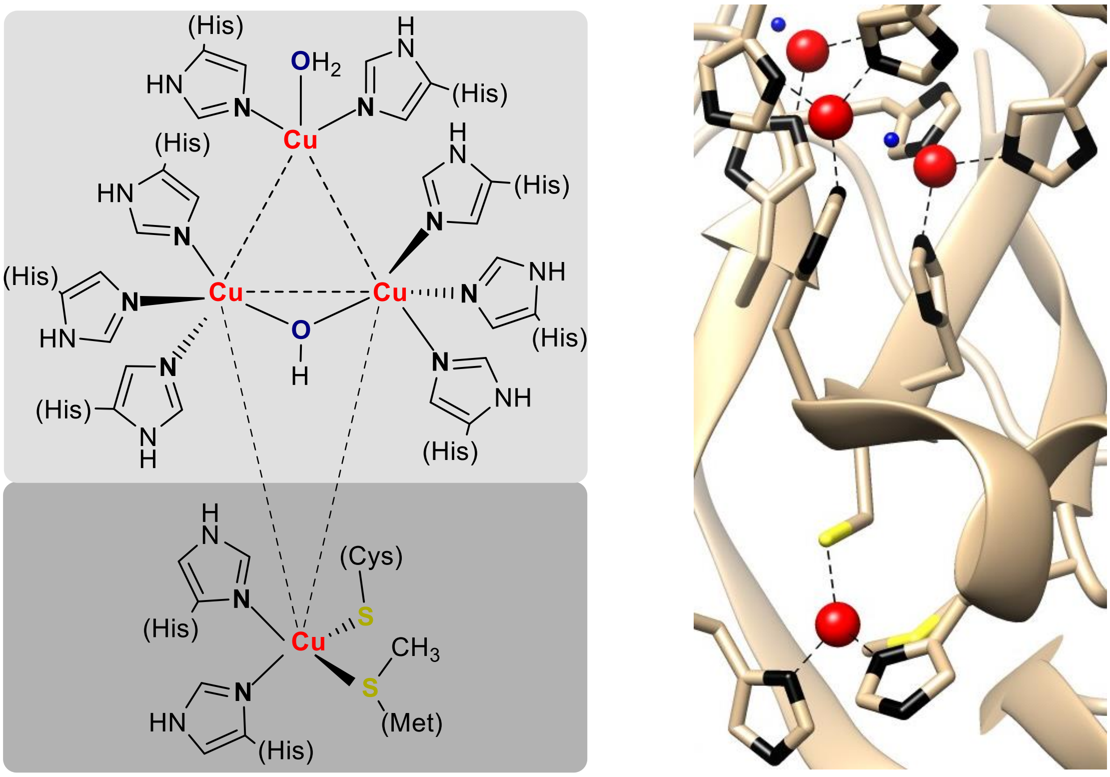

Figure 6. Multicopper oxidase (MCO) active site as in laccase.[56,58,59] Highlighted areas showing the assembly of a type I (dark grey) and a type II/type III (light grey) copper cluster.

With the help of extensive mechanistic studies, the process of the four electron reduction of dioxygen to water was elucidated (Scheme 2).[51,60] Hereby, the fully reduced trinuclear cluster reacts with oxygen and forms the so-called 'peroxide intermediate' (PI).[61,62] This dioxygen reduction is coupled to the oxidation of two Cu^{I} to Cu^{II} ions of the trinuclear cluster.

It should be noted that the newly formed PI shows different spectroscopic properties than the previously described μ-η^2:η^2-peroxide (Section 2.3), which should therefore not be correlated to the active center of MCOs. Calculations indicated a μ_3-1,1,2 binding mode in which all three Cu ions are bridged by the peroxide.[51] Subsequently, the oxygen-oxygen bond is cleaved, and the PI is transformed into the so called 'native intermediate' (NI), which proceeds by transfer of at least one electron from the type I center. In this intermediate, all four copper ions are oxidized to the Cu^{II} oxidation state, forming a μ_3-oxo and μ_2-hydroxide bridge and thus completing the $4e^-$ reduction of oxygen.[49,59,63] The fully reduced intermediate is regained upon fast proton coupled electron transfer (PCET) due to the high basicity of the μ_3-oxo core.[64,65]

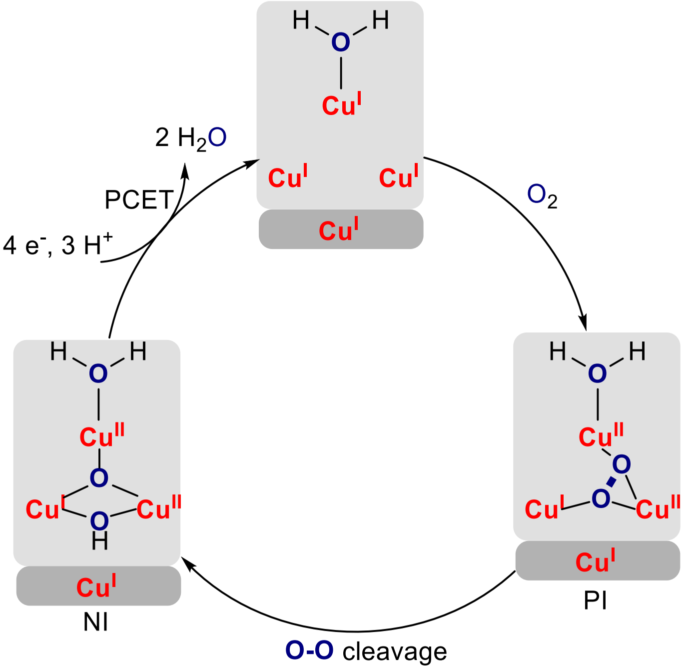

Scheme 2. Mechanism for the 4**e**$^-$ reduction of oxygen to H_2O at multicopper oxidases.[51]

2.5 Heme-Copper Oxidase Examples: Cytochrome *c* Oxidase and N_2O Reductase

Cytochrome *c* Oxidase (C*c*O) belongs to the class of heme-coppper oxidases and is essential for respiration. The active site catalyzes (like MCOs) the 4e⁻ reduction of O_2 to 2 H_2O and features a key role in the process of proton-pumping, which is utilized by the ATP synthase.[66] The active center of O_2 reduction in C*c*O is displayed in Scheme 3, containing a copper ion, so called Cu_B, coordinated by two regular histidines and a third histidine covalently linked to the phenol of tyrosine and with a heme iron center in proximity of 4.3-5.4 Å.[14]

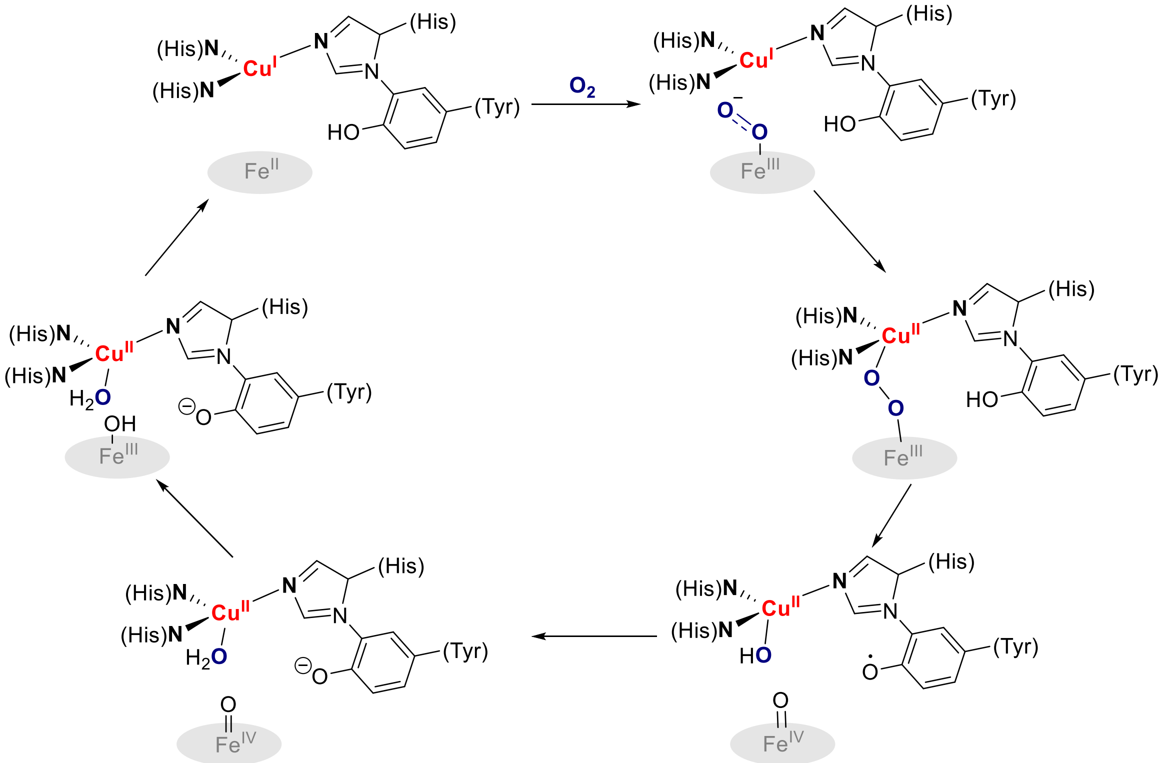

Scheme 3. Mechanism of the 4**e**⁻ reduction of O_2 to H_2O in heme copper oxidases. For simplification the coordination site of heme iron is not depicted.[67]

Hereby, the fully reduced Cu^I Fe^{II} core initially forms a Fe^{III}-superoxide adduct with dioxygen, which could be verified by resonance RAMAN experiments. Subsequently, fast O–O cleavage and transformation to a Fe^{IV}-oxo species, cupric hydroxide and a tyrosyl radical is observed.[67] Three electrons of the 4e⁻ reduction of dioxygen are provided by the oxidation of Fe^{II} to Fe^{IV} and Cu^I to Cu^{II} and the last electron is transferred via hydrogen atom transfer (HAT) of the cross linked tyrosine residue. Further, computational investigations as well as model chemistry also imply that the process of O–O cleavage proceeds via a reactive peroxo species, even though an intermediate has not been observed experimentally so far.[68–70]

All heme-copper oxidases also contain an additional low-spin heme site, coordinated by two axial histidins, which is responsible for transferring electrons to the catalytic heme/Cu_B site, the electrons originate from further redox cofactors, e. g. Cu_A sites and/or heme(s). Those Cu_A sites contain (Figure

7) two copper ions bridged via two cysteine-thiolates, yielding a Cu_2S_2 diamond core structure which shows an intense purple color, originating from a S(Cys) to Cu charge transfer (LMCT).[71,72] The coordination sphere of the metal ions is complemented by one histidine each and a methionine for one copper ion and an oxygen donor of a peptide bond for the other copper ion. The active site of Cu_A enables fast electron transfer by switching between the fully delocalized $Cu^{1.5}/Cu^{1.5}$ and the Cu^I/Cu^I redox states.[73,74]

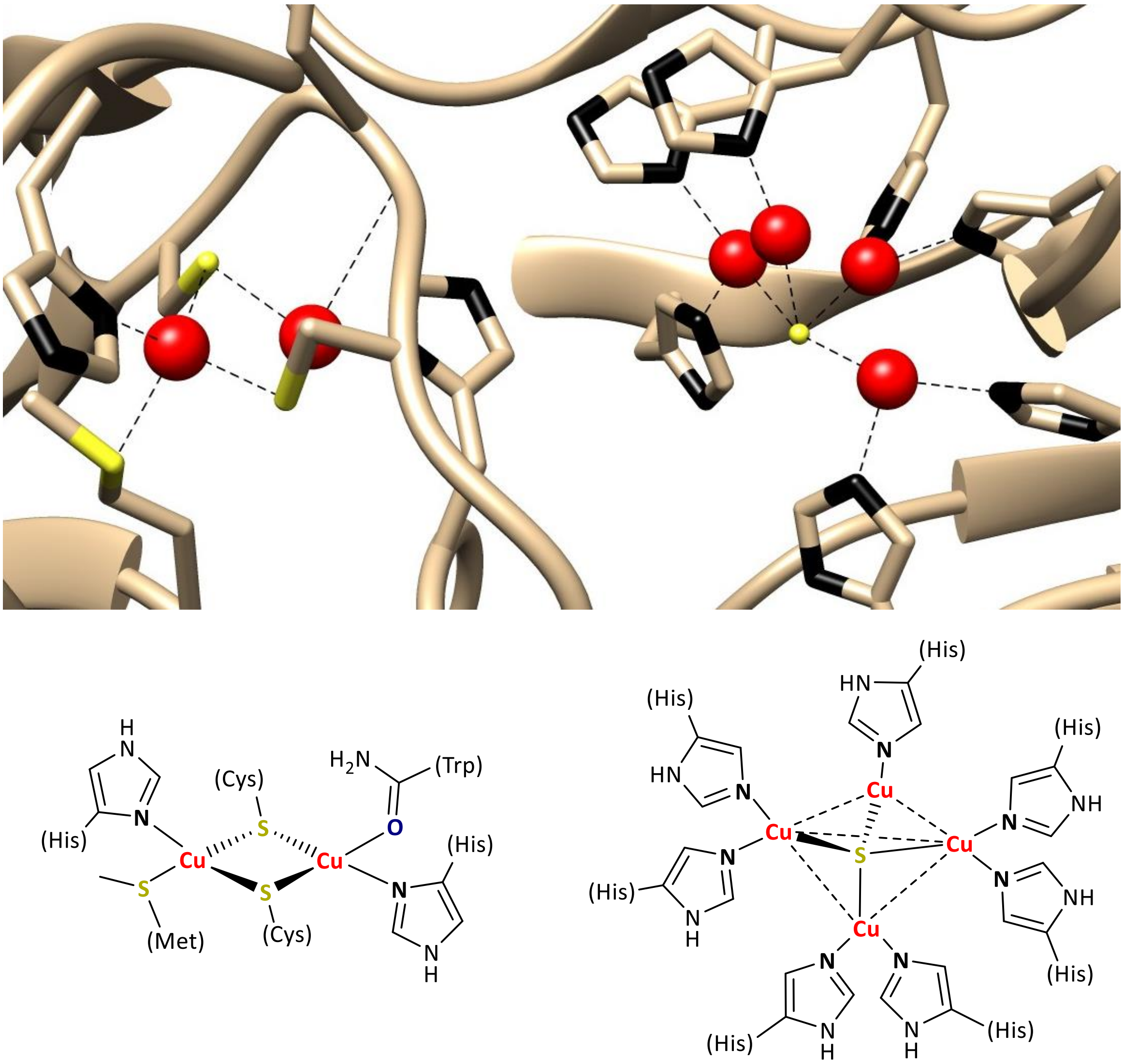

Figure 7. Active site of N_2O reductase, containing a Cu_A (left) and Cu_Z (right) center (PDB:1FWX).[72,75]

As already mentioned in Section 2.2, copper containing enzymes play an important role in the denitrification process. The final 2e⁻ reduction of nitrous oxide to dinitrogen and water is also performed by a copper enzyme, namely N_2O reductase, which contains a Cu_A active site for electron transfer and a tetranuclear Cu_Z active site with a μ_4-bridging sulfide for substrate binding (Figure 7).[76,77] The exact mechanism of the final denitrification step is still a topic of ongoing debate,[78–80] also due to the structural differences aerobically and anaerobically prepared N_2O reductases have, namely the loss of one bridging sulfide ligand.[81,82]

2.6 pMMO and LPMO

In the last couple of years cupric metalloenzymes that can activate C–H bonds have received more and more attention, whereby the conversion of inert aliphatic compounds under mild conditions as efficient as metalloenzymes is actively researched.[83–88]

Copper containing enzymes, such as the particulate methane monooxygenase (pMMO) are able to perform such reactions. More precisely, pMMO can be found in methanotrophic bacteria that are able to convert methane via hydroxylation to methanol. The active site of pMMO is still investigated and mechanistic studies are a topic of ongoing debate.[88]

Similar to pMMO the copper containing lyctic polysaccharide monooxygenase (LPMO) is able to activate C–H bonds. Instead of methane, LPMO can degrade cellulose, chitin, and other polysaccharides by C–H bond activation. The general active site of LPMO is depicted in Figure 8. The single copper ion is coordinated by a histidine and a second histidine and its side chain nitrogen atom, which is called the 'histidine brace'.[85,89] Further structural varieties can arise, according to the respective LPMO. The exact molecular mechanism and active oxidant of LPMOs is still investigated and remains elusive. In this context the involvement of cupric superoxo, hydroperoxo and even oxyl species are discussed to enable the catalysis of LPMO.[90]

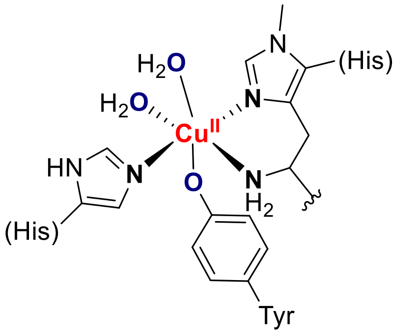

Figure 8. Representative active site of LPMO, containing the characteristic 'His-brace' binding motive.[85,89,90]

Besides pMMOs and LPMOs there are various other cupric monoxygenases, like Peptidylglycine-α-hydroxlating monooxygenase (PHM) and Dopamine-β-Monooxygenase (DβM) that are able to activate C–H bonds, demonstrating the broad range of catalytic reactions mediated by copper containing enzymes, and the necessity to investigate those in detail.[91,92]

3 Model Complexes of Copper Active Sites

In the last section the broad versatility of copper active sites in nature was demonstrated, revealing their ability to oxidize substrates and to interconvert dioxygen and water. Comprehension of these mechanisms and therein involved species has been an ambition over decades in the field of bioinorganic chemistry.[14,26,60,93,94] Over this timeframe low-molecular copper/oxygen model complexes have been developed and studied, which helped to elucidate mechanisms and putative key intermediates of the parent copper enzymes (Scheme 4). It should also be noted that copper oxygen complexes in this thesis will be named according to the peroxo/superoxo/hydroperoxo nomenclature, which is common in the bioinorganic community. Although, according to recommendations by IUPAC, more precise naming of such complexes would be peroxido/superoxido/hydroperoxido.

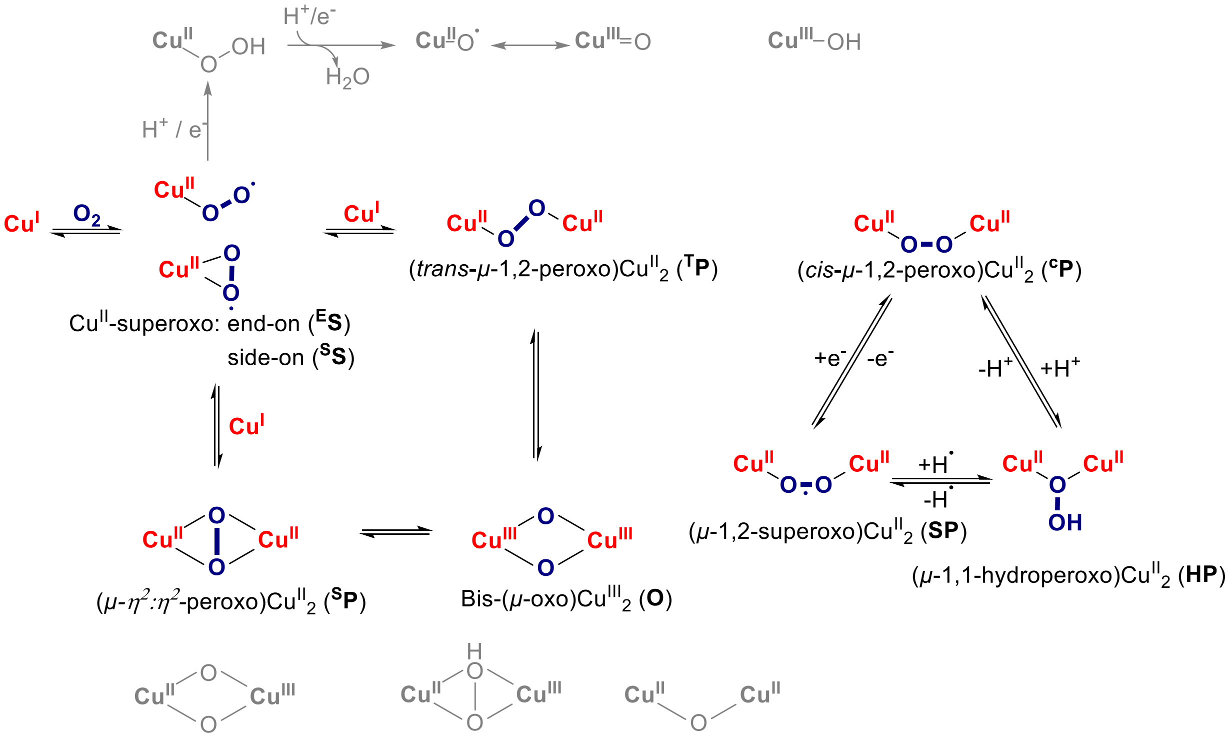

Scheme 4. Overview of isolated copper oxygen adducts, potentially relevant in bioinorganic processes.[14,95] The binding motives which will be discussed in more detail in this work are colored.

Furthermore, as described vide supra (Section 2.2 and 2.3), certain copper enzymes are able to activate C–H bonds (LPMOs, PHM, pMMO and tyrosinase) and therefore might be a starting point to design new catalysts that are able to convert substrates relevant for renewable energy sources.

Thereby, a huge variety of ligand scaffolds has been developed containing mainly N but also O and S donors forming mononuclear or dinuclear complexes to mimic the natural binding site of copper ions (Figure 9).[15] Steric demand, flexibility and substituents of the ligands have a tremendous impact on the electronic structure and reactivity of the desired copper oxygen complexes. In this context, the formation of potential intra- and intermolecular hydrogen bonds should also be considered since those might have strong influence on potential complex stability and reactivities.[96,97]

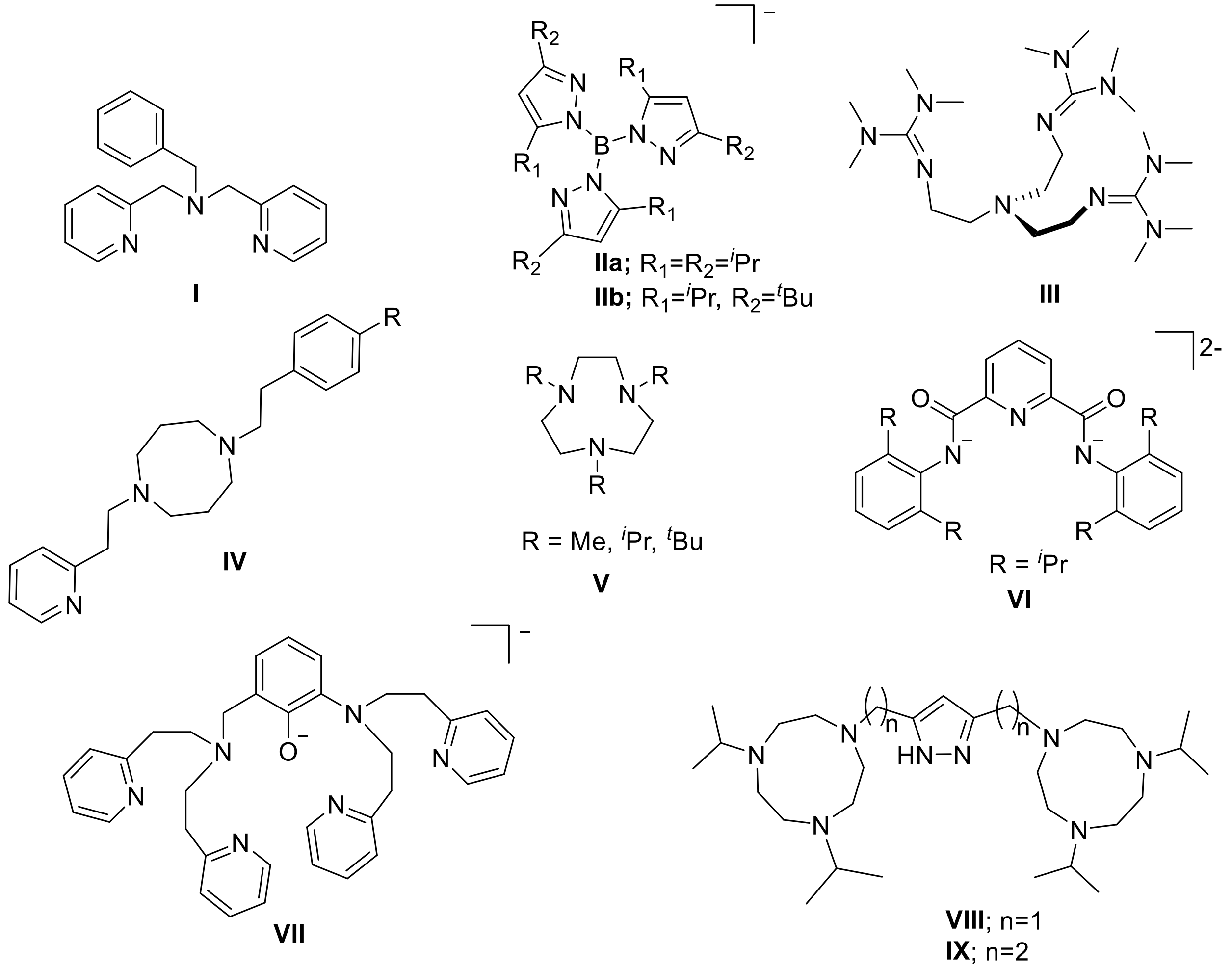

Figure 9. Selection of established ligand systems that stabilize copper/oxygen motivs.[15]

Hence, it should also be noted that the herein presented ligands are only a limited selection of the large number of versatile ligand frameworks used in bioinspired copper/dioxygen chemistry.

3.1 Mononuclear Copper Oxygen Complexes

The ligand frameworks **I-V** initially form mononuclear copper oxygen adducts. Upon reaction of the corresponding Cu^{I} complex with dioxygen, or of the Cu^{II} complex with superoxide, formation of either end-on η^1 (^{E}**S**) or side on η^2 superoxide (^{S}**S**) intermediates (Scheme 4) is observed. Since those mononuclear complexes are often transient intermediates to the formation of dinuclear complexes via dimerization, specific ligand design is required for stabilization.

Those mononuclear complexes exhibit an intense electronic absorption feature around 400 nm ($\varepsilon \approx 1000\ M^{-1}cm^{-1}$), originating from a O_2 to Cu ligand to metal charge transfer (LMCT). Further O–O and Cu–O vibrations can be observed between 950 cm^{-1} and 1200 cm^{-1}, respectively 430-560 cm^{-1}, in the resonance RAMAN spectrum.[15] The relatively broad energetic range of O–O vibrations for various η^2 complexes can be explained by considering the resonance structures of the η^2 binding mode, namely a copper(II) superoxide versus a copper(III) peroxide complex and therefore the extend of O_2 reduction, which is reflected by the O–O stretching frequency, respectively bond order. Hereby, stabilization of the Cu^{III}-O_2^{2-} species with strong electron-donor ligands was observed and therefore highlighting the influence of the ligand design on electronic properties, such as the extend of charge transfer from the metal ion to the oxygen ligand.[15]

The first structurally characterized η^2-superoxo complex **X** (Figure 10) from FUJISAWA,[98] contains a tris(pyrazolyl)borate with bulky substituents at the 3 and 5 positions of the pyrazolate to prevent the commonly observed dimerization to the dicopper species, which occurs upon binding of a second Cu^{I} ion and subsequent electron transfer (Section 3.2.1).

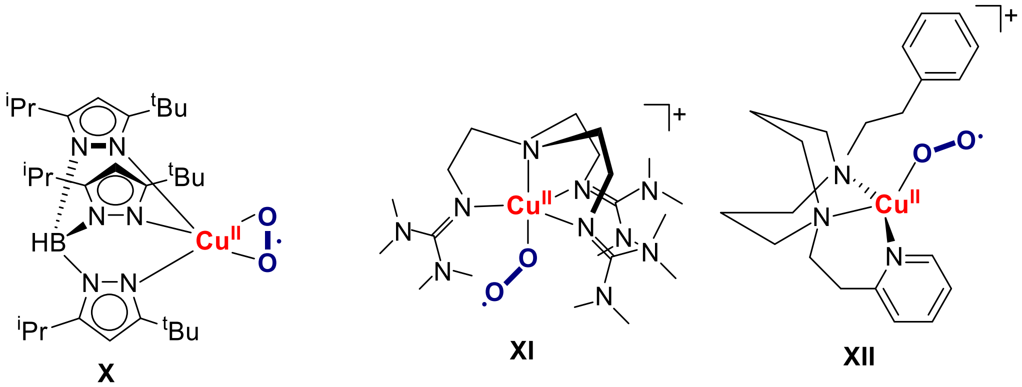

Figure 10. Mononuclear copper/oxygen complexes exhibiting η^2 (**X**[98]) and η^1 superoxo binding motives (**XI**[99,100], **XII**[92])

Thus, the first isolation of an end on η^1-superoxo complex suitable for X-ray diffraction was achieved by using TMG_3tren, a bulky ligand framework with strong N-donor properties, to stabilize the superoxo complex **XI**.[99,100] Interestingly, treatment of **XI** with CF_3CO_2H led to the formation of an adduct via H-bonding of the distal superoxide to the hydrogen atom of the carboxylic acid, which could also be observed by a blue shift of the characteristic LMCT band of 62 nm and an increase of the O–O vibration of 30 cm^{-1}.[101] Those hydrogen bonding properties, observed by KARLIN and coworkers,[102] demonstrate the necessity to not only considerate ligand design but also hydrogen bonding in the context of copper/oxygen model complexes.

Further, Itoh *et al.* were able to isolate the superoxo complex **XII**[92] with a relatively simple ligand framework and demonstrated its ability to perform intramolecular hydroxylation and therefore the activation of a C−H bond, which also occurs in enzymes like PHM, DβM, LPMO and Galactose Oxidase (Section 2.6).[14] Additionally, there are more mononuclear copper oxygen adducts, such as alkyl/hydroperoxide or high valent hydroxide species which show interesting properties but would extend the scope of this thesis and are therefore not further discussed.[90,103]

3.2 Binuclear Copper Oxygen Complexes

3.2.1 Peroxo Model Systems

There are various isomeric structures of dicopper dioxygen complexes, differing in the hapticity of the dioxygen bridging ligand. However, the *trans*-μ-1,2-, μ-η^2:η^2-peroxo, bis(μ-oxo) and recently isolated *cis*-μ-1,2-peroxo binding motives can be regarded as the most prominent cores in Cu_2/O_2 research and will be discussed consecutively.

As already stated in the previous section, mononuclear copper dioxygen complexes tend to dimerize if not stabilized by ligand design, to the corresponding dicopper complexes, which are depicted in Figure 11. Those exemplary model complexes of Karlin[104] and Kitajima[105] were used to elucidate the binding motive in type III dicopper proteins by comparison of distinct spectroscopic features before molecular structures of the oxy forms of the enzymes were available. In particular, Oxy-Hc exhibits an intense charge transfer band in the UV/Vis spectrum around 350 nm (ε ≈ 20000 M^{-1} cm^{-1}), originating from the peroxide→copper(II) transition and an O−O vibration at 749 cm^{-1} ($\Delta^{16}O_2{-}^{18}O_2$ = 41 cm^{-1}). Both have been also observed for Kitajima's tris(pyrazolyl)borate complex **XIV**, which is distinctive for side on bound μ-η^2: η^2-peroxo dicopper adducts.

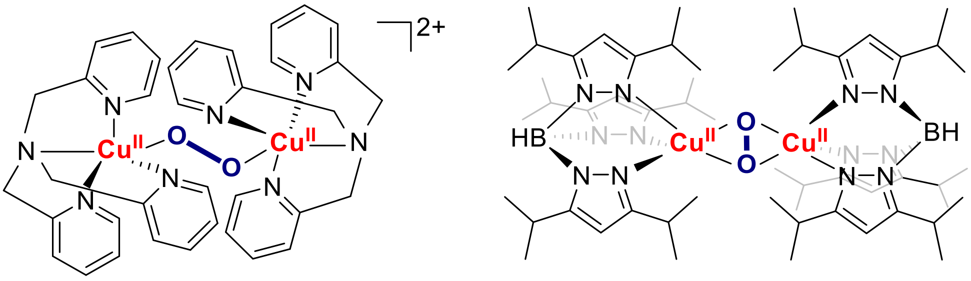

XIII **XIV**

Figure 11: Exemplary model systems for *trans*-1,2 (^{T}**P**) and μ-η^2: η^2 peroxo (^{S}**P**) binding motives.[104,105]

In comparison to this, Karlin's complex **XIII** exhibited characteristic electronic absorptions around 525 and 590 nm and an O−O vibration at around 832 cm^{-1} ($\Delta^{16}O_2{-}^{18}O_2$ = 45), being typical for the ^{T}**P** binding motive. The intensity and energy of the O_2^{2-} →Cu^{II} charge transfer bands in Karlin's complex is about half the intensity of that in Kitajima's presented complex **XIV** (Figure 12), which is due to the different hapticity of the end-on and side on bridged peroxide and the therefore resulting decreased number of donor interactions between peroxide and Cu^{II} ions (2 vs. 4 donors).

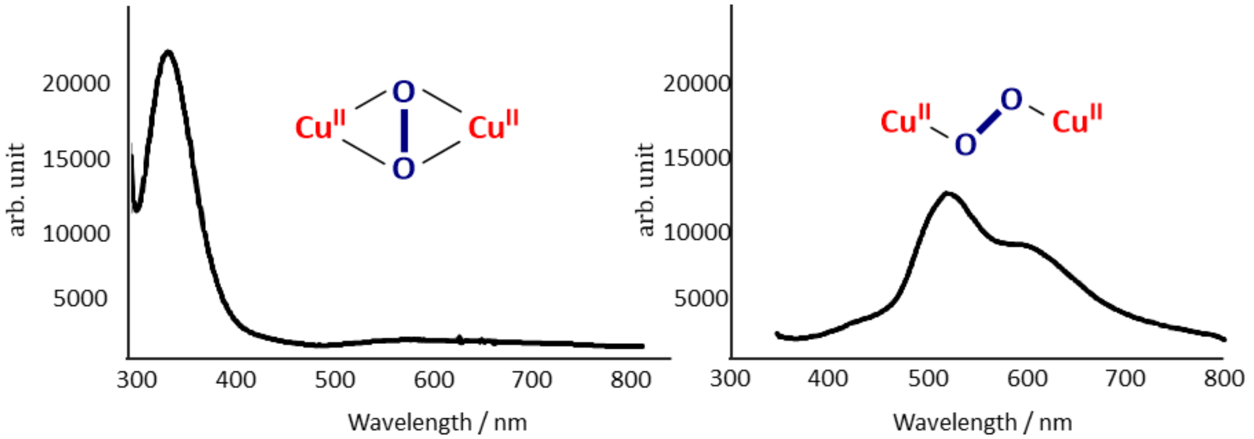

Figure 12. Schematic UV/Vis absorption spectra of side on and end on bridged peroxodicopper(II) complexes.[14]

The doubly degenerated π* HOMO set of the bridging peroxide splits in energy upon binding to the copper ions, whereby the π_σ^* orbital interacts strongly with the LUMO (symmetric combination of the $d_{x^2-y^2}$ orbitals) and the π_v^* orbital rather weakly with the Cu^{II} ions (Figure 13).[51] The strong π_σ^* (O_2^{2-}) → Cu^{II} LUMO interactions results in the mentioned characteristic charge transfer, responsible for the purple color. While this transfer of electron density from the anti-bonding π* peroxide orbital would in principle increase the O–O vibration, the observed decrease of the O–O vibration from the $^{\mathrm{T}}$**P** to the $^{\mathrm{S}}$**P** binding mode can be explained by considering the binding interaction of the σ* orbital of the peroxide with the copper-centered HOMO.[59] This back-bonding interaction transfers electron density from the copper ions into the anti-bonding orbitals of the peroxide, in fact lowering the frequency of the O–O vibration.[106]

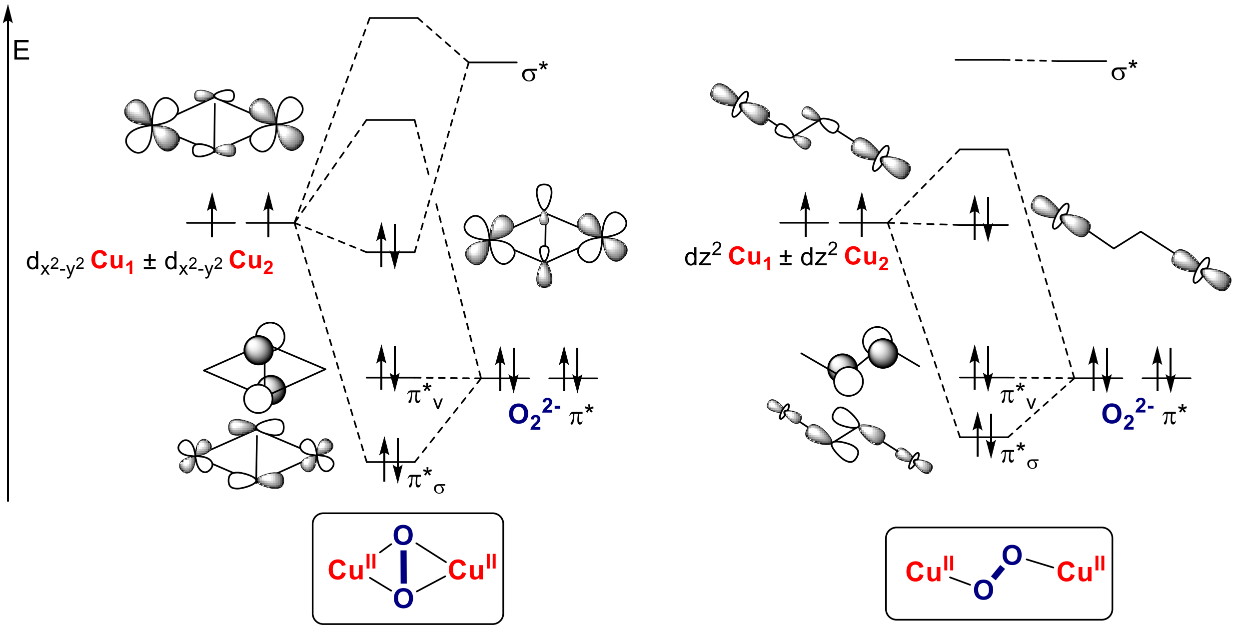

Figure 13. Approximate MO diagrams for the Cu_2/O_2 side on and end on bridged peroxodicopper(II) isomers. Copper d orbitals are drawn at the same energy.[14,107]

Those contributions are also the explanation for the strong antiferromagnetic coupling ($-2J \geq 600$ cm^{-1}) of side on bound peroxo complexes, due to the large HOMO/LUMO splitting.[14]

Furthermore, the μ-η^2:η^2-peroxodicopper(II) and the bis(μ-oxo)dicopper(III) core can be interpreted as valence tautomers (Figure 14). Stabilization of one isomer over the other can be controlled via reaction conditions, such as solvents or ligand design. Tolman and coworker observed the formation of a μ-η^2: η^2 peroxodicopper(II) complex **XV** upon exposure of a monocopper complex with a 1,4,7-triazacyclononane (tacn) ligand to air at low temperatures.[108] Remarkably, by changing the solvent, the corresponding bis(μ-oxo)dicopper complex **XVI** formed, which could be distinguished by their characteristic electronic absorption spectra and the disappearance of the O–O vibration in the resonance RAMAN spectrum for complex **XV** as well as the appearance of breathing vibrations of the Cu_2O_2 diamond core.[108,109]

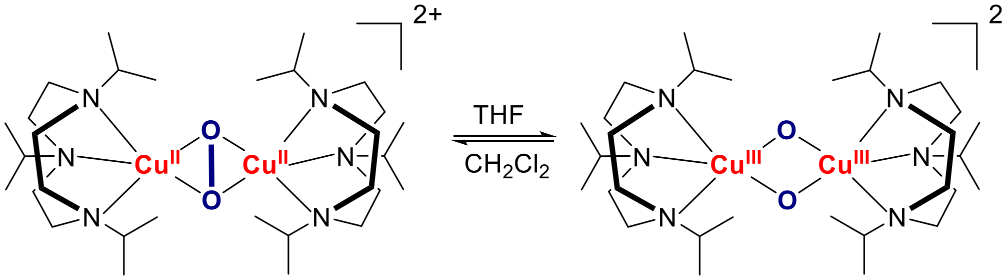

XV **XVI**

Figure 14. μ-η^2: η^2 -peroxodicopper(II) and bis(μ-oxo)copper(III) complex equilibrium based on a tacn ligand scaffold.[108]

Although bis(μ-oxo) complexes are not an essential part of this work, they should be recognized as important species because of their possible involvement in enzymatic processes.[110,111]

As already stated in Section 2.3 binding of dioxygen at the hemocyanin active site and formation of the antiferromagnetically coupled (S = 0) dicopper(II) center proceeds via an intermediate with near orthogonal overlap of the magnetic orbitals of the Cu_2O_2 core in which both Cu^{II} ions are ferromagnetically coupled (S = 1). By employing the compartmental pyrazolate/tacn hybrid ligand **L^1**, Meyer and coworkers could isolate and structurally characterize two model complexes (Figure 15) representing snapshots of such O_2 binding trajectory at type III copper centers.

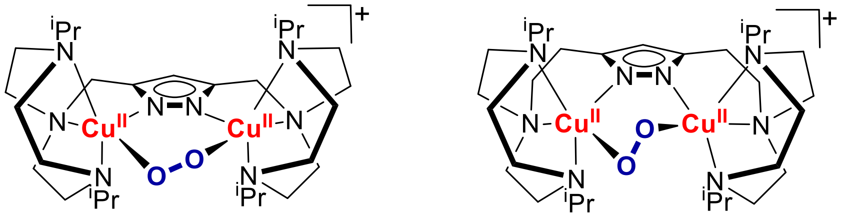

XVII **XVIII**

Figure 15. Pyrazolate/tacn hybrid ligands **L^1** and **L^2** enabling the isolation of μ-η^1:η^1 peroxo complexes **XVII** and **XVIII**.[52,112,113]

Modification of the ligand scaffold by elongating the linker units between the tacn side arms and the central pyrazolate bridge (**L^2**) induces a shorter Cu···Cu distance and consequently a tilting of the peroxo unit within the bimetallic pocket.[112] Remarkably, the elongation of the linker between the pyrazolate and the tacn compartment had also dramatic influence on the magnetic properties of the respective peroxodicopper(II) complexes **XVII** and **XVIII**. Thus, complex **XVII** shows comparatively weak antiferromagnetic coupling, attributed to the overlap of magnetic orbitals reflected by a relatively small Cu–O–O–Cu torsion (ϕ = 55°).[113] In comparison, peroxo complex **XVIII** exhibits a torsion angle close to 90°, which is the intermediate state where the superexchange pathway breaks down, switching from the singlet to the triplet ground state. Indeed, complex **XVIII** exhibits strong ferromagnetic coupling and an S = 1 ground state and is therefore the only one of its kind, until now.[112]

Interestingly, the shorter linker between pyrazolate and tacn units of the ligand scaffold **L¹** employs a more exposed Cu_2O_2 core in complex **XVII** enabling the interaction with LEWIS acids (Figure 16). Hence, MEYER and coworkers could show strong interaction of alkali metal ions (Li^+, Na^+, K^+) with **XVII** in solution and the solid state, affecting the Cu–O–O–Cu torsion angle and also the magnetic exchange coupling of the Cu^{II} ions. [52,113]

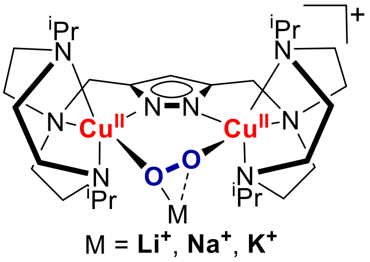

M = **Li⁺**, **Na⁺**, **K⁺**

XVII+M

Figure 16. Peroxodicopper(II) complex **XVII** enables the isolation of alkali metal ion adducts in solution and the solid state.[52,113]

The potential capability of metal-ion binding events to stabilize novel reactive fragments and to control O_2 activation in biomimetic systems was also recently highlightes by ROBINSON and coworkers, who reported the reversible interconversion of the *cis* and *trans* peroxo complexes **XIII^{cis}** and **XIII^{trans}** mediated by Ca^{2+} binding at the Cu_2O_2 core (Scheme 5).[114]

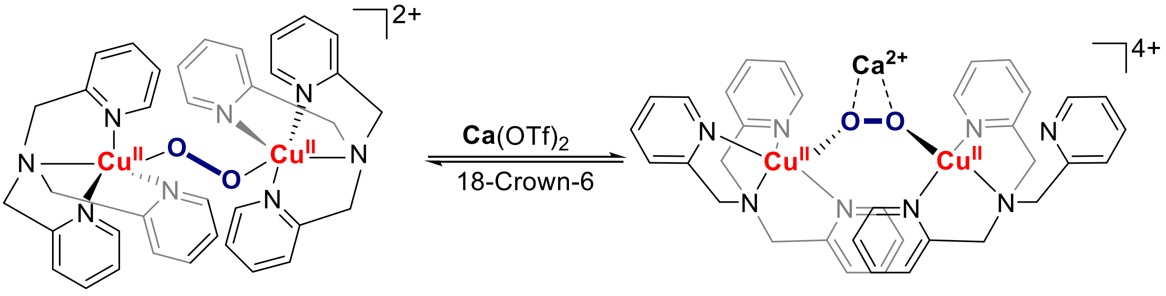

XIII^{cis}

XIII^{trans}

Scheme 5. Reversible interconversion of **XIII^{cis}/XIII^{trans}** mediated by $Ca(OTf)_2$.[114]

Earlier KARLIN and coworkers demonstrated that addition of $Sc(OTf)_3$ mediated the reversible interconversion of a side-on bound peroxo complex and a dicopper(III) bis(μ-oxo) complex by promoting dissociation of the axillary-bound tertiary amine donor of the N-methyl-N,N-bis[3-(dimethylamino)propyl]amine (MeAN) ligand.[115] Besides those metal-ion binding interactions, the influence of hydrogen bonding interactions on copper-oxygen species is barely understood. Previous work of SZYMCZAK and coworkers reported a *trans*-1,2-peroxodicopper(II) complex stabilized by H-bonding groups of the modified tris(2-pyridyl-methyl)amine (tpa) ligand framework, revealing significant influence of the intramolecular hydrogen bonds on thermal stability of the peroxo complex.[116]

3.2.2 Superoxo Model Systems

While the synthesis of mononuclear superoxo complexes is achieved by preventing the dimerization process through specific ligand design, the synthesis of dinuclear superoxo complexes usually requires a different approach. The scarce literature known examples of dinuclear superoxo complexes were synthesized by chemical or electrochemical oxidation of the corresponding peroxo complex or upon addition of dioxygen to a mixed valent Cu^{I}/Cu^{II} complex.[117,118] For example, the unsymmetric binucleating ligand framework **VII** allowed for isolation of such a mixed valent Cu^{I}/Cu^{II} compound. The corresponding superoxo complex **XXI** exhibits intense absorption features around 400 nm ($\varepsilon \approx 5400$ M^{-1} cm^{-1}) and 635 nm ($\varepsilon \approx 670$ M^{-1} cm^{-1}), which is common for dinuclear superoxo complexes. In case of **XXI** two isotope sensitive features around 1100 cm^{-1} were observed in the Raman spectrum, originating from the two μ-1,1- and μ-1,2-superoxide isomers. Similar properties were also observed for structurally related superoxo complex **XXII.**[118,119]

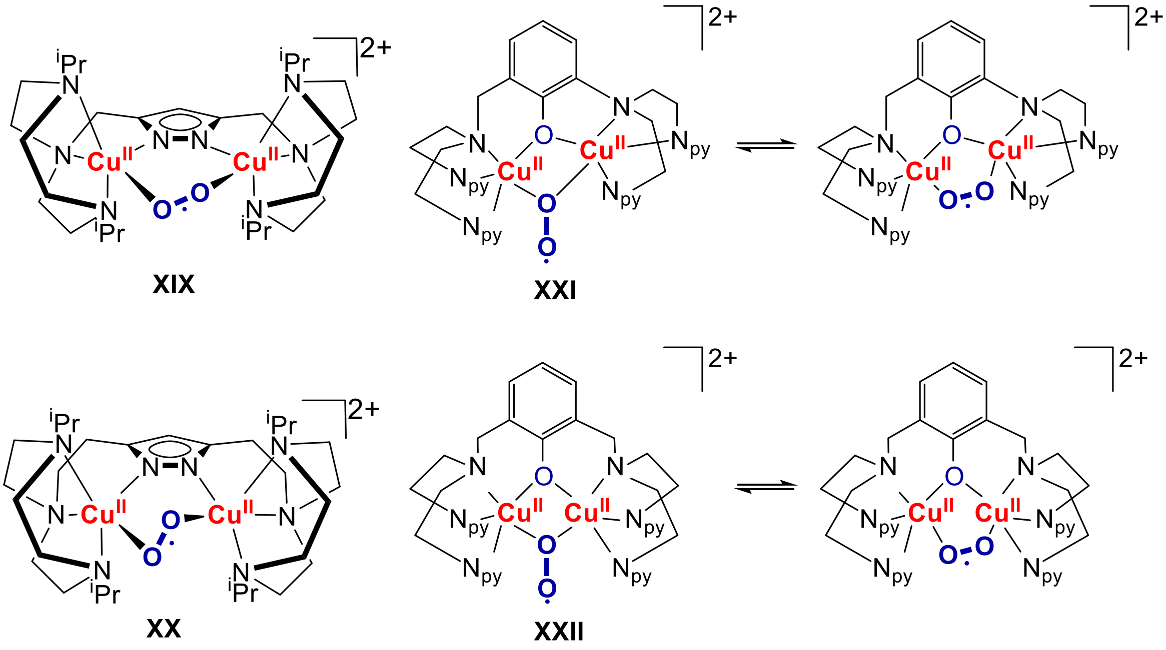

Figure 17. μ-1,2-superoxo complexes **XIX** and **XX** as well as both isomers of superoxo complexes **XXI** and **XXII.**[118–120]

Further examples derive from (electro)chemical one-electron oxidation of the peroxo precursors to yield **XIX** and **XX.**[113,117] Both complexes show intense absorption bands at around 440 nm ($\varepsilon \approx$ 10000-11000 M^{-1} cm^{-1}) and shoulders around 550 nm ($\varepsilon \approx 2100$ M^{-1} cm^{-1}) and exhibit only one isotope sensitive feature in the resonance RAMAN spectrum. More specifically, a O–O vibration around 1073 cm^{-1} ($\Delta^{16}O_2$–$^{18}O_2$ = 60 cm^{-1}) for complex **XIX** and 1070 cm ($\Delta^{16}O_2$–$^{18}O_2$ = 59 cm^{-1}) for complex **XX**, confirmed the presence of only one superoxide isomer in contrast to KARLIN's reported superoxo complex (**XXI**).

The μ-1,2 binding motive of the superoxide is further confirmed via EPR studies, which displays for complex **XX** a typical axial Cu^{II} spectrum, where the unpaired electron of the superoxo moiety is strongly antiferromagnetically coupled with one electron of the Cu^{II} ions. In case of complex **XIX**, crystalline material could be obtained, making it the first example of a dinuclear superoxo complex that could be structurally characterized.[113] Comparison of the structurally derived O−O bond length of the peroxodicopper(II) complex **XVII** (1.441 Å) and the superoxodicopper(II) complex **XIX** (1.329 Å) as well as spectroscopic signatures ($\tilde{\nu}$(^{16}O−^{16}O) = 793 cm^{-1} for **XVII** vs. 1073 cm^{-1} for **XIX**) reflects that the redox process occurs at the bridging O_2 unit.[121] Both complexes, **XIX** and **XX** show reversible redox processes for the peroxo/superoxo redox couple at rather low potentials (**XIX**; E^0= −0.58 V vs. Fc/Fc$^+$, **XX**; E^0= −0.59 V vs. Fc/Fc$^+$) and could be chemically and/or electrochemically interconverted. Studying of such radical Cu_2/O_2 species is of high interest as they can potentially mediate H-atom abstractions and thus serve as model complexes for key intermediates of parent copper enzymes (e.g. LPMO, pMMO) and potential green catalysts for organic molecule trasformations.[117,122]

3.2.3 Hydroperoxo Model Systems

The isolation of dinuclear hydroperoxo complexes can be considered as relatively hard due to their increased thermal decomposition similar to the beforehand mentioned superoxo adducts. While there are few spectroscopically characterized model systems, the number of those characterized by X-ray crystallography is even smaller due to their instability.[123,124] Characteristic spectroscopic features are an intense electronic absorption band around 350-430 nm, originating from a LMCT of the μ-1,1-hydroperoxide to the Cu^{II} ions and a O–O vibration of these compounds around 860 -890 cm^{-1}. [15]

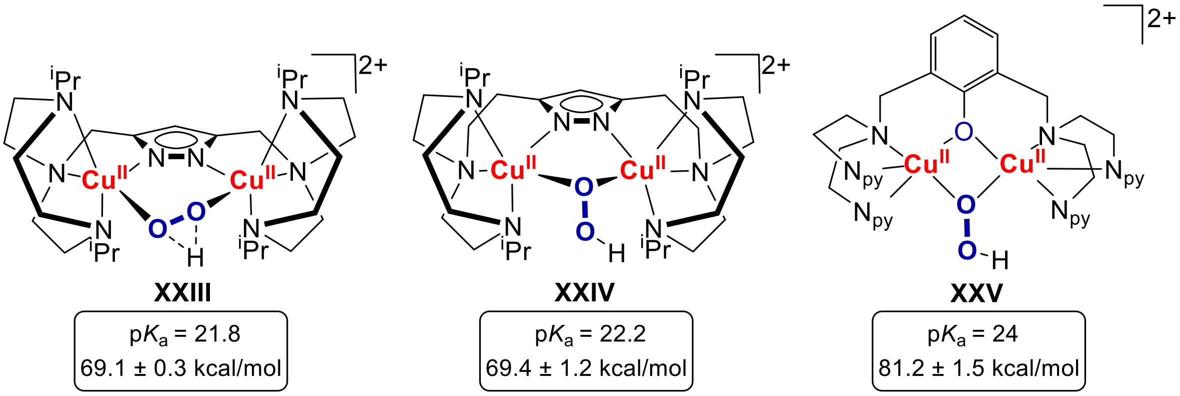

Figure 18. Dinuclear hydroperoxo complexes and their respective pK_a values as well as bond dissociation free energies (BDFE).[113,117,119]

The dicopper hydroperoxo complexes represent the products formed upon HAT reactions of the superoxo complexes **XIX**, **XX** and **XXII**. Complexes shown in Figure 18 are the only examples of hydroperoxo complexes, where thermodynamic parameters have been derived.[113,117,119] Hereby, complex **XXIV** can be considered as the first complex where reversible protonation-deprotonation reactions of the peroxo/hydroperoxo core were observed and therefore a pK_a value of the Cu_2OOH moiety in MeCN of around 22.2 could be determined. Later, pK_a values for complex **XXIII** and **XXV** were also obtained, reflecting a steady increase of interest in such thermodynamic parameters.

By employing the pK_a value of the hydroperoxo complex and the peroxo/superoxo redox potential to set up a thermodynamic square scheme (Figure 19), the bond dissociation free energy of the OO–H bond can be derived according to the BORDWELL relationship (Equation 1) and thus estimating the potential H-atom abstractor strength of the corresponding superoxo complex.[125–127]

$$\mathrm{BDFE(OO{-}H)} = 1.37\,\mathrm{p}K_a + 23.06\,E^0 + C_{\mathrm{G,solv}} \qquad \mathbf{1}$$

$C_{\mathrm{G,solv}}$ describes the $H^+/H^\cdot$ standard reduction potential in a given solvent and includes the free energy of formation of $H^\cdot$, the free energy of solvation of $H^\cdot$ as well as the nature of the reference electrode.[126,127]

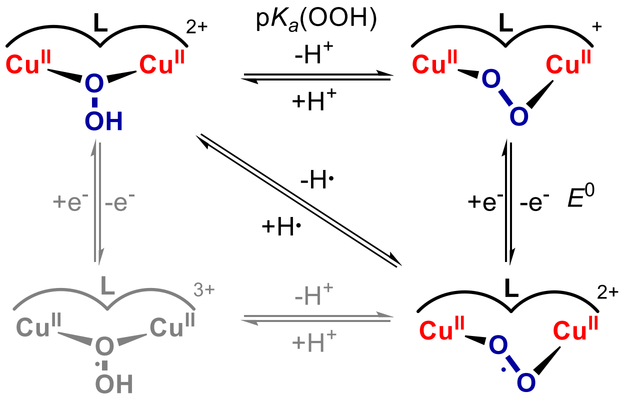

Figure 19. Thermodynamic square scheme relevant to the interconversion of peroxo, superoxo and hydroperoxo dicopper(II) intermediates , wherefrom the OO-H BDFE of **XXIII**, **XXIV** and **XXV** was derived. The monoanionic pyrazolate/tacn, respectively phenolate-bridged ligand frameworks are now shown. [113,117,119]

Remarkably, hydroperoxo complexes based on the phenolate and pyrazolate bridged ligand scaffolds showed large differences in the corresponding BDFE of the OO–H unit, and therefore on the HAT reactivity of the superoxo complex, emphasizing the great impact of ligand design on thermochemistry.[119] To fully understand those results further thermodynamic parameters of various ligand scaffolds are required, which may also yield deeper insights into enzymatic processes and the synthesis of potential biomimetic catalysts.

3.3 Binuclear Copper/NO complexes

Even though the chemistry of metal nitrosyl complex has been the focus of many research activities for several years,[128] the number of isolated copper nitrosyl complexes is still very limited,[129–133] whereby dinuclear complexes are particularly scarce, despite the high biological relevance of the combination of copper and NO in nature.

Dicopper nitrosyl complexes usually exhibit an isotope sensitive IR band around 1550 cm^{-1}, which reveals first information on the type of bridging NO unit. The first isolated complex by KARLIN and coworkers (**XXVII**, Figure 20) was synthesized by reaction of the corresponding dicopper(I) complex with NO$^+$.[131] The complex exhibits intensive electronic absorptions at 382 nm ($\varepsilon \approx 5300$ M^{-1} cm^{-1}), 545 nm ($\varepsilon \approx 2200$ M^{-1} cm^{-1}) and 730 nm ($\varepsilon \approx 500$ M^{-1} cm^{-1}) and an intense infrared absorption around 1536 cm^{-1}. A solid-state structure of complex **XXVII** showed a N–O bond length of 1.176 Å. The nature of the bridging NO moiety was therefore described as NO$^-$ (nitroxyl). Recently[132], KARLIN et al. also reported the formation of a mixed-valent Cu^{I}/Cu^{II} nitroso complex (**XXVI**) with a IR band at 1670 cm^{-1} that forms a peroxynitrite dicopper complex upon exposure to O$_2$. This is of great interest, since imbalances in copper homeostasis, as well as extensive peroxynitrite production, might play a major role in ALZHEIMER'S disease.[8]

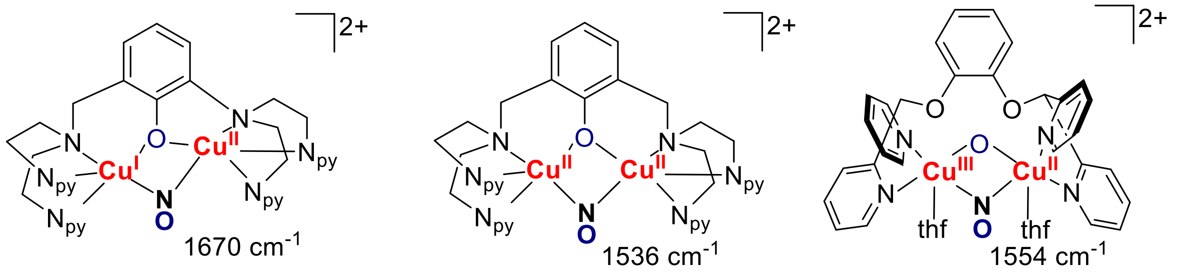

XXVI **XXVII** **XXVIII**

Figure 20. Dicopper μ-nitrosyl complexes and their characteristic N-O infrared vibration.[131–133]

Lately, ZHANG *et al.* were able to isolate a μ-oxo μ-nitrosyl dicopper complex (**XXVIII**) after addition of NO or NO$_2^-$ to the corresponding dicopper precursor. The resulting complex undergoes versatile reactivity, e.g., oxygen and hydrogen atom transfer and C–H hydroxylation and also redox-neutral S-nitrosation of a thiols.[133,134]

4 Thesis Objective

Previous work has already demonstrated how well pyrazolate/tacn hybrid ligands are suited for the synthesis of dinuclear copper complexes that give relatively stable Cu_2O_2 intermediates.[52,112,113,117,124] Those unique ligand scaffolds provide two flexible {N_4} binding pockets, consisting of the macrocyclic tacn side arms and the pyrazole bridging unit, providing the required flexibility to stabilize the Cu^I and Cu^{II} oxidation states was well as suitable metal-metal separation for stabilization of various copper oxygen adducts. Further, peripheral *iso*-propyl groups at the tacn macrocycles provide sufficient steric shielding of the metal binding site and formed Cu_2O_2 intermediates. A brief overview of the so far reported copper oxygen derivatives of the ligand scaffolds **L¹** and **L²** are presented in Figure 21.

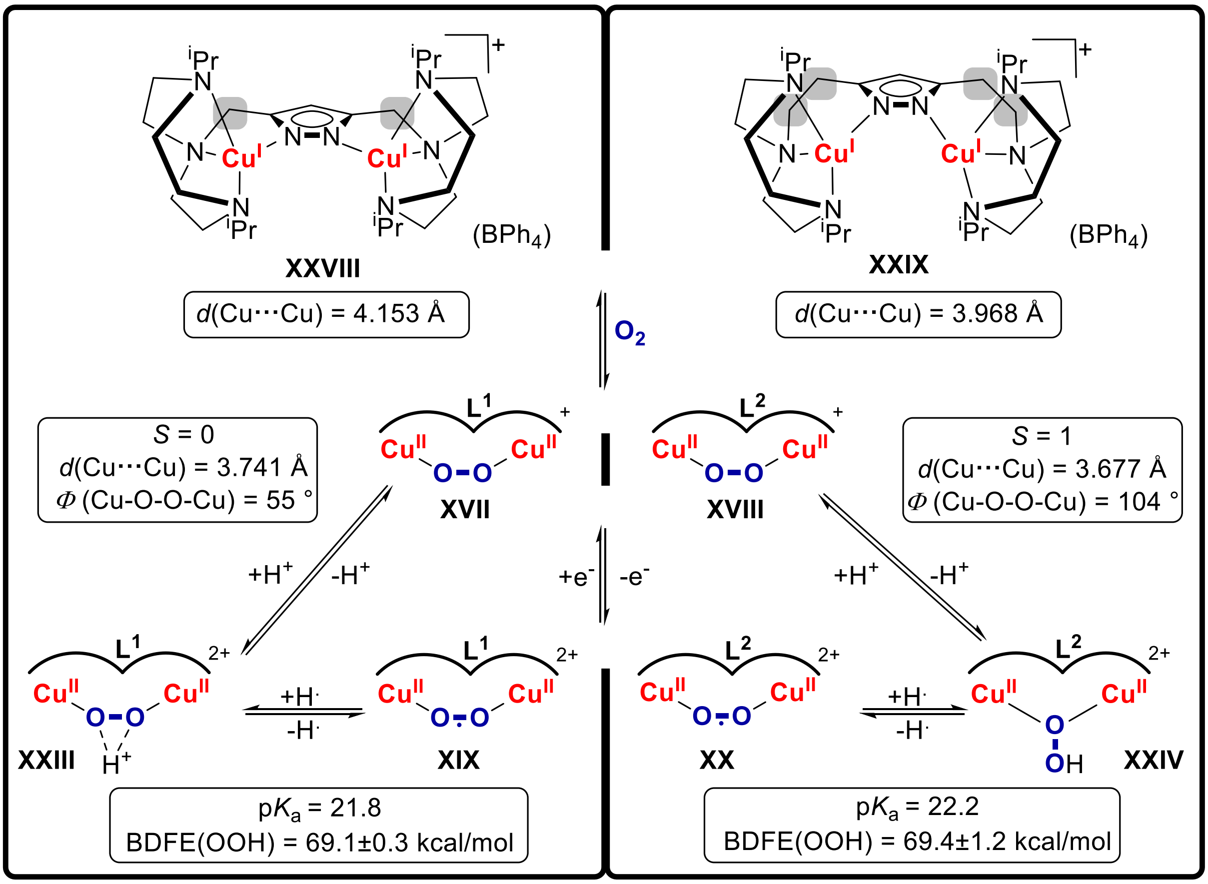

Figure 21. Copper oxygen complexes based on the pyrazolate/tacn ligands **L¹** and **L²** and their transformations.[52,112,113,117,124]

Both dicopper(I) complexes **XXVIII** and **XXIX** are reacting readily with dioxygen to form μ-1,2-peroxo adducts. This particular binding mode has not been observed in nature so far but can be interpreted as a biomimetic snapshot of the initial steps of dioxygen binding at type III copper proteins such as hemocyanin. **XVII** exhibited a Cu···Cu separation of 3.741 Å and a Cu–O–O–Cu dihedral angle of 55°, giving rise to relatively weak antiferromagnetic coupling ($J = -54\ cm^{-1}$) of the Cu^{II} ions and therefore a singlet $S = 0$ ground state. The ligand framework **L²** in complex **XVIII** features an ethylene instead of a methylene linker between pyrazole and tacn side arms, leading to a Cu···Cu separation of 3.677 Å, which is much shorter than the peroxodicopper(II) complex of ligand **L^1**.[112,113] The change of the ligand scaffold led to particularly outstanding electronic properties of the resulting peroxodicopper(II) complex **XVIII**. The alteration of the Cu–O–O–Cu torsion angle from 55° for complex **XVII** to 104° leads to a near orthogonal arrangement of the magnetic orbitals and therefore ferromagnetic coupling and consequently a triplet $S = 1$ ground state.

Further conversions into biomimetically relevant copper oxygen adducts were investigated, such as the formation of superoxo complexes by chemical or electrochemical oxidation or as well as formation of the respective hydroperoxo complexes **XVII** and **XVIII** by reversible protonation/deprotonation were monitored. As a result, the bond dissociation free energy of the hydroperoxo OO–H bond could be derived and kinetic studies of hydrogen atom transfer (HAT) reactions were conducted, showing that elongation of the spacer unit between tacn and pyrazolate in **L^2** results in a stronger shielding of the superoxide unit and thus a decreased HAT reactivity.[113,117]

Since both ligand scaffolds exhibit significantly different electronic and kinetic properties, despite almost identical BDFEs, the synthesis of a non-symmetric ligand system seems particularly attractive to elucidate the influence of rational ligand design on those properties. Therefore, the ligand **L^{1,2}** is synthesized, which can be regarded as a combination of structural fragments of the ligand frameworks **L^1** and **L^2**. This approach has already been applied to nickel complexes in the past[135] and it should now be extended to the herein presented pyrazolate/tacn copper chemistry for the potential isolation and characterization of interesting dicopper(II) peroxo, hydroperoxo and superoxo species. In particular, the influence of the non-symmetric ligand scaffold **L^{1,2}** on the electronic structure of the corresponding peroxo adduct is of great interest, given the possibility to generate a Cu–O–O–Cu torsion angle between 55° and 104°, being even closer to the 90° superexchange breakdown situation.

While the peroxo complex **XVII** revealed strong affinity to LEWIS acids, such as alkali metal ions, this behavior was not observed for **XVIII** due to the strong steric encumbrance of the peroxo moiety. Therefore, a non-symmetric peroxo complex based on the ligand scaffold **L^{1,2}** might exhibit attenuated interactions with LEWIS acids and reveal the tunability of those interactions in dependence of the employed pyrazolate/tacn ligand **L^1**, **L^2** or **L^{1,2}**.

Additionally, kinetic studies of the corresponding superxo complex towards HAT processes should be investigated and correlated to the series of previously reported pyrazolate/tacn complexes **XIX** and **XX**, elucidating the influence of ligand design on the thermodynamic and kinetic properties of superoxodicopper(II) complexes.

Further, based on the exceptional stability of copper/oxygen complexes derived from the ligand scaffold **L^2**, the reactivity of the dicopper(I) complex **XXIX** towards nitric oxide will be investigated in this thesis.

5 Results and Discussion

5.1 Pyrazolate/tacn Ligands

In the last couple of years pyrazolate/tacn frameworks were used to establish versatile dinuclear copper/oxygen complexes.[52,112,113] Hereby, the macrocyclic N-donor 1,4,7-triazacyclononane (tacn) units provide high complex stability upon binding of Cu^I and Cu^{II} ions and could additionally be modified by different substituents at the nitrogen atoms (methyl or *iso*-propyl groups), which can sterically shield the formed copper/oxygen adduct and alter their respective properties. Further, the pyrazole bridge enables tunable metal to metal separation by variation of the spacer between the pyrazole and the tacn side arms (Figure 22).

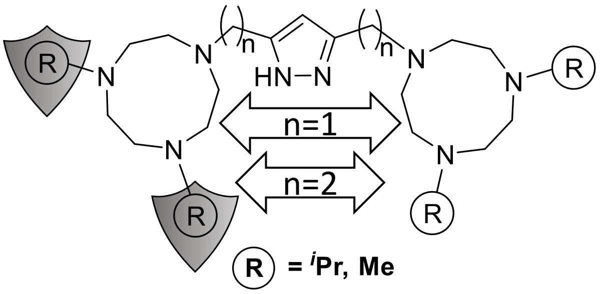

Figure 22. Schematic representation of pyrazole/tacn ligands, indicating the shielding of copper/oxygen complexes by the tacn substituents, as well as the influence of the spacer unit on the metal to metal separation.

Depicted in Figure 23 are various pyrazole/tacn ligand scaffolds derived from different spacers and substituents at the side arms.

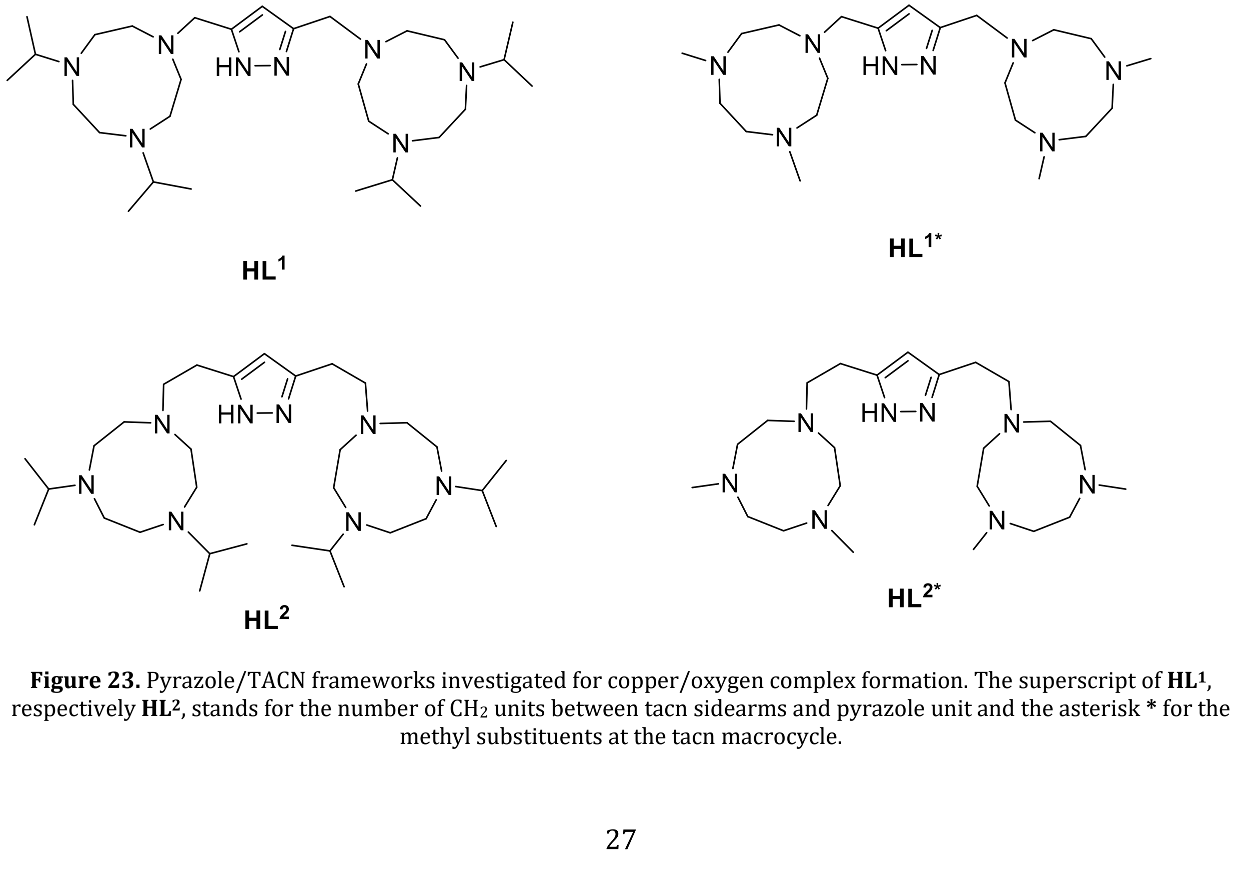

Figure 23. Pyrazole/TACN frameworks investigated for copper/oxygen complex formation. The superscript of $\mathbf{HL^1}$, respectively $\mathbf{HL^2}$, stands for the number of CH_2 units between tacn sidearms and pyrazole unit and the asterisk * for the methyl substituents at the tacn macrocycle.

So far, copper oxygen complexes based on the ligand scaffolds **L^1** and **L^2** are the most well studied, since the *iso*-propyl groups of the tacn side arms provide increased stability of reactive intermediates, making the isolation feasible. By alteration of the spacer unit, the metal to metal separation could be tuned and the size of the binding pocket modified. For example, the corresponding μ-hydroxo complex of the ligand framework **L^2** exhibits a Cu···Cu separation of 3.41 Å, whereby its methylene spaced analogue **L^1** reveals a Cu···Cu distance of 4. 38 Å between the metal ions and a (H)O···HO(H) bridging unit within the binding pocket (more details in Section 5.2.6).

The isolation of copper oxygen intermediates based on the methyl substituted tacn ligands **L^{1*}** and **L^{2*}** is still a matter of current research but extremely challenging, due to the short lifetime of those complexes which is most likely based on the increased exposure of the Cu_2O_2 core. Recently, MEYER and coworkers presented the isolation of a hexanuclear copper(I) hydride complex upon reduction of a dicopper(II) formate complex based on the ligand **L^{1*}**.[136]

Since modification of the linker between pyrazole and tacn results in major electronic changes of the corresponding copper oxygen complexes, variation of only one spacer is particularly interesting since an even more accurate picture of ligand design on structural properties can be obtained. The non-symmetrical pyrazolate/tacn ligand **L^{1,2}** was priorly synthesized and successfully employed for the isolation of a dinuclear μ-hydroxo nickel complex (Figure 24). Similar to the binding situation described above, usage of **L^1** as a ligand for dinickel(II) complexes leads to an increase of the Ni···Ni distance from 3.5 Å to 4.48 Å and a (H)O···HO(H) bridging unit.[135]

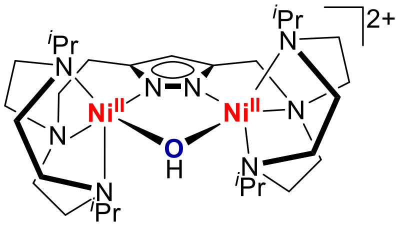

XXIX

Figure 24. Prior synthesized dinickel(II) complex **XXIX**, based on the ligand framework **L^{1,2}**.[135]

As already described in previous sections, the ligands **L^1** and **L^2** have a strong influence on the copper-oxygen core properties. Therefore, synthesis of the non-symmetric ligand **L^{1,2}** should be synthesized first to isolate and characterize the corresponding copper-oxygen adducts. In the following, the multi-step synthesis of **L^2** and **L^{1,2}** will be described, particularly focusing on the synthesis of the non-symmetric ligand scaffold and its purification, since synthesis of **L^2** has been already reported previously.[112,137]

5.1.1 Ligand Synthesis

For the synthesis of the macrocyclic tacn sidearm different literature known procedures were employed and will be presented in the following. A slightly modified synthesis according to SCARBOROUGH and coworkers[138] which is depicted in Scheme 6 started from the commercially available *N,N'*-di-*iso*-propylethylenediamine (**a**), which was converted to the respective amide **b** upon addition of chloroacetyl chloride. Subsequently, cyclization to the elementary tacn macrocycle **c** was achieved upon addition of benzylamine. Reduction of the amide functions with $LiAlH_4$ (**d**) and removal of the benzylic protection group with Pd/C led to the isolation of the 1,4-Di-*iso*-propyl-7-benzyl-1,4,7-triazacyclononan (**e**) in moderate overall yields up to 15%.

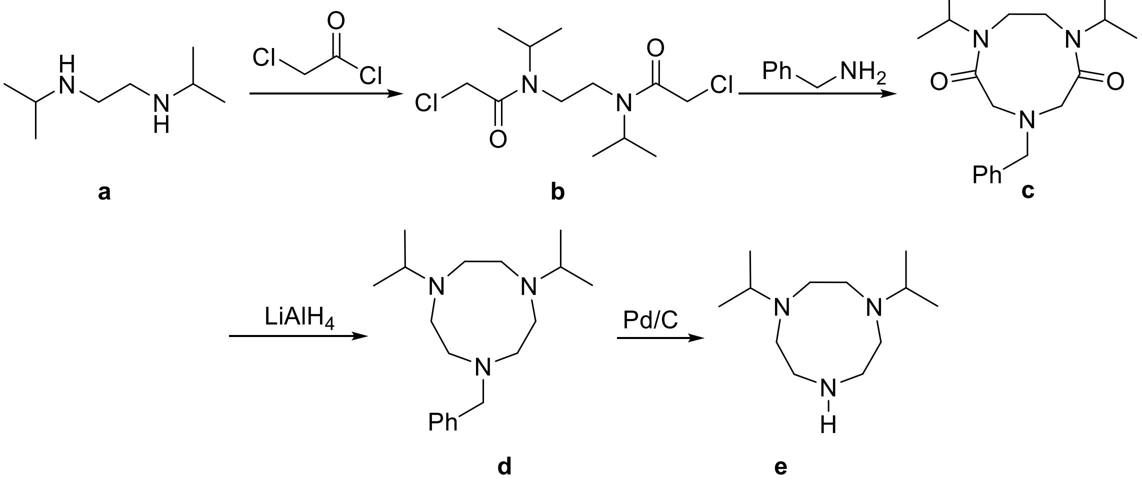

Scheme 6. Synthesis of 1,4-Di-*iso*-propyl-1,4,7-triazacylononan according to SCARBOROUGH and coworkers.[138]

Additionally, a synthetic routine according to GROS and HASSERODT[139] (Scheme 7) was employed, which started with the reductive amination of diethylenetriamine (**f**) with acetone and $NaBH_4$, forming 1,7-Di-*iso*-propyl-diethylentriamine (**g**). Consecutive reaction with chloroacetaldehyde led to the formation of an octahydroimidazo[1,2-*a*]pyrazine (**h**). Subsequent addition of benzylbromide led to the formation of the ammonium salt (**i**), which underwent ring opening to 1,4-Di-*iso*-propyl-7-benzyl-1,4,7-triazacyclononane (**d**) after addition of sodium borohydride. Again, deprotection with Pd/C yielded the desired tacn compound (**e**) in relatively low yield of 5%.

Both synthetic approaches led to the isolation of the tacn side arm, however due to their limited scalability and moderate yields the well-known routine according to TOLMAN, RICHARD and ATKINS (Scheme 8) was preferred.[140,141]

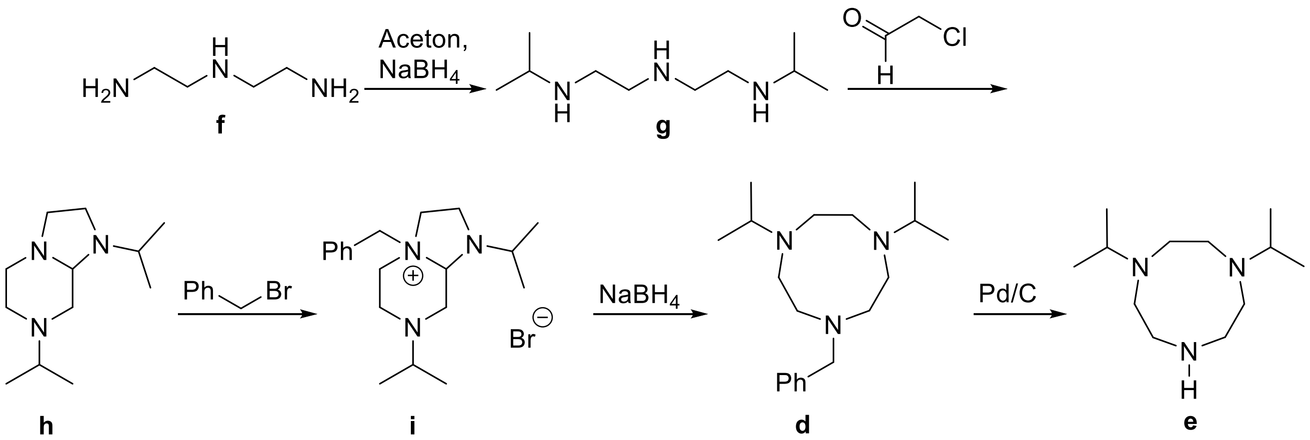

Scheme 7. Modified synthesis of 1,4-Di-*iso*-propy-1,4,7-triazacylononan according to GROS and HASSERODT.[139]

Therefore, upon sulfonylation of ethylene glycol and diethylentriamine compounds **j** and **k** were obtained. Subsequent ring-closure led to the isolation of the tosylate protected Ts$_3$tacn (**l**). Functionalization of the tacn unit was achieved upon selective deprotection of two nitrogen groups (**m**) with HBr/Phenol and subsequent conversion with 2-bromopropane to yield compound **n.** Treatment with concentrated sulfuric acid led to the desired deprotection of the amine functionality. As already reported in previous works, upon vacuum distillation clean material of **e** was obtained. The overall benefit of this routine was its easy scalability to synthesize large quantities with comparatively little risk and an overall yield of roughly 50%.

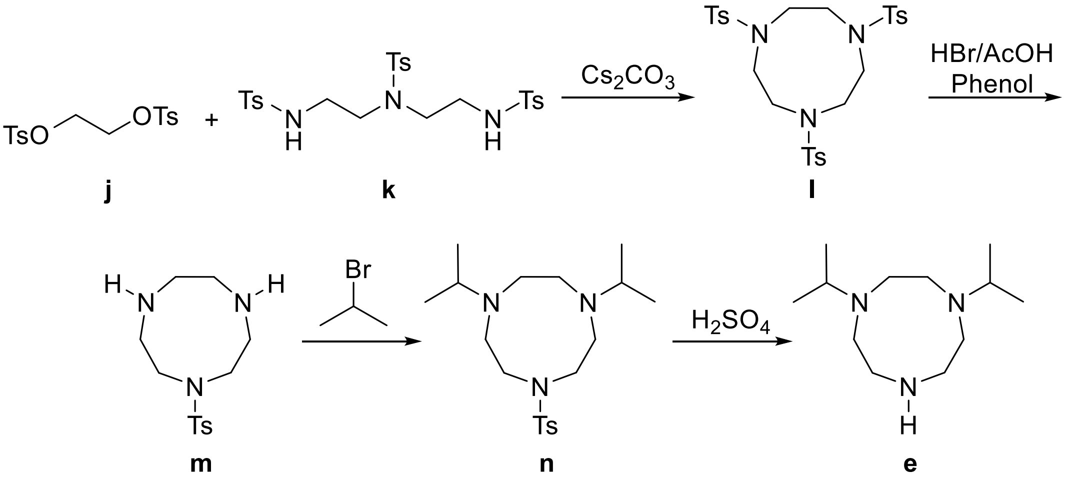

Scheme 8. Synthesis of 1,4-Di-*iso*-propyl-1,4,7-triazacylononan (^{iPr}tacn) required for **L^1** and **L^{1,2}**.[140,141]

The desired unprotected 1,4-Di-*iso*-propyl-1,4,7-triazacylononan ^{iPr}tacn (**e**) could be stored at −20°C under argon but even then, degradation products were observed over time which could be removed again after distillation. Since the corresponding hydrobromide salt of **m** showed no decomposition over time, storing of this compound was preferred and when required conversion to the desired product applied.

The synthetic procedure for the pyrazole building block varied according to the length of the spacer in the 3 and 5 positions. The 3,5-bis(chloroethyl)pyrazole hydrochloride requires a multistep synthesis[137,142,143] starting from 3,5-dioxopimelate and was usually synthesized by converting the 3,5-bis(hydroxyethyl)pyrazole (**o**), which was provided by the MEYER working group, with thionyl chloride to compound **p** (Scheme 9).

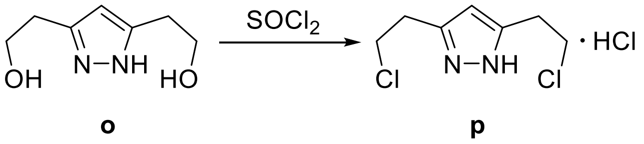

Scheme 9. Synthetic route for the symmetric pyrazole building block **p**.

In contrast, the non-symmetric building block 3-(β-chloroethyl)-5-chloromethylpyrazole hydrochloride was synthesized in a convenient two-step routine, according to literature known procedures.[135,144] Cyclization of the commercially available 1,6-dihydroxy-2,4-hexadiyne (**q**) with hydrazine monohydrate led to the isolation of **r** (Scheme 10). It should be noted that the yield was highly dependent on the purity of commercially available building block **q**. For conversion of 3-(β - hydroxyethyl)-5-hydroxymethylpyrazole to the corresponding substituted chloride, isolation of the hydrochloride (**r**) and purification by extensive washing with diethyl ether prior to conversion was found to be beneficial for the purity and yield of **s**. The 3-(β-chloroethyl)-5-chloromethylpyrazole hydrochloride could be further purified by extensive washing with diethyl ether and was stored under argon, due to its hygroscopic nature.

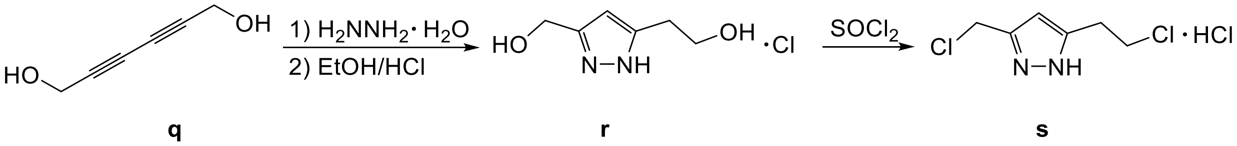

Scheme 10. Synthetic routine for the non-symmetric pyrazole **i.**

Previous works have already discussed the ideal conditions for the reaction of the tacn unit with the respective pyrazole building block. In general, nucleophilic substitution proceeds faster when the chloride is in the pseudo-benzylic position of the pyrazole, as it is the case for the synthesis of $\mathbf{L^1}$. However, the pyrazole **p** for the synthesis of the ligand framework $\mathbf{L^2}$ exhibited a decreased reactivity towards nucleophilic substitution due to the ethylene extension in the 3 and 5 positions. Previous studies from NICOLE KINDERMANN suggested the synthesis of $\mathbf{L^2}$ at temperatures around 40°C, which was based on the observation that synthesis at elevated temperatures led to the increased formation of byproducts, such as monosubstituted pyrazoles or vinyl derivatives derived from elimination of hydrogen chloride.[137]

However, those findings could not be confirmed for the synthesis of both ligands $\mathbf{L^2}$ and $\mathbf{L^{1,2}}$, even when the corresponding pyrazole building block was reacted with the tacn unit **e** at temperatures up to 120 °C for 48 h. The formation of undesired side products was monitored by ESI-MS and ^{1}H-NMR spectroscopy and was observed in all cases in same quantities, regardless the temperature. No significant increase of byproducts could be observed at temperatures around 120 °C or a decrease at 40 °C. However, the higher reaction temperature led to a slightly increased yield and shorter reaction times made this procedure overall more beneficial.

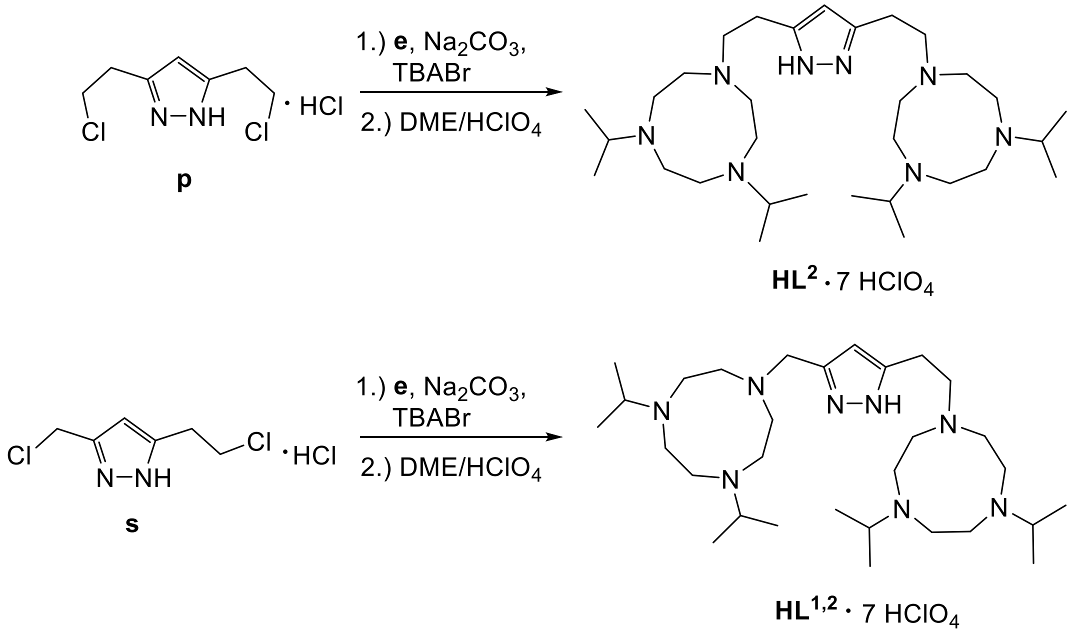

Scheme 11. Synthetic procedures for **HL²** and **HL¹˒²**.

The formed byproducts could be removed partly upon precipitation with perchloric acid in DME and subsequent extensive stirring in ethanol and diethyl ether for several days provided the required purity for the synthesis of demanding Cu_2/O_2 complexes. However, it should be noted that similar to the reported **L¹**, the ligand **L¹˒²** could not be obtained in analytically pure form, even though column chromatography and crystallization was attempted. The protonation state and therefore amount of associated $HClO_4$ was determined via ^{1}H-NMR experiments with sodium benzoate as an internal standard, yielding also approximately seven perchloric acid molecules per ligand **HL¹˒²**.

5.1.2 Summary and Conclusion

The ligand scaffold $\mathbf{L}^{1,2}$ was successfully isolated, employing a new synthetic route for the synthesis of non-symmetric pyrazole/tacn frameworks. Prior reported observations of an increase of byproducts at higher reaction temperatures could not be verified. However, a decrease in reaction time with unchanging yield was also achieved for the ligand $\mathbf{L}^2$. In addition, purification methods derived from the synthetic procedure of $\mathbf{L}^2$ could be refined and adjusted to the synthesis of $\mathbf{L}^{1,2}$.

While the synthesis of copper/oxygen complexes based on the ligand $\mathbf{L}^2$ are already investigated in detail, the ligand framework $\mathbf{L}^{1,2}$ was only used for the synthesis of dinickel(II) complexes so far. Therefore, the combination of structural fragments of the ligands $\mathbf{L}^1$ and $\mathbf{L}^2$ completes the series of *iso*-propyl protected pyrazole/tacn ligand frameworks for dicopper complexes. Isolation of those Cu_2/O_2 adducts based on this new ligand should therefore provide more refined studies on the influence of ligand frameworks on structural, magnetic and kinetic properties of the resulting copper oxygen compounds.

5.2 A Non-Symmetric Peroxodicopper(II) Complex

The isolation of μ-1,2-peroxodicoppper(II) complexes ,based on pyrazolate/tacn scaffolds, has been reported in previous works by the MEYER group (see also Section 3.2.1).[52,112] Initially, the respective dicopper(I) precursor is isolated and undergoes oxidation upon treatment with dioxygen. Interestingly, small changes in the ligand framework, namely variation of the bridging unit between the pyrazolate backbone and tacn sidearms, lead to dramatic changes in the electronic structure and magnetic properties of the resulting peroxodicopper(II) core.[112,113]

Based on the solid-state structures and magnetic properties of peroxo complexes **$[L^1Cu_2O_2](BPh_4)$** (**XVII**) and **$[L^2Cu_2O_2](BPh_4)$** (**XVIII**) a correlation between the Cu−O−O−Cu torsion angle (ϕ) and the extent of ferromagnetic and antiferromagnetic coupling between the Cu^{II} ions could be derived. While **XVII** exhibits weak antiferromagnetic coupling (J = −54 cm^{-1}) between both copper(II) ions, complex **XVIII** was the first isolated ferromagnetically coupled (J = +70 cm^{-1}) peroxodicopper(II) complex. The respective complexes possess dihedral angles of 55° for **XVII** and 104° for **XVIII** and demonstrate the change from the singlet to the triplet ground state, when φ approaches 90° (more in Section 5.2.4).

While the peroxodicopper(II) complexes **XVII** and **XVIII** can already be considered as adequate model complexes for the initial steps of dioxygen binding in type III copper proteins, this chapter will focus on the isolation of a non-symmetrical peroxo complex based on the ligand scaffold **$L^{1,2}$**. Therefore, isolation of the respective dicopper(I) complex is initially presented. Further, the isolation of a non-symmetric peroxodicopper(II) complex is demonstrated and the influence of the new ligand scaffold on magnetic and structural properties is revealed.

5.2.1 Synthesis of a Non-Symmetric Dicopper(I) Precursor

The synthesis of the dicopper(I) complex **1** was carried out by combining synthetic procedures of its symmetric congeners **$[L^1Cu_2](BPh_4)$** (**XXVIII**) and **$[L^2Cu_2](BPh_4)$** (**XXIX**).[113,137] Therefore, the ligand **HL^2**·7 $HClO_4$ was deprotonated with a small excess of KO^tBu (approx. 8.5 Eq.) and then reacted with two equivalents of $[Cu(MeCN)_4]ClO_4$ in methanol (Scheme 12). Subsequent removal of $KClO_4$ by filtration and addition of $NaBPh_4$ in MeOH to the gold-brown solution led to precipitation of the raw product. Interestingly, complex **1** could also be obtained by using NaO^tBu for deprotonation, however the full removal of sodium ions proved to be difficult and was therefore not further developed.

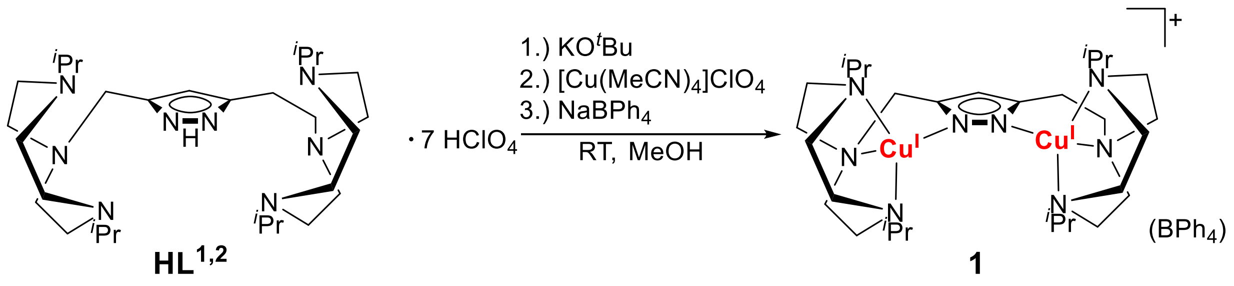

Scheme 12. Synthetic route for the isolation of the dicopper(I) complex **1**.

The purification of the crude dicopper(I) complex **1** turned out to be rather challenging, since formation of crystalline material was usually accompanied by the formation of a brown viscous oil, probably originating from impurities of the ligand synthesis. Therefore, several crystallization attempts were conducted, using highly concentrated solutions of **1** in acetone, MeCN or EtCN. Those solutions were exposed to diffusion of Et$_2$O for 24-48 h, whereby initially a brown oil and a clear solution formed. The clear solution was taken and used for a second run of diffusion with diethyl ether, before formation of contaminated crystalline material took place. This process had to be repeated several times, whereby the formed oil was always discarded, and the clear solution taken for further diffusion. After several purification cycles, pure crystalline material of complex **1** in moderate quantities up to 20% yield could be obtained.

Thus, the diamagnetic dicopper(I) complex **1** could be investigated by means of NMR spectroscopy (Figure 25).

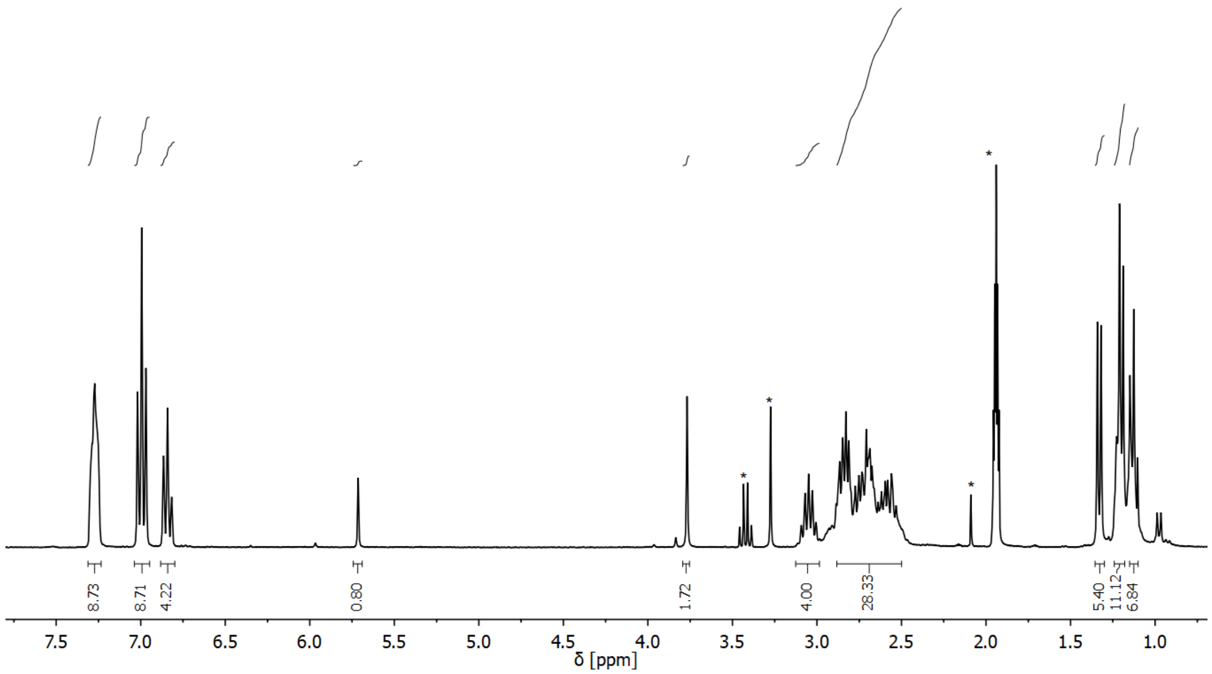

Figure 25. ^{1}H-NMR Spectra of complex **1** in CD$_3$CN at 298 K. Signals of solvent molecules are marked with an asterisk (*).

Exact assignment of the proton signals and differentiation of the ethylene and methylene spaced side arms tends to be difficult, despite 2D-NMR spectroscopy, due to the C_1 symmetry of complex **1** and strong overlap of proton signals. Nevertheless, the multiplets between 1.10-1.15 ppm, 1.18-1.24

ppm and the doublet at 1.33 ppm are assigned to the methyl groups of the *iso*-propyl groups of the tacn side arms since coupling to the characteristic CH-septet of the isopropyl moiety at 3.05 ppm, can be observed in the ^{1}H-^{1}H COSY spectrum (Figure 26). The singlet at 3.77 ppm is assigned to the CH_2 protons of the methylene bridging unit between the pyrazolate and the tacn side arm and the distinctive singlet at 5.71 ppm to the pyrazole CH proton. Further CH_2 groups of the tacn side arms as well as the ethylene bridging unit are assigned to the multiplet between 2.47 ppm and 2.96 ppm.

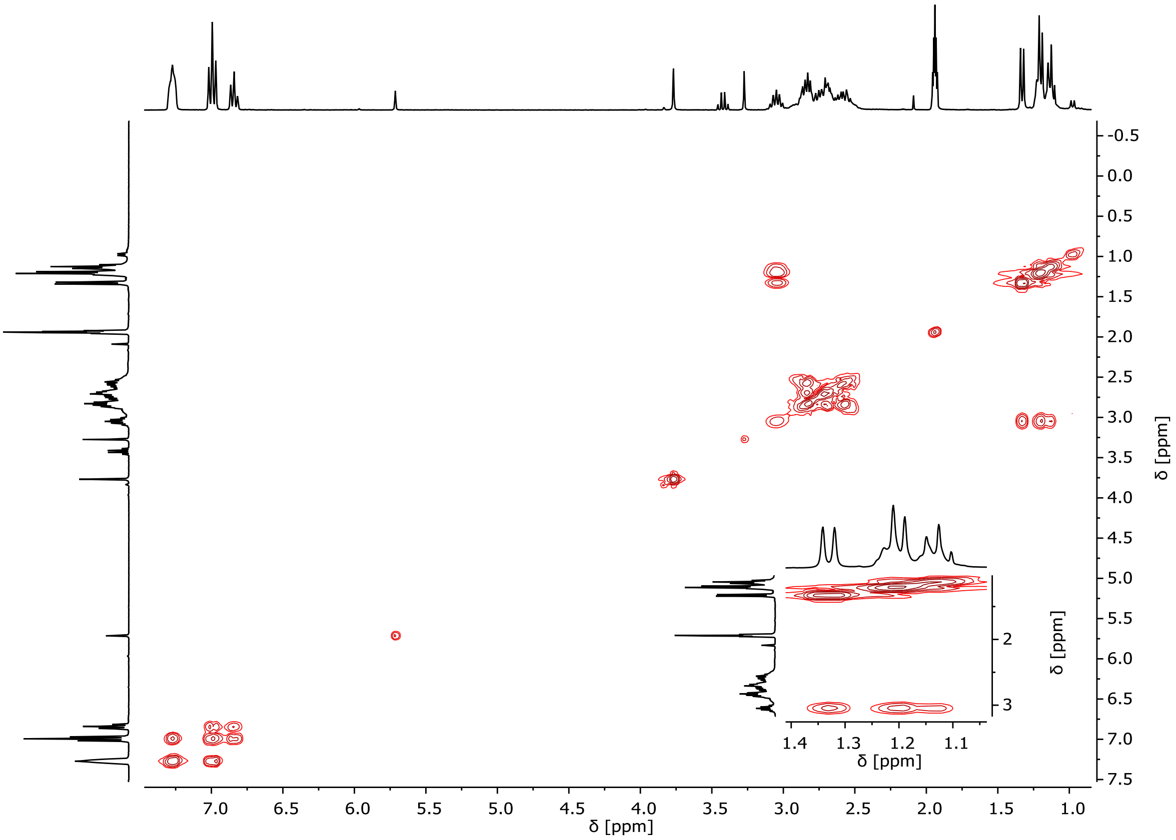

Figure 26. ^{1}H-^{1}H COSY (300 MHz) spectrum of complex **1** in CD_3CN.

The structure of **1** was determined by X-ray diffraction, containing two independent molecules of **1** per asymmetric unit and hence the molecular structure of its cation is depicted in Figure 27. Both Cu^I ions exhibit a distorted tetrahedral coordination environment, which is reflected by the geometry index τ_4 (0.642 for Cu1 and 0.596 for Cu2) that describes the coordination geometry according to $\tau_4 = \frac{360^\circ - (\alpha+\beta)}{141^\circ}$ whereby α and β are the largest bond angles.[145] Thus, an ideal tetrahedral coordination geometry exhibits a τ_4 value of 1 and a perfect square planar geometry of $\tau_4 = 0$.

Both Cu^I ions are coordinated by $\{N_4\}$ binding site of the tacn and pyrazolate nitrogen atoms of the ligand framework. Interestingly, the Cu–N bonds differ significantly between the pyrazolate (Cu1–N1 = 1.93 Å, Cu2–N2 = 1.92Å) and the tacn side arms (Cu1–N3,4,5 = 2.06-2.31Å, Cu2–N6,7,8 = 2.16-2.20), a common trait of all reported pyrazolate/tacn copper complexes. The newly isolated non-symmetric dicopper(I) complex exhibits a metal-metal separation of 4.081 Å. Therefore complex **1** combines metric parameters of the ethylene and methylene bridged dicopper(I) complexes and can therefore be regarded as a link between the previously isolated complex **[L^{1}Cu$_2$](BPh$_4$)** (4.153 Å), which shows a comparatively large Cu···Cu distance and **[L^{2}Cu$_2$] (BPh$_4$)** (3.968 Å), exhibiting a contracted metal to metal separation.

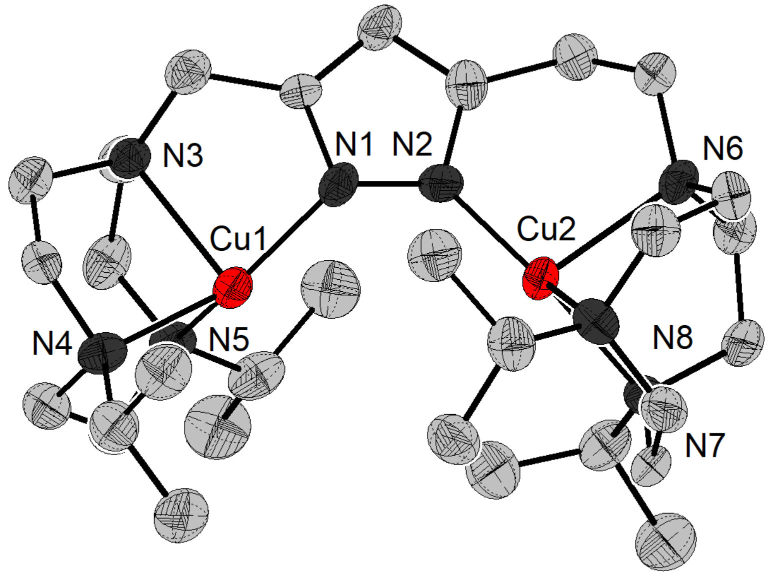

Figure 27. Molecular structure of the cationic portion of complex **1**. Thermal displacement ellipsoids given at 50% probability. Hydrogen atoms, solvent molecules and counter ions are omitted for clarity. Selected bond lengths [Å] for **1**: Cu1···Cu2 4.0807(13) Cu1–N1 1.933(8), Cu1–N4 2.055(9), Cu1–N3 2.233(7), Cu1–N5 2.306(8), Cu2–N2 1.921(8), Cu2–N8 2.156(8), Cu2–N7 2.159(8), Cu2–N6 2.195(8).

The metric parameters of **[L^{1,2}Cu$_2$](BPh$_4$)** (**1**) and its symmetrical predecessors are combined in Table 1.

Table 1. Metric parameters of dicopper(I) complexes **[L^{1}Cu$_2$](BPh$_4$)**, **[L^{1,2}Cu$_2$](BPh$_4$)** and **[L^{2}Cu$_2$](BPh$_4$)** obtained from the solid state structure via X-ray diffraction.[113,137] τ_4 can be derived from the largest bond angles α and β and the equation $\tau_4 = \frac{360° - (\alpha+\beta)}{141°}$.[145]

	[L^{1}Cu$_2$](BPh$_4$)	**[L^{1,2}Cu$_2$](BPh$_4$)**	**[L^{2}Cu$_2$](BPh$_4$)**
Cu1···Cu2 (Å)	4.153	4.081	3.968
τ_4 [Cu1, Cu2]	0.637, 0.641	0.642, 0.596	0.602, 0.596
Cu1–N1 (Å)	1.907	1.933	1.905
Cu2–N2 (Å)	1.916	1.921	1.914
Cu1–N3,4,5 (Å)	2.09–2.22	2.06–2.31	2.11–2.21
Cu2–N6,7,8 (Å)	2.09-2.22	2.16–2.20	2.15–2.20

The small structural differences of the respective metal binding sites, induced by the non-symmetric ligand scaffold, might also be beneficial to stabilize a mixed valent Cu^{I}Cu^{II} complex similar to the ligand framework **VII** from Karlin and coworkers.[120] Therefore, the potential isolation of a Cu^{I}Cu^{II} complex on the basis of **L^{1,2}** should be investigated, since this might expand the series of pyrazolate/tacn derived copper/oxygen complexes. However, initial experiments in bulk synthesis, according to the synthetic routine of KARLIN and coworkers[120] by adding one equivalent of an adequate oxidizing agent (e.g. Fc^+) to the dicopper(I) complex **1**, only led to the formation of the decomposition product presented in section 5.2.6.

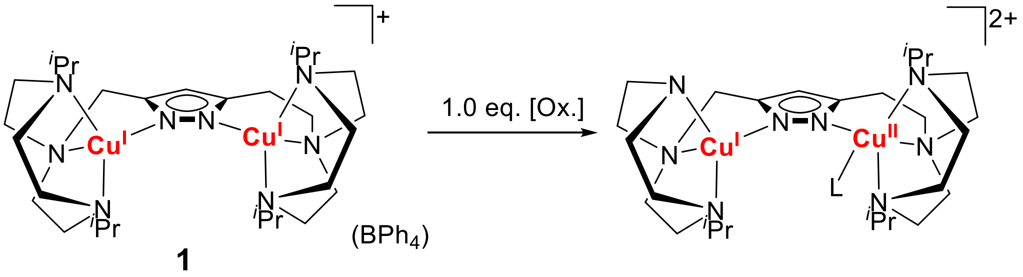

Scheme 13. Putative formation of a mixed-valent Cu^I Cu^{II} complex on the basis of synthetic routines from KARLIN and coworkers.[120] The binding site of the Cu^{II} ion might be complemented by a solvent molecule L.

5.2.2 Formation of a Peroxodicopper(II) Complex in Solution

Since precursor complex **1** could be isolated in pure form, its reactivity towards dioxygen was investigated. Similar to its symmetrical homologues, solutions of the dicopper(I) complex reacted readily with molecular dioxygen, which was accompanied by an intense color change from pale yellow to intense purple (Figure 28), being a characteristic feature of μ-1,2-peroxodicopper(II) complexes.[14,15,107]

Figure 28. Gradual conversion (left to right) of complex **1** in acetone at room temperature to the corresponding peroxodicopper(II) complex **2** by diffusion of ambient air.

The binding of dioxygen according to Scheme 14 was observed in various solvents (Aceton, MeCN, EtCN, MeOH, EtOH) and also for solid material of complex **1**, always revealing a purple colorization when exposed to dioxygen.

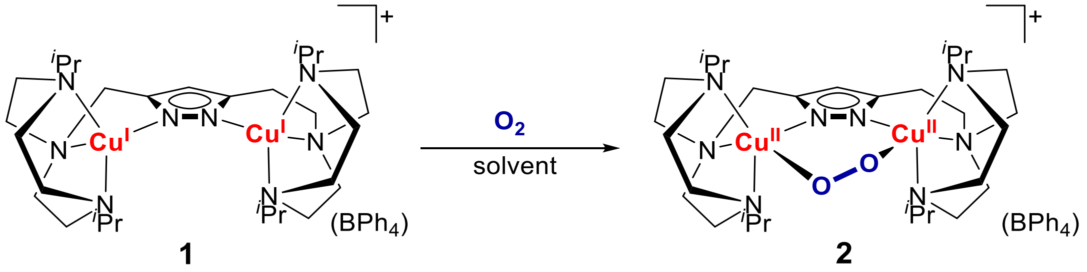

Scheme 14. Conversion of complex **1** to the μ-1,2-peroxodicopper(II) complex **2**.

When the binding of O_2 by the dicopper(I) complex was investigated by means of UV/Vis absorption spectroscopy, the featureless spectrum of **1** undergoes a dramatic change by an increase of an intense absorption band around 520 nm (ε = 5500 M^{-1} cm^{-1}) with a shoulder around 617 nm (ε = 3300 M^{-1} cm^{-1}) and a less pronounced shoulder around 437 nm (ε = 2000 M^{-1} cm-1) (Figure 29). Thus, the electronic absorption spectrum of **2** shows strong resemblance to the prior reported pyrazolate/tacn complexes **XVII** and **XVIII**, whose absorption features are characteristic for μ-1,2-peroxodicopper(II) complexes (also see Section 3.2.1) originating from $O_2^{2-} \rightarrow Cu^{II}$ charge transfer transitions.[50,146]

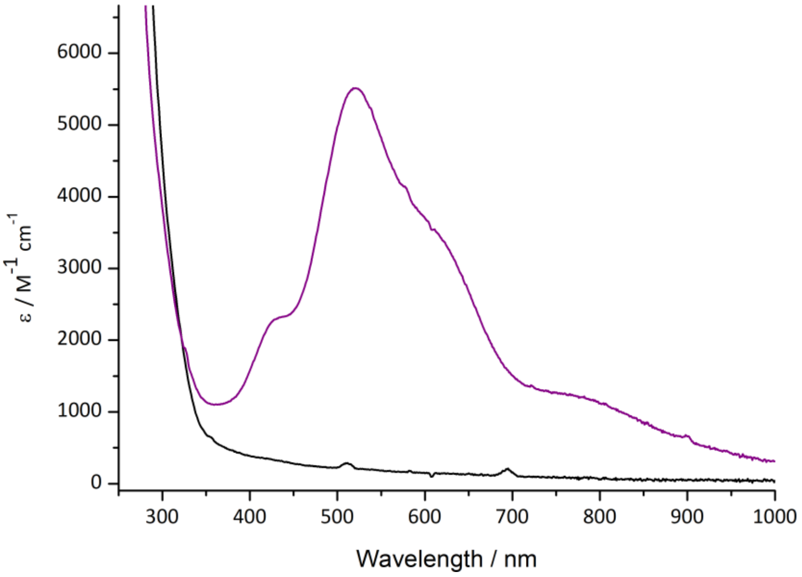

Figure 29. UV/Vis spectrum of complex **1** (black line) and formation of complex **2** (purple line) after addition of molecular dioxygen in MeCN at −40 °C.

Previous conducted TD-DFT calculations for complex **XVII** revealed that the transition around 520 nm arises from σ-interaction between the π^*_σ orbital of the peroxide and Cu-centered magnetic orbitals, while the transition around 650 nm derives from interactions of the π_v^* orbital.[113] The small changes in the electronic absorption spectra of **XVII**, **XVIII** and **2** (Figure 30) can therefore attributed to variation of the Cu−O−O−Cu torsion angle and therein contained mixing of π^*_σ and π_v^* orbitals, as well as the deviation from the ideal trigonal-bipyramidal or square-pyramidal coordination geometry of the copper ions.[93]

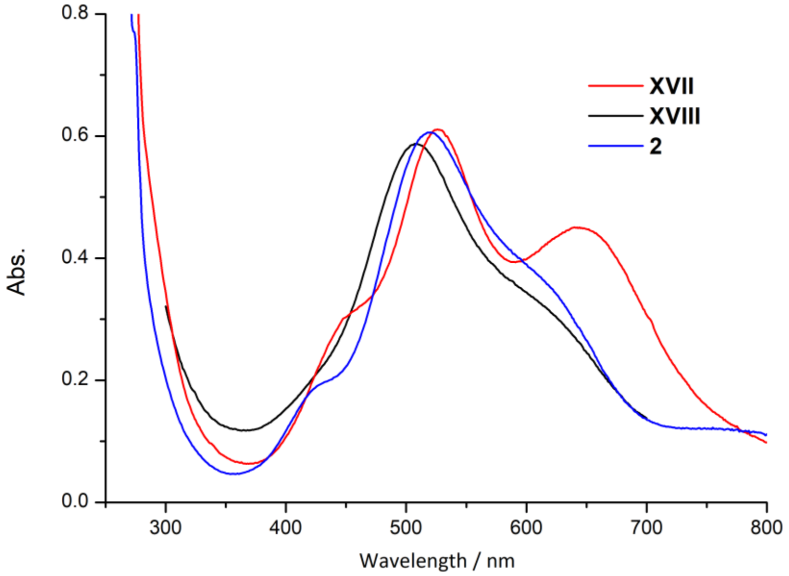

Figure 30. UV/Vis spectra of **XVII**, **XVIII** and **2** in MeCN at −40°C.[112,113]

Complex **2** was further investigated by resonance RAMAN spectroscopy, whereby acetonitrile solutions of the dicopper(I) precursor **1** inside a YOUNG-NMR tube were reacted at −20 °C with $^{16}O_2$, respectively $^{18}O_2$. Upon excitation (λ_{ex} = 633 nm) of those isotope-labelled samples, the following spectra were obtained (Figure 31).

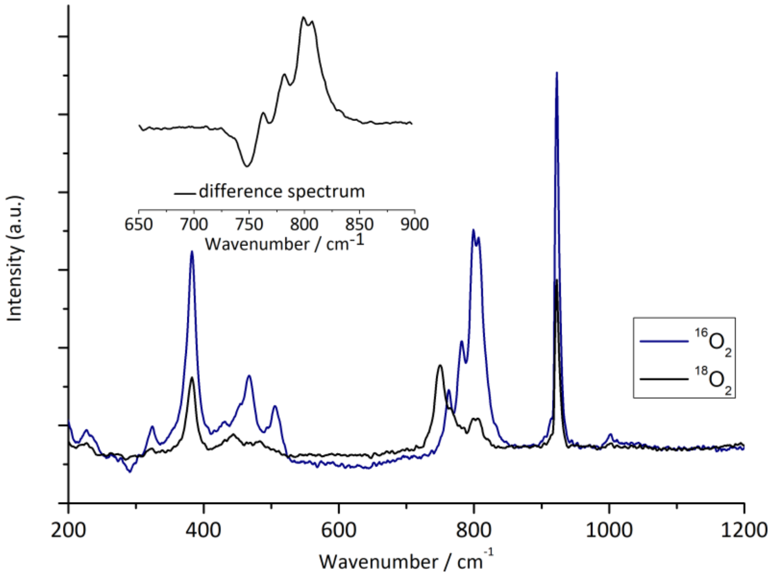

Figure 31. Resonance RAMAN spectrum of complex **2** in acetonitrile at room temperature (λ_{ex} = 633 nm). Isotope labeled samples were prepared by exposure of complex **1** to $^{16}O_2$, respectively $^{18}O_2$. The inset shows the difference spectrum between 650 and 900 nm.

Remarkably, the $^{16}O_2$ derived complex **2** exhibited a rather complex set of signals, having local maxima at 764 cm^{-1}, 783 cm^{-1}, 800 cm^{-1} and 807 cm$^{-1,}$ which merged into one major signal at 750 cm^{-1} after labeling of complex **1** with $^{18}O_2$. Additionally, also trace impurities deriving from atmospheric $^{16}O_2$ were observed for the $^{18}O_2$ labeled complex.

This observed multiplet formation and merging after $^{18}O_2$ labeling might be explained by FERMI resonance, which describes the interaction of a fundamental band with a combination or overtone band of approximately the same energy. The occurrence of this FERMI resonance has been reported in several μ-1,2-peroxodicopper(II) complexes, including the pyrazolate/tacn complexes **XVII** and **XVIII**.[112,113,147,148] However, in comparison to the prior reported symmetric complexes, the peroxodicopper(II) complex **2** showed a significantly stronger extent of this behavior, which might be due to the non-symmetry of the ligand system and therefore increased number of RAMAN-active vibrational modes. Further features in the RAMAN spectrum were also observed at lower energy at 467 cm^{-1} and 505 cm^{-1} and might originate from Cu−O stretching vibrations of the respective copper ions in the non-symmetric ligand scaffold, since complex **XVII** exhibited a Cu−O vibration around 415 cm^{-1} and **XVIII** at 506 cm^{-1}.[113,137] However, a clean assignment of the Cu−O vibration could not be done, due to the poorly resolved spectrum of the $^{18}O_2$ labelled complex in this region.

5.2.3 Solid State Properties

Solutions of complex **2** exhibited substantial decomposition at room temperature within several hours ($t_{1/2} \approx 32$ h), leading to bleaching of the purple solution to light blue over time. This observation will be discussed in detail in section 5.2.6.

However, thermal decay could be significantly reduced by storing solutions of complex **2** at –26 °C, even for several months. To elucidate the influence of the ligand scaffold on the formed peroxo moiety in the solid state, crystallization attempts were performed. Thus, various solvents (acetone, MeCN, MeOH, EtCN, EtOH) and different complex concentrations were tested. Hereby, mixtures of acetone/diethyl ether solutions have proven to be the most effective combination for crystallization, from which single crystals suitable for X-ray analysis were obtained in moderate yields up to 40% by slow vapor diffusion at –26 °C of diethyl ether. When solutions of pure acetone were employed for crystallization, significant contamination of the respective decay product was observed, leading to co-crystallization and a diminished yield of peroxo complex **2**.

The successful isolation of pure material of complex **2** also allowed to conduct further spectroscopic measurements. Solid state UV/Vis spectroscopy of the newly isolated peroxodicopper(II) complex reveals similar electronic absorption features as in solution and therefore confirms the presence of the same μ-1,2-peroxo binding motive in both states (Figure 32).

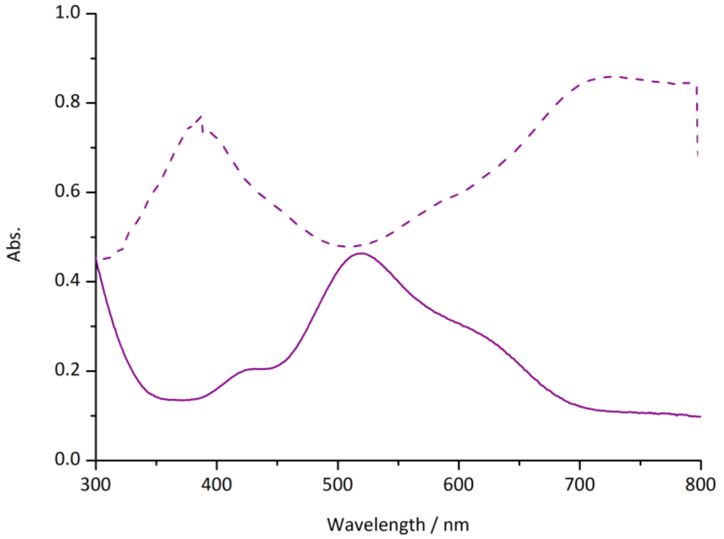

Figure 32. Comparison of electronic absorption spectra of peroxo complex **2** in solution (solid line) and the reflectance of the solid state within a KBr matrix (dotted line).

Further, crystalline material of $^{16}O_2$ and $^{18}O_2$ labeled complex **2** were investigated by resonance RAMAN spectroscopy (λ_{ex} = 633 nm). The corresponding spectra are depicted in Figure 33 and resembles the spectra recorded in solution.

A less complex spectrum with a maximum around 807 cm^{-1} and a minor resonance around 780 cm^{-1} is observed with natural abundance dioxygen. Shifting to a major signal at 757 cm^{-1} was observed with $^{18}O_2$, being in line with harmonic oscillator considerations and characteristic for the O–O stretching vibration. In addition, a more resolved signal for the Cu–O vibration was observed at around 515 cm^{-1} that shifted to 492 cm^{-1} ($\Delta^{16}O_2-^{18}O_2$ = 23 cm^{-1}) upon labeling with $^{18}O_2$, being in good agreement with an isolated harmonic Cu–O oscillator ($\tilde{\nu}(^{16}O-^{16}O)/\tilde{\nu}(^{18}O-^{18}O)$ = 1.047, calculated 1.097).

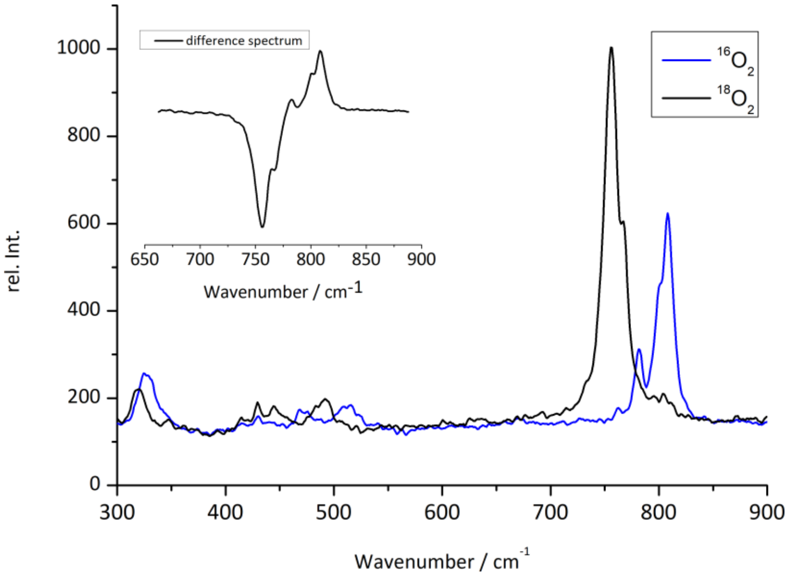

Figure 33. Solid state RAMAN spectrum of $^{16}O_2$ and $^{18}O_2$ peroxodicopper(II) complex **2** at room temperature (λ_{ex} = 633 nm).

As for previously reported pyrazolate/tacn peroxodicopper(II) complexes the molecular structure of the cationic part of **2** (Figure 34) indeed confirms the μ-1,2-peroxo binding motive.

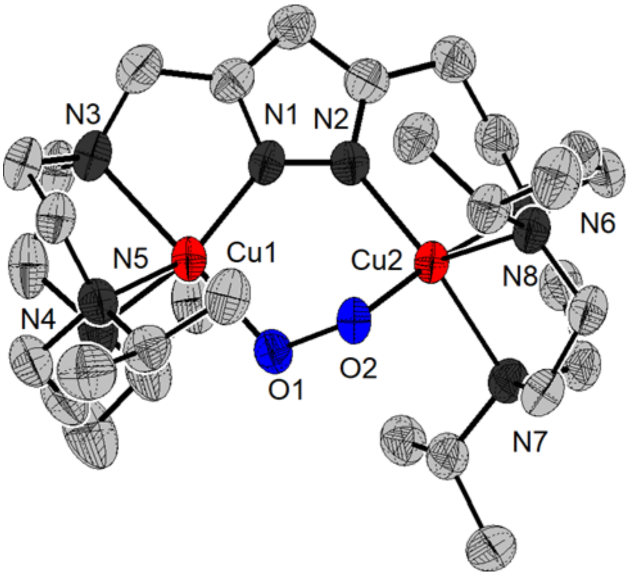

Figure 34. Molecular structure of the cationic part of complex **2**. Thermal displacement ellipsoids given at 50% probability. Hydrogen atoms, solvent molecules and counter ions are omitted for clarity. Selected bond lengths [Å] for **2:** Cu1···Cu2 3.6964(7) Cu1–O1 1.884(3), Cu1–N1 1.932(4), Cu1–N3 2.131(4), Cu1–N4 2.187(4), Cu1–N5 2.174(4), Cu2–O2 1.897(3), Cu2–N2 1.980(4), Cu2–N6 2.113(4), Cu2–N7 2.135(4), Cu2–N8 2.278(4), O1–O2 1.4524(41).

The coordination geometry of both copper ions differs slightly, insofar that the Cu^{II} ion coordinated by the methylene spaced tacn sidearm is coordinated in a distorted trigonal bipyramidal geometry

(τ_5 = 0.547 (Cu1)), featuring the same coordination environment as the Cu^{II} ions in the symmetrical complex **XVII**. In contrast, the Cu^{II} ion of the ethylene spaced tacn side arm exhibits a distorted square pyramidal geometry (τ_5 = 0.202 (Cu2)) as it has also been observed for the corresponding complex **XVIII**. In general, the observed Cu–N lengths differ between those involving the pyrazolate (Cu1–N1 = 1.93 Å, Cu2–N2 = 1.98 Å) or tacn (Cu1–N3,4,5 = 2.13-2.19 Å, Cu2–N6,7,8 = 2.11-2.28 Å) nitrogen atoms. The formed peroxo adduct **2** reveals a decrease of the Cu···Cu distance from 4.081 Å to 3.696 Å in comparison to the dicopper(I) complex **1**. The O–O bond exhibits a length of 1.452 Å and therefore fits in the range of previously reported μ-1,2-peroxo adducts.[15,107] The mentioned structural parameters are also summarized in Table 2.

Table 2. Metric parameters of the cationic parts of the peroxodicopper(II) complexes **XVII**, **2** and **XVIII** derived from the solid state structure via X-ray absorption spectroscopy.[112,113] τ_5 can be derived from the largest bond angles α and β and the equation $\tau_5 = \frac{\beta-\alpha}{60°}$.[145]

	XVII	**2**	**XVIII**
Cu1···Cu2 (Å)	3.741	3.696	3.677
Cu1–N1/Cu2-N2 (Å)	1.91/1.90	1.93 / 1.98	2.01/1.99
Cu1–N3,4,5/Cu2–N6,7,8 (Å)	2.18-2.26	2.13-2.19/2.11-2.28	2.10-2.29
O1–O2 (Å)	1.441	1.452	1.460
τ_5 [Cu1, Cu2]	~0.62	0.547, 0.202	~0.20
Cu1–O1/Cu2–O2 (Å)	1.890 / 1.897	1.884 / 1.897	1.8697 / 1.8748
Cu–O–O–Cu (°)	55	86	104
Cu–N–N–Cu (°)	18	29	38

Remarkably, the anticipated Cu–O–O–Cu torsion angle (ϕ) in **2** featuring the non-symmetrical ligand scaffold $\mathbf{L}^{1,2}$ indeed provides an in-between structure of the prior reported 104° for **XVIII** and 55° for **XVII.** With a torsion angle ϕ of 86° complex **2** can be regarded as the most accurate model system for the 90° bonding situation during initial steps of dioxygen activation at type III copper proteins.[50] Accordingly, the near 90 ° situation and therefore strict orthogonality of the copper oxygen orbitals should suppress the extent of antiferromagnetic coupling between the copper(II) ions and promote strong ferromagnetic coupling between them, which will be further elucidated in Section 5.2.3.

To further illustrate the influence of ligand design on structural properties of the respective copper oxygen complexes, space-filling model representations of the molecular structures of the cationic portion of the peroxo complexes **XVII**, **XVIII** and **2** are visualized in Figure 35.

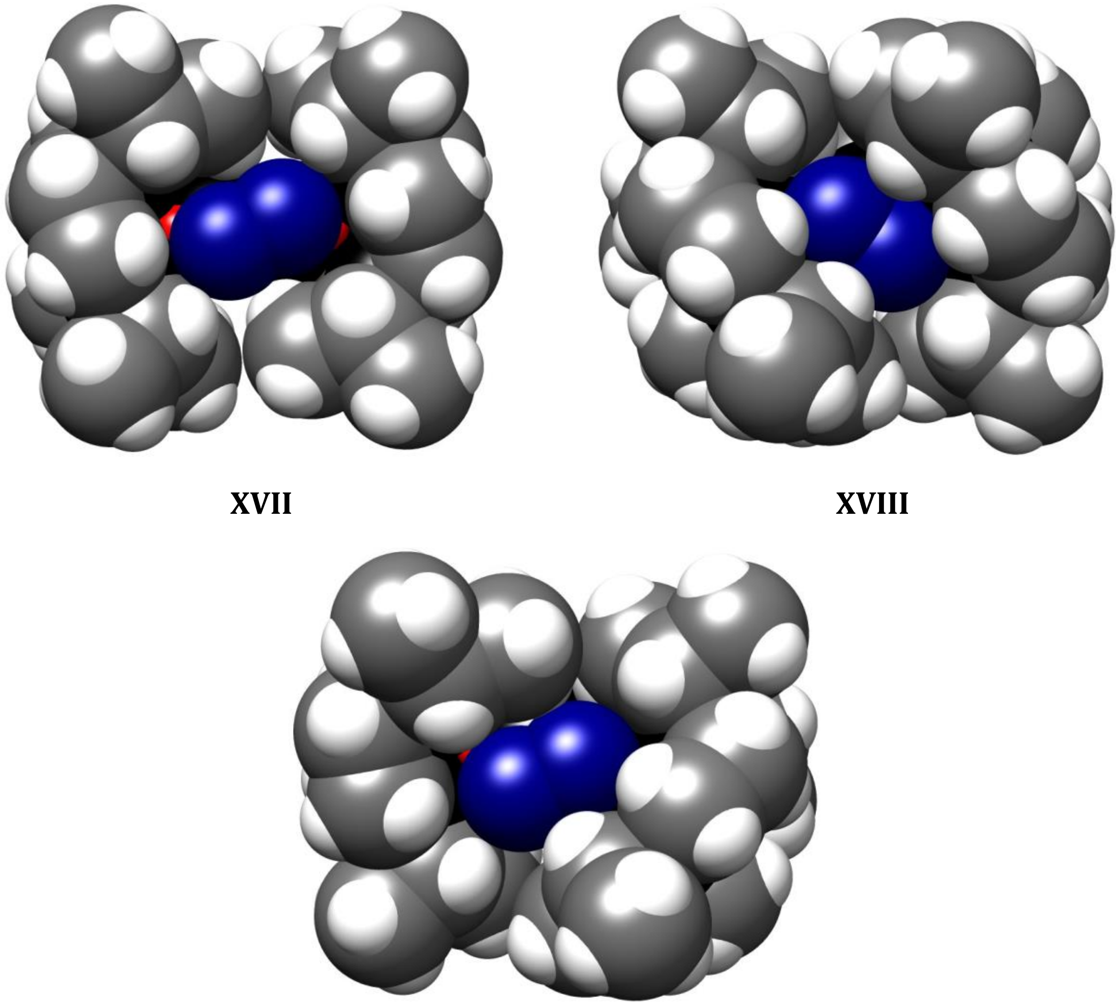

XVII **XVIII**

2

Figure 35. Space-filling models of the cationic parts of the peroxodicopper(II) complexes **XVIII**, **XVII** and **2**.[112,113] Oxygen atoms depicted in blue, nitrogen atoms in dark black and copper atoms in red.

Hence, a gradual increase of shielding of the peroxo core by the *iso*-propyl groups of the tacn moieties is observed upon elongation of the linker between the pyrazolate bridge and the tacn arms. Therefore, **XVII**, which possesses the ligand scaffold **L¹**, shows a comparatively high accessibility of the peroxide to a point where strong alkali metal interactions with the peroxide could be investigated in solution and the solid state.[52,113] In contrast, the increased steric encumbrance of the peroxo moiety in complex **XVIII**, which is based on the ethylene bridged ligand scaffold **L²**, led to no significant interactions with alkali metal ions but a rather increased stability of the Cu_2/O_2 adducts.[124] Further, the accessibility of the copper-oxygen core by substrates has also great influence on the reactivity of the corresponding superoxo complexes towards hydrogen atom transfer (HAT) reactions which will be discussed in Section 5.4.3. In comparison to **XVII** and **XVIII**, the space filling model of **2** shows steric shielding of the peroxide to an extent that combines structural properties of its symmetrical congener. The resulting properties regarding LEWIS acid interactions and potential reactivity studies of the superoxo complex will be discussed in the following sections.

5.2.4 Magnetic Properties

To reveal the influence of the close to 90° Cu–O–O–Cu torsion angle ϕ on the magnetic properties of complex **2**, magnetic susceptibility data were recorded via a superconducting quantum interference device (SQUID) in the temperature range between 2 K to 295 K. Therefore, finely ground material of crystalline complex **2** was used, which was recrystallized at least two times prior to use. The corresponding data are depicted in Figure 36. The increase in susceptibility with decreasing temperature and a maximum at 20 K reveals significant ferromagnetic coupling of the Cu^{II} ions and therefore a triplet ground state.

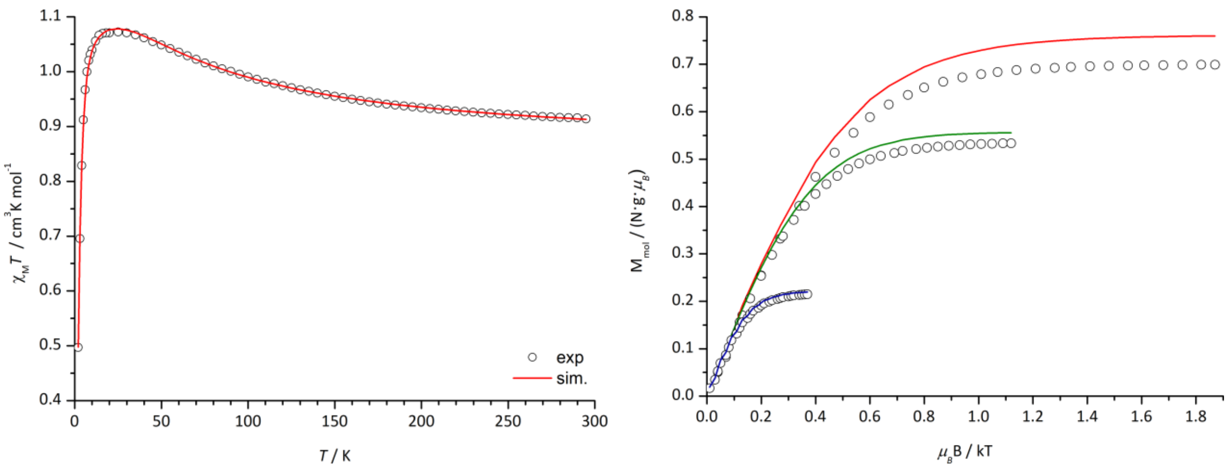

Figure 36. χ_mT vs. T measurement in the temperature range of 2–295 K at 0.5 T (left) and variable temperature/variable field (VTVH) magnetization measurements at fields of 1 T, 3 T, and 5 T presented as M_{mol} vs. μ_BB/kT (right) for crystalline samples of **2**. The solid lines represent the best global fit for both data sets, including antisymmetric DM interaction. Parameters obtained: J = +28.0 cm^{-1}; g = 2.030, 2.030, 2.347; TIP = -10 × 10^{-6} cm^3 mol^{-1}.

Fitting of the experimental data was done by taking the antisymmetric and anisotropic DZIALOSHINSKY-MORIYA (DM) interaction into account in a spin Hamiltonian (equation **2**) which has also been used to describe the magnetic coupling of complex **XVIII**.

$$\widehat{\mathrm{H}} = -2J\vec{S}_1\vec{S}_2 + \vec{d}\vec{S}_1 x\vec{S}_2 + g\mu_B(\vec{S}_1 + \vec{S}_2)\vec{B} \tag{2}$$

A coupling constant of J = +28 cm^{-1} with $\vec{d}$ = (39, 0, 0) cm^{-1} and g = 2.03, 2.03, 2.35 could be derived for **2**, extending the rare series of ferromagnetically coupled peroxodicopper(II) complexes. The strong decrease of $\chi_m T$ below 20 K indicates zero-field splitting (ZFS), which was also confirmed by variable-temperature and variable-field (VTVH) measurements that show significant nesting of the curves.

Figure 37 shows the alteration of the Cu–O–O–Cu torsion angle ϕ of the peroxodicopper(II) complexes **XVII**, **2** and **XVIII** depending on the employed pyrazolate/tacn ligand scaffold. As already stated in Section 2.3, strong antiferromagnetic coupling, respectively a 'superexchange' pathway, occurs when the Cu–O–O–Cu core is arranged in a near-linear fashion (ϕ = 180°) as it is the case in *trans*-μ-1,2-peroxo systems.

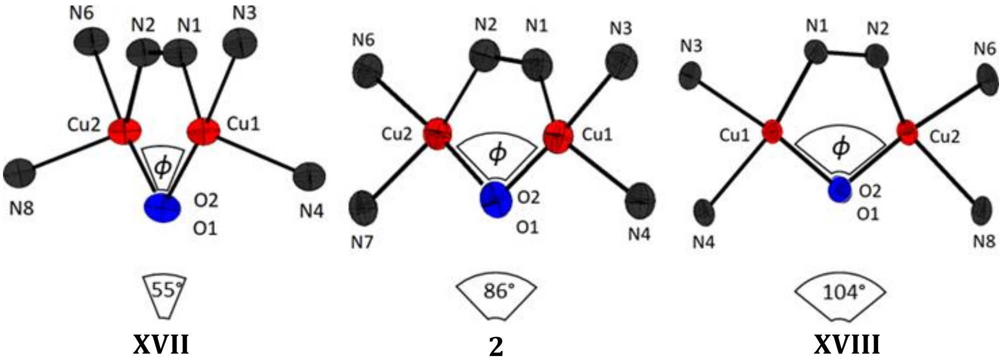

Figure 37. Comparison of the Cu–O–O–Cu torsion angle ϕ of the core structure of the cationic parts of peroxo complexes **XVII**, **2** and **XVIII**. The torsion angle is visualized by looking along the O–O bond.

However, when ϕ approaches 90° the antiferromagnetic contribution is breaking down due to decreased overlap of magnetic orbitals, to a point where ferromagnetic exchange dominates.

Thus, the methylene spaced pyrazolate/tacn peroxo core of **XVII**, which possesses a dihedral angle ϕ of around 55° exhibits an already diminished extent of antiferromagnetic coupling ($J = -54$ cm^{-1}) but still a singlet ($S = 0$) ground state.[113] In contrast, **XVIII** has a Cu–O–O–Cu torsion angle of 104°, approaching the 90° situation where the antiferromagnetic coupling term is suppressed, resulting in ferromagnetic coupling of the copper(II) ions ($J = +72$ cm^{-1}) and therefore a triplet ground state.[112] The magnetic properties of **XVII**, **2** and **XVIII** are summarized in Figure 38.

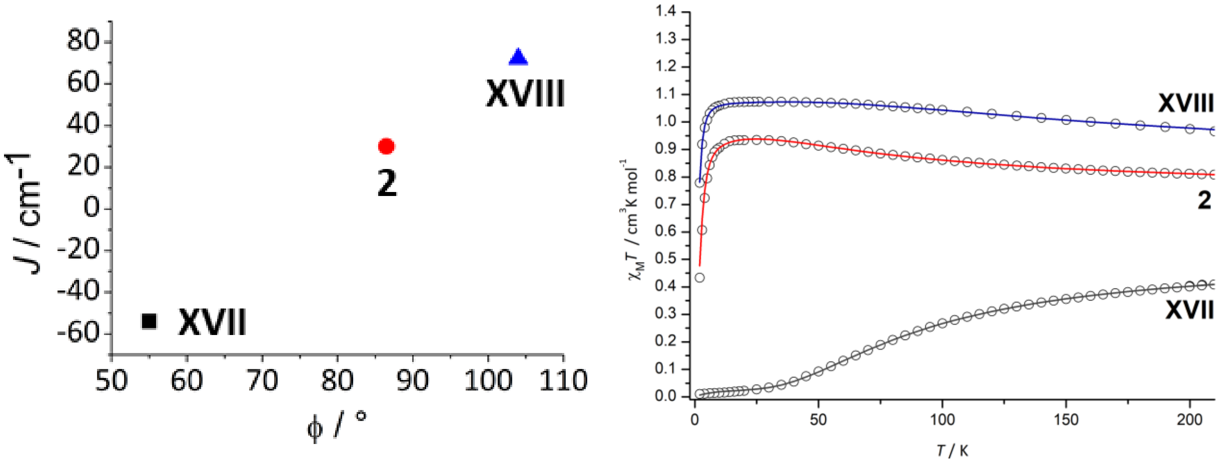

Figure 38. Correlation between the Cu–O–O–Cu torsion angle ϕ and the magnetic coupling J of the peroxo complexes **XVII**, **2** and **XVIII** (left). χ_mT vs. T measurement in the temperature range of 2–295 K at 0.5 T for **[L^{2}Cu$_2$(O$_2$)](BPh$_4$)**, **[L^{1,2}Cu$_2$(O$_2$)](BPh$_4$)**, and **[L^{1}Cu$_2$(O$_2$)](BPh$_4$)**.[112,113] The solid lines represent the best global fit, including antisymmetric DM interaction (right).

Remarkably, direct comparison of the magnetic properties reveals that complex **2** shows less ferromagnetic coupling than **XVIII**, even though the Cu–O–O–Cu torsion angle is closer to 90°, which should therefore suppress the antiferromagnetic coupling contribution. While the peroxide ligand can be regarded as the dominant factor that influences the magnetic properties of the corresponding peroxodicopper(II) complexes the respective coordination geometries of each copper ion should also be considered.

The newly isolated peroxo core features two copper(II) ions with significantly different coordination geometries which might contribute to the magnetic orbital overlap. An intermediate coordination geometry between the ideal square pyramide and trigonal bipyramide will lead to significant mixing of the $d_{x^2-y^2}$ and d_{z^2} magnetic orbitals with the pyrazolate and peroxide orbitals. Consequently, a decrease of antiferromagnetic interaction is observed as the distortion of the copper ion geometry increases from square pyramidal to trigonal bipyramidal.[149,150] However, this explanation might not be sufficient, since complex **XVIII** exhibits rather square pyramidal coordination for both copper ions ($\tau_5 = \sim 0.20$) and should therefore exhibit less suppressed antiferromagnetic coupling. Further magnetic contributions of the pyrazolate should also be considered even though those are comparatively small ($J = -(15\text{-}36)$ $\mathrm{cm^{-1}}$), as reported for complexes where the pyrazolate is the only bridging unit.[151–153] However, since complex **2** approaches the 90° situation and exhibits rather weak ferromagnetic coupling, the pyrazolate mediated coupling should definitely be taken into account.

Therefore, **2** can be regarded as a completion to peroxo complex **XVIII**, modelling the proposed 90° situation of initial stages of O_2 binding at type III copper proteins. To elucidate the electronic structure and ferromagnetic and antiferromagnetic coupling contributions in more detail, investigations in collaboration with THOMAS LOHMILLER at the HELMHOLTZ Zentrum in Berlin are currently ongoing.

5.2.5 DFT Calculation

In the previous section the influence of structural parameters such as the Cu−O−O−Cu torsion angle or the respective coordination geometry of each copper ion on the magnetic exchange coupling were qualitatively discussed.

The general interaction of two copper(II) ions initially gives rise to either a molecular spin singulet ($S = 0$) or a molecular spin triplet ($S = 1$), whereby the singlet to triplet energy gap is conventionally denoted by $2J$. [146,147] Per definition, for the singlet ground state ($2J < 0$) the interaction is overall antiferromagnetic and for the triplet ground state ($2J > 0$) ferromagnetic.[149] However, the singlet-triplet energy gap, respectively overall magnetic coupling J can be regarded as the sum of ferromagnetic and antiferromagnetic contributions ($J = J_{\text{ferromagnetic}} + J_{\text{antiferromagnetic}}$), which are both counteracting each other.[149,150,154] Hereby, the antiferromagnetic contribution is dependent on the overlap integral of the magnetic orbitals and is diminished to a minimum when the overlap integral approaches zero. Hence, the ferromagnetic coupling term dominates when the magnetic orbitals approach orthogonality. Therefore, for peroxodicopper complexes, magnetic coupling is highly dependent on the Cu−O−O−Cu torsion angle. To get further insights into those orbital interactions in case of complex **2**, DFT calculations were performed based on the solid-state structure of complex **2**.

Geometry optimization of only the H-atom positions were conducted since full geometry optimization led to a divergence of the experimentally observed Cu−O−O−Cu torsion angle of 86°. It has recently been shown that the potential associated with the Cu−O−O−Cu dihedral angle is shallow.[121] Optimization was done, using the ORCA[155] software with the B3LYP functional, RIJCOSX approximation and def2-tzvp and def2-tzvp/j basis sets.[156,157] A broken-symmetry (BS) approach was employed to derive the coupling constant J according to different methods[158–162].

$$J^{(1)} = \frac{E^{(HS)} - E^{(BS)}}{S_{max}^{2}} = +173\ \text{cm}^{-1} \tag{3}$$

$$J^{(2)} = \frac{E^{(HS)} - E^{(BS)}}{S_{max}(S_{max}+1)} = +86\ \text{cm}^{-1} \tag{4}$$

$$J^{(3)} = \frac{E^{(HS)} - E^{(BS)}}{<S^2>^{(HS)} - <S^2>^{(BS)}} = +171\ \text{cm}^{-1} \tag{5}$$

All determined values were higher than the experimentally obtained value of $J = +28\ \text{cm}^{-1}$, but indeed confirmed the ferromagnetic exchange coupling. Interestingly, the derived coupling constant are comparatively smaller than the also by DFT calculations determined values of complex **XVIII** ($J^{(1)} = +199\ \text{cm}^{-1}$, $J^{(2)} = 100\ \text{cm}^{-1}$, $J^{(3)} = 199\ \text{cm}^{-1}$), fitting well to the experimentally observed decrease of ferromagnetic coupling from **XVIII** to complex **2**.

Overlap of the magnetic orbitals was derived by broken-symmetry state analysis of the corresponding orbitals 187α and 187β (Figure 39), revealing a value of 0.09 for the magnetic overlap integral, which is significantly higher than for complex **XVIII** (0.003). Thus, the increased magnetic overlap of complex **2** might explain an increase of the antiferromagnetic contribution term ($J_{\text{antiferromagnetic}}$) and hence weaker overall ferromagnetic coupling for complex **2**. The relevance of further magnetic contributions, e.g., by the pyrazolate bridge, are currently under investigation.

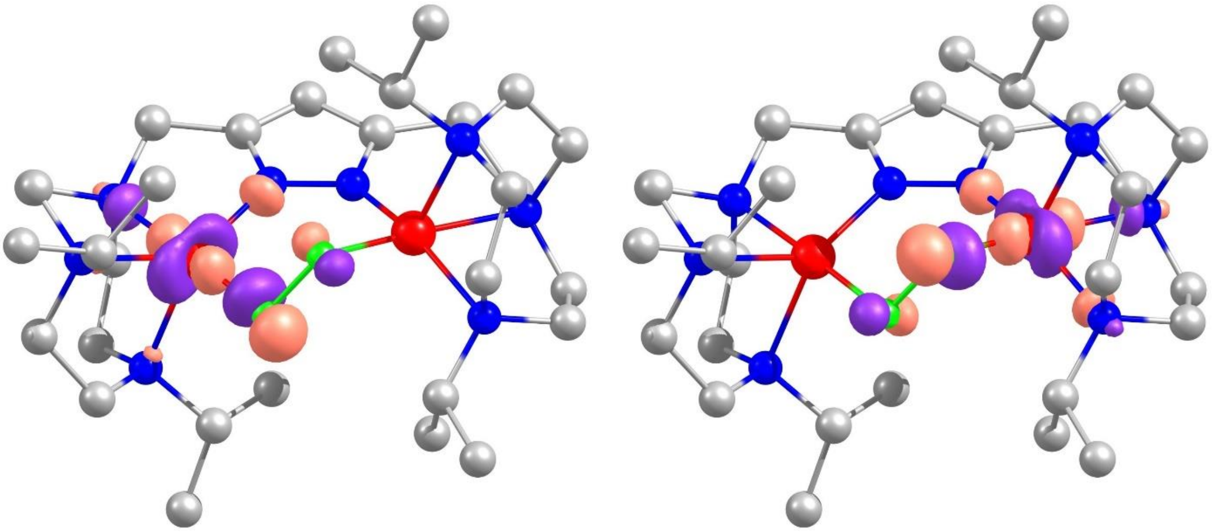

Figure 39. Magnetic orbital pair 187α (left) and 187β (right) of complex **2** for the broken-symmetry state with a contour value of 0.08. (Copper in red, oxygen in green, nitrogen in blue, carbon in grey, hydrogen atoms are omitted for clarity).

5.2.6 Decay Properties

While complex **2** is almost infinitely stable at low temperatures (−20 °C) in the solid state, significant decomposition can be observed even at temperatures down to −40 °C in solution. The decay of peroxo complex **2** in MeCN, EtCN or acetone is accompanied by a drastic color change from intense purple to pale blue/green (Scheme 15), which can be readily monitored by UV/Vis spectroscopy.

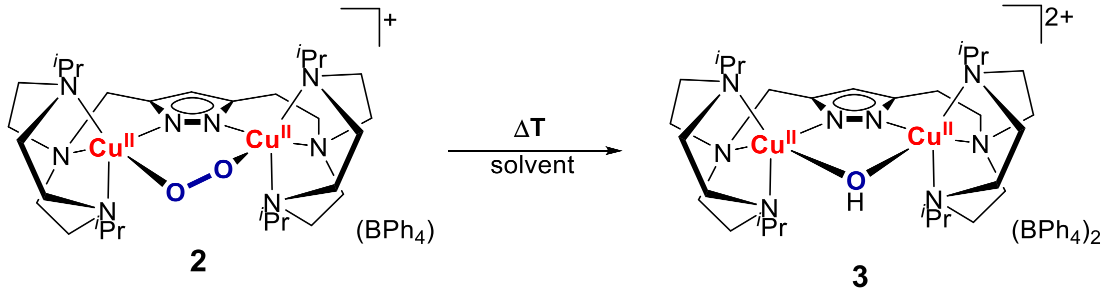

Scheme 15. Decomposition of complex **2** to the corresponding μ-hydroxo complex **3**.

The gradual decomposition of complex **2** is depicted in Figure 40, exhibiting a *pseudo*-isosbestic point at 413 nm. Further, a plot of the most distinct absorption features at 374 nm for the decomposition product and 520 nm for complex **2** versus time revealed decay kinetics of higher order. Therefore, the half-life time of the complex was estimated based on the decay of the absorption band at 520 nm, resulting in $t_{1/2} \approx 32$ h for the half maximum absorption; this value is significantly higher than for complex **XVIII** ($t_{1/2} \approx 10$ h in EtCN).

The whole decay reaction is accompanied by a decrease of the characteristic peroxodicopper(II) features around 520 nm, 617 nm and 437 nm together with an increase of new LMCT bands around 374 nm (ε = 4500 $M^{-1}cm^{-1}$) and d-d transitions around 626 nm (ε = 240 $M^{-1}cm^{-1}$), being characteristic for μ-hydroxodicopper(II) complexes of pyrazolate/tacn ligands.

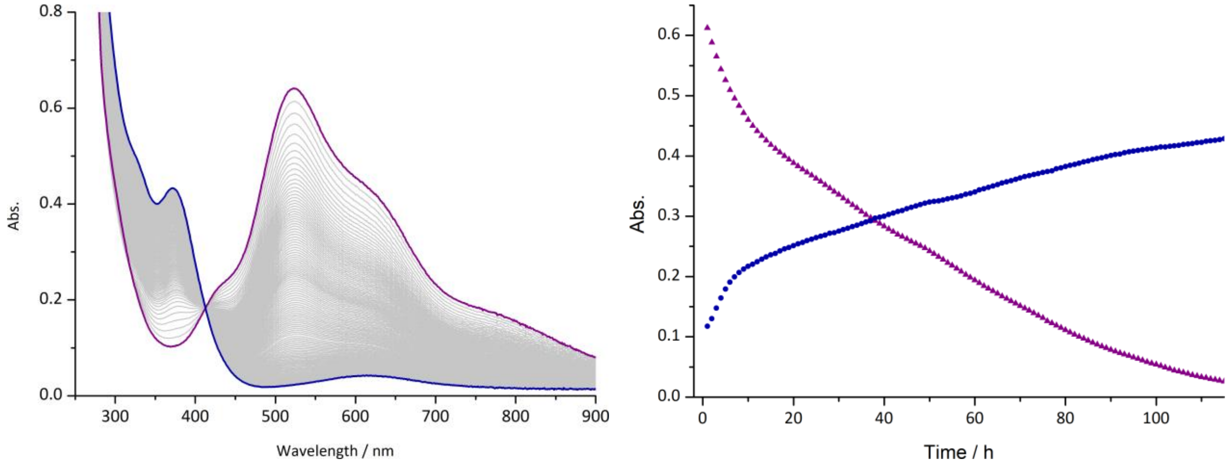

Figure 40. Thermal decay of complex **2** in MeCN at RT (left). Change of Absorption at 374 (●) and 520 nm (▲) versus time (right).

The decomposition product could also be isolated in the solid state using different synthetic procedures. Either by adding $NaBPh_4$ to solutions of peroxo complex **2** in MeCN and subsequent Et_2O diffusion at room temperature or by complexation of the bare ligand with $Cu(ClO_4)_2 \cdot 6\ H_2O$ and subsequent counter ion exchange with $NaBPh_4$, followed by $MeCN/Et_2O$ diffusion at room temperatures. Both synthetic routes generated crystalline material in high yields between 55-85% that exhibited the same electronic absorption features as the decay product (Figure 41) and which were suitable for X-ray analysis, verifying that the decomposition product is indeed the corresponding μ-hydroxo complex **3**.

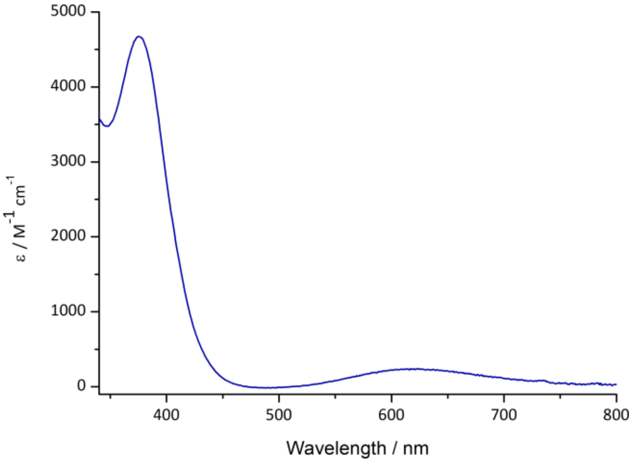

Figure 41. UV/Vis absorption spectrum of complex **3** in MeCN at RT.

The molecular structure of complex **3** (Figure 42) exhibits two copper ions with a slightly distorted square pyramidal coordination geometry (τ_5(Cu1) = 0.15, τ_5(Cu2) = 0.05), originating from ligation by the four nitrogen atoms of the pyrazolate/tacn scaffold and the oxygen atom of the hydroxide ligand. In comparison to complex **2** the copper-copper separation decreases from 3.70 Å to 3.43 Å. A greater distortion towards a trigonal-bipyramidal coordination geometry is observed for the copper(II) ion which is coordinated by the ligand side with methylene linker between the pyrazolate and the tacn, which was also observed for its respective symmetrical congener.

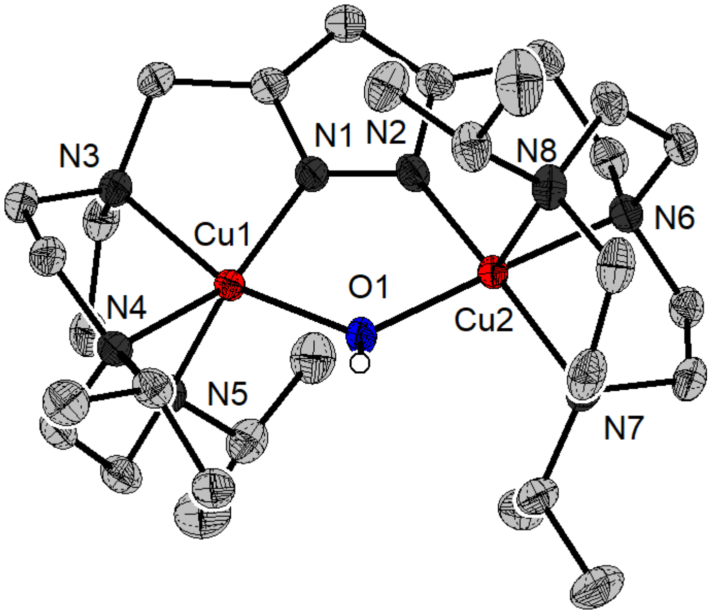

Figure 42. Molecular structure of the cationic part of complex **3**. Thermal displacement ellipsoids given at 50% probability. Hydrogen atoms, solvent molecules and counter ions are omitted for clarity. Selected bond lengths [Å] for **3**: Cu1⋯Cu2 3.4324(5), Cu1–O1 1.9608(12), Cu2–O1 1.9677(12), Cu1–N1 1.8927(14) Cu1–N4 2.0567(14), Cu1–N3 2.0929(13), Cu1–N5 2.3081(15), Cu2–N2 1.9489(14), Cu2–N6 2.0544(14), Cu2–N7 2.0697(14), Cu2–N8 2.3219(15).

As already stated in previous sections, the elongated ligand scaffold **L**^{2} generally provided a shorter metal to metal separation as **L**^{1} of their respective μ-1,2-peroxodicopper(II) complexes. Thus, the structures of the corresponding hydroxo complex vary according to the employed ligand framework (Figure 43). Hence, complex **XXXI** also revealed a μ-hydroxo binding motive like complex **3** with a Cu···Cu separation of 3.41 Å. In contrast, the methylene spaced ligand framework of complex **XXX**, led to an increase of the copper copper distance to 4.38 Å, whereby the formation of monoatomic bridge was highly unfavored. Hence, the corresponding decomposition product of complex **XVII** exhibits a H_3O_2 bridge between both Cu$^{\text{II}}$ ions.

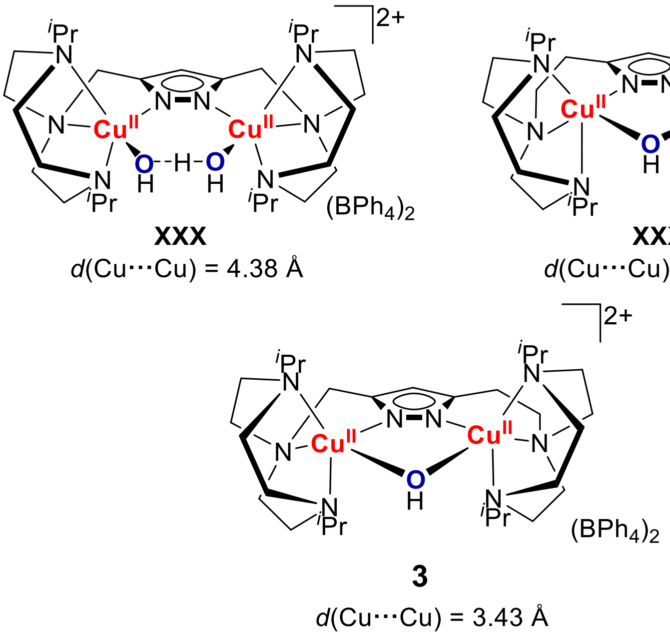

Figure 43. Thermal decomposition products of the corresponding Cu_2/O_2 adducts with different pyrazolate/tacn ligand scaffolds.[112,113]

The magnetic properties of complex **3** were investigated by magnetic susceptibility measurements between 2 K and 295 K using powdered crystalline material (Figure 44). Thereby, strong antiferromagnetic coupling between both Cu$^{\text{II}}$ ions (J = –294 cm^{-1}) was observed, which is common for pyrazolate bridged hydroxodicoppper(II) complexes and strongly influenced by the Cu–O-Cu angle, whereby the antiferromagnetic coupling term dominates for Cu–O-Cu angle > 97.5°.[163] Further structural components that might influence the extent of antiferromagnetic coupling are the Cu–O distances and the out-of plane displacement of the H atom of the hydroxide ligand.[164–166]

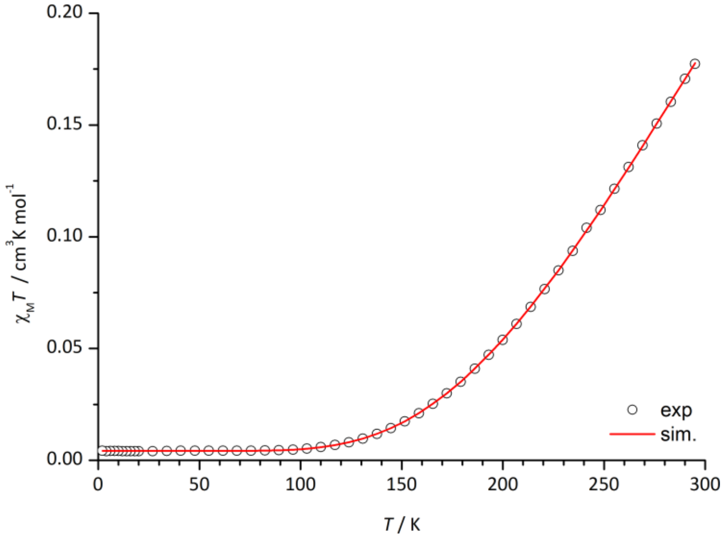

Figure 44. Magnetic Susceptibility data of complex **3** between 2K and 295 K (○) together with the best simulation fit (–). Parameters obtained: $J = -293.9$ cm^{-1}, $g = 2.195$, PI = 1.1%, TIP = -54×10^{-6} cm^3 mol^{-1}.

Interestingly, the observed magnitude of antiferromagnetic coupling even exceeds that of complex **XXXI** ($J = -184$ cm^{-1}).[137] While the Cu–O–Cu angle might not be an explanation for this observation, since Cu–O–Cu of **3** was slightly smaller (121.8° vs. 123.3°), the increased antiferromagnetic coupling might originate from slightly different Cu–O bond lengths (1.97 Å vs. 1.93 Å) and less out of plane displacement of the OH unit.[165,166] Hence, a larger σ in-plane overlap between the coplanar $d_{x^2-y^2}$ magnetic orbitals and the bridging unit.

Magnetic and structural parameters for the decomposition products **XXX**, **3** and **XXXI** are summarized in Table 3.

Table 3. Metric and spectroscopic parameters of hydroxodicopper(II) complexes **XXX**, **3** and **XXXI** derived from the solid state structure via X-ray absorption spectroscopy.[137,153]

	XXX	**3**	**XXXI**
Cu1···Cu2 (Å)	4.380	3.432	3.405
τ_5 [Cu1, Cu2]	~0.46	0.15, 0.05	~0.08
Cu–O–Cu (°)	–	121.8	123.3
J (cm^{-1})	–36	–294	–184

Due to the time consuming multistep synthesis of pyrazolate/tacn ligand frameworks and their corresponding dicopper complexes, the potential recycling of the thermodynamically stable complex **3** appears to be of great benefit. As already demonstrated in previous work, the hydroxo complex **XXX** can be converted back into the more reactive dicopper(I) species under reductive conditions.[113]

In a typical UV/Vis titration experiment, complex **3** was treated with a suitable reductant,[167] namely $CoCp_2$ (E^0 = –1.34 V vs. Fc/Fc^+) to reduce the dicopper(II) complex (Scheme 16).

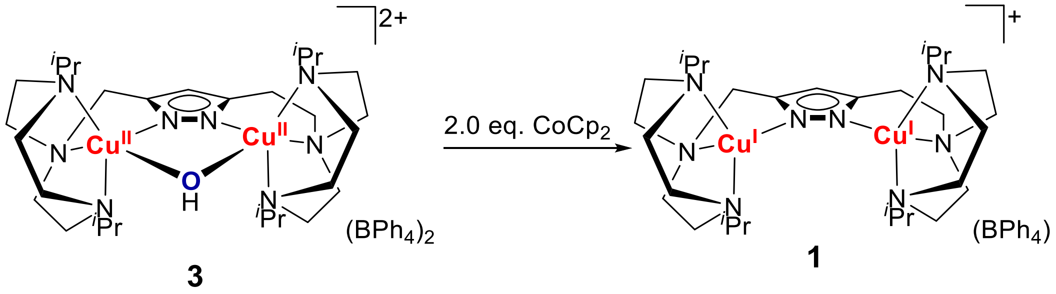

Scheme 16. Recycling of complex **3** to the precursor complex **1** by conversion with cobaltocene.

For this purpose, a tenfold more concentrated solution than usually employed for UV/Vis experiments (see also Section 7.2 for general information) was employed for the stepwise titration of complex **3** (c = 1.05 mM) with cobaltocene at room temperature. Due to the absorption properties of the $CoCp_2/CoCp_2^+$ species the change in absorption of the characteristic Cu^{II} d-d transition at 626 nm was followed, which is depicted in Figure 45.

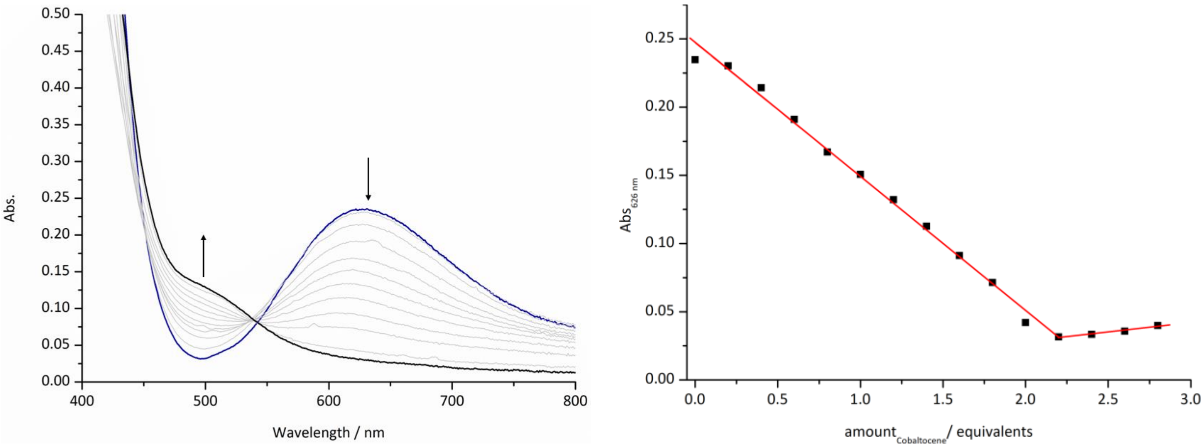

Figure 45. UV/Vis Titration of complex **3** with $CoCp_2$ at room temperature in EtCN (left) and a plot of the absorption at 626 nm vs. amount of $CoCp_2$.

A gradual decrease of the d-d transition band of the copper(II) ions was observed, which corresponds to the reduction of the Cu^{II} to Cu^I ions and thus the re-formation of complex **1**.

The whole process is accompanied by the decrease of all characteristic absorption features of the μ-hydroxo complex **3** (333 nm, 375nm and 626 nm), whereby a *pseudo*-isosbestic point at 538 nm shifts slightly, which might be due to potential site reactions of the elusive transformation mechanism or potential involvement of a mixed-valent Cu^ICu^{II} species. However, the presence of only one pseudo-isosbestic point hints towards a direct conversion from the $Cu^{II}Cu^{II}$ core to the Cu^I Cu^I motif without a mixed-valent Cu^ICu^{II} intermediate. Previously reported acetate dicoppper(II) complexes of the MEYER group, which employed the methylene spaced pyrazolate and methyl substituted tacn scaffold demonstrated the necessity of an acetate ion to stabilize the Cu^ICu^{II}

intermediate upon reduction with $CoCp_2$. The exact reduction mechanism of hydroxo complex **3** and the fate of the hydroxo moiety is still a subject of ongoing research.

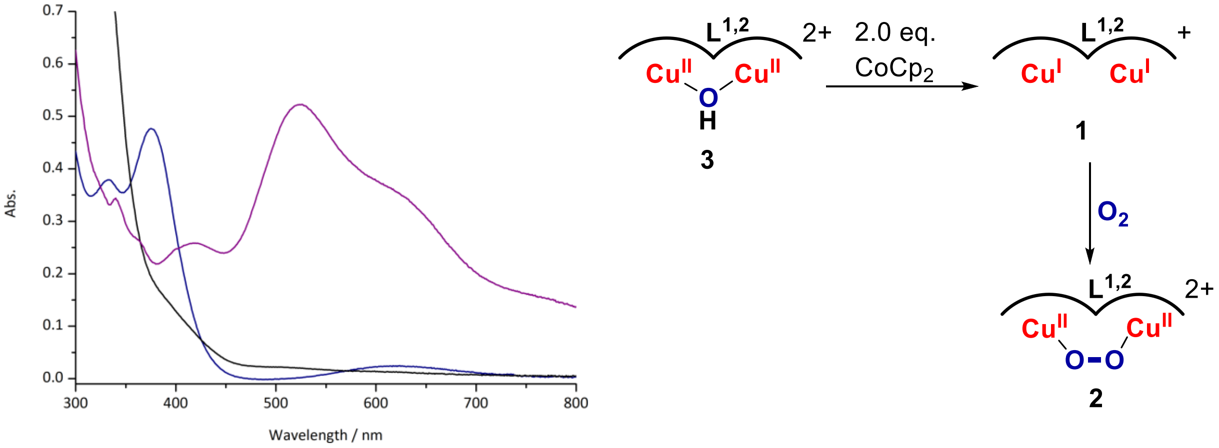

Figure 46. UV/Vis spectrum of complex **3** (dark blue) with $CoCp_2$ at RT in EtCN (black) and subsequent addition of molecular dioxygen (purple) and schematic representation of the involved copper/oxygen species, whereby the counter ions and full ligand scaffold are omitted for simplification.

After reduction to the dicopper(I) complex **1**, subsequent addition of molecular dioxygen leads to the formation of the characteristic absorption bands of peroxodicopper complex **2** (Figure 46), demonstrating the successful recycling of the decomposition product **3**.

5.2.7 Summary and Conclusion

The ligand framework **$L^{1,2}$** was employed for the isolation of the dinuclear copper(I) complex **1** which was successfully synthesized and characterized by X-ray diffraction and NMR spectroscopy. Thereby, it was demonstrated that the structural properties of the newly isolated non-symmetric dicopper(I) precursor can be regarded as an amalgamation of the previously reported symmetrical complexes.

Additionally, the series of peroxodicopper(II) adducts based on pyrazolate/tacn ligands was extended by the non-symmetric complex **2**, which was initially investigated by UV/Vis and resonance RAMAN spectroscopy. Isolation of crystalline material also provided a solid-state structure from which it was possible to derive a Cu−O−O−Cu torsion angle ϕ of 87 °, completing the series of prior reported complex **XVII** (ϕ = 54°) and **XVIII** (ϕ = 104°). Comparison of structural and spectroscopic properties of the peroxodicopper(II) complexes **XVII**, **XVIII** and **2** are summarized in Table 4.

The newly isolated peroxodicopper(II) adduct can be considered an excellent model for the key step of oxygen activation on type III copper proteins and the 90° situation prior to the singlet to triplet intersystem crossing event. Magnetic susceptibility data of complex **2** revealed a comparatively weaker ferromagnetic coupling of $J = +28\ \mathrm{cm}^{-1}$, which was compared to the magnetic properties of **XVII** and **XVIII**. While **XVII** exhibited weak antiferromagnetic coupling ($J = -54\ \mathrm{cm}^{-1}$), due to the decreased superexchange pathway, ferromagnetic coupling for complex **XVIII** was observed due to the almost orthogonality of the magnetic orbitals (90° situation). Thus, the newly isolated complex **2** provides a more refined picture of the correlation between the Cu−O−O−Cu torsion angle ϕ and the magnetic properties. Since the non-symmetric peroxodicopper(II) complex show weaker ferromagnetic magnetic coupling than **XVIII**, further contributions of the pyrazolate bridge should be considered due to the unique nearly 90° binding situation in **2**; these and other effects and are currently investigated. Initial DFT calculations reveal a comparatively higher magnetic integral overlap integral for **2** than for **XVIII**, confirming the experimental trend.

As already stated in previous works, copper/oxygen adducts on the basis of pyrazolate/tacn frameworks tend to form the corresponding hydroxodicopper(II) complex after thermal decomposition. Thus, the decay reaction from **2** to the hydroxo complex **3** was followed via UV/Vis spectroscopy, revealing kinetics of higher order. Further, complex **3** was characterized by X-ray diffraction and magnetic measurements, revealing very strong antiferromagnetic coupling ($J = -294\ \mathrm{cm}^{-1}$).

Table 4. Metric and spectroscopic parameters of peroxodicopper(II) complexes **[$L^1Cu_2(O_2)$](BPh$_4$)**, **2** and **[$L^2Cu_2(O_2)$](BPh$_4$)** derived from the solid state structure via X-ray absorption spectroscopy.[112,113]

	XVII	**2**	**XVIII**
Cu1···Cu2 (Å)	3.741	3.696	3.677
O1–O2 (Å)	1.441	1.452	1.460
τ_5 [Cu1, Cu2]	~0.63	0.547, 0.202	~0.20
Cu1–O1/Cu2-O2 (Å)	1.890 / 1.897	1.884 / 1.897	1.8697 / 1.8748
φ (°)	55	86.5	104
λ_{max} (nm) [ε(M^{-1}cm^{-1})]	456 [2600], 527 (5000), 648 (3900)	437 [2000], 520 [5500], 617 [3000], 790 [1500]	506 [4800], 607 [3000], 800 [1100]
$\tilde{\nu}_{O-O}$ (cm^{-1})	809	~804	803
J (cm^{-1})	–54	+28	+72

Since the synthesis of copper complexes based on those ligand frameworks is very time-consuming, recovery from the decay product appears particularly attractive. Recently, ALEXANDER BRINKMEIER has demonstrated that under reductive conditions the respective hydroxo complex can be converted back again into the dicopper(I) precursor.[113] Therefore, the potential recycling of hydroxo complex **3** was investigated through reduction, whereby conversion from **3** to **1** was observed. Since the exact mechanism is still unclear, further work should address this conversion and the extent to which the isolation of mixed-valent Cu^ICu^{II} species is possible. This seems to be particularly attractive since the non-symmetric ligand scaffold might provide sufficient stabilization of a Cu^ICu^{II} complex, which upon reaction with O_2 might extend the series of potential copper/oxygen adducts based on pyrazolate/tacn ligand frameworks.

5.3 Reversible Peroxo/Hydroperoxo Interconversion

In the previous section, the isolation and characterization of a novel non-symmetric peroxodicopper(II) complex, based on the compartmental pyrazolate/tacn ligand scaffold **L1,2** was presented. Since dioxygen-mediated catalysis in cupric metalloenzymes involves a large variety of potential key motifs, such as peroxido, superoxido or hydroperoxido species, the isolation of those structural intermediates and the elucidation of their properties is highly demanded.[14,15,51,92,168–170]

As already demonstrated in Section 2, the redox chemistry of copper-containing metalloenzymes is strongly linked to proton transfer processes. Among others, cuprous hydroperoxide motifs are discussed as relevant species in a variety of enzymes or during the formation of H_2O_2 by the 4 e^- reduction of oxygen in multi-copper oxidases. Since this stepwise process is not yet fully understood, the investigation of the basicity and reduction potentials of metal-bound oxygen species appear to be particularly interesting and have received significant attention in recent years.

The previously reported symmetric pyrazolate/tacn hydroperoxo complexes **XXIII** and **XXIV** could be isolated upon protonation of the respective peroxo complex. The reversible protonation/deprotonation of the peroxo/hydroperoxo core allowed to derive the pK_a value and therefore the acidity of the metal-bound hydroperoxide species.[113,124]

This section will focus on the isolation and characterization of a hydroperoxodicopper(II) complex based on the non-symmetric ligand scaffold **L1,2** and the determination of its pK_a value to compare the influence of ligand design on the acidity of the respective pyrazolate/tacn hydroperoxodicopper(II) complexes.

5.3.1 Formation in Solution

The protonation of the peroxo complex **2** was investigated according to Scheme 17 by employing a suitable acid, such as lutidinium triflate (pK_a = 14.41 in MeCN[171]), which has also been used for the conversion of the symmetric peroxo complexes **XVII** and **XVIII**.

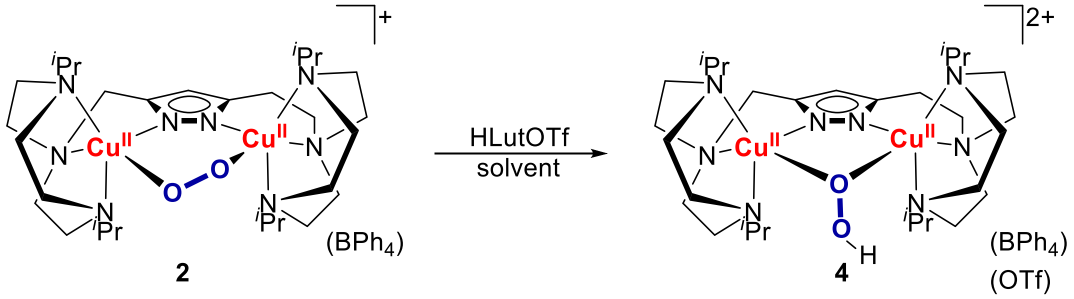

Scheme 17. Synthesis of hydroperoxodicopper(II) complex **4** from protonation of complex **2** with HLutOTf in acetonitrile.

The addition of approximately 1.0 equivalent of lutidinium triflate at −40 °C in acetonitrile led to a decrease of the characteristic electronic absorption bands of the peroxodicopper(II) complex and a new species with absorption features at 374 nm(ε = 4600 M^{-1} cm^{-1}), 424 nm (ε = 6500 M^{-1} cm^{-1}) and

614 nm (ε = 700 M^{-1} cm^{-1}) was observed in the UV/Vis spectra. Those features are reminiscent of the absorption features of the prior reported hydroperoxodicopper(II) complexes **XXII** and **XXIII**. For those and also further reported hydroperoxodicopper(II) complexes, a distinct LMCT absorption band between ~350-440 nm was observed, which was attributed to charge transfer transitions of the newly formed hydroperoxide ligand.[15] All hydroperoxo complexes based on pyrazolate/tacn ligand scaffolds exhibited weak and broadened absorption features around 600 nm, originating from d-d transitions of the Cu^{II} ions. Furthermore, for complex **XXII** an additional distinct maximum around 374 nm was observed, while **XXIII** exhibited only a strongly attenuated shoulder in this region. Interestingly, the same feature is also observed for **4**, being less pronounced as for complex **XXII** but more as for **XXIII**. Therefore complex **4** demonstrates the gradual impact of ligand design on spectroscopic properties of the resulting dicupric hydroperoxide species.

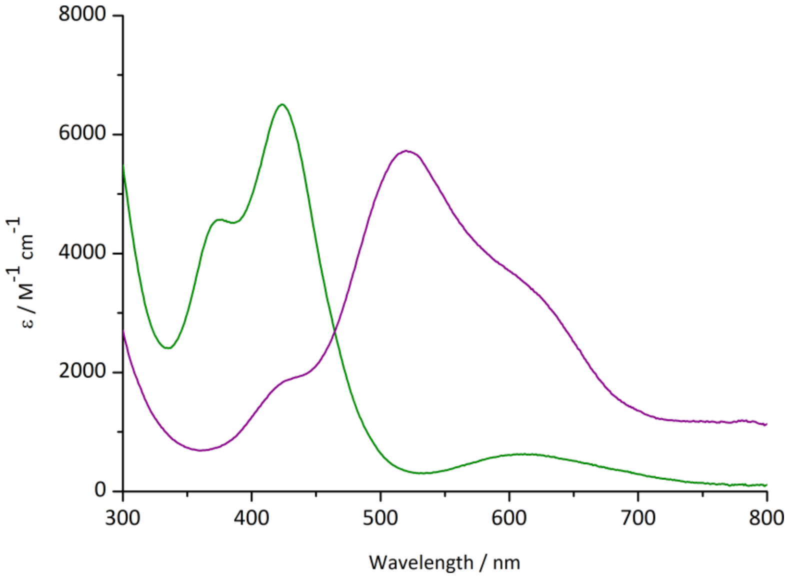

Figure 47. UV/Vis spectrum of complex **2** (purple line) and formation of complex **4** (green line) after addition of HLutOTf in MeCN at –40 °C.

The newly synthesized hydroperoxo complex **4** was further investigated by means of resonance RAMAN spectroscopy. Therefore, freshly prepared solutions of crystalline material of isotope labelled peroxo complex **2** were converted with 1.0 equivalent of HLutOTf in acetonitrile. The resulting spectra of $^{16}O_2$ and $^{18}O_2$ labeled compound **4** are depicted in Figure 48.

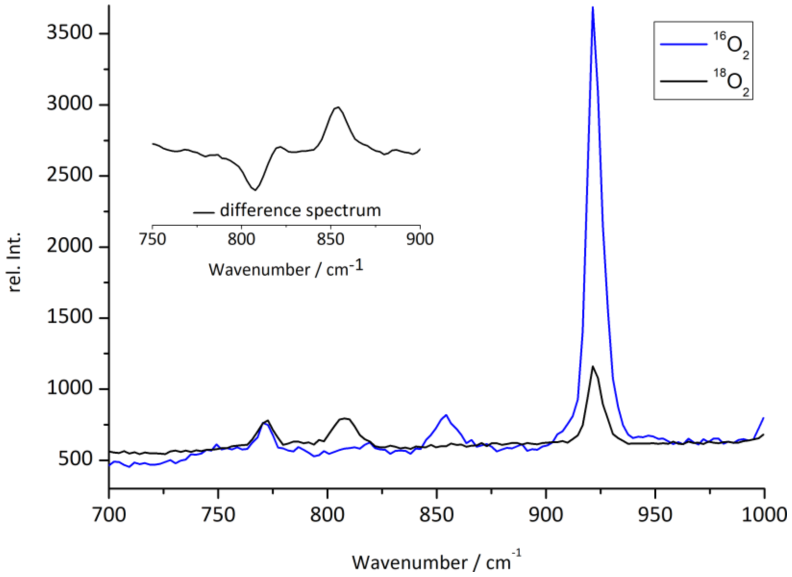

Figure 48. Resonance RAMAN spectrum of **4** in acetonitrile at room temperature (λ_{ex}=457 nm).

Hereby, a significant shifting of the O–O vibration band is observed in comparison to the peroxdicopper(II) complex. While peroxo complex **2** exhibited a O–O vibration around ~800 cm^{-1}, an isotope-sensitive band for hydroperoxo complex **4** at 853 cm^{-1} ($\Delta^{16}O_2$–$^{18}O_2$ = 46 cm^{-1}) was observed, which is similar to the O–O stretching frequency of free H_2O_2 (877 cm^{-1}).[172] The same phenomenon has been reported for complex **XXIII** and was mainly attributed to significant mechanical coupling between O–O and Cu–O vibrations.[124,173–175] No further isotope sensitive features, such as Cu–O vibrations, could be observed due to poor resolution of the spectra.

The clean isolation of complex **4** also allowed to conduct NMR experiments (Figure 49), which were also highly anticipated based on NMR measurments of the reported hydroperoxo complex **XXIII**. However, while complex **4** indeed reveals almost diamagnetic behavior (more in Section 5.3.4), no clean assignment of the proton signals was feasible, besides distinction of the methyl groups of the *iso*-propyl tacn units and various CH_2 fragments. Interestingly, complex **4** showed significant broadening at low temperatures and more resolved proton signals at elevated temperatures. However, at temperatures of around 323 K fast decomposition of **4** was observed, making the applicability of 2D-NMR experiments difficult.

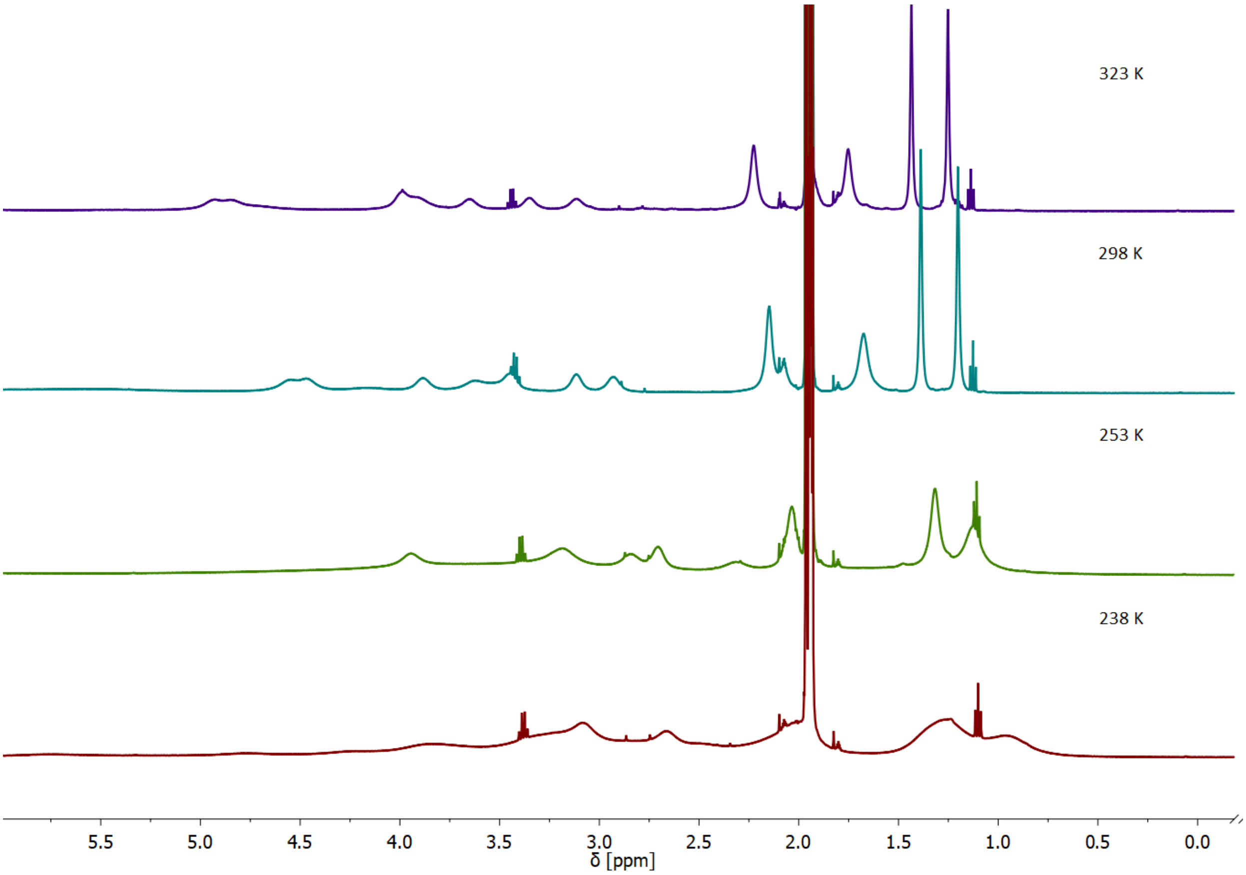

Figure 49. ^{1}H-NMR Spectra at various temperature between 238 K and 323 K of complex **4** in CD_3CN.

5.3.2 pK_a Determination

To investigate the protonation mechanism in more detail, UV/Vis titration experiments were conducted. Therefore, the *in situ* generated peroxo complex **2** was reacted stepwise with 0.05 equivalents of lutidinium triflate at −20 °C in acetonitrile, revealing the sequential change in absorption shown in Figure 50.

No significant change in absorption is observed after addition of 1.0 equivalent of HLutOTf to complex **2**, yielding the corresponding hydroperoxodicopper(II) complex **4**. The one-to-one conversion of complex **2** to **3**, without any significant formation of byproducts is also reflected by an isosbestic point at 465 nm.

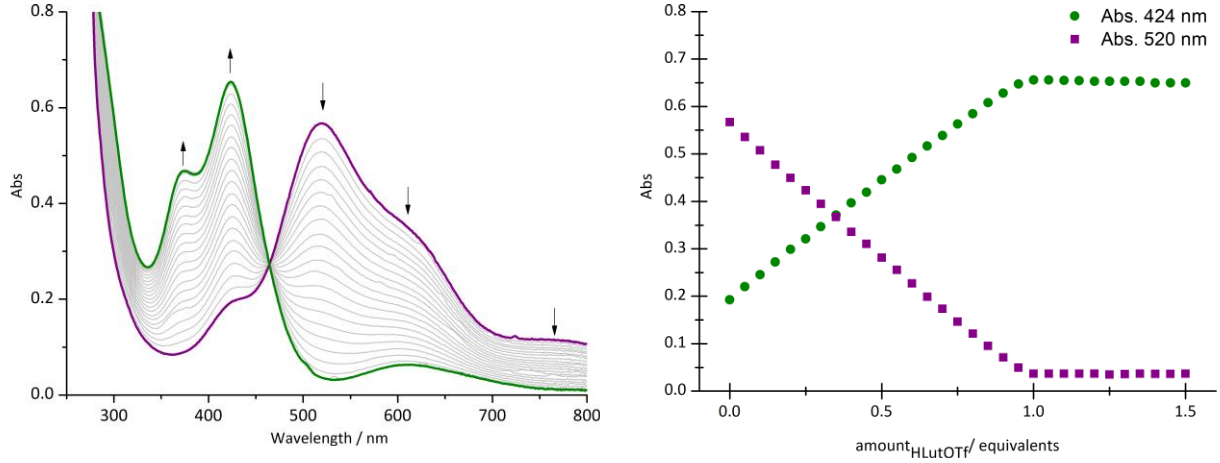

Figure 50. UV/Vis spectra of the stepwise titration of complex **2** with HLutOTf (0.1 eq. steps) in MeCN at −20°C (left) and a plot of the absorption at 424nm and 520 nm versus equivalents of acid added (0.05 eq. steps, indicating the full conversion after approx. 1.0 eq).

Since the newly isolated non-symmetric hydroperoxo complex **4** exhibited similar spectroscopic features as the prior reported complexes **XXIII** and **XXIV**, the investigation of its acidity (pK_a) stands to reason.

XXIV can be regarded as one of the first hydroperoxodicopper(II) complexes which could be reversible protonated and deprotonated, due to his extraordinary stability. Therefore, UV/Vis back titration experiments with 1,1,3,3-tetramethylguanidine (TMG) yielded a pK_a value of 22.2 ± 0.3 (MeCN, −20 °C).[124] In contrast, the pK_a value determination of complex **XXIII** required a different approach since employment of bases like DBU, TMG and even the sterically demanding (phenylimino)tripyrrolidinophosphorane (PHNP$_{pyr}$) always led to significant interactions of the corresponding protonated bases with the peroxo core likely via H-bonding. This observation was based on the increased accessibility of the peroxide in complex **XVII**. Hence, a more sterically demanding base was required, whose corresponding protonated form would not interact with the Cu_2O_2 moiety. This problem was solved, by providing freshly prepared crystalline material of peroxodicopper(II) complex **XVIII** as a suitable sterically demanding base, whereby it was possible to derive a pK_a value of 21.8 (MeCN, −40 °C) for complex **XXIII.**[113]

To reveal the acidity of the newly formed hydroperoxo complex **4** initial experiments with 1,8-diazabicyclounde-7-ene (DBU) and TMG (Scheme 18) were conducted.

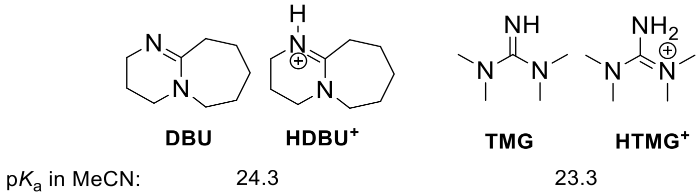

Scheme 18. Employed bases 1,8-diazabicyclounde-7-ene (DBU) and 1,1,3,3-tetramethylguanidine(TMG) and their corresponding acids as well as their pK_a values.[171,176]

In a typical UV/Vis titration experiment, the *in situ* generated peroxo complex **2** was protonated with one equivalent of lutidinium triflate and afterwards backtitrated with the respective base at −20 °C in acetonitrile. The stepwise addition of DBU (pK_a = 24.3 in MeCN[171]) to complex 4 is depicted in Figure 51 and led to gradual depletion of the absorption features of complex **4** and simultaneous rise of the respective features of peroxo complex **2**. The clean conversion was again confirmed by the presence of an isosbestic point at 465 nm, which shifted slightly during the backtitration with DBU. This might be due to partial decomposition, which is in line with the observation that the absorption features of complex **2** could only be recovered up to around 90%.

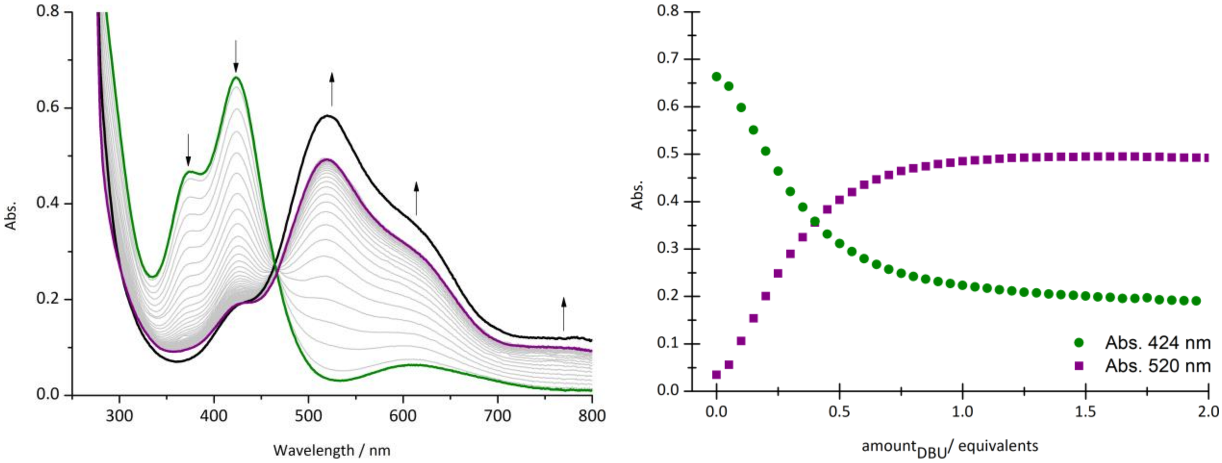

Figure 51. UV/Vis titration experiment of hydroperoxocomplex **4** with DBU in steps of 0.05 eq. in acetonitrile at −20 °C. The bold black line in the absorption spectrum represents the initial amount of complex **2** prior to protonation with HLutOTf.

In this case, titration experiments with DBU revealed no substantial interaction of the peroxo core of complex **2** with the corresponding protonated base HDBU$^+$ as reported for **XVII**. However, a plot of equivalents of DBU versus the distinctive hydroperoxo/peroxo absorption features at 424 nm and 520 nm revealed full conversion after addition of 1.0 equivalent of base to complex **4**, indicating a larger basicity of DBU compared to the peroxo complex **2**. However, the flattening of the absorption curve already reveals that the pK_a value of DBU is in close proximity to that of hydroperoxo complex **4**.

Therefore the weaker base 1,1,3,3-tetramethylguanidine(TMG) was used (Figure 52), which features a pK_a value of 23.3 in acetonitrile[176] and which was already employed for determining the pK_a value of **XXIII**. As expected, the absorption spectra of the back titration with TMG revealed the same spectroscopical changes as with the base DBU. Viz a decrease of the characteristic hydroperoxo bands and an increase of the corresponding peroxo bands with an isosbestic point at 467 nm. Further, a plot of equivalents of TMG vs. the characteristic absorption features of **2** and **4** reveals that complete conversion is achieved after approximately three equivalents. Thus, reflecting a proper equilibrium situation from which the equilibrium constant K_a can be derived.

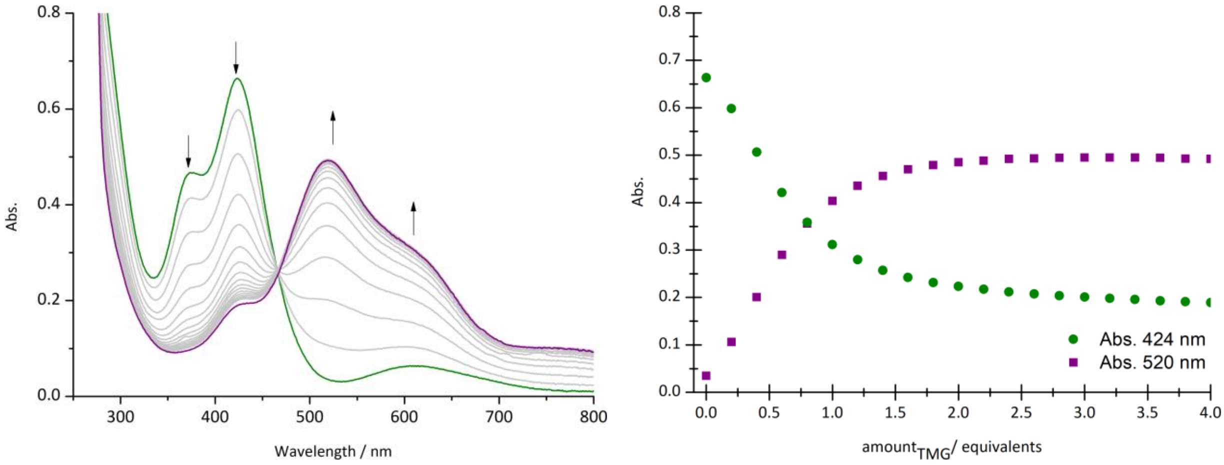

Figure 52. UV/Vis titration experiment of hydroperoxocomplex **4** with TMG in steps of 0.2 eq in acetonitrile at −20 °C. The bold black line in the absorption spectrum represents the initial amount of complex **2** prior to protonation with HLutOTf.

In approximation, the equilibrium of the deprotonation/protonation reaction can be outlined by the following Scheme 19. Hereby, rearrangement of the peroxide ligand was not considered, and the reaction simplified according to an equilibrium between two bases.

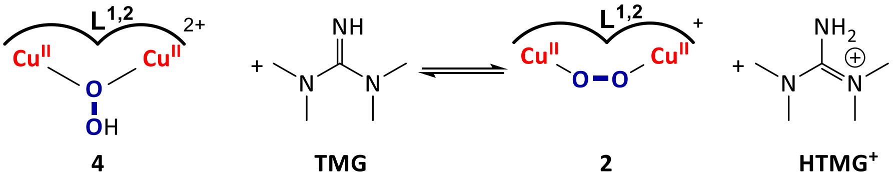

Scheme 19. Schematic representation of the assumed equilibrium between the acid/base pairs to derive the equilibrium constant *K*. The full ligand framework of the copper complexes is omitted for clarity.

The equilibrium constant *K* can therefore be described as the fraction between product and educt activities, respectively concentrations (equation **6**).

$$K = \frac{[\mathbf{HTMG^+}][\mathbf{2}]}{[\mathbf{TMG}][\mathbf{4}]} \tag{6}$$

From Scheme 19 the relative basicity of the proton can be described by the following expression

$$\Delta \mathrm{p}K_\mathrm{a} = \mathrm{p}K_\mathrm{a}(\mathbf{HTMG^+}) - \mathrm{p}K_\mathrm{a}(\mathbf{4}) = \log\frac{[\mathbf{HTMG^+}][\mathbf{2}]}{[\mathbf{TMG}][\mathbf{4}]} \tag{7}$$

Therefore, the pK_a of hydroperoxo complex **4** can be derived by

$$\mathrm{p}K_\mathrm{a}(\mathbf{4}) = \mathrm{p}K_\mathrm{a}(\mathbf{HTMG^+}) - \log\frac{[\mathbf{HTMG^+}][\mathbf{2}]}{[\mathbf{TMG}][\mathbf{4}]} \qquad \mathbf{8}$$

It was also assumed that peroxo complex **2** and the protonated base $HTMG^+$ form in equimolar amounts, resulting in this simplified expression for the pK_a of **4**

$$\mathrm{p}K_\mathrm{a}(\mathbf{4}) = \mathrm{p}K_\mathrm{a}(\mathbf{HTMG^+}) - \log\frac{[\mathbf{2}]^2}{[\mathbf{TMG}][\mathbf{4}]} \qquad \mathbf{9}$$

Thus, the equilibrium constant K can be derived from a plot of [**2**]^2 / [**4**] versus TMG, which is depicted in Figure 53. Hence, from the slope of the linear regression a value of 16.72 ± 0.91 for the equilibrium constant K at −20 °C in acetonitrile was obtained.

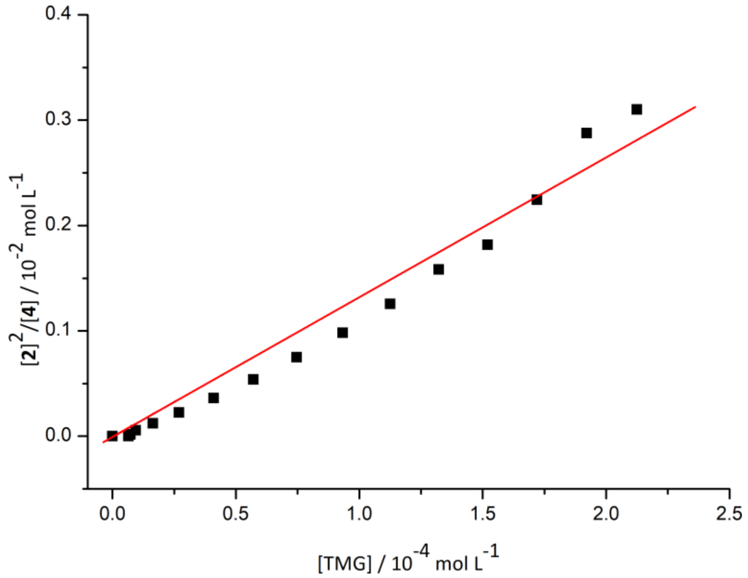

Figure 53. [**2**]^2/ [**4**] versus TMG with a fixed intersection with the y-axis at zero ($R^2 = 0.993$). Data were derived from the absorbances, which are proportional to the respective concentration of species **2** and **4** during the backtitration with TMG.

Therefrom a pK_a of 22.1 ± 0.2 could be obtained for the dicupric hydroperoxide **4**. The determined pK_a value was also confirmed by conducting experiments with the base (phenylimino)tripyrrolidinophosphorane (PhNPpyr$_3$), which features a pK_a value of 22.3 in acetonitrile.[177] Addition of this base to the hydroperoxo complex **4** led to a maximal conversion of 50% to the peroxo complex **2**, even after addition of up to 20 equivalents of base, verifying the determined pK_a value.

In the context of Section 5.5, in which a temperature driven equilibrium between a newly formed peroxo adduct and its corresponding hydroperoxo species will be presented, K was also determined at different temperatures (Figure 54). Those investigations were based on the VAN-'T-HOFF equation, which describes the temperature dependence of equilibrium constants and therefore also of the pK_a.

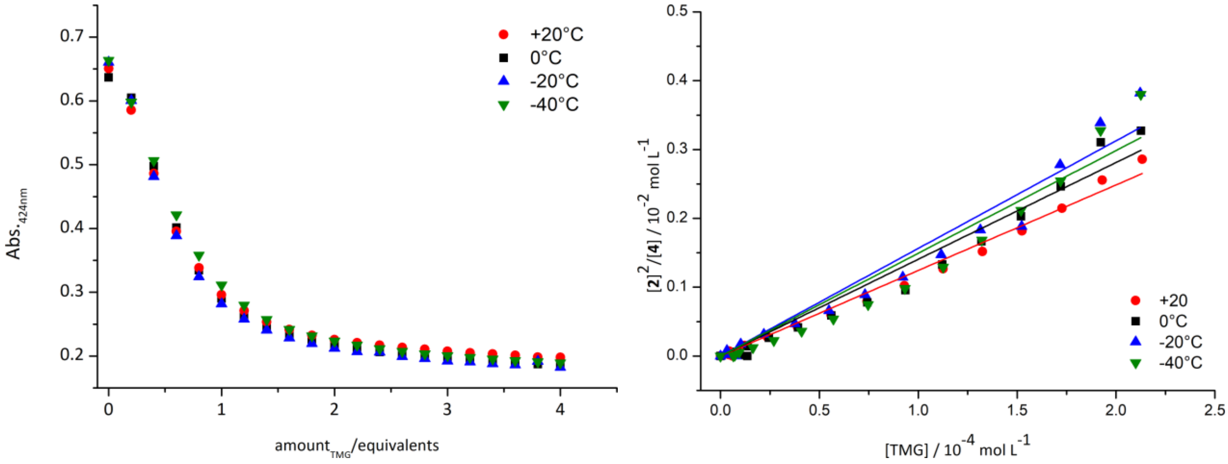

Figure 54. UV/vis titration of complex **4** with TMG at various temperatures (+20°C, 0°C, −20 °C, −40 °C). A plot of the absorption at 424 nm versus equivalents of TMG is depicted on the left and a plot of $[\mathbf{2}]^2/[\mathbf{4}]$ versus TMG to determine K_a at different temperatures on the right.

Thus, further titration experiments with TMG as described *vide* supra were conducted at +20 °C, 0 °C and −40 °C, revealing similar curve shapes of the plot of absorption at 424 nm vs. equivalents of base. Therefore, no significant change for the equilibrium constant *K* and therefore also the pK_a of **4** could be observed within a temperature range of 60 °C (Table 5), highlighting the fact that entropic contribution is negligible.

Table 5. Determined equilibrium constants *K* and pK_a values of the hydroperoxo complex **4** at various temperatures in acetonitrile. A temperature-dependency of the pK_a value of HTMG$^+$ was not considered when pK_a(**4**) was determined.

	K	pK_a(**4**)
20°C	12.92 ± 0.33	22.1 ± 0.2
0°C	15.38 ± 0.63	22.1 ± 0.2
−20 °C	16.72 ± 0.91	22.1 ± 0.2
−40 °C	16.60 ± 0.87	22.1 ± 0.2

The determined pK_a value of 22.1 was close to the values of the symmetrical pyrazolate/tacn hydroperoxo complexes **XXIII** and **XXIV**, which are given in Figure 55. The near identical ligand scaffold provides no significant influence on the basicity of the peroxo core and hence similar pKa values of the dicupric hydroperoxide. In contrast, hydroperoxide complex **XXV** reported by KARLIN and coworkers exhibits a pKa value of 24 and therefore increased basicity of the respective peroxo complex.[119]

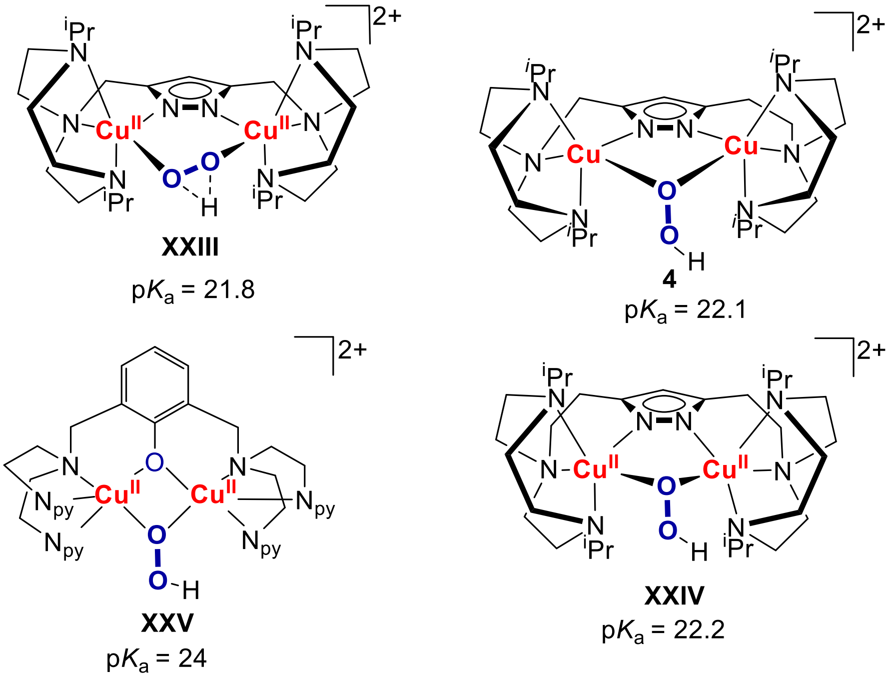

Figure 55. Hydroperoxo complexes **XXIII**, **4** and **XXV and XXIV** and their corresponding p*K*a values determined in MeCN, respectively MeTHF for **XXV**. Counter ions are omitted for simplification.[113,119,124]

The increased basicity, which also had major impact on the HAT reactivity (which will be discussed in Section 5.4.3), was attributed to potential differences in the peroxo core binding motivs (μ-1,2 vs. μ-1,1), emphasizing the role of ligand design for the properties of copper/oxygen intermediates.[119]

5.3.3 Solid State Properties

The isolated hydroperoxo complex **4** showed almost unlimited stability between −20 and −40 °C in solution and a half-life of about 12 h at room temperature in acetonitrile, thus exhibiting almost identical stability as the previously reported complex **XXIV** ($t_{1/2} \approx 9$ h). It should also be noted that crystallographic structure determination and therefore elucidation of the binding motif of the prior reported hydroperoxo complex **XXIII**, which utilizes the ligand scaffold **L**[1], was not possible due to lower stability and preferred formation of the respective hydroxo complex.

Crystalline material of complex **4** was obtained upon exposure of the dicopper(I) precursor **1** to molecular dioxygen and subsequent addition of HLutOTf at −40 °C in MeCN or EtCN. The layering technique with diethyl ether was employed and the solutions kept at −26°C. Crystallization of the hydroperoxo complex **4** proceeded rather fast and was usually complete within 48 h to 72 h without any significant formation of the decomposition product **3**. Hence, X-ray diffraction of those crystals led to the molecular structure of complex **4** in solid state, which is depicted in Figure 56.

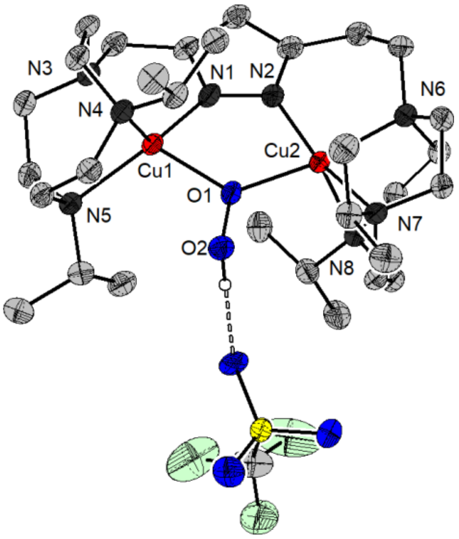

Figure 56. Molecular structure of the cationic part of complex **4** without the second counter ion tetraphenylborate. Thermal displacement ellipsoids given at 50% probability. Hydrogen atoms, solvent molecules and counter ions are omitted for clarity. Selected bond lengths [Å] and angles [°] (sorted) for **4**: Cu1−N1 1.902(2), Cu2−N2 1.959(2), Cu1−O1 1.9849(17), Cu2−O1 2.0452(17), Cu1−N3 2.091(2), Cu1−N4 2.226(2), Cu1−N5 2.131(2), Cu2−N6 2.110(2), Cu2−N7 2.097(2), Cu2−N8 2.303(2).

The coordination environment of both copper ions can be best described as distorted square-pyramidal. While the Cu1 ion, which is coordinated by the methylene spaced side arm exhibits a rather strong distortion ($\tau_5 = 0.255$), the Cu2 ion, which is coordinated by the ethylene spaced side arm shows comparatively small distortion ($\tau_5 = 0.09$) towards a trigonal bipyramidal coordination geometry. Both copper ions are coordinated by the three nitrogen atoms of the tacn unit and one nitrogen atom of the pyrazolate as well as one oxygen atom of the hydroperoxide bridging moiety. Like in the prior reported copper oxygen complexes of the ligand scaffold **L**[1,2] the Cu−N bond lengths differ and are significantly shorter for the Cu−pyrazolate bonds (Cu1−N1 = 1.90 Å, Cu2−N2 = 1.96 Å) compared to those of the copper–tacn bonds (Cu1–N3,4,5 = 2.09-2.23 Å, Cu2–N6,7,8 = 2.10-2.30 Å), whereby the longest bond (Cu1–N4, Cu2–N8) is the axial one of the square-pyramidal geometry.

In comparison to the peroxodicopper(II) complex reported in Section 5.2, complex **4** exhibits shortening of the copper-copper distance from 3.70 Å to 3.55 Å, which originates from the different binding modes of the respective bridging units (μ-1,2-peroxide vs. μ-1,1-hydroperoxide). The Cu–O bonds differ slightly, according to the methylene or ethylene spaced ligand side arm (Cu1–O1 = 1.99 Å, Cu2–O1 = 2.05 Å). Further, no significant change of the O–O bond length was observed upon protonation of complex **2** to the hydroperoxo complex **4** (1.46 Å). Additionally, the highly crystalline material allowed for the observation of hydrogen bonding interactions between the hydroperoxide proton and the triflate anion in the solid state, which was also observed for the prior reported hydroperoxo complex **XXIV**. The potential influence of hydrogen bonds on copper/oxygen adduct properties was already stated in Section 3 and will be further elaborated in section 5.5.2.

Crystalline material of $^{16}O_2$ and $^{18}O_2$ labeled complex **4** was investigated by means of RAMAN spectroscopy (Figure 57), revealing a distinct peak at 845 cm^{-1} for the $^{16}O_2$ derivative. However, due to poor signal to noise ratio for the $^{18}O_2$ labeled complex, unambiguous assignment of the corresponding signal is difficult. However, a peak at 795 cm^{-1} ($\Delta ^{16}O_2 - ^{18}O_2$ = 50 cm^{-1}) was found, being in line with expected values from the harmonic oscillator approximation.

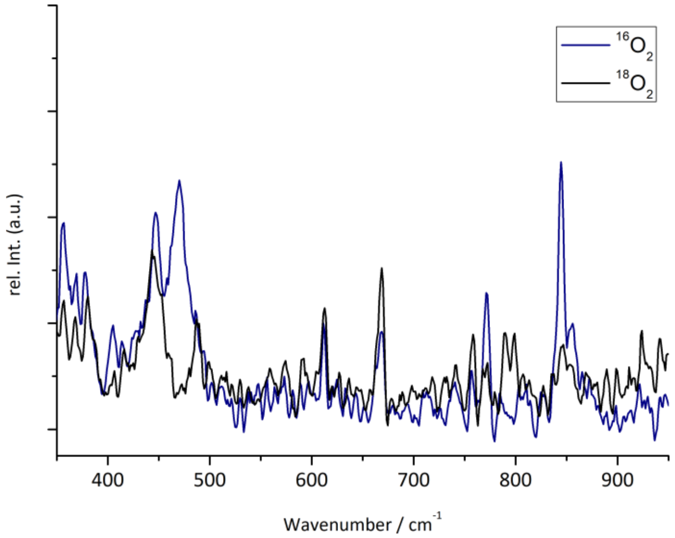

Figure 57. Solid state resonance RAMAN spectrum of $^{16}O_2$ and $^{18}O_2$ labeled complex **4** (λ_{ex} = 633 nm).

Besides this, a strong peak at 470 cm^{-1} was observed for **4**[$^{16}O_2$], which might originate from Cu–O vibrations, but no significant redshifting with $^{18}O_2$ labeled complex **4** was observed.

5.3.4 Magnetic Properties

The magnetic properties of complex **4** were investigated by magnetic susceptibility measurements between 2 K and 295 K using powdered crystalline material. The experimental data are depicted in Figure 58 by a plot of $\chi_\mathrm{m}T$ versus T and a fitting simulation on the basis of the spin Hamiltonian for isotropic exchange coupling and ZEEMAN splitting.

$$\hat{\mathrm{H}} = -2J\hat{S}_1\hat{S}_2 + g\mu_B\vec{B}\,(\vec{S}_1 + \vec{S}_2) \qquad \mathbf{10}$$

Hereby, extremely strong antiferromagnetic coupling between both copper ions was observed, revealing a coupling constant of J = −527 cm^{-1} and therefore a strongly stabilized singlet ground state (S = 0). The observed extent of antiferromagnetic coupling was in the same order of magnitude as for the previously reported hydroperoxo complex **XVIII** (J = −538 cm^{-1}), originating from mediated superexchange coupling of the μ-1,1-hydroperoxide.

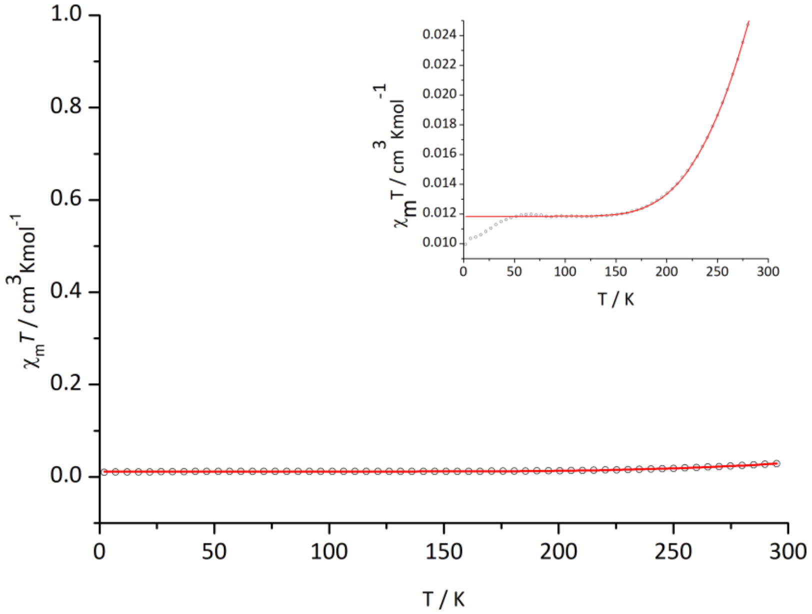

Figure 58. Magnetic Susceptibility data of the non-symmetric hydroperoxo dicopper (II) complex **4** in the temperature range between 2 K and 295 K and a field of 0. 5 T together with a fit of the data set. Parameters: J = −527, g = 2.021, PI = 3.1%, TIP = 22.8·10^{6} emu.

5.3.5 Summary and Conclusion

In this chapter, the protonation of peroxo complex **2** with lutidinium triflate to the μ-1,1-hydroperoxo complex **4** was demonstrated. Hereby, the newly isolated hydroperoxo complex **4** exhibited almost unlimited stability below −20 °C and rather slow decomposition within several hours at room temperature. Therefore, UV/Vis backtitration experiments with TMG, DBU and $PhNPpyr_3$ were conducted from which a pK_a value of 22.1 ± 0.2 in acetonitrile was derived. Additional titration experiments at various temperatures were performed, which showed no significant change of the acidity of the Cu_2OOH core, respectively pK_a value, between +20°C and −40 °C.

The increased stability of complex **4** also allowed for further characterization, such as RAMAN spectroscopy and magnetic measurements, which revealed strong antiferromagnetic coupling ($J = -527$ cm^{-1}) and an isotope-sensitive O−O vibration band at 845 cm^{-1}. Therefore, **4** shows strong resemblance to the prior reported hydroperoxo complex **XXIV**.

Additionally, complex **4** could also be investigated by X-ray diffraction, confirming the μ-1,1-hydroperoxide binding motif and therefore extending the list of rare structurally characterized hydroperoxodicopper(II) complexes. From the solid-state structure of **4** hydrogen bond interactions of the hydroperoxide proton with the triflate counter ion could be observed, marking the potential relevance of hydrogen bonds within copper/oxygen model complexes which will be discussed further in Section 5.5.2.

5.4 A Non-Symmetric Superoxodicopper(II) Complex

In recent years, copper-superoxo complexes have gained more and more attention, due to their ability to perform hydrogen atom abstraction (HAA) reactions and their potential involvement in copper-oxygen mediated catalysis of parent metalloenzymes, as well as their potential relevance in copper-mediated water oxidation and oxygen reduction catalysis.[102,117–119,178] However, copper-superoxo intermediates are usually unstable and hard to isolate. The focus of this section will be on the isolation and characterization of a non-symmetric superoxodicopper(II) complex. Further, to determine the bond dissociation free energy of the $Cu_2OO{-}H$ core, which was presented in the previous section, the electrochemical properties of complex **2** will be investigated and correlated with the pK_a value of complex **4** by a thermodynamic square scheme. A conclusive comparison of HAT kinetics and thermodynamic parameters of the series of pyrazolate/tacn superoxo complexes and the role of ligand identity on those will be drawn.

5.4.1 Formation in Solution

The formation of dinuclear superoxo complexes usually proceeds via oxidation of the respective peroxo complex or addition of molecular dioxygen to a mixed valent $Cu^{I}Cu^{II}$ species.[117,118,120] According to the previously reported peroxodicopper complexes **XVII** and **XVIII**, which were electrochemically and chemically oxidized to form the corresponding μ-1,2-superoxo complexes,[113,117] the peroxo adduct **2** was investigated in the same manner (Scheme 20).

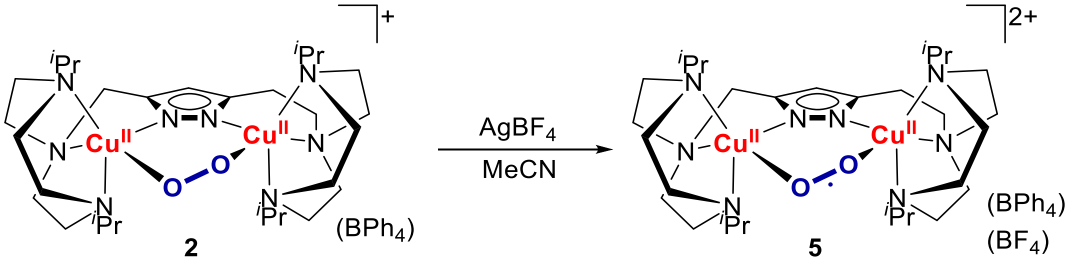

Scheme 20. Synthetic route for complex **5** via one electron oxidation of corresponding peroxo complex **2** with $AgBF_4$.

Cyclic voltammetry (CV) measurements of complex **2** at decreased temperatures were conducted to investigate the formation of the putative non-symmetric superoxo complex **5** (Figure 59).

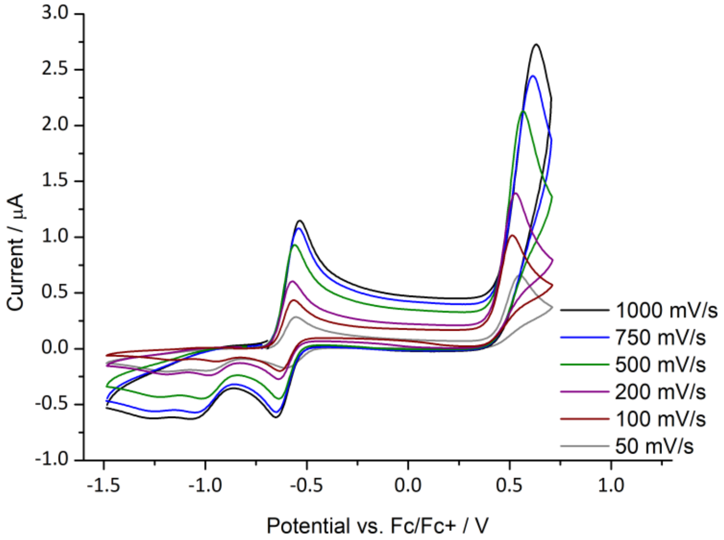

Figure 59. Cyclic voltammograms of complex **2** in MeCN (NBu_4PF_6 0.1 M) at 0 °C at different scan rates.

Complex **2** was measured at 0 °C in NBu_4PF_6 (0.1 M) /MeCN solution (GC WE) and revealed a reversible 1 e^- redox process at −0.58 V vs. Fc/Fc$^+$ (Figure 60) as well as an irreversible oxidation at higher potential (E_{pa} =+0.6 V) and two further irreversible reductions at E_{pc} = −1.1 V and −1.3 V that might originate from the reduction of the Cu^{II} ions. The irreversible oxidation event at +0.6 V was also observed for the prior reported pyrazolate/tacn peroxodicopper(II) complexes and can be attributed to the oxidation of the superoxide and therefore release of molecular dioxygen.

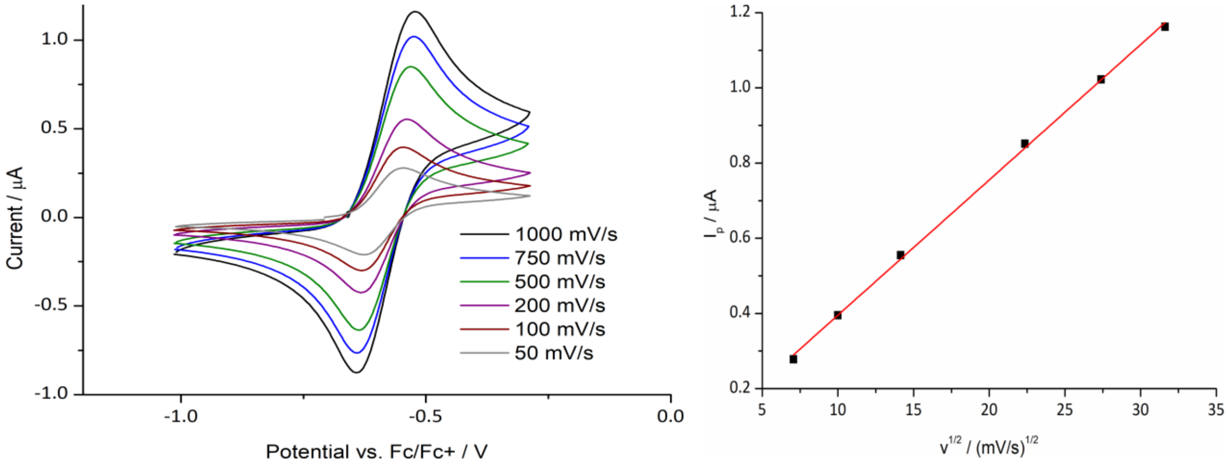

Figure 60. Cyclic voltammograms of complex **2** in MeCN (NBu_4PF_6 0.1 M) at 0 °C at different scan rates between −1.0 V and −0.25 V (left) and a plot of the anodic peak current I_p versus the square root of the scan rate (right).

Complex **2** could also be oxidized by using an adequate oxidizing agent,[167] such as $AgBF_4$ (E^0 = 0.04 V vs. Fc/Fc$^+$in MeCN) or $FcBF_4$, and these reactions were monitored by means of UV/Vis titration experiments (Figure 61).

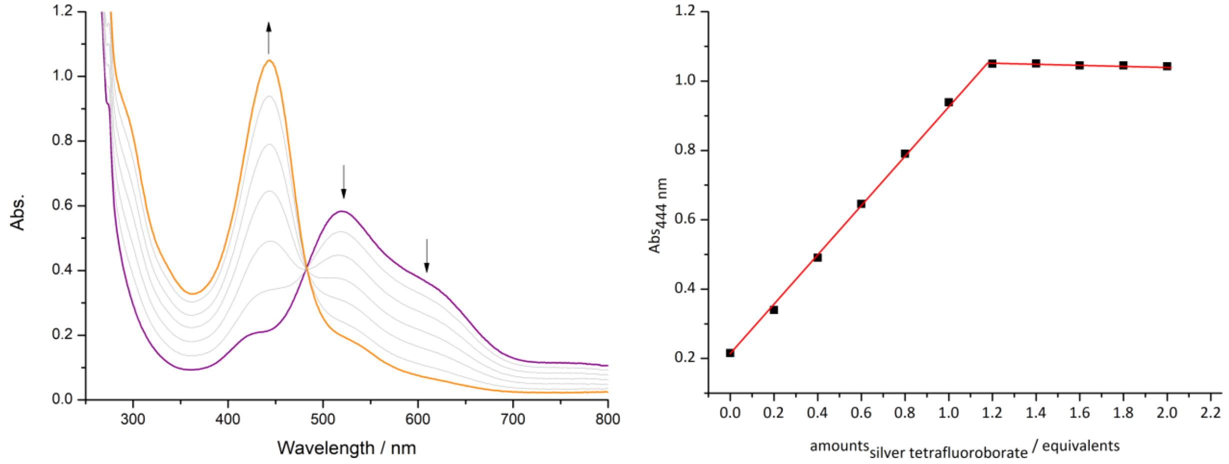

Figure 61. UV/Vis Titration of peroxo complex **2** with $AgBF_4$ at –40 °C in MeCN, indicating the clean conversion to complex **2** to the corresponding superoxo complex **5**. The inset shows the change of absorption at 444 nm vs. equivalents of $AgBF_4$.

Thereby, a significant change of the absorption features of the peroxo complex **2** is observed, whereby its characteristic bands diminish and a distinct maximum at 444 nm (ε = 10300 M^{-1} cm^{-1}) begins to rise with a shoulder around 535 nm (ε = 1700 M^{-1} cm^{-1}), which is strongly reminiscent of the μ-1,2-superoxide dicopper(II) complexes of the symmetrical pyrazolate/tacn ligands and also to the superoxo complexes based on UNO and XYLO[1] ligand frameworks reported by KARLIN and coworkers.[113,117,119] Clean conversion is indicated by an isosbestic point around 480 nm and full oxidation is achieved after addition of ~1.1 equivalents of the oxidizing agent.

Further, the newly formed complex **5** was also investigated with respect to its thermal decomposition, which becomes relevant for further kinetic investigations. (Section 5.4.3). The decay of freshly prepared solutions of complex **5** was monitored by UV/Vis spectroscopy, revealing a decomposition rate of k_{obs} (+20°C) = $43\cdot10^{-5}$ s^{-1} and therefore a half lifetime of 25 min in acetonitrile by assuming a first order decay.

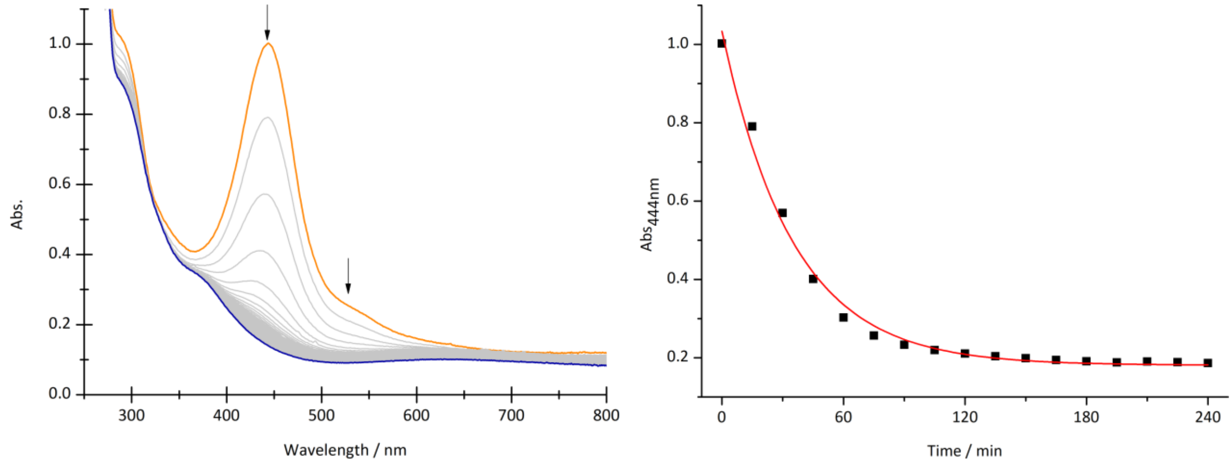

Figure 62. UV/Vis monitoring of the decay of superoxo complex **5** at RT in MeCN (left) and a plot of the absorption at 444 nm versus time, exhibiting a half life time of $t_{1/2}$= 25 min. The red line is a fit assuming first-order decay kinetics.

---

[1] Binucleating *m*-xylyl (XYLO) and *m*-toluidine (UNO) derivative, containing a bridging phenolate ligand and two bis(2-{2-pyridyl}-ethyl)amine arms[119]

As presumed, the decomposition product exhibits spectroscopic features similar to those of the hydroxo complex **3** around 370 nm and 630 nm. Similar obvservations have also been made for the prior reported superoxo complexes **$[L^1Cu_2O_2]^{2+}$** (**XIX**) and **$[L^2Cu_2O_2]^{2+}$** (**XX**), but were only partially quantified. Therefore decompositon reactions of freshly prepared complex **XIX** and **XX** were also investigated (Table 6). In comparison, the methylene bridged superoxo complex **XIX** revealed the highest stability in solution, whereas **XX** exhibited rather fast decomposition at +20°C. The newly isolated dicupric superoxide **5** exhibits a decomposition rate between those of the prior mentioned complexes.

Table 6. Decay rates and half-life time of various pyrazolate/tacn superoxo dicopper complexes at +20°C in MeCN.

	XIX	**5**	**XX**
k_{obs} (+20°C) [s^{-1}]	$6.5 \cdot 10^{-5}$	$43 \cdot 10^{-5}$	$238 \cdot 10^{-5}$
$t_{1/2}$(+20°C) [min]	101	25	5

This observation might be contraintuitive at first glance, since in complex **XX** the superoxo core is less shielded, hence a higher exposure towards substrates and hence also higher reactions rates in hydrogen atom abstraction than for complex **XIX** was anticipated, since the latter is strongly shielded by the *iso*-propyl groups of the tacn units.

It was therefore assumed that the extraordinary stability of complex **XX** can be attributed to its thermodynamic decomposition product, which contains a entropically unfavored H_3O_2 bridge in comparison to a μ-hydroxide ligand for **XIX** and **5** (Section 5.2.6). The absence of residual water in solution, which is required for the formation of the H_3O_2 bridge might therefore slow down the decomposition reaction of complex **XX**.

To corroborate the presence of a superoxide species, resonance RAMAN spectroscopy measurements were conducted. Therefore, freshly prepared solutions of $^{16}O_2$ and $^{18}O_2$ labelled complex **2** in acetonitrile were oxidized by $AgBF_4$, filtered at low temperatures to remove silver particles, and then frozen in liquid nitrogen. The corresponding spectra revealed an isotope sensitive feature around 1074 cm^{-1} (($\Delta^{16}O_2–^{18}O_2$ = 58 cm^{-1}, $\tilde{\nu}(^{16}O–^{16}O)/\tilde{\nu}(^{18}O–^{18}O)$ = 1.057, calculated 1.060 for an isolated harmonic O–O oscillator) (Figure 63), which is in line with previously reported dicopper superoxo complexes.[113,117] The shifting to higher frequencies of the O–O vibration after oxidation of complex **2** results from removing an electron from the π* orbitals of the peroxide, hence the bond order increases and therefore the resonance frequency of the O–O vibration increases.

The presence of only one O–O vibration band in the RAMAN spectrum also indicated the presence of only one binding mode for the superoxide as in the previously reported pyrazolate/tacn complexes. In contrast, KARLIN and coworkers superoxo complexes **XXI** and **XXII** revealed the formation of two isomers with a *μ*-1,2- and *μ*-1,1-superoxo binding mode.[118,119]

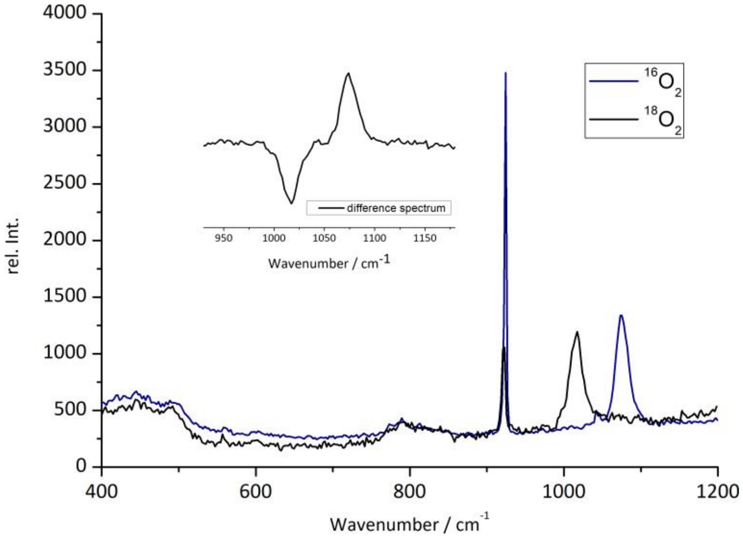

Figure 63. Resonance RAMAN spectrum of superoxo complex **5** in frozen acetonitrile at room temperature (λ_{ex} = 457 nm).

Besides tremendous effort to obtain crystalline material of complex **5** suitable for X-ray diffraction, no crystallization attempt led to the isolation of suitable single-crystals. Crystallization was carried out in different solvents (MeCN, EtCN and Aceton), various complex concentrations and via different crystallization methods (layering and diffusion with pentane, hexane, Et_2O) at temperatures between −20 °C and −80 °C, always leading to polycrystalline material. Also the usage of different oxidizing agents ($AgBF_4$, $AgPF_6$, $[Fc]BF_4$, $[Fc]PF_6$, $[Fc]SbF_6$), with variation of the counter ions, led to no significant improvement of the obtained material.

5.4.2 EPR Spectroscopy

To further confirm the μ-1,2 binding mode of the superoxide in **5**, EPR studies were conducted in collaboration with ECKHARD BILL from the MAX-PLANCK-Institut für Kohleforschung in Mülheim. X-Band EPR measurements of a frozen acetonitrile solution of complex **5** revealed significant Cu^{II} hyperfine coupling and the spectrum was simulated with $g_x = 2.01$, $g_y = 2.10$, $g_x = 2.20$ and $A_1 = 14$ G, $A_2 = 14$ G, $A_3 = 132$ G (Figure 64), whereby hyperfine coupling to only one Cu^{II} ion was assumed.

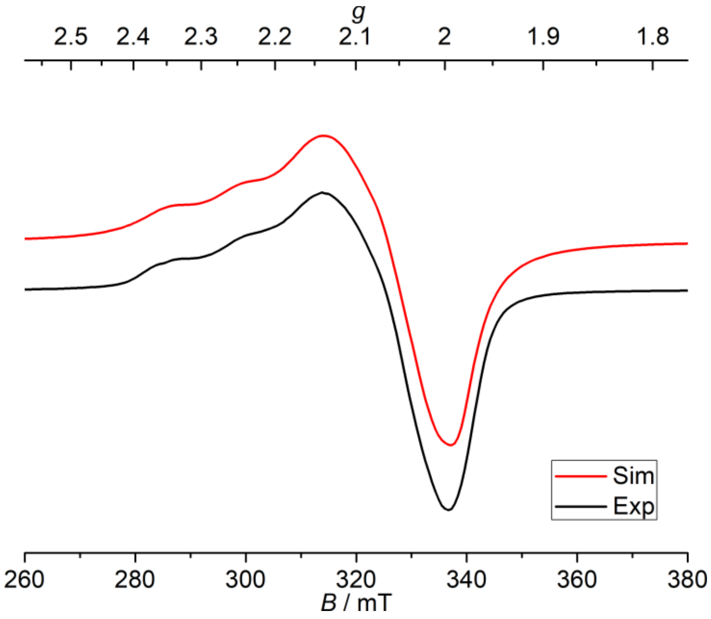

Figure 64. X-band EPR spectrum of complex **5** (black) and its corresponding simulation (red) in frozen acetonitrile solution at 4.9 K.

The depicted EPR spectrum shows strong similarities to the prior reported superoxo complexes **XIX** and **XX**, which was rationalized by the μ-1,2-binding motif.[113,117] Hereby, the coupling scheme of the pyrazolate/tacn based superoxodicopper(II) complexes **XX** and **5** can be basically deduced to strong antiferromagnetic coupling between the superoxide and one Cu^{II} ion, yielding a typical axial copper(II) spectrum for the remaining metal ion (according to Scheme 21).[117]

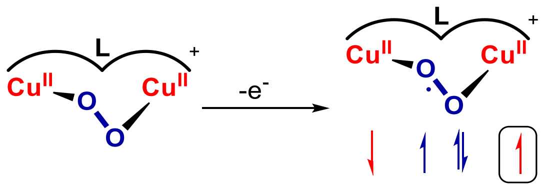

Scheme 21. Simplified coupling scheme of pyrazolate/tacn based superoxodicopper(II) complexes.

Comparison of the EPR spectra of the pyrazolate/tacn based superoxo complexes **XIX**, **XX** and **5** yields a more refined picture of the ligand influence on the electronic structure (Figure 65). In contrast to **XX**, the extent of asymmetric coupling initially starts to decrease for **5**, where sizeable broadening of the Cu^{II} hyperfine coupling spectrum is observed, which might originate from the formation of structural conformers based on the non-symmetric ligand scaffold $\mathbf{L^{1,2}}$. However, for

XX excellent fits could be obtained by assuming full symmetry and hyperfine coupling to both Cu^{II} ions.[121]

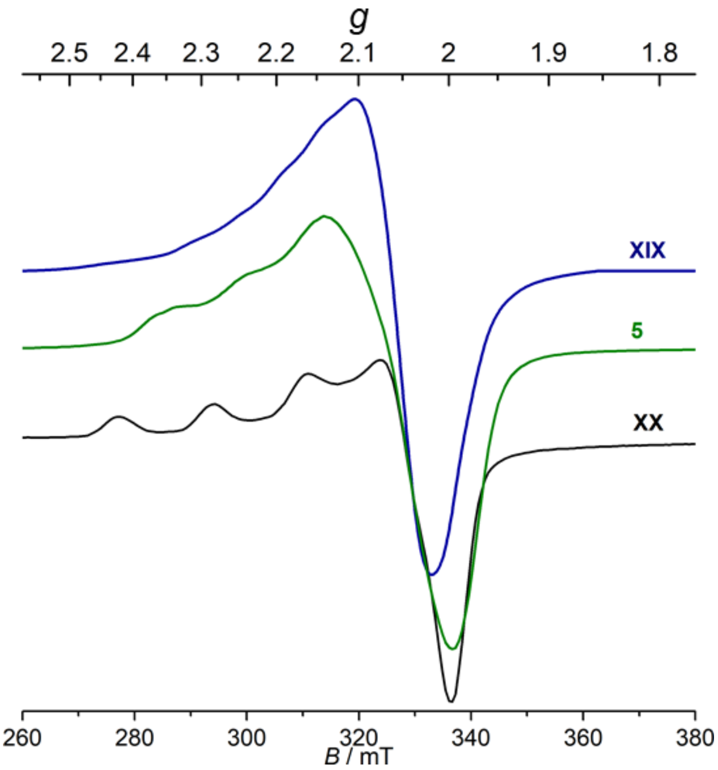

Figure 65. Comparison of X-band EPR spectra of the prior reported pyrazolate/tacn superoxo complexes **XIX**, **XX** and of complex **5** of this work.[117,121]

5.4.3 Hydrogen Atom Transfer Reactivity

As already shown in Section 2, proton-coupled electron transfer (PCET) reactions play a significant role in copper metalloenzymes. In this context superoxo complexes are of key importance, due to their potential role for C–H bond activation. Since the number of characterized dinuclear superoxo complexes is relatively low, the influence of ligand design on thermodynamic and kinetic properties is poorly understood.

To investigate superoxo complex **5** towards its ability to perform HAT reactions, a thermodynamic square scheme was derived (Scheme 22).

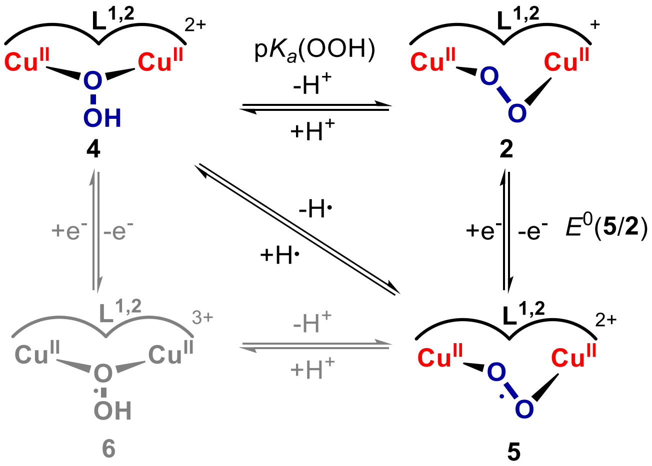

Scheme 22. Thermodynamic Square Scheme for the Cu_2/O_2 species based on the non-symmetric ligand framework $\mathbf{L^{1,2}}$.

By employing the following Bordwell relationship,[126] the bond dissociation free energy (BDFE) of complex **4** could be derived from the pK_a= 21.1 of complex **4** (see Section 5.3.2), the redox potential E^0(**5**/**2**) = −0.58 V (vs. Fc/Fc$^+$) and $C_{g,MeCN}$ = 52.6 kcal mol^{-1}.[127]

$$\mathrm{BDFE(OOH)} = 1.37\mathrm{p}K_\mathrm{a} + 23.06E^0 + C_\mathrm{g,MeCN} \qquad \mathbf{11}$$

Therefore, a BDFE of 69.5 ± 1.5 kcal mol^{-1} could be derived for the OO–H bond of complex **4**. Hence, the corresponding superoxo complex **5** was tested towards its ability to perform HAT reactions. Therefore first reactions were carried out with TEMPO–H with exhibits a rather weak O–H bond (BDFE(O–H) = 66 kcal mol^{-1} in MeCN[127]) viz Scheme 23.

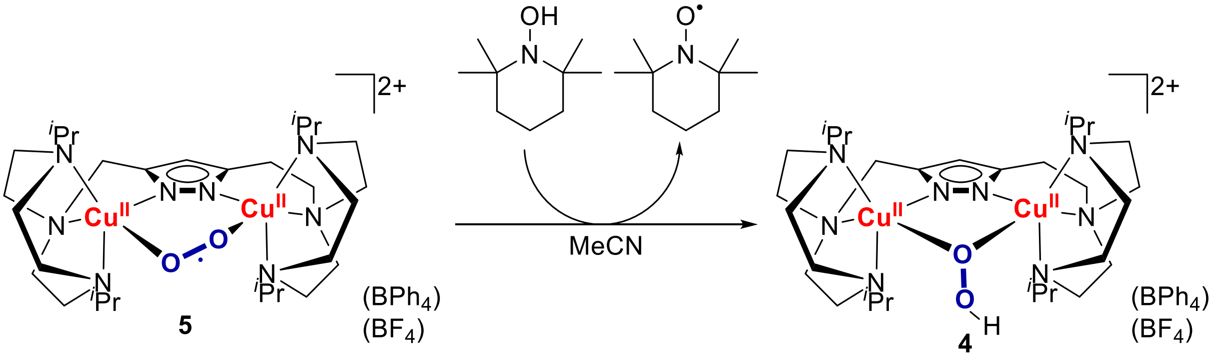

Scheme 23. HAA reaction of the superoxodicopper(II) complex **5** with TEMPO–H to form the hydroperoxo complex **4**.

Depicted in Figure 66 is the reaction of the superoxo complex **5** with 2.0 equivalents of TEMPO−H in acetonitrile at −40 °C followed by UV/Vis spectroscopy, revealing an immediate decrease of the absorption features of **5** after addition of the substrate and the simultaneous increase of absorption features at 374 nm, 424 nm and 614 nm, being characteristic for the hydroperoxo complex **4**. Isosbestic points at 350 nm, 403 nm and 710 nm indicate a clean conversion from **5** to **4**.

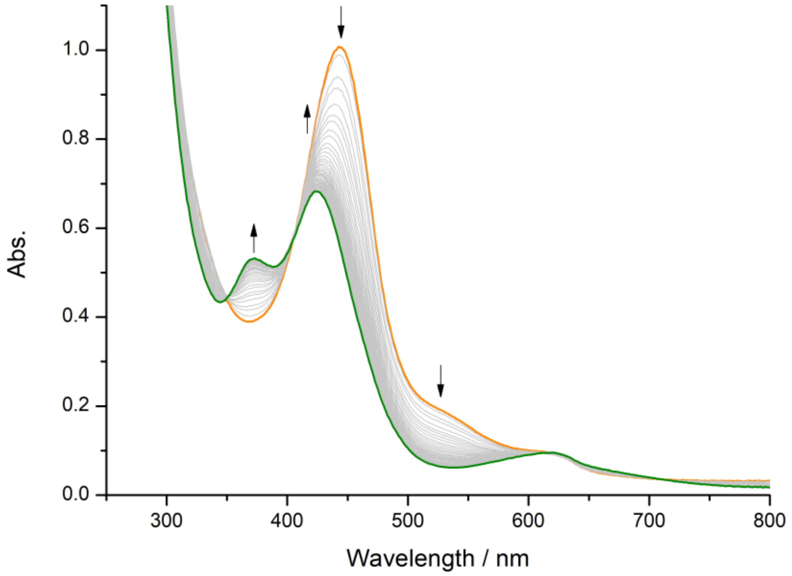

Figure 66. Monitored UV/Vis spectra of the reaction of complex **5** with 2.0 equivalents of TEMPO−H in acetonitrile at −40 °C.

Based on this, further kinetic measurements were conducted by UV/Vis spectroscopy at various temperatures and substrate concentrations via initial rate experiments. Hereby, first order kinetics were assumed due to the applied excess of TEMPO−H in the range of 10-50 equivalents. The determined k_{obs} values have been obtained by monitoring the reaction progress at a fixed wavelength of 444 nm and were plotted versus the substrate concentration to yield the second order rate constant $k(T)$ (Table 7). From those individual rate constants $k(T)$, the activation parameters of the PCET reaction could be derived from an EYRING plot (Figure 67).

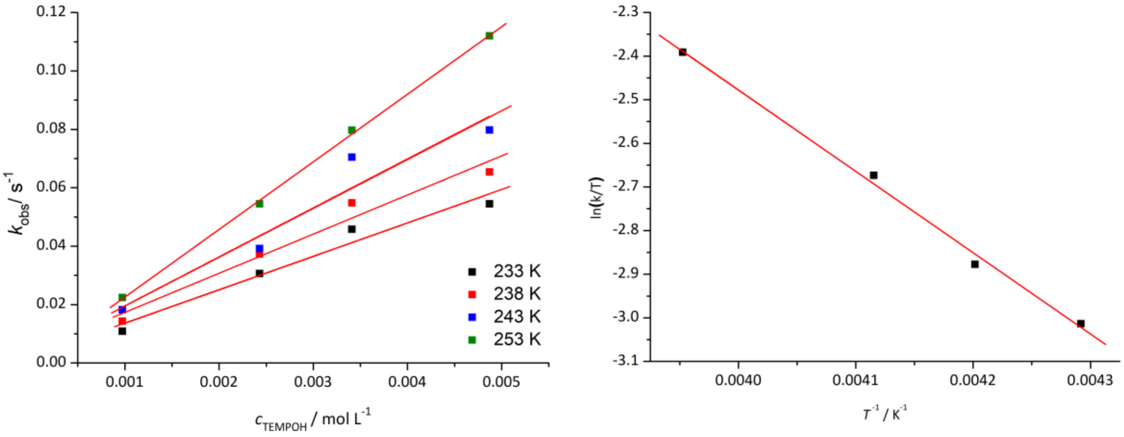

Figure 67. Plot of the different reaction rates k_{obs} vs. the concentration of TEMPO−H; experiments conducted in MeCN with a complex concentration of 0.1 mM (left) and an EYRING plot, which correlates the second order rate constants $k(T)$ and the temperature (right).

The EYRING-POLANYI equation, which is shown in the following:

$$ln\left(\frac{k}{T}\right) = -\frac{\Delta H^{\ddagger}}{RT} + ln\left(\frac{k_b}{h}\right) + \frac{\Delta S^{\ddagger}}{R} \qquad \mathbf{12}$$

correlates the activation enthalpy as well as the activation entropy with the reaction rate and temperatures. Therefore, the slope of the EYRING plot yields $\Delta H^{\ddagger}$ and the intersection with the y-axis $\Delta S^{\ddagger}$.

Table 7. Reaction rates k_{obs} derived from the reaction of complex **5** with various equivalents of TEMPO–H at different temperatures, as well as the derived second order rate constants $k(T)$.

	k_{obs}(−40 °C) [10^{-4} s^{-1}]	k_{obs}(−35 °C) [10^{-4} s^{-1}]	k_{obs}(−30 °C) [10^{-4} s^{-1}]	k_{obs}(−20 °C) [10^{-4} s^{-1}]
50 eq.	0.0545	0.0654	0.0798	0.112
35 eq.	0.0458	0.0548	0.0705	0.0797
25 eq.	0.0306	0.0373	0.0392	0.0545
10 eq.	0.0109	0.0143	0.0182	0.0224
k(T) [m^{-1} s^{-1}]	11.45	13.40	16.77	23.16

Thus, for the reaction of superoxo complex **5** with TEMPO-H, the thermodynamic parameters of $\Delta H^{\ddagger}$ = 15.5 ± 0.7 kJ mol^{-1}, $\Delta S^{\ddagger}$ = −156.0 ± 3.1 J mol^{-1} K^{-1} and $\Delta G^{\ddagger}$ = 51.9 ± 1.5 kJ mol $^{-1}$ were obtained. The large activation entropy together with the small activation enthalpy points towards an associative HAT mechanism.

To verify the assumption of a concerted hydrogen atom transfer versus a sequential electron and proton transfer, thermodynamic parameters of both potential pathways were considered. Hereby, the free energy for the reaction of TEMPO–H with complex **4** can be calculated according to the following equation **13**.

$$\Delta G^0_{\mathrm{HAT}} = \mathrm{BDFE(TEMPO\text{-}H)} - \mathrm{BDFE}(\mathbf{4}) = -3.5\ \mathrm{kcal\ mol^{-1}} = -15.0\ \mathrm{kJ\ mol^{-1}} \qquad \mathbf{13}$$

Further, the free energy for the electron and proton transfer can be derived by using the following equations:

$$\Delta G^0_{ET} = -zF\Delta E^0 = -(23.06\ \mathrm{kcal\ mol^{-1}\ V^{-1}})\Delta E^0 = 29.7\ \mathrm{kcal\ mol^{-1}} = 124\ \mathrm{kJ\ mol^{-1}} \qquad \mathbf{14}$$

$$\Delta G^0_{PT} = -\mathrm{RT}\ln(K_a) = 2.303\ \mathrm{RT}\Delta pK_a = 20.0\ \mathrm{kcal\ mol^{-1}} = 83.7\ \mathrm{kJ\ mol^{-1}} \qquad \mathbf{15}$$

Whereby the following patameters were used: E^0 $(\mathbf{2}/\mathbf{5})$ = −0.58 V vs. Fc/ Fc$^+$, E°(TEMPO–H/TEMPO–H$^{\cdot+}$) = +0.71 V, pK_a(**4**) = 22.2 in MeCN , pK_a(TEMPO–H) = 41 in MeCN and the gas constant R and FARADAY constant F.

The determined activation free energy exhibited a value of $\Delta G^{\ddagger}$ = 51.9 kJ mol^{-1} at 233 K, being significantly smaller than the calculated free energy values for the initial steps of the sequential pathways of electron and proton transfer (ΔG^0_{ET} = 124 kJ mol^{-1} and ΔG^0_{PT} = 83.7 kJ mol^{-1}). Therefore, the stepwise pathway can be safely excluded, and the hydrogen atom transfer most likely proceeds via a concerted mechanism.

Conceptionally, the hydrogen atom transfer reaction can be described by the MARCUS Theory,[179,180] according to the following equation:

$$\Delta G^{\ddagger} = \frac{(\Delta G^0 + \lambda)^2}{4\lambda} \qquad \mathbf{16}$$

The energy barrier $\Delta G^{\ddagger}$ correlates with the reaction free energy ΔG^0, which can be regarded as the driving force of the reaction, and the reorganization energy λ. The reorganization energy contains of an inner sphere reorganization energy (λ_{in}), which describes the free-energy change between the reactants (change of bond lengths and angles), and an outer sphere reorganization energy (λ_{out}), which is associated with the reorganization of solvent molecules along the reaction coordinates.[181]

According to the MARCUS theory, bimolecular reactions proceed via the initial formation of a precursor complex (PC), which forms a successor complex (SC) after the hydrogen atom transfer that subsequently dissociates to form the reaction products according to Scheme 24. Hereby, formation of the precursor complex is influenced by steric properties of the reactants and potential hydrogen bond formation between the hydrogen atom abstractor and donor moiety.[182,183]

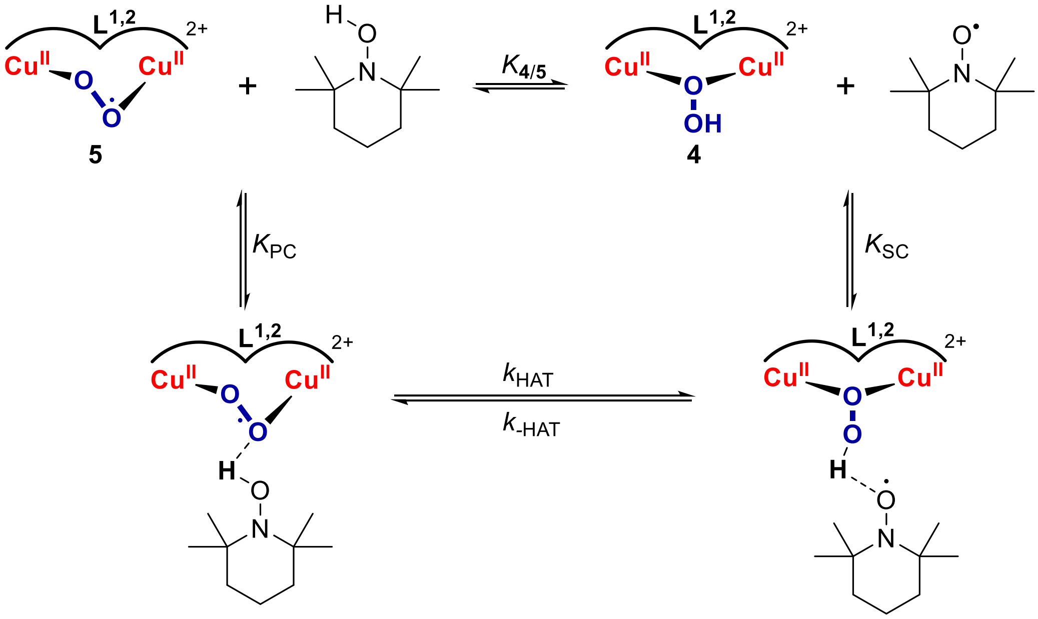

Scheme 24. Schematic precursor (PC) and successor (SC) complex formation of the reaction of superoxo complex **5** with TEMPO–H.

Since the μ-1,2 superoxo binding motive of complex **5** could be spectroscopically derived and the μ-1,1-hydroperoxo binding fashion of complex **4** was even confirmed in the solid state, qualitative assumptions of the HAT process was taken into account.

Thus, when considering the binding motifs of the superoxo complex **5** and hydroperoxo complex **4**, it is apparent that hydrogen atom abstraction must either occur from the spectroscopically observed μ-1,2 superoxide or from a μ-1,1-binding mode, which has not been observed so far. However, potential rearrangement of the μ-1,2 to a μ-1,1 superoxo binding mode prior to hydrogen atom transfer as well as consecutive rearrangement after H-atom abstraction from the μ-1,2 superoxide, involves rather large reorganization of the system. Hence, the rather large reorganization energy λ might lead to an increased reaction barrier and therefore decreased hydrogen atom transfer rate in comparison to systems with minor reorganization.

Comparison of thermodynamic parameters of the HAT reaction of complex **5** and the prior reported superoxodicopper(II) complexes **XIX**, **XX** revealed strong similarities. All hydroperoxo complexes feature approximately the same bond dissociation free energy and also the activation parameters reveal no significant differences except for the rather large activation enthalpy $\Delta H^‡$ of complex **XX**.

Table 8. Derived thermodynamic parameters for the reaction of superoxo complexes **XIX**, **5** and **XX** based on the compartmental pyrazolate/tacn scaffolds with TEMPO–H.

	XIX	**5**	**XX**
BDFE [kcal mol^{-1}]	69.1 ± 0.3	69.5 ± 1.5	69.4±1.2
$\Delta H^‡$ [kJ mol^{-1}]	16.0 ± 0.8	15.5 ± 0.7	37.8 ± 1.7
$\Delta S^‡$ [J mol^{-1} K^{-1}]	–137 ± 3	–156.0 ± 3	–112 ± 7
$\Delta G^‡$(233 K)[kJ mol^{-1}]	47.9 ± 0.7	51.9 ± 1.5	63.9 ± 3.3
k_{HAT}(–40 °C) [M^{-1} s^{-1}]	93	11.4	0.08 (–25°C)

While all presented pyrazolate/tacn superoxo complexes can be regarded as rather sluggish H-atom abstractors, due to their relative low bond dissociation free energies, significant differences are observed for the kinetic reaction rates within the series of those superoxo complexes. While complex **XX** reveals a comparatively low reaction rate constant of 0.08 M^{-1} s^{-1} (–25 °C), complex **5** exhibits a hundred times higher reaction rate of 11.4 M^{-1} s^{-1} (–40 °C) and superoxo complex **XX** possesses the highest reaction rate of 93 M^{-1} s^{-1} (–40 °C). Those pronounced differences of the reaction rates are mainly attributed to the different steric encumbrance of the dicupric superoxide from **XIX** to **5** to **XX**.

The space filling model of the cationic part of the first structurally characterized superoxo complex **XIX** revealed no significant difference to its peroxodicopper(II) precursor regarding the accessibility of Cu_2O_2 core.[121] Since no solid state structures for complex **5** and **XX** could be determined so far, the respective space filling models of the peroxodicopper(II) complexes are taken into account to display the accessibility of the superoxo core. As visualized in Section 5.2.3 a gradual increase of shielding of the peroxide, respectively superoxide, is observed upon elongation of the spacing unit between the pyrazolate and tacn units. Hence, formation of a precursor complex is more likely in complex **XIX** than **XX**, leading to a higher reaction rate. This assumption is also substantiated by the observed reaction rate of the non-symmetric superoxo complex **5**, which displays an extend of sterical shielding between complex **XIX** and **XX**.

To experimentally verify the determined BDFE of hydroperoxo complex **4** and to investigate the reversibility of the hydrogen atom transfer reaction, experiments with the 2,4,6-tri-*tert*-butylphenoxy radical (BDFE(2,4,6-tri-*tert*-butylphenol) = 74.8 kcal mol^{-1} in MeCN[127]) were conducted.

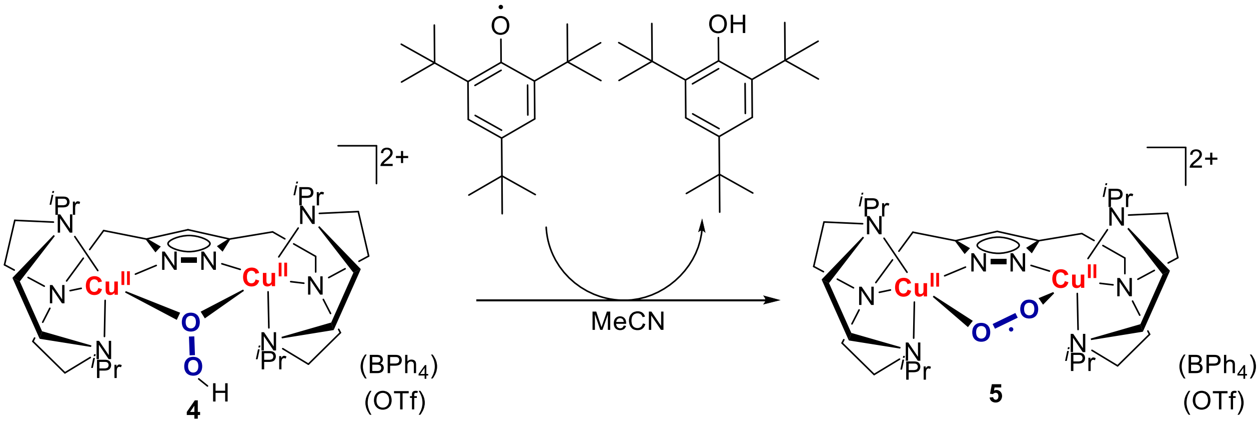

Scheme 25. Reaction of hydroperoxo complex **4** with 2,4,6-tri-*tert*-butylphenoxy radical, forming the superoxo complex **5**.

UV/Vis titration experiments of freshly prepared complex **4** with the phenoxy radical are depicted in Figure 68. Gradual increase of the absorption features of superoxo complex **5** and a simultaneous decrease of the corresponding hydroperoxo complex features is observed. The whole transformation proceeds via isosbestic points at 350 nm, 410 nm, 600 nm and 710 nm, indicating the clean conversion from **4** to complex **5**. Further, the absorption of the newly formed product reveals quantitative conversion and no significant difference to the spectral properties of **5** prepared by oxidation of complex **2**.

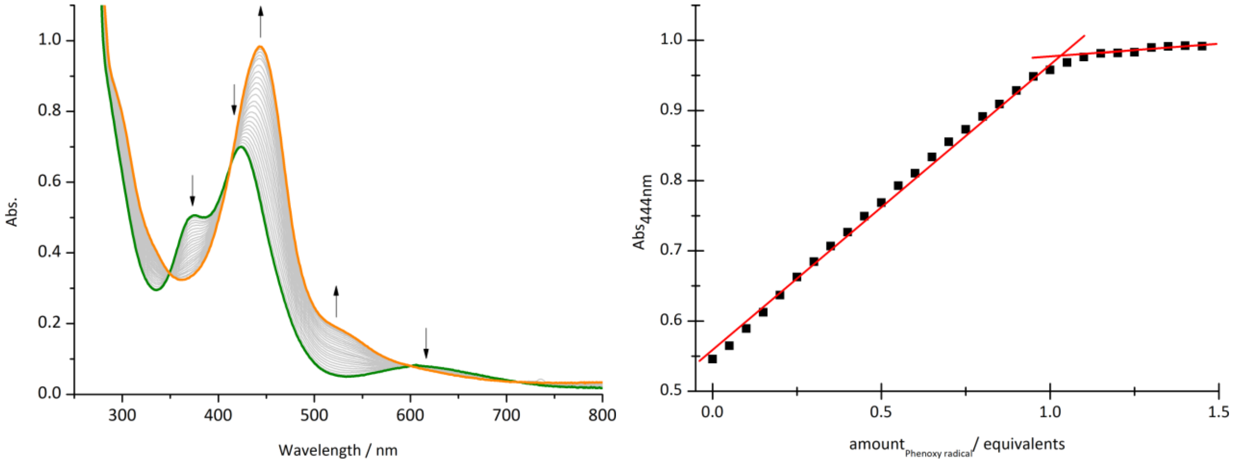

Figure 68. UV/Vis titration experiment of the hydroperoxo complex **4** with 2,4,6-tri-*tert*-butylphenoxy radical at −40°C in acetonitrile to form the corresponding superoxo complex **5** (left) and a plot of the absorption at 444 nm versus amount of phenoxy radical added, indicating the conversion after addition of one equivalent (right).

Besides TEMPO-H, further substrates were tested towards HAT reactions with complex **5**, which are summarized in Table 9; the results are in line with the determined BDFE of hydroperoxo complex **4**.

Table 9. Employed substrates for reactivity studies with their BDFEs and the observed HAT reactivity.

	BDFE in MeCN [kcal mol^{-1}]	HAT reactivity
Fluorene	77[126]	No
9,10-Dihydroanthracene	75[126]	No
Thioxanthene	74[a, 184]	No
1,4-Cyclohexadiene	73[a, 126]	No
TEMPO–H	66[127]	yes

[a] BDFEs in MeCN were derived from tabulated gas phase BDFEs according to $\mathrm{BDFE_{solv}(XH)} \approx \mathrm{BDFE_{gas}(XH)} + \Delta G_{solv}^{\circ}(\mathrm{H\cdot})$, assuming that $\Delta G_{solv}^{\circ}(\mathrm{R\cdot}) - \Delta G_{solv}^{\circ}(\mathrm{RH}) \approx 0$.[126,184]

5.4.4 Summary and Conclusion

In this section, the non-symmetric superoxodicopper(II) complex **5** was presented, which could be isolated upon chemical or electrochemical oxidation of the peroxodicopper(II) complex **2**. A μ-1,2-superoxide binding motive was confirmed, using resonance RAMAN spectroscopy and EPR measurements.

A thermodynamic square scheme could be established since E^0(**5**/**2**) and the acid-base equilibrium of **2** and the corresponding hydroperoxo complex **4** were derived during this work. The obtained bond dissociation free energy of the hydroperoxo OO-H bond of **4** is 69.5 ± 1.5 kcal mol^{-1}, fitting well into the series of previously reported dinuclear copper(II) superoxo complexes.

Kinetic investigations towards hydrogen atom transfer (HAT) reactions of superoxo complex **5** with TEMPO–H were conducted, revealing clean and quantitative conversion to complex **4** and reaction rates two orders of magnitude larger than for superoxo complex **XX** and one order smaller than for **XIX**. Further, activation parameters could be obtained by an EYRING plot, revealing no significant differences for the series of pyrazolate/tacn complexes **XX**, **XIX** and **5** (Figure 69).

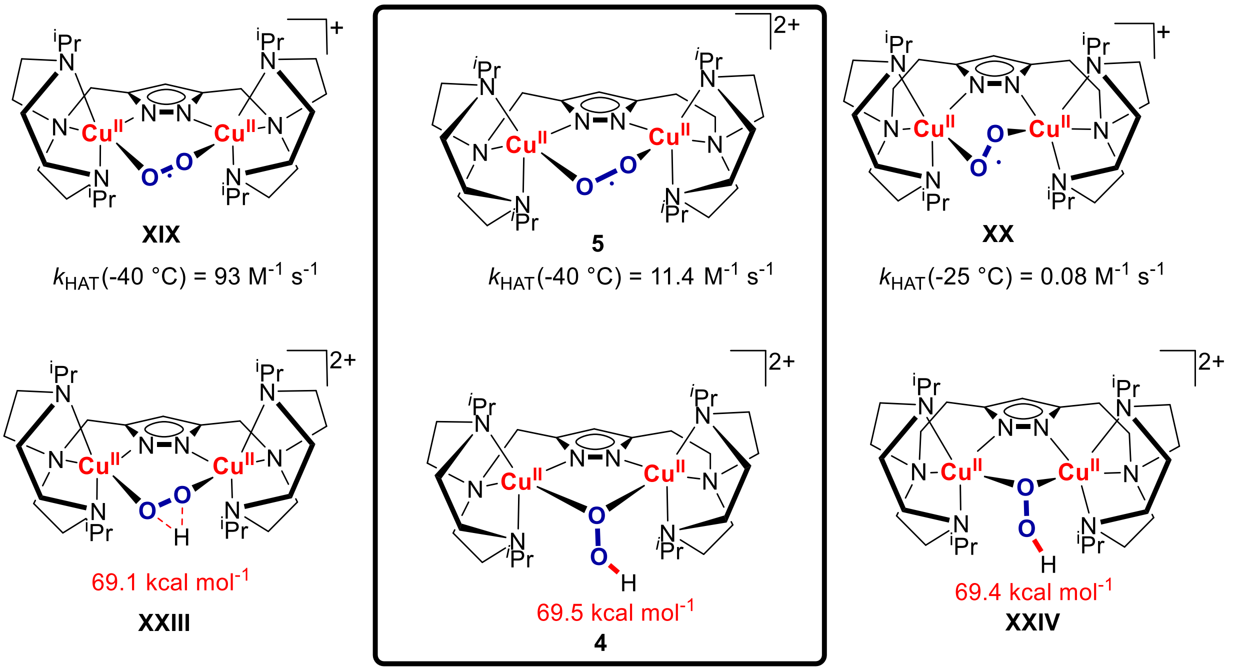

Figure 69. Superoxo and hydroperoxo complexes of pyrazolate/tacn ligand scaffolds without counter ions and their reaction rate for hydrogen atom abstraction with TEMPO–H in acetonitrile and determined BDFE of the hydroperoxo OO–H bond respectively.

The newly derived data for the CPET process of complex **5** to **4** indicate that that the accessibility of the superoxo cavity is prevailing for substrate coordination and conversion. Comparison of the HAT properties of pyrazolate/tacn based superoxo complexes with those of complex **XXII** which is derived from a XYLO ligand scaffold, reveals drastic differences of the respective hydroperoxide O–H BDFE's (Table 10). Hence, **XXII** was able to perform HAT reactions with stronger O–H and even C–H bonds. Initial explanations of those behavior, were based on the slightly increased oxidative power of the superoxide, as well as increased basicity of the peroxide and the putative formation of a μ-1,1-superoxide.

Table 10. Thermodynamic parameters of the pyrazolate/tacn based complexes **XIX**, **5** and **XX** in MeCN and the phenolated-bridged XYLO superoxodicopper(II) complex in MeTHF.[113,117,119]

	XIX	**5**	**XX**	**XXII (XYLO)**
E^0 [V][a]	–0.58	–0.58	–0.59	–0.525
pKa	21.8	22.1	22.2	24
BDFE [kcal mol^{-1}]	69.1 ± 0.3	69.5 ± 1.5	69.4 ± 1.2	81.2 ± 1.5

[a] Redox potential versus Fc/**Fc**$^+$

However, the scarcity of dinuclear copper/oxygen complexes does not allow for solid correlations between structural features and thermodynamic as well as kinetic properties.

5.5 Interactions with Alkali Metal Ions and H-Bond Donor Substrates

In the past it could be demonstrated that dicopper(II) peroxides based on pyrazolate/tacn ligand frameworks exhibit interesting binding properties towards LEWIS acids, such as alkali metal ions.

Hereby, KRISTIAN DALLE and ALEXANDER BRINKMEIER were able to reveal strong interactions between peroxo complex **XVII** and the alkali metal ions Li$^+$, Na$^+$ and K$^+$ to an extend where those adducts could also be isolated in the solid state.[113,153] The alteration of the electronic structure of peroxodicopper(II) complex **XVII** was observed by UV/Vis spectroscopy, also revealing an increase of the association constant $K_{\text{assoc.}}$ of the adduct formation dependent on the LEWIS acidity of the metal according to the HSAB concept.[113]

Interestingly, for the more sterically encumbered peroxo moiety of complex **XVIII**, different observations for the interaction with LEWIS acids (Sc^{3+}, Zn^{2+}, Li$^+$) were observed. Namely the formation of spectroscopical features identical to the hydroperoxo complex **XXIV**, which was mainly attributed to hydrolyzed traces of water in solution. Remarkably though, since complex **XXIV** could be isolated in the solid state, hydrogen bond interactions of the hydroperoxide proton with a triflate anion could be observed, indicating the relevance of acid-base interactions for copper/oxygen complexes.[124]

Therefore, this section will investigate the potential formation of alkali metal ion adducts as well as the formation of hydrogen-bond donor adducts with the newly isolated non-symmetric peroxo complex **2**.

5.5.1 Adduct Formation with Alkali Metal Ions

5.5.1.1 Formation in Solution

To investigate the potential alkali metal ion adduct formation in solution, crystalline material of precursor **1** was reacted with dioxygen to form the corresponding peroxo complex **2**. Subsequent titration with the respective alkali metal salt (MOTf, M = Li$^+$, Na$^+$, K$^+$) according to Scheme 26 was followed by UV/Vis spectroscopy.

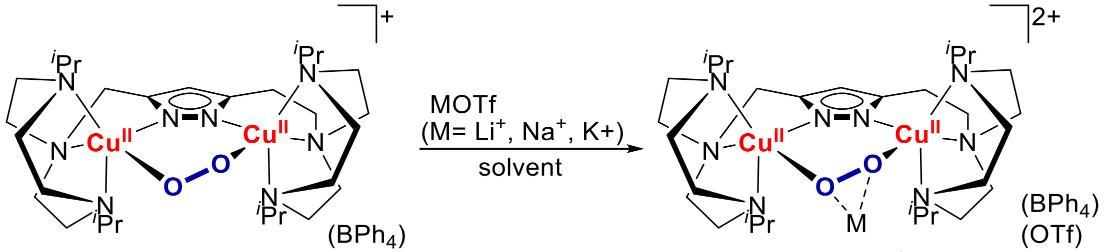

2

6; M = **Li$^+$**
7; M = **Na$^+$**

Scheme 26. Alkali metal ion adduct formation after treatment of peroxo complex **2** with the respective triflate salt.

In a typical titration experiment, substochiometric amounts of a LiOTF solution were added to complex **2** in acetonitrile at – 40 °C. A decrease of the absorption features of peroxo complex **2** at

520 nm and 617 nm was observed, accompanied by an increase of new features at 367 nm (ε = 2200 M^{-1} cm^{-1}) and 434 nm (ε = 4000 M^{-1} cm^{-1}). An isosbestic point at 468 nm is indicating clean conversion. However, in comparison with the prior reported conversions (e.g. the protonation of peroxodicopper(II) complex **2** to **4**), small deviations can be observed, attributed to potential side reactions.

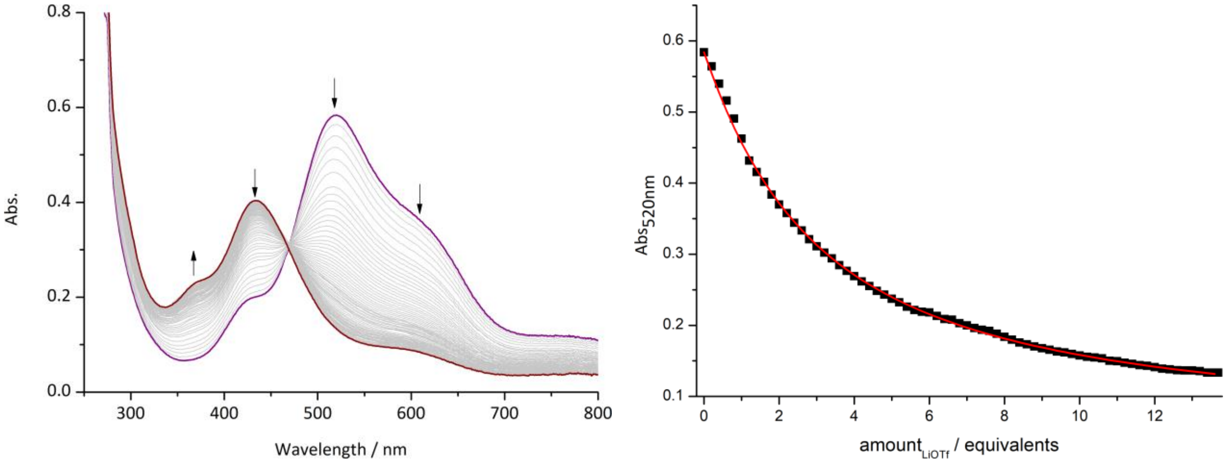

Figure 70. Left: Titration of complex **2** with LiOTf in steps of 0.2 eq. in MeCN at −40 °C. Right: Plot of absorption at 520 nm versus equivalents of LiOTf and a fit using the BindFit 0.5 software[185] (red line).

Upon addition of approximately 14.0 equivalents of LiOTf no significant change of the overall spectrum is observed. In comparison, for the methylene spaced peroxo complex **XVII**, no further change of the absorption features was observed after addition of only 1.5 equvialents of LiOTf.[113]

The formation of complex **6** (respectively **2+Li**$^+$) could be analyzed by employing the association constant K_{assoc} (equation **17**)., which resembles the binding affinity of the guest towards the host molecule and is described according to the following fraction, whereby c^0 = 1 mol L^{-1} is introduced, since association constants are unitless.

$$K_{assoc.} = \frac{[\mathbf{6}]c^0}{[\mathbf{2}][\mathbf{Li}^+]} \qquad \mathbf{17}$$

The diminishing absorption features of complex **2** at 520 nm and 617 nm were used to employ a fitting model, using the BindFit v0.5 software from THORDARSON[185] (Figure 81). Thus, a binding constant of $K_{\mathrm{assoc.}} = 0.4\cdot10^4 \pm 18\%$ could be derived.

Therefore, comparisons with titration experiments of ALEXANDER BRINKMEIER revealed a dramatically decreased binding affinity of the lithium cation to the peroxo moiety of complex **2** compared to **XVII** ($K_{\mathrm{assoc.}} = 69\cdot10^4 \pm 23\%$).[113] At this point it should also be noted that for the sterically shielded ethylene-spaced peroxo complex **XVIII** a large excess of LiOTf was employed (>100 equivalents) prior to any significant change of the respective peroxo complex absorption features. However the only observed changes exhibited strong reminiscence to the formation of the respective hydroperoxo complex.[137] It should therefore be considered that the use of a large excess of the respective alkali metal ion salt might lead to either an increased hydrolysis of residual water in solution or the introduction of trace impurities of the salt that favor the formation of the dicopper(II) hydroperoxide.

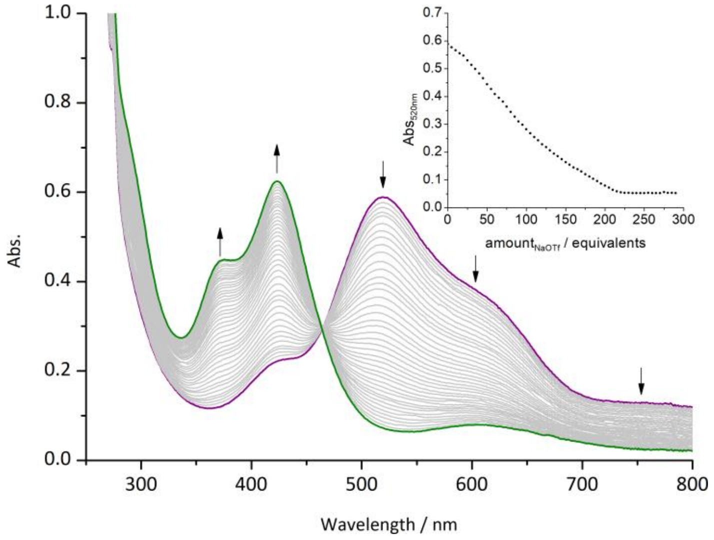

Figure 71. UV/Vis titration of peroxo complex **2** with NaOTf in steps of 5.0 eq. in MeCN at – 40 °C. The inset shows a plot of the absorption at 520 nm vs. the amount of added sodium triflate.

Similar behavior was observed upon titration with NaOTf to the peroxo complex **2** as depicted in Figure 71. Stepwise addition of the alkali metal ion only led to small changes of the electronic absorption spectra, even though much larger quantities were employed than for the titration with LiOTf. After addition of approximately 200 equivalents of NaOTf, no significant change of the formed bands at 374 nm, 424 nm and 614 nm, which are identical to those of hydroperoxo complex **4**, could be observed. Further experiments with potassium triflate resulted in similar observations. Stepwise addition of up to 500 equivalents of KOTf to complex **2** only led to the formation of species with spectroscopic features identical to those of the dicopper(II) hydroperoxide **4**.

Those findings fit well into the preliminary reports of the sterically unprotected peroxo complex **XVII**, which has a readily accessible Cu_2O_2 binding site, and the strongly encumbered peroxide of complex **XVIII**. Hence, the newly isolated peroxodicopper(II) complex **2** reveals binding properties towards alkali metal ions in between of those and therefore can be regarded as a link between its symmetric congeners.

5.5.1.2 Solid State Properties

Although ambiguous observations were made for the potential alkali metal ion adduct formation in solution, attempts were made to obtain those adducts in crystalline form. This was motivated by the prior reported bulk synthesis for alkali metal ion adducts of complex **XVII**, which revealed successful conversion of the peroxo complex to the respective adduct upon addition of between 1.0 and 2.0 equivalents of the alkali metal ion.[113]

Therefore, crystallization attempts were conducted starting from in situ generated solutions of complex **2** (acetone, MeCN, EtCN). The addition of the respective alkali metal salt (LiOTf, NaOTf, KOTf) at around −40 °C was accompanied by a sudden color change from deep purple to brown and subsequent crystallization by diffusion or layering with Et_2O at −26 °C was attempted.

In most cases, isolation of crystalline material suitable for X-ray analysis tended to be rather difficult, since decomposition to the thermodynamically stable hydroxo complex **3** or the formation of polycrystalline material was observed. However, isolation of single crystals for X-ray diffraction could be achieved in relatively low yields (5-10%) for the sodium cation peroxo adduct **7** (**$2+Na^+$**), wherefrom the molecular structure shown in Figure 72 was derived.

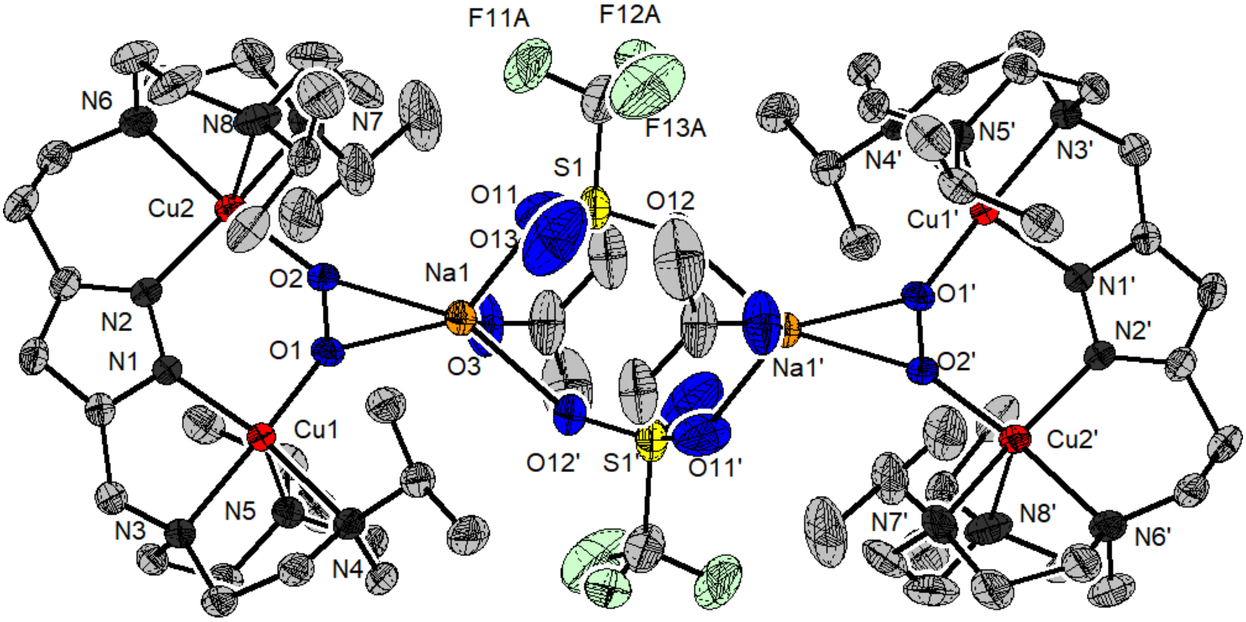

Figure 72. Molecular structure of the dimer of the cationic part of complex **7** (**$2+Na^+$**). Thermal displacement ellipsoids given at 50% probability. Hydrogen atoms, solvent molecules and counter ions are omitted for clarity. Selected bond lengths [Å] and angles [°] for **7**: Cu1⋯Cu2 3.7736(5), O1–Na1 2.2560(16), O2–Na1 2.3917(15), Cu1–O1 1.8799(15), Cu1–N1 1.9448(18), Cu1–N3 2.1139(18), Cu1–N5 2.1599(19), Cu1–N4 2.2605(19), Cu2–O2 1.9107(16), Cu2–N2 1.9838(19), Cu2–N6 2.120(2), Cu2–N7 2.144(2), Cu2–N8 2.284(2), O1–O2 1.4786(24).

The formation of a dimer consisting of two peroxo units is observed. Each peroxodicopper(II) unit is coordinated by a sodium cation, which is bridged to the other monomeric unit by two triflate anions. Further, each copper ion is coordinated by four nitrogen atoms, originating from the tacn sidearm and the pyrazolate unit. Again, significant differences in the coordination geometry of the respective Cu^{II} ion can be observed. While the Cu1 ion on the methylene bridged binding site favors a coordination geometry between a trigonal bipyramidal and square pyramidal environment

(τ_5 = 0.601), the coordination geometry of the Cu2 ion in the ethylene bridged binding pocket can be described as a slightly distorted square pyramide (τ_5 = 0.189). The Cu−N bonds originating from the pyrazolate are significantly shorter (Cu1−N1 = 1.94 Å, Cu2−N2 = 1.98 Å) than those of the tacn units (Cu1−N3,4,5 = 2.11−2.26 Å, Cu2−N6,7,8 = 2.12-2.28 Å) nitrogen. The Cu···Cu separation is 3.77 Å**,** being slightly elongated in comparison to parent peroxo complex **2**, which has a Cu···Cu distance of 3.70 Å. The O−O bond length of 1.48 Å of the sodium ion adduct shows only minor changes to the precursor complex **2**. Those structural parameters are also summarized in Table 11.

Table 11. Metric parameters of peroxodicopper(II) complex **2** and the sodium ion adduct **7** derived from the solid state structure via X-ray absorption spectroscopy.

	2	**7 (2+Na$^+$)**
Cu1···Cu2 (Å)	3.696	3.774
Cu1−N1/Cu2-N2 (Å)	1.93 / 1.98	1.94/1.98
Cu1−N3,4,5 / Cu2−N6,7,8 (Å)	2.13-2.19/2.11-2.28	2.11-2.26/2.12-2.28
O1−O2 (Å)	1.452	1.479
τ_5 [Cu1, Cu2]	0.547, 0.202	0.601 / 0.189
Cu1−O1/Cu2-O2 (Å)	1.884 / 1.897	1.878 / 1.911
Cu−O−O−Cu (°)	86	82

Interestingly, binding of the sodium ion leads to a slight decrease of the Cu−O−O−Cu torsion angle ϕ from 86° to 82° for complex **2**. However, for complex **XVII** the binding of alkali metal ions led to an increase of the dihedral angle, which had a significant influence on the magnetic properties.[52]

Furthermore, first attempts to isolate the complex **6** (**2+Li$^+$**) in the solid state only led to the isolation of polycrystalline material so far. Thus, the improvement of synthetic routines for the isolation of further alkali metal ion adducts of complex **2** should therefore be conducted in near future to investigate those findings in more detail.

5.5.2 Adduct Formation with Hydrogen Bond Donor Substrates

5.5.2.1 Formation in Solution

Bioinorganic chemistry has employed a large variety on ligand scaffolds in the last years to replicate the properties of metalloproteins active sites. While those studies primarily focus on the design of the primary coordination sphere, mimicking the electronic structure and spectroscopical properties of their parent enzymes, the second coordination sphere is often neglected or barely considered.

This approach seems contradictory since the chemical microenvironment of metals in active sites is crucial for regulation and enhancement of catalytical reactions.[96,186] Recent studies revealed the stabilization of binuclear Cu_2/O_2 and mononuclear hydroperoxo adducts through hydrogen bonds[96,116,187–189] and KARLIN and coworkers[97] were also able to demonstrate the strong influence of hydrogen bonding on the reactivity copper/oxygen complexes, modifying the HAT reactivity of a mononuclear superoxo complex through hydrogen bonds.

Therefore, initial studies on the interaction of the peroxodicopper(II) complex **2** with hydrogen bond donor (HBD) substrates were conducted under consideration of their HBD strength[190–192] and respective pK_a values.[176,193,194] Hence, initial experiments were employed adding a large excess (100 μL) of pure methanol ($pK_a = 28.7$ in MeCN[193]) to a solution of freshly prepared complex **2** ($c = 0.102$ M) at −40 °C in acetonitrile. The obtained UV/Vis spectrum is depicted in Figure 73.

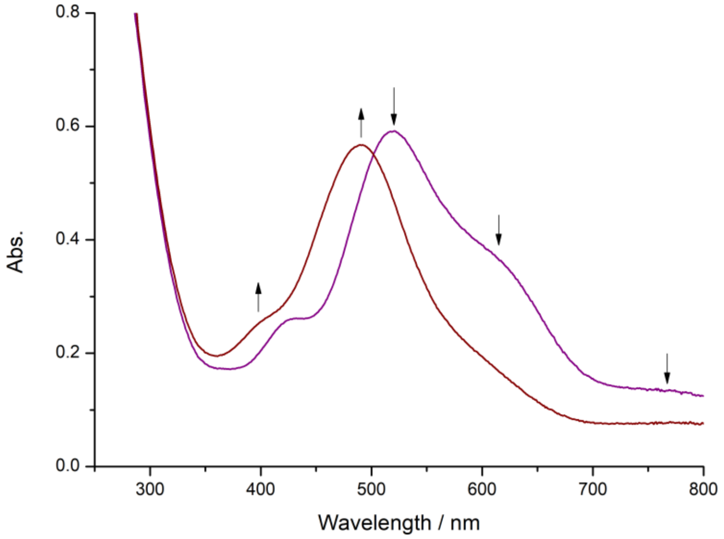

Figure 73. UV/Vis spectra of the peroxo complex **2** before and after addition of pure methanol in acetonitrile at −40 °C.

A significant change of the electronic absorption features of the peroxo complex **2** could be detected, whereby strong blueshifting of the intense band at 520 nm to 490 nm ($\varepsilon = 5500\ M^{-1}cm^{-1}$) was observed. Further, the shoulder at 437 nm also shifted to 395 nm ($\varepsilon = 2400\ M^{-1}cm^{-1}$) and the shoulder at 617 nm vanished almost completely. Those changes hint towards slight alterations of the peroxide π* orbitals, which are responsible for the characteristic peroxodicopper(II) absorption features.

Investigation of the decay properties upon addition of methanol revealed comparatively faster decomposition than the pure peroxo complex **2**. A half-life time of approximately $t_{1/2} = 15$ h was determined by assuming first order decay kinetics (Figure 74). Thus, the newly formed adduct revealed significant faster decomposition than pure complex **2** ($t_{1/2} \approx 32$ h).

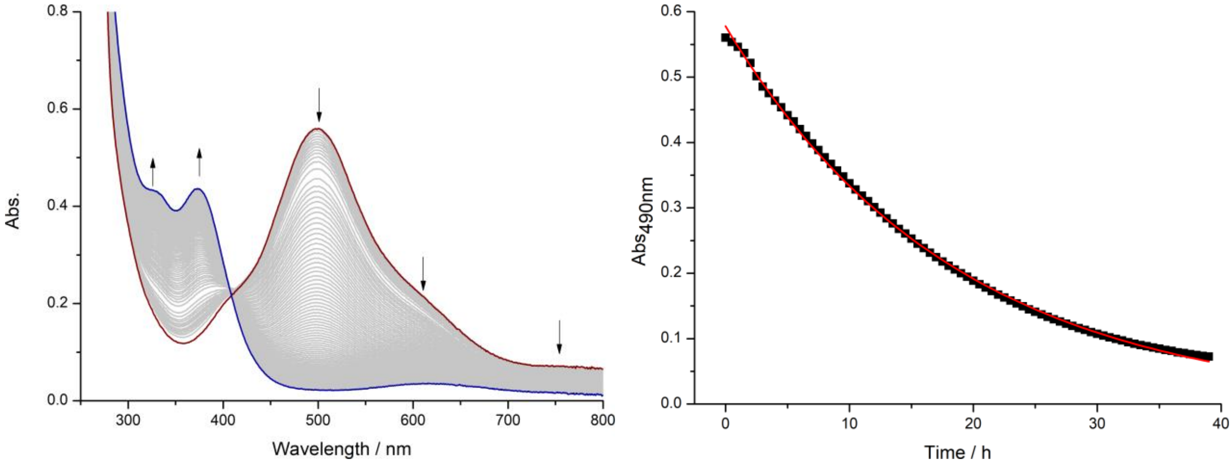

Figure 74. Decay of peroxodicopper complex **2** with an excess of MeOH in MeCN at RT followed by UV/Vis spectroscopy (left) and a plot of the absorption at 490 nm versus time (right) and an assumed first order decay fit (red line).

Based on this, further protic substrates with comparatively stronger HBD strength were chosen under consideration of their respective pK_a value in correlation to lutidinium triflate, which was used to fully protonate peroxo complex **2** to hydroperoxo complex **4**. Thus, 2,2,2-trifluoroethanol (TFE, pK_a = 35.4 in MeCN[195,196]) and phenol (pK_a = 29.1 in MeCN[197]) were employed, whereby an elusive temperature dependent transformation could be observed that will be discussed in detail in the Section 5.5.2.3.

Exemplarily, the addition of a defined amount of TFE (300 eq.) to peroxo complex **2** is depicted in Figure 75, whereby a significant change of the absorption features of complex **2** can be observed. Again, strong blueshifting of the characteristic peroxo maxima is observed from 520 nm to 495 nm (ε = 5800 $M^{-1}cm^{-1}$) and 437 nm to 404 nm (ε = 2100 $M^{-1}cm^{-1}$).

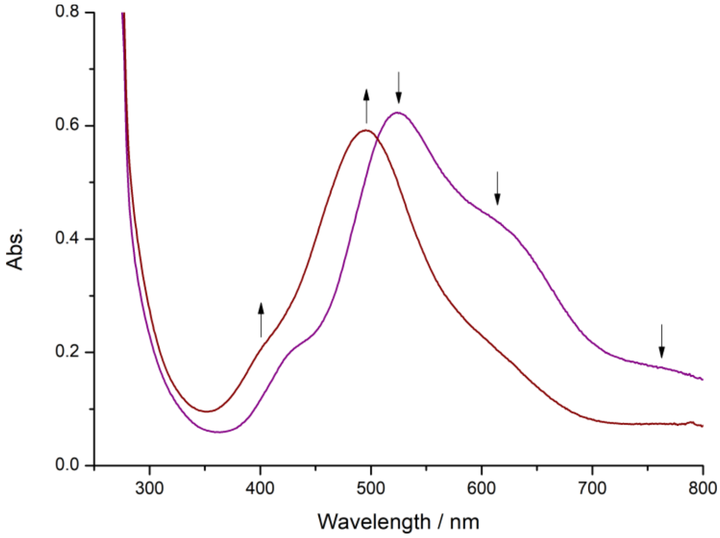

Figure 75. UV/Vis spectra of the peroxo complex **2** before and after addition of pure TFE (300 eq.) in acetonitrile at −40 °C.

5.5.2.2 Solid State Properties

The isolation of single crystalline material of those adducts proved to be extremely challenging, especially with TFE. In case of the methanol bound peroxo adduct, good results could be achieved by addition of a small excess of methanol to crystallization attempts of peroxo complex **2** in acetone/Et_2O solutions at −26 °C and subsequent diethyl ether diffusion. Further, discarded MeOH solutions from the synthesis of precursor complex **1** could also be employed in the same way (Scheme 27).

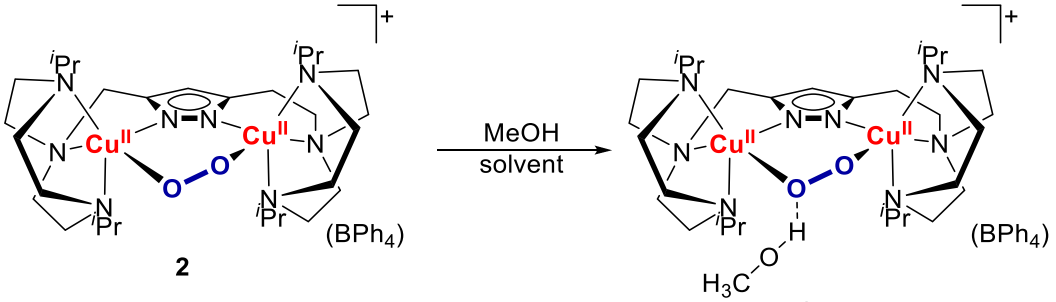

2

8

Scheme 27. Hydrogen-bounded methanol peroxo adduct **8**.

The obtained crystalline material was suitable for X-ray diffraction analysis and hence the solid-state structure of the methanol bound peroxo adduct in **8** is depicted in Figure 76. Similar to the peroxo complex **2**, both copper(II) ions are coordinated by the {N_4} binding pocket of the pyrazolate and tacn nitrogen atoms. The coordination sphere of both metals differs slightly, while Cu1 exhibits a distorted geometry between a trigonal bipyramide and a square planar pyramide ($\tau_5 = 0.509$), the Cu2 ion has a less distorted square pyramidal coordination geometry ($\tau_5 = 0.181$).

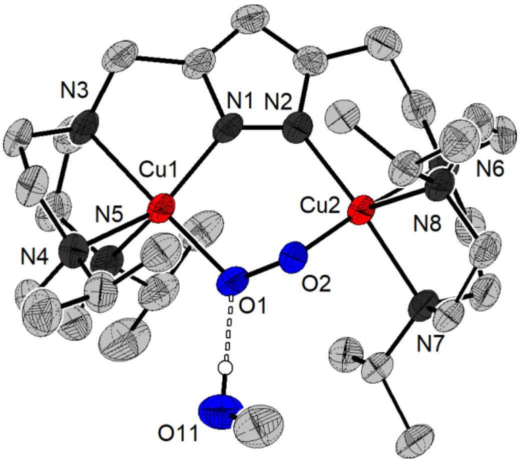

Figure 76. Molecular structure of the cationic part of complex **8**. Thermal displacement ellipsoids given at 50% probability. Hydrogen atoms, solvent molecules and counter ions are omitted for clarity. Selected bond lengths [Å] and angles [°] for **8**: Cu1⋯Cu2 3.7252(8), Cu1–O1 1.907(3), Cu1–N1 1.945(4), Cu1–N3 2.104(4), Cu1–N4 2.184(4), Cu1–N5 2.187(4), Cu2–O2 1.915(3), Cu2–N2 1.974(4), Cu2–N6 2.110(4), Cu2–N7 2.125(4), Cu2–N8 2.300(4), O1–O2 1.4428(42).

The isolated H-bonded methanol peroxo adduct **8** has a Cu⋯Cu distance of 3.725 Å which is similar to complex **2** (d(Cu⋯Cu) = 3.696 Å). Further, the O–O bond exhibited a length of 1.443 Å being nearly as long as in the pure peroxo complex (d(O–O) = 1.452 Å). The high-quality X-ray diffraction data even allowed to determine the position of the hydrogen atom of the bound methanol, wherefrom a

O1–$H_{Methanol}$ distance of 1.724 Å and significant shortening of the O11–$H_{Methanol}$ from 0.956[198] Å to 0.840 Å could be derived. In addition, the O1···O11 distance is 2.559 Å, verifying the hydrogen-bonding interaction.[199,200] The coordination of the methanol to the peroxide moiety seemed to have no significant influence on the Cu–O–O–Cu torsion angle ϕ which changed only minorly from 86° to 87°. However, slight elongation of the Cu1–O1 bond from 1.884 Å for complex **2** to 1.907 Å for **8** was observed.

The isolation of solid material also allowed for further spectroscopical investigation by means of solid-state UV/Vis and resonance RAMAN spectroscopy. Comparison of solid state and solution electronic absorption spectra of complex **8** revealed similar characteristic features but no significant shifting of the O–O vibration in the resonance RAMAN spectrum was observed (see below).

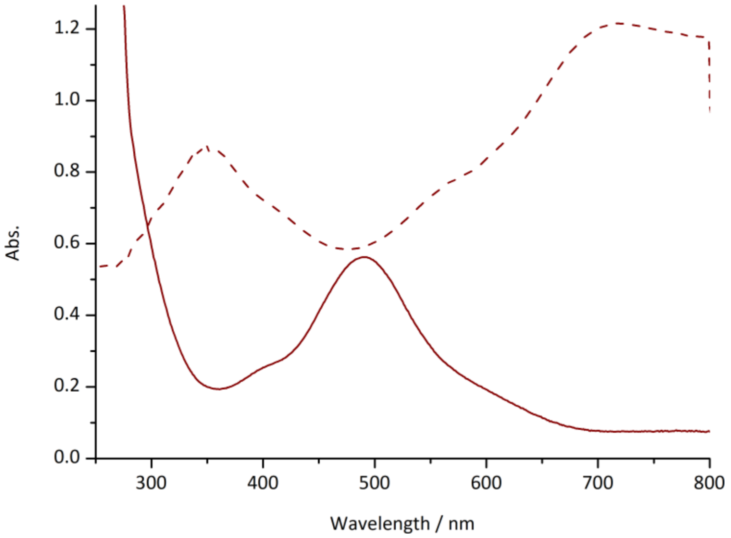

Figure 77. UV/Vis absorption features of complex **8** in MeCN at −40 °C (solid line) and reflectance of the solid state in a KBr matrix at RT (dotted line).

Even though the influence on structural parameters of the peroxo core is only minor, magnetic susceptibility data of complex **8** were recorded using a superconducting quantum interference device (SQUID) in the temperature range between 2 K to 295 K. Since pure material of the adduct could be obtained in bulk, powdered crystalline material of complex **6** was used. The corresponding spectrum depicted in Figure 78 reveals ferromagnetic coupling of the Cu^{II} ions.

Fitting of the experimental data was done by taking the antisymmetric and anisotropic DZIALOSHINSKY-MORIYA (DM) interaction into account in the spin Hamiltonian (equation **18**) as it has also been done for complex **2**.

$$\hat{H} = -2J\vec{S}_1\vec{S}_2 + \vec{d}\vec{S}_1 x\vec{S}_2 + g\mu_B(\vec{S}_1 + \vec{S}_2)\vec{B} \qquad \textbf{18}$$

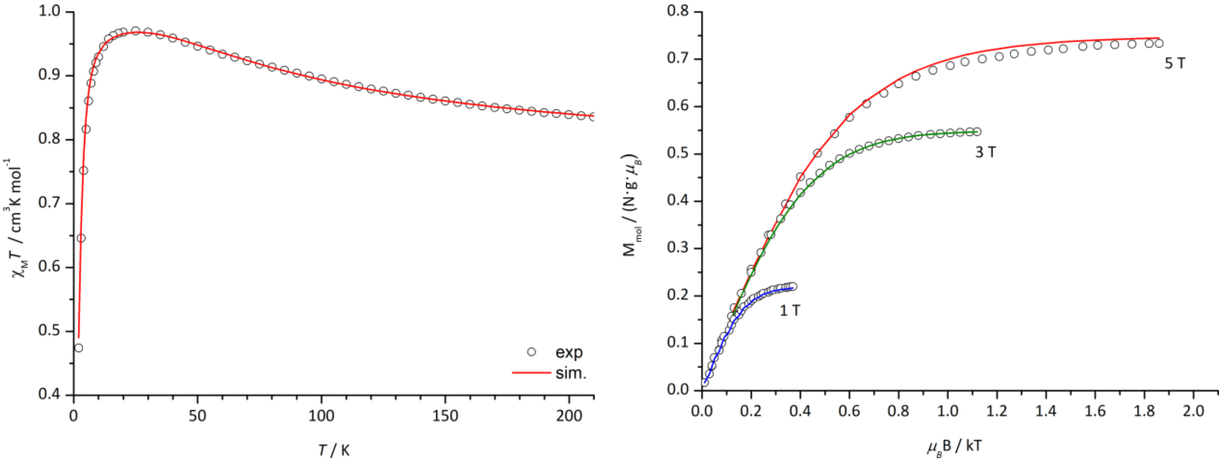

Figure 78. χ_mT vs. T measurement in the temperature range of 2–295 K at 0.5 T (left) and variable temperature/variable field (VTVH) magnetization measurements at fields of 1 T, 3 T, and 5 T presented as M_{mol} vs. $_{\mu B}$B/kT (right) for crystalline samples of **6**. The solid lines represent the best global fit for both data sets, including antisymmetric DM interaction. Parameters obtained: J = +33.2 cm^{-1}, g = 2.000, 2.000, 2.048, PI = 0%, TIP = -175 × 10^{-6} cm^3 mol^{-1}.

The derived coupling constant of J = +33 cm^{-1} confirmed the ferromagnetically coupled singlet (S = 1) ground state, with $\vec{d}$ = (39, 0, 0) cm^{-1} and g = 2.00, 2.00, 2.05. Strong resemblance with the magnetic properties of parent complex **2** could be observed, such as the strong decrease of χ_mT below 20 K, which indicates significant zero-field splitting (ZFS), which was also confirmed by variable-temperature and variable-field (VTVH) measurements and therein observed nesting. Therefore, no substantial influence of the methanol on the magnetic properties could be observed (Table 12).

Table 12. Best fit values for the magnetic data of complex **2** and **8**.

	2	**8 (2·MeOH)**
J [cm^{-1}]	+28	+33
S	1	1
g	2.03, 2.03, 2.35	2.00, 2.00, 2.05
$\vec{d}$ [cm^{-1}]	(39, 0, 0)	(39, 0, 0)

Since initial UV/Vis experiments with TFE revealed significant interaction with the peroxo moiety of **2**, extensive screening of various crystallization conditions had to be conducted since decomposition to the hydroxo complex **3** or protonation to the hydroperoxo complex **4** was facile (more in Section 5.5.2.3). While low temperatures prevented the decay of the TFE bound peroxo adduct **9** to the hydroxo complex **3**, it was also observed that the formation of the presumed adduct was highly disfavored at lower temperatures and strongly dependent on the concentration of TFE. Therefore, different solvents were tested (acetone, MeCN, EtCN) with different TFE concentrations at various temperatures. The synthetic procedure is described in detail in Section 7.13, finally yielding single crystalline material suitable for X-ray diffraction. The molecular structure of the hydrogen bound TFE peroxo adduct **9** is depicted in Figure 79.

The copper ion bound on the methylene bridged binding pocket reveals a coordination geometry between a trigonal bipyramide and a square planar pyramide (τ_5 = 0.556). The second copper ion on the ethylene bridged binding pocket resembles a less distorted square pyramidal coordination geometry (τ_5 = 0.208).

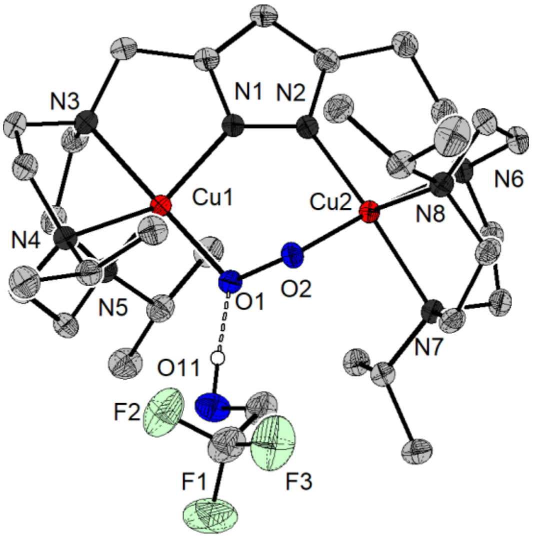

Figure 79. Molecular structure of the cationic part of complex **9**. Thermal displacement ellipsoids given at 50% probability. Hydrogen atoms, solvent molecules and counter ions are omitted for clarity. Selected bond lengths [Å] and angles [°] for **9**: Cu1⋯Cu2 3.7566(5), Cu1–O1 1.8936(12), Cu1–N1 1.9499(14), Cu1–N3 2.0999(14), Cu1–N5 2.1776(15), Cu1–N4 2.2045(15), Cu2–O2 1.9011(12), Cu2–N2 1.9803(14), Cu2–N6 2.1035(15), Cu2–N7 2.1282(14), Cu2–N8 2.3006(15), O1–O2 1.4857(17).

Complex **9** exhibited a Cu⋯Cu separation of 3.757 Å which is similar to the one in peroxo complex **2** (d(Cu⋯Cu) = 3.696 Å). The oxygen oxygen bond length is 1.486 Å, alike to the previously presented complex **2** (d(O–O) = 1.452 Å). From the high-quality molecular structure of **7** the position of the hydrogen atom of the bound 2,2,2-trifluoroethanol could be determined. A distance of 1.604 Å could be derived for the O1–H_{TFE} hydrogen bond and 0.974 Å for the O11–H_{TFE} bond. The O1⋯O11 distance in **9** is 2.573 Å, verifying the hydrogen-bonding interaction.[199,200] Further, the bound TFE did not seem to alter the Cu–O–O–Cu torsion angle ϕ of 86 ° significantly. Metric parameters of the peroxo complex **2** as well as of the methanol, respectively TFE, bound adduct **8** and **9** are summarized in Table 13.

Table 13. Metric parameters of the cationic parts of the peroxodicopper(II) complexes **2**, **8** and **9** derived from the solid state structure via X-ray absorption spectroscopy.

	2	**8 (2·MeOH)**	**9 (2·TFE)**
Cu1⋯Cu2 [Å]	3.6964(7)	3.7252(8)	3.7566(5)
Cu1–O1 / Cu2–O2 [Å]	1.884(3)/ 1.897(3)	1.907(3) / 1.915(3)	1.8936(12) / 1.9011(12)
O1–O2 [Å]	1.4524(41)	1.4428(42)	1.4857(17)
O11–H⋯O1 [Å]	-	2.5586(50)	2.5732(19)
ϕ (Cu–O–O–Cu) [°]	86	87	86
τ_5 [Cu1, Cu2]	0.547, 0.202	0.509, 0.181	0.556, 0.208

The isolation of crystalline material also allowed to record a resonance RAMAN spectrum, revealing no significant shifting of the O–O vibration around 805 cm^{-1} (Figure 80).

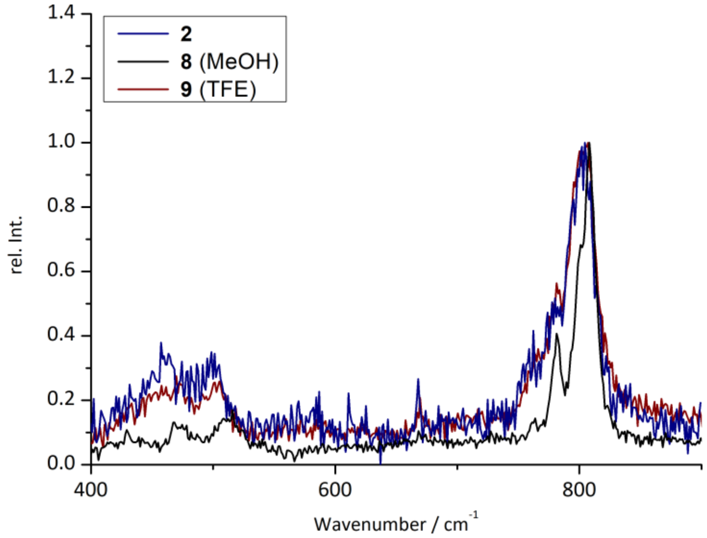

Figure 80. Solid state RAMAN spectrum of the peroxo complexes **2**, **8** and **9** (λ_{ex} = 633 nm).

5.5.2.3 Temperature Dependent Adduct Equilibrium

As already mentioned, the TFE peroxo adduct **9** showed significant temperature dependence, which will be presented in the following. For the association of TFE to complex **2** in solution according to Scheme 28 an association constant $K_{\text{assoc.}}$ was derived by assuming a 1:1 host guest ratio.

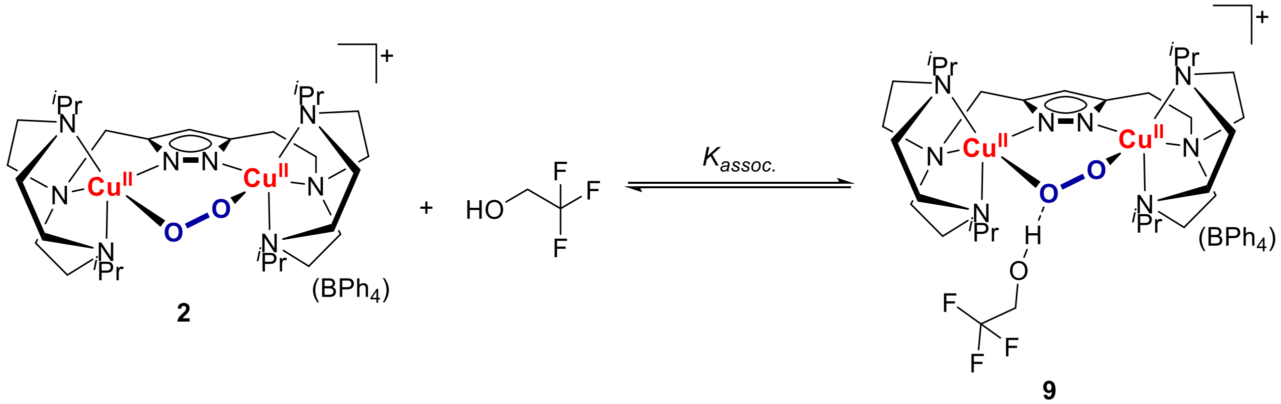

Scheme 28. Adduct formation of complex **9** in solution after addition of TFE to peroxo complex **2**.

An association constant resembles the binding affinity of the guest towards the host molecule and is described in a similar way as described for the alkali metal ion adduct formation in the previous section. Hence, $K_{assoc.}$ can be calculated as followed:

$$K_{assoc.} = \frac{[\mathbf{9}]c^0}{[\mathbf{2}][\mathbf{TFE}]} \qquad \mathbf{19}$$

The diminishing absorption features of complex **2** at 520 nm and 637 nm were used to employ a fitting model, using the BindFit v0.5 software from THORDARSON (Figure 81).[185]

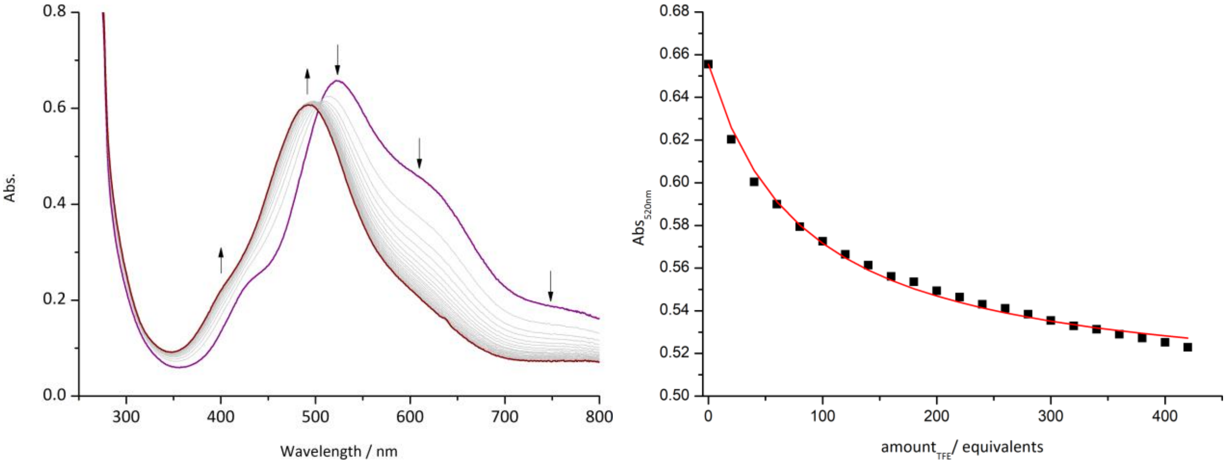

Figure 81. UV/Vis absorption spectra of the titration of complex **2** with TFE at 0°C in MeCN in steps of 20 equivalents (left) and a plot of the absorption at 520 nm versus the amount of TFE added with a fit using the BindFit 0.5 software (right).

An association constant of $K_{\text{assoc.}}$ = 120 ± 4% could be derived. Interestingly, the further stepwise addition of a large excess of TFE revealed a subsequent process, whereby the absorption features at 404 nm and 495 nm start to further decrease while new features at 372 nm and 425 nm begin to rise. An isosbestic point at 451 nm also suggests clean transformation (Figure 82). Thus, the newly formed species shows electronic absorption features reminiscent of the μ-1,1- hydroperoxo complex **4**.

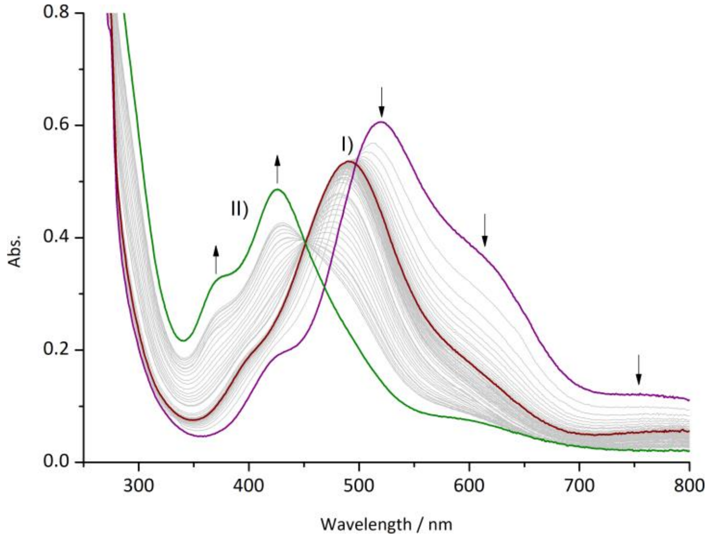

Figure 82. UV/Vis spectra of the conversion of peroxo complex **2** after addition of TFE at 0 °C in MeCN. I) TFE-Peroxo adduct **9** formation. II) Stepwise addition of an excess TFE leading to absorption features similar to hydroperoxo complex **4**.

In a further UV/Vis experiment, addition of TFE at 0°C to a ETCN solution of complex **2** was investigated (Figure 83). The HBD substrate TFE was added in excess until absorption bands at 372 nm and 425 nm start to form. Subsequent cooling down in 10 °C intervals led to a significant increase of those absorption features until −80 °C. Warming up of those solutions led to regeneration of the absorption features around 404 nm and 495 nm. The reversible process was accompanied by a pseudo-isosbestic point at 460 nm, whose shifting was attributed to partial decomposition and also shifting of the base line.

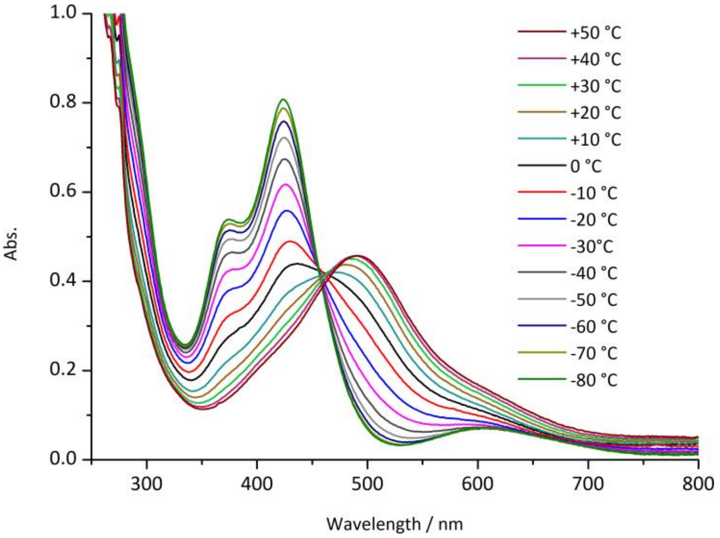

Figure 83. UV/Vis spectra of peroxo complex and an excess of TFE recorded at various temperatures in EtCN.

It should be noted that the reversibility of this process was observed in an additional experiment since warm-up of the cuvette within the UV/Vis device required several minutes to reach constant temperature, whereby significant decomposition and side reactions might occur. Therefore, cuvettes were removed from the instrument and warmed up by a water bath to RT and immediately measured by UV/Vis spectroscopy. An intense color change from deep green at around –80°C to brown at room temperature could also be observed by synthesis in larger scale. Those findings could also not be falsified by the mere presence of traces of acid from TFE, which might be responsible for protonation since temperature-dependent pK_a determinations revealed no significant changes on the basicity of the peroxo core (Section 5.3.2.). Those observations led to the assumption of the in Scheme 29 depicted transformation.

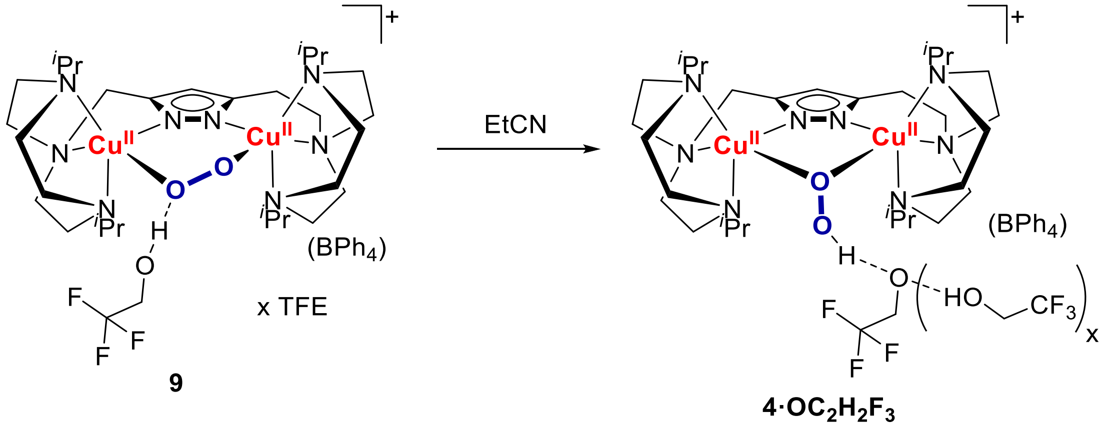

Scheme 29. Assumptive transformations of TFE bound peroxo adduct **9** and the putative hydroperoxo species.

A large excess of TFE and subsequent cooldown of the temperature leads to the formation of the *μ*-1,1-hydroperoxo complex **4·OC₂H₂F₃**. The protonation derives most likely from the bound TFE molecule, whose corresponding alcoholate anion might form hydrogen bonds to the hydroperoxide moiety, similar to complex **4** (Scheme 30).

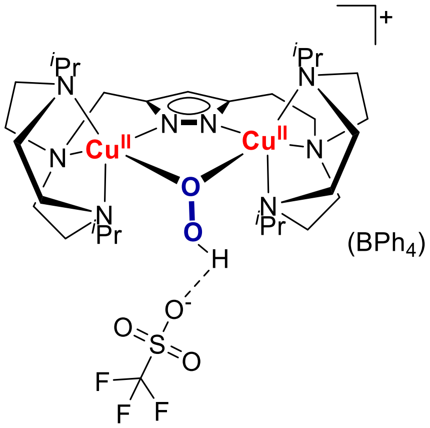

Scheme 30. Hydrogen bond formation between the triflate anion and hydroperoxide moiety of complex **4**, derived from X-ray diffraction.

The distinct absorption feature at 425 nm for **4·OC₂H₂F₃**, respectively 495 nm for **9**, were used to quantify both species. Thus, the equilibrium ratio K_{eq}= c(**4·OC₂H₂F₃**)/ c(**9**) was determined based on the assumption that the maximum concentration of **4·OC₂H₂F₃** was found at –80°C, respectively at +50°C for compound **9**. Based on the derived equilibrium constants a VAN'T HOFF plot could be obtained, according to the following equation:

$$\ln(K_{eq}) = -\frac{\Delta H^0}{RT} + \frac{\Delta S^0}{R} \qquad \mathbf{20}$$

Thus, a plot of $\ln(K_{\mathrm{eq}})$ versus T^{-1} yields a linear correlation from which ΔH^0 can be derived from the slope and ΔS^0 from the intercept of the y-axis.

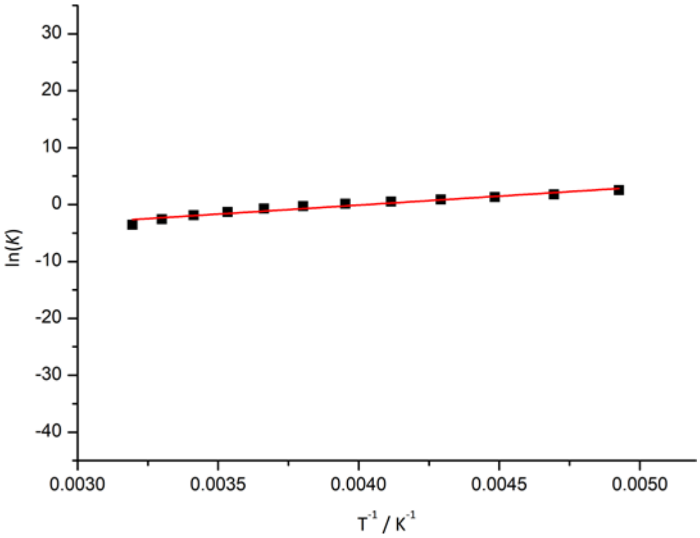

Figure 84. VAN'T-HOFF plot for the temperature sensitive peroxo- to hydroperoxo-equilibrium in EtCN. $\boldsymbol{\Delta H^0}$ = −26.3±1.9 kJ mol^{-1}, $\boldsymbol{\Delta S^0}$ = −105.7±7.5 Jmol^{-1} K^{-1}.

The obtained values of ΔH^0= −26.3±1.9 kJ mol^{-1} and ΔS^0= −105.7±7.5 J mol^{-1} K^{-1} are typical for the exothermic reaction of the transformation of **9** to **4·OC$_2$H$_2$F$_3$**.

This result might also explain the tremendous difficulty to crystallize the TFE bound peroxo adduct **9**. Several months were required to determine the ideal amount of TFE, since the equilibrium was dependent not only on concentration of TFE but also in temperature. Additionally, formation of the species with absorption features similar to hydroperoxo complex **4** also seemed to be favored over time, leading to a decolorization from brown to dark green within several days at temperatures around −20°C.

Since the assumed transformation proceeds via dramatic changes of the respective magnetic properties from a triplet ground state for the peroxo complex **9** to a singlet ground state for the putative hydroperoxo complex **4·OC$_2$H$_2$F$_3$**, initial magnetic susceptibility measurements via SQUID magnetometry of EtCN/TFE solutions of peroxo complex **2** were conducted. However, due to the extremely high concentrations ($c \approx 20.4$ mM) required for such experiments, rapid decomposition was observed prior to successful measurement.

Further substrates were employed for potential adduct formation, according to their HBD strength and their respective acidity (Table 14).

Table 14. Employed substrates and their pK_a values in acetonitrile for potential H-bonding adduct formation with complex **2.**

Substrate	pK_a in MeCN	Substrate	pK_a in MeCN
H_2O	38-40[197]	$(CF_3)_2CHOH$	22.5[193,195]
CF_3CH_2OH (TFE)	35.4[195,196]	3-Nitrophenol	23.9[201]
MeOH	28.7[193]	4-Nitrophenol	20.7[201]
Phenol	29.1[197]		

The substrates $(CF_3)_2CHOH$, 3-Nitrophenol and 4-Nitrophenol revealed no observable adduct formation by UV/Vis spectroscopy but rather direct conversion to the hydroperoxo complex **4**, even at room temperature.

Interestingly, first UV/Vis experiments with phenol revealed similar observations as for the conversion with TFE. Stepwise addition of 20 equivalents of phenol led to a significant change of the absorption features of complex **2**. Again, a new species with absorption features around 388 nm and 474 nm was observed, for which an association constant $K_{assoc.}$= 130 ± 2 could be derived. Further conversion was observed after addition of more phenol (200 eq. steps), forming again a species with similar absorption features as hydroperoxo complex **4.**

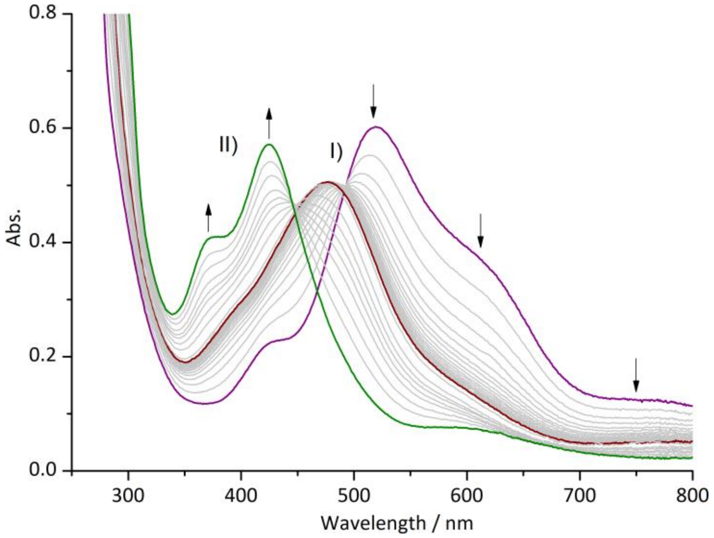

Figure 85. UV/Vis spectra of the stepwise addition of an excess of phenol to complex **2** in MeCN at −40 °C. I) Phenol-Peroxo adduct formation. II) Stepwise addition of an excess phenol (in steps of 200 eq.) leading to absorption features similar to hydroperoxo complex **4**.

Addition of H_2O_2 (35% in H_2O) at 5 °C led to no adduct formation but rather direct conversion to the hydroperoxo complex **4**. Interestingly, addition of aqueous acetonitrile solutions to complex **2** did not show immediate conversion to hydroxo complex **3**(Figure 86). Confirming the general stability of the peroxo complex **2** in the presence of water. However, it revealed the formation of a putative H_2O bound peroxo adduct with absorption features at 377 nm, 467 nm and 605 nm similar to the previously described adducts (Scheme 31).

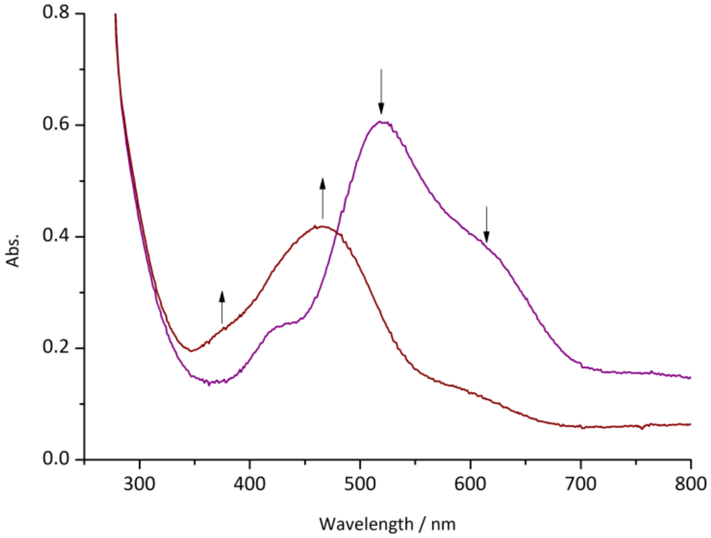

Figure 86. UV/Vis spectra of the peroxo complex **2** before (purple line) and after addition of aqueous acetonitrile solution at 5°C in MeCN (brown line).

Such an adduct might also be a key intermediate of the decomposition reaction of pyrazolate/tacn copper oxygen adducts and should therefore investigated in detail in the future. Also, isolation of the respective HBD bound hydroperoxide intermediate should be targeted to confirm those preliminary results, which emphasize the possibility of HBD substrate formation with dicupric peroxides and the relevance of hydrogen-bonding interactions for copper oxygen adducts.

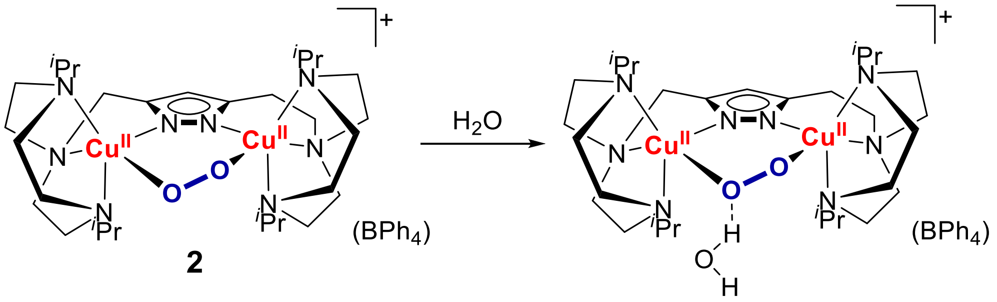

Scheme 31. Putative water-bound peroxo adduct of peroxodicopper(II) complex **2**.

5.5.3 Summary and Conclusion

In this section the isolation of various peroxo adducts was presented (Scheme 32). The non-symmetric ligand scaffold of complex **2** enabled the interaction of the peroxo moiety with alkali metal ions, albeit with a lower binding constant compared to the previously reported complex **XVII**. Formation upon addition of the respective alkali triflate salt could be monitored by UV/Vis spectroscopy, revealing change of the characteristic peroxo absorption features after coordination of the alkali metal ion. For interaction studies in solution only the Li^+ cation seemed to be suitable, for the larger ions Na^+ and K^+ no substantial formation of an adduct could be observed in the UV/Vis experiment scale but rather the formation of the hydroperoxo complex **4** or significant decomposition upon addition of a large excess of the metal triflate. However, synthesis in bulk allowed for the isolation of the Li^+ and Na^+ peroxo bound adducts, revealing strong similarities to those of complex **XVII**, though no significant influence on the Cu–O–O–Cu torsion angle ϕ and other metric parameters of the Cu_2O_2 core was observed in the present case.

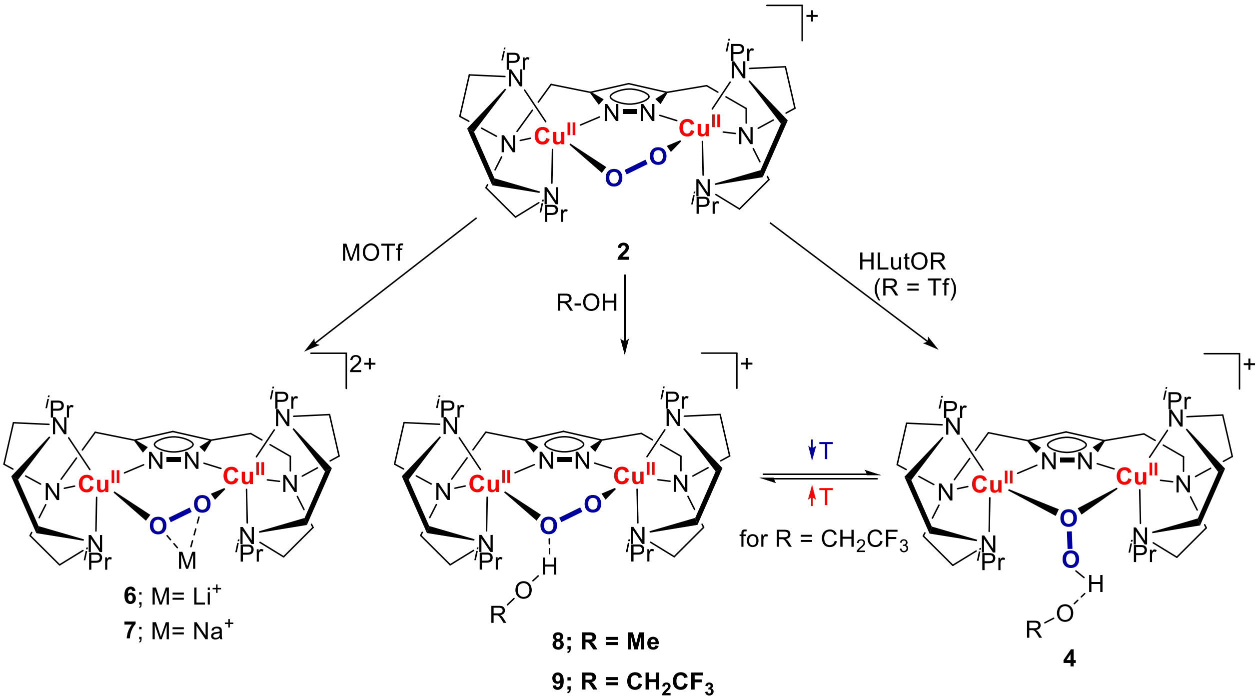

Scheme 32. Adduct formation and protonation of peroxo complex **2** with alkali metal ions and alcohols, respectively lutidinium triflate and the proposed temperature-dependent peroxo/hydroperoxo equilibrium.

Further, the formation of hitherto novel HBD peroxo adducts was observed, employing substrates that were prone to form hydrogen bonds (MeOH, TFE, Phenol), revealing strong interaction with the peroxo core in solution, which could be monitored by UV/Vis spectroscopy. The isolation of such adducts was also possible in the solid state for MeOH and TFE as HBD verifying the coordination to the peroxo moiety with only minor effects on structural properties (Table 15). Additional influence on the electronic properties of the peroxo adducts was also investigated by RAMAN spectrocopy as well as magnetic measurements, revealing so far no significant alteration.

Table 15. Structural parameters of bound peroxodicopper(II) adducts obtained from X-ray diffraction.

	2	**7 [2+Na$^+$]**	**8 [2·MeOH]**	**9 [2·TFE]**
Cu1···Cu2 (Å)	3.696	3.774	3.725	3.757
Cu1–O1 / Cu2–O1	1.884 / 1.897	1.878 / 1.911	1.907 / 1.915	1.894 / 1.901
O1–O2 (Å)	1.452	1.479	1.443	1.486
Cu–O–O–Cu (°)	86	82	87	86

Remarkably, formation of those adducts in solution revealed a temperature-driven equilibrium between the μ-1,2-peroxo and μ-1,1-hydroperoxo binding motifs, which has been not observed for copper/oxygen complexes so far. Those snapshots of peroxo to hydroperoxo conversion demonstrate the necessity of ligand design and consideration of solvent effects as well as potential adduct formation when it comes to fully elucidate copper active sites in nature. The investigation of further adducts and their influence on all copper/oxygen adducts might therefore be beneficial for a deeper understanding of copper metalloenzymes and should be investigated in the future.

5.6 A Novel μ-Nitroso Dicopper(II) Complex

The previous chapters have focused on a large variety of copper oxygen complexes and their respective properties. However, besides dioxygen also nitric oxide plays an important role in bioinorganic copper chemistry.[14] The influence of nitric oxide on physiological functions such as blood pressure, nerve impulses and the immune system has been explored in detail.[202–206] In the context of the biological relevance of NO, the mitochondrial cytochrome *c* oxidase (CcO) is often noted[207–210]; the heme-a$_3$/Cu$_B$ active centre of CcO is not only able to mediate the $4e^-$ reduction of oxygen to water in the respiratory chain, but also to interact with nitrite (NO_2^-) and nitric oxide to regulate cellular O_2 concentrations.[211,212] The reaction of NO with the superoxide radical forms the highly reactive peroxynitrite (PN),[213] which seems to be crucial in the context of ALZHEIMER'S disease and other pathological processes.[9,214]

However, the number of copper nitrosyl complexes is still very limited,[129–133] whereby the number of dinuclear complexes is even more scarce, despite the high biological relevance of copper/NO in nature. The first reported dicopper nitrosyl complex was isolated by KARLIN *et al.* based on the XYLO ligand scaffold described earlier (Section 5.4). The complex exhibited a μ-1,1-NO, which is better described as a nitroxyl since the bridging NO ligand is formally a negatively charged NO^- in **XXVII** (Figure 87).[131] Recently, KARLIN and coworkers reported the formation of the mixed-valent Cu^{I}Cu^{II} nitroso complex **XXVI** based on the UNO ligand that forms a peroxynitrite dicopper complex upon exposure to O_2, emphasizing the relevance of copper ions in the biological context.[132] Lately, ZHANG *et al.* were able to isolate the μ-oxo-μ-nitrosyl dicopper complex **XXVIII**, after reaction of NO or NO_2^- with the corresponding dicopper precursor, whereby the resulting complex exhibits versatile oxidative reactivity.[133]

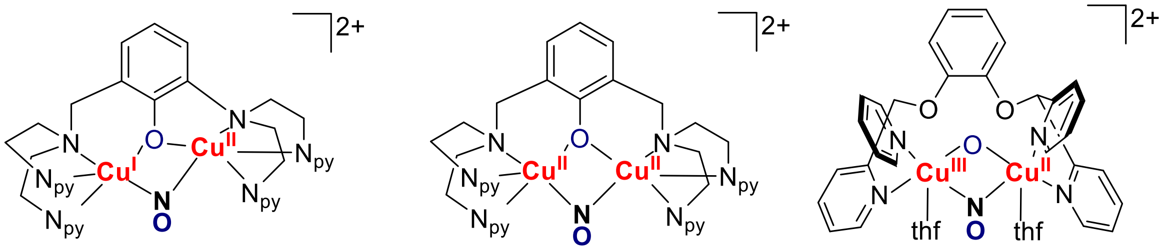

XXVI **XXVII** **XXVIII**

Figure 87. Dicopper μ-nitrosyl complexes.[131–133]

As demonstrated in this thesis and previously, pyrazolate/tacn ligand scaffolds are well suited for the isolation of copper/oxygen species (e. g. μ-1,2-peroxo, μ-1,2-superoxo, μ-1,1-hydroperoxo).[52,112,117,124] Due to the often stated reminiscence of the oxygen redox forms (O_2, O_2^-, O_2^{2-}) to those of nitric oxide (NO^+, $NO^\bullet$, NO^-),[215] the reactivity of the sterically encumbered dicopper(I) complex **XXIX** with the latter was initially investigated.

5.6.1 Formation in Solution

First experiments of Nicole Kindermann did not lead to the isolation of any dicuprous nitrosyl complexes after addition of nitric oxide to the dicopper(I) complex **XXIX**, even at temperatures down to −80°C. The employment of NO transfer reagents, such as trityl-S-nitrosothiol (Ph_3CSNO), was also tested but showed no reaction, which was attributed to the steric shielding of the dicopper core.

Thus, complex **XXIX** was investigated towards reaction with $NOBF_4$. The addition of $NOBF_4$ to a solution of the dicopper(I) complex in MeCN, EtCN or DCM led to a sudden color change from pale yellow to intense red (Scheme 33). Subsequent addition of $NaBPh_4$ and precipitation upon addition of Et_2O proved to be a crucial step in the reaction sequence since the newly formed complex **10** showed gradual decomposition at room temperature. However, the reaction yield for **10** was always relatively low (<10%), even when pre-cooled solvents were used, which was attributed to the fact that $NOBF_4$ is also a strong oxidant[167] which leads to simple oxidation of the dicopper(I) complex without coordination of NO to the dicopper core.

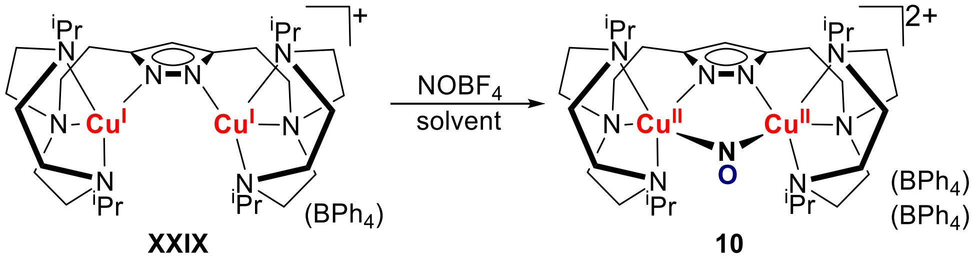

Scheme 33. Synthesis of μ-nitrosyldicopper(II) complex **10** upon addition of $NOBF_4$ to precursor **XXIX**.

ESI-MS analysis of the reddish precipitate in MeCN solution revealed the presence of one dominant peak at m/z = 335.7 which was assigned to the oxidized species $[L^2Cu^ICu^{II}]^{2+}$, likely due to the facile loss of NO from **10**. Besides this, only two other small peaks at m/z = 350.2 and 671.4 were observed which could be identified as $[LCu_2(\mu\text{-NO})]^{2+}$ and $[LCu_2]^+$ (Figure 88).

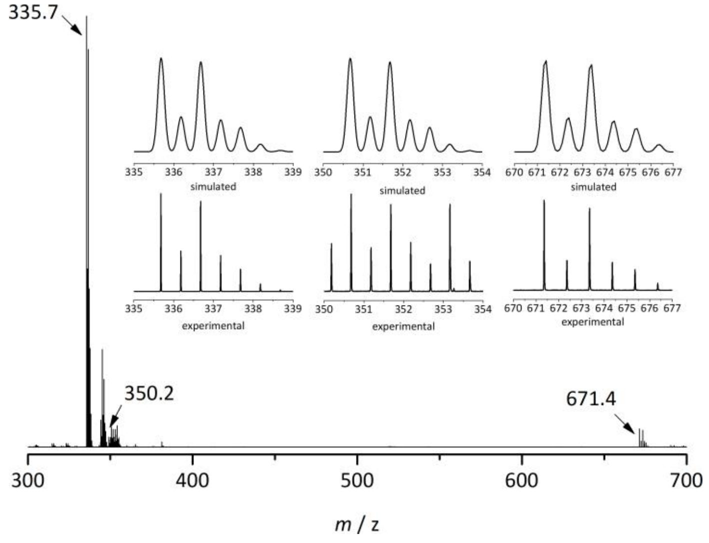

Figure 88. ESI-MS Spectrum of Complex **10** in MeCN. The inset shows the experimental and simulated peaks at m/z =335.7, 350.2 and 671.4 and the simulations of the isotopic patterns of $[L^2Cu_2]^{2+}$, $[L^2Cu_2(\mu\text{-NO})]^{2+}$, $[L^2Cu_2]^+$.

UV/Vis absorption spectroscopy of complex **10** (Figure 89) revealed a maximum close to 354 nm (ε = 10400 M^{-1} cm^{-1}) with a shoulder at around 394 nm (ε = 6500 M^{-1} cm^{-1}) and a less pronounced maximum at around 524 nm (ε = 5500 M^{-1} cm^{-1}); **10** therefore exhibits similar spectroscopic properties as the μ-nitrosyl dicopper(II) complex **XXVII** reported by KARLIN.[131]

Due to the observed decomposition of complex **10** in solution, its thermal decay was also monitored by UV/Vis spectroscopy, revealing a half-life time of $t_{1/2} \approx$ 12 h in MeCN at room temperature, being in the same order of magnitude as the corresponding peroxo complex, which exhibits a half-life time of around 10 h in EtCN.[112] The thermal decay led to a diminishing of the characteristic absorption bands of **10**, whereby spectral features of the corresponding hydroxo complex **XXXI** began to appear at 356 nm and 613 nm (Figure 89).

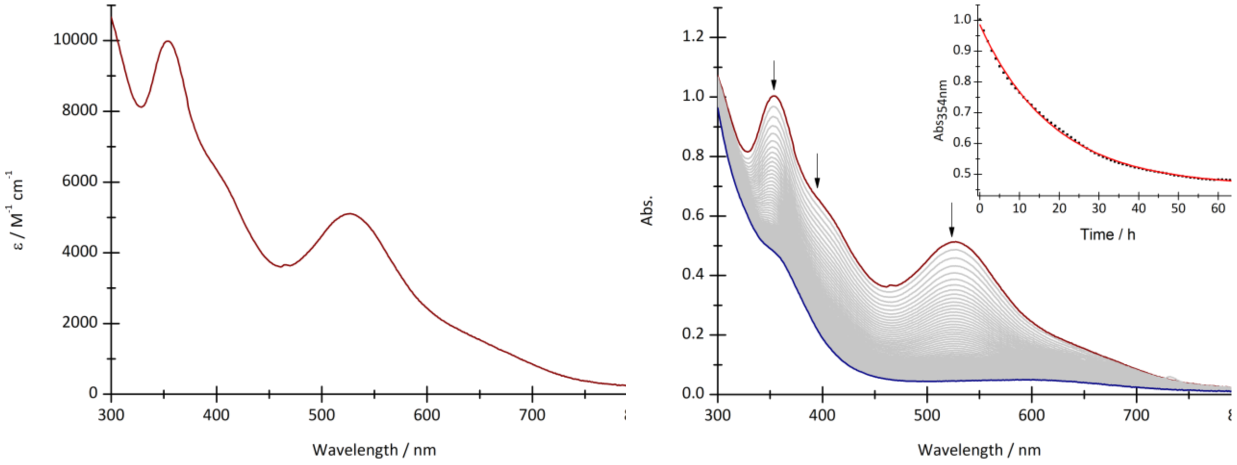

Figure 89. UV/Vis spectrum of complex **10** in acetonitrile at −40 °C (left) and its decomposition to the corresponding hydroxo complex **XXXI** at RT (right).

Previous experiments with the dicopper(I) complexes based on the ligand frameworks **L^1** and **L^{1,2}** revealed the potential formation of similar nitrosyl complexes by bulk synthesis. However, increased thermal decomposition at room temperature was observed, which might be attributed to the more exposed binding pocket. However, the isolation of further nitrosyl complexes based on this pyrazolate/tacn frameworks should be investigated in the future.

5.6.2 Solid State Properties

The isolation of solid material of complex **10** also allowed for UV/Vis measurements in the solid state that revealed the same spectroscopic features as in solution.

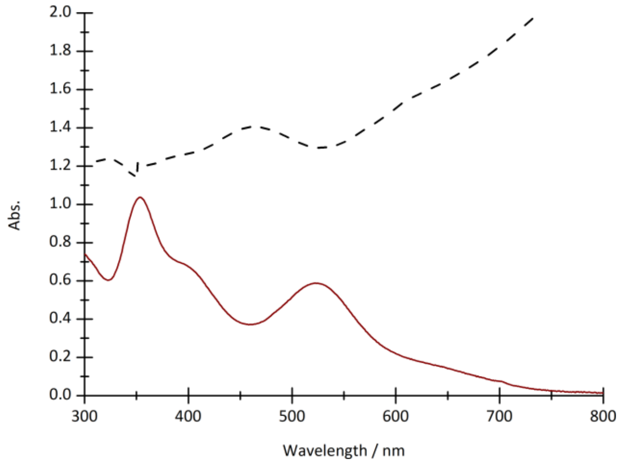

Figure 90. Comparison of UV/Vis absorption features in MeCN solution (solid line) and the reflectance of complex **10** in the solid state in a KBr matrix (dotted line).

As described vide supra the obtained yield of complex **10** is comparatively low, attributed to significant formation of byproducts. Therefore, the purification and crystallization of the crude product was particularly time consuming. Suitable material for X-ray diffraction was obtained by slow evaporation of Et_2O into a solution of complex **10** in MeCN at −30 °C for several weeks. However, even at low temperatures larger quantities of the corresponding hydroxo complex **XXXI** were formed. Recrystallization for several times diminished the yield to be under 5%. The molecular structure of single crystalline material of complex **10** is depicted in Figure 2.

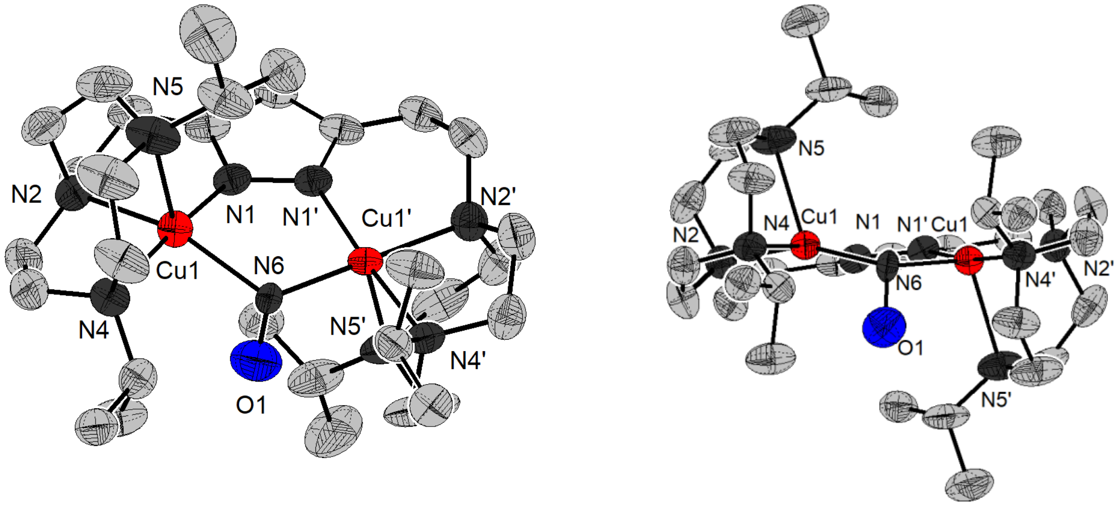

Figure 91. Molecular Structure of the cationic part of complex **10** (top and front view) with thermal displacement ellipsoids drawn at 50%. Hydrogen atoms and counter ions BPh_4^- are omitted. Selected bond lengths [Å] and angles [°] for **10**: Cu1···Cu1' 3.4525 (6) Cu1–N1 1.905(3), Cu1–N2 2.044(4), Cu1–N6 2.088(11), Cu1–N4 2.102(4), Cu1–N5 2.312(4), N6–O1 1.3297(107), Cu1–N6–Cu1' 116.530, Cu1–N6–O1 106.944(562). Symmetry operation used to generate equivalent atoms ('): 2-x, 1-y, z.

Both copper ions exhibit a moderately distorted square pyramidal coordination geometry (τ_5 = 0.215), whereby both ions are bound by the {N_4} binding side of the pyrazolate/tacn scaffold. The copper nitrogen bonds of the pyrazolate are significantly shorter (Cu1–N1 = 1.91 Å) than those of the tacn side arm (Cu1–N2,4,5 = 2.04-2.31), whereby the nitrogen atom of the tacn moiety in axial position reveals the longest Cu-N bond. The bridging μ-NO moiety causes a shortening of the Cu···Cu distance from 3.968 Å for the dicopper(I) complex **XXIX**[112] to 3.453 Å. The rather long nitrogen-oxygen bond length of 1.330 Å indicates a reduced nitroxyl (NO^-) bridging moiety when compared to the bond length of free nitric oxide (d(N–O) =1.15 Å).[215,216] In particular as it is longer than in the reported nitrosyl containing copper complexes from KARLIN[131,132] and ZHANG[133] that exhibited N-O bond lengths of 1.176 Å and 1.154 Å respectively. Significant bending of the NO moiety with respect to the plane defined by the pyrazolate and the metal ions is observed, which is reflected by the Cu1–N6–O1 bond angle of 106.9°. The molecular structure of **10** is strongly reminiscent to the structure of the respective hydroxo complex **XXXI**, which features the same square pyramidal coordination geometry of the copper ions and also by a shortened Cu···Cu distance of 3.405 Å in comparison to the dicopper(I) precursor **XXIX**.

The isolation of pure crystalline material also allowed to record meaningful ^{1}H-NMR spectra indicating the absence of unpaired electrons for the Cu(NO)Cu core and therefore diamagnetic character of complex **10** (Figure 92). Assignment of the signals was achieved by 2D-NMR experiments.

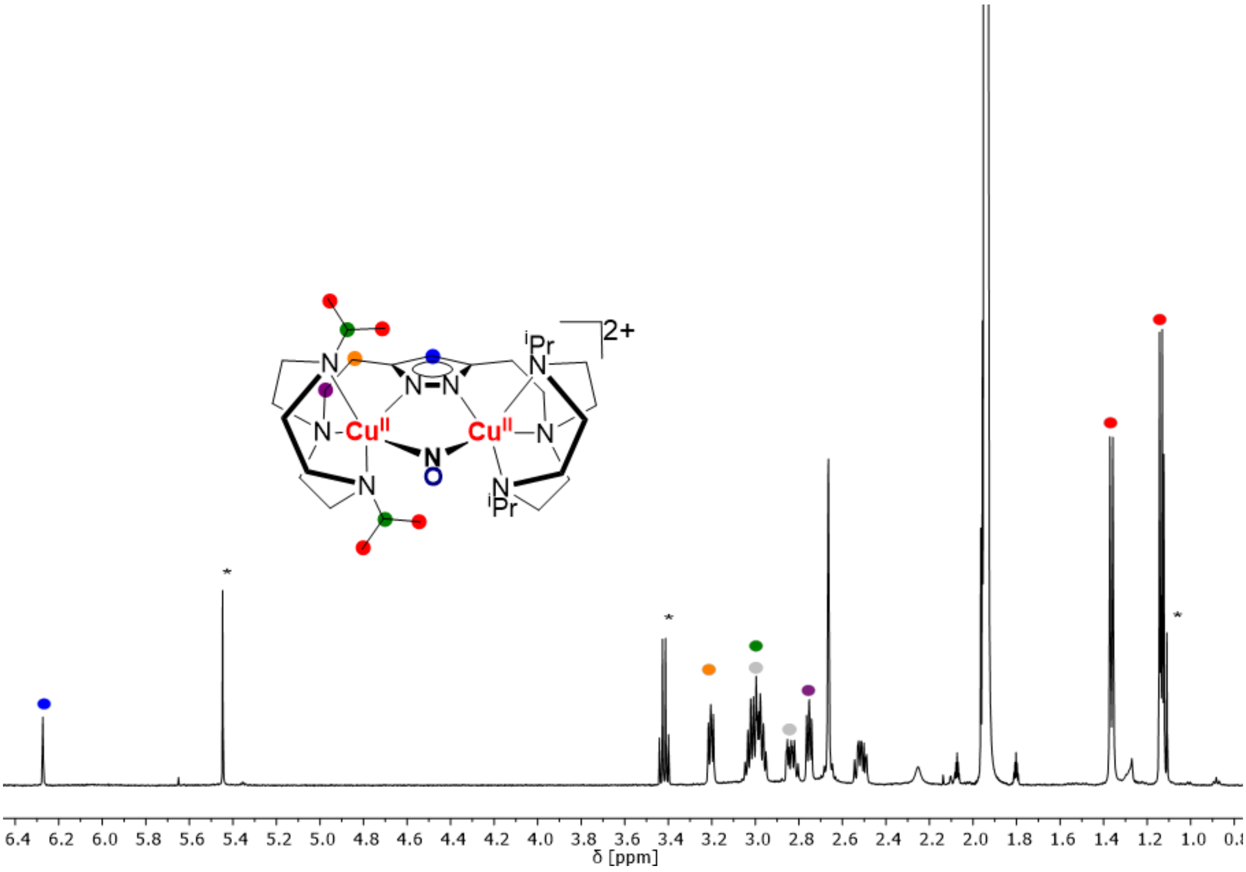

Figure 92. ^{1}H-NMR at 298 K in CD_3CN of complex **10** at 500 MHz. Solvent signals are marked with an asterisk (*).

The isolation of ^{15}NO labeled complex **10** enabled determination of the ^{15}N-NMR chemical shift of the NO moiety to be at around 228 ppm vs. MeNO$_2$. Other reported nitrosyl complexes reveal resonances in the range between 350 and 900 ppm for bend nitrosyl complexes, respectively 50-200 ppm for linear nitrosyl complexes.[217–219] However, since there are no reported ^{15}N–O resonances for dicopper μ-NO complexes until now a direct comparison is hard. However, the signal is in close proximity to the resonance of a bridging nitroxyl ligand of a reported dinitrosyliron complex ($\delta(^{15}NO) \approx 200$ ppm) and therefore corroborates the presence of the **NO⁻** ligand in **10**.[216]

The nitric oxide molecule exhibits a distinctive stretching vibration at a frequency of around 1860 cm^{-1}, which usually shifts upon binding to a metal center according to the extent of reduction.[219] Therefore, IR spectroscopy was conducted with ^{15}NO and ^{14}NO labeled samples of complex **10** (Figure 93). While the spectra revealed several peaks in the characteristic region for metal nitrosyl complexes between 1300 cm^{-1} and 1900 cm^{-1}, no isotope-sensitive peak could be unambiguously assigned.

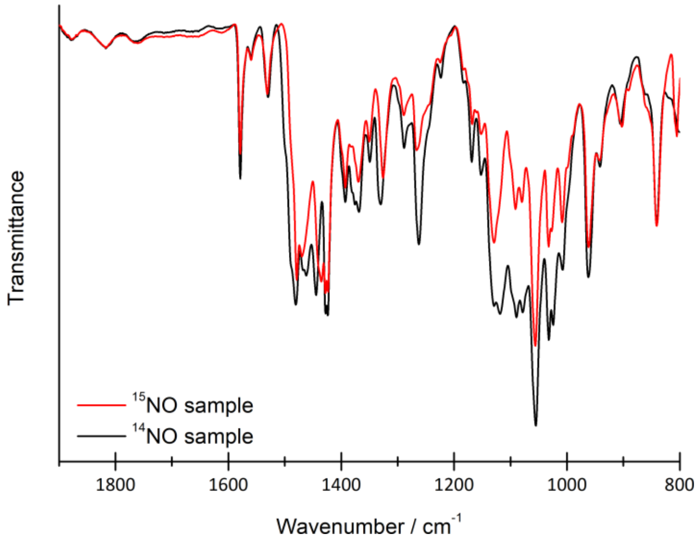

Figure 93. IR spectra of solid material of complex ^{14}NO-**10** (black line) and the corresponding ^{15}NO derivative (red line) in a KBR matrix.

In contrast, the reported nitrosyl complexes of KARLIN and ZHANG revealed assignable vibration bands at around 1550 cm^{-1}, complex **10** showed significant overlay of various other bands in this region. DFT calculations (Section 5.6.5) also predicted the presence of a distinctive NO stretching vibration band at 1530 cm^{-1} for complex **10**. However, measuring highly purified material of the nitrosyl dicopper(II) complex **10** either by attenuated total reflection (ATR) or in a KBr matrix or in solution did not lead to any improvement. Also, resonance RAMAN spectroscopy of isotope labeled samples in frozen acetonitrile solution revealed no clearly assignable isotope-sensitive vibration.

5.6.3 Transformation Reactions

Complex **10** revealed no reaction with molecular dioxygen and could even be stored under aerobic conditions. However, when the nitrosyl complex was treated with a solution of KO_2 and Kryptofix®222 (crypt) in MeCN at −40 °C the characteristic UV/Vis absorption features at 354 nm, 394 nm and 524 nm disappeared, which is accompanied by the simultaneous rise of spectral features of the corresponding peroxodicopper(II) complex at 506 nm and 600 nm with a clean isosbestic point at 470 nm (Figure 94). Multiple titration experiments resulted in an ambiguous stoichiometry of complex to potassium superoxide of 1.0-1.5, which was attributed to insolubility issues of the KO_2, even though a cryptand was used.

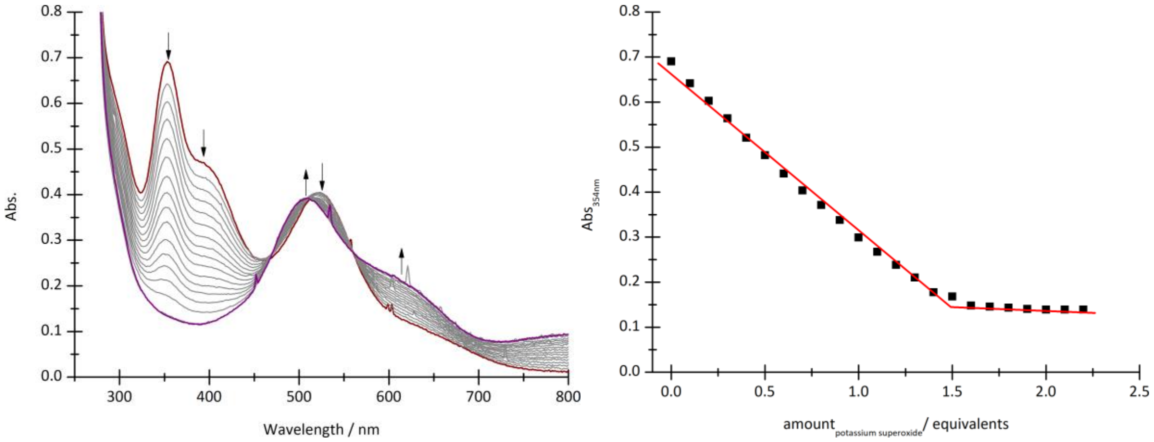

Figure 94. UV/vis Titration of complex **10** with KO_2/Kryptofix® in MeCN at –40 °C (left) and a plot of equivalents of potassium superoxide versus the absorbance at 354 nm.

Further, UV/Vis stopped-flow analysis of the reaction of complex **10** with KO_2 at −40 °C in MeCN was performed, revealing fast conversion of complex **10** into the peroxo complex **XVIII** within 0.3 seconds (Figure 95). It should be noted that the conversion proceeds so fast that the initial absorption features of the nitrosyl complex were unobservable in the spectra. Interestingly, the reaction of complex **10** to the corresponding peroxo complex takes place via an unidentified intermediate with a relatively intense absorption at 636 nm (ε = 16000 M^{-1} cm^{-1}).

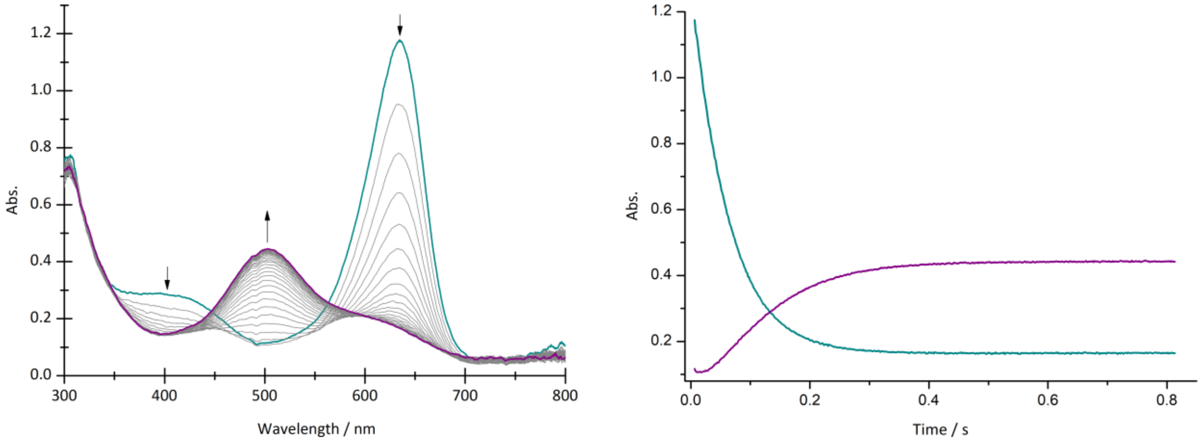

Figure 95. UV/vis spectra of complex **10** and an excess of KO_2/Kryptofix® in MeCN at –40 °C recorded via stopped-flow analysis with a time interval between each spectrum is 16 ms (left). Change of Absorbance at 636 nm (teal line) and 506 (purple line) nm over time (right).

Progression of the traces at 636 nm and 506 nm in Figure 95 reveals full conversion after approximately 0.3 s. Remarkably, slight delay of the formation of the peroxo complex is observed by the respective trace at 506 nm, indicating the involvement of a further species, which might be the dicopper(I) complex. Since potassium superoxide can act as a reductant,[167] the following reaction sequence was assumed (Scheme 34). Reaction of complex **10** with potassium superoxide leads to the formation of O_2 and a putative reduced complex, which exhibits an intense and characteristic absorption feature at 636 nm. The reduced species is assumed to readily release nitric oxide to form the dicopper (I) complex. Binding of dioxygen then leads to the formation of the peroxodicoppper(II) complex.

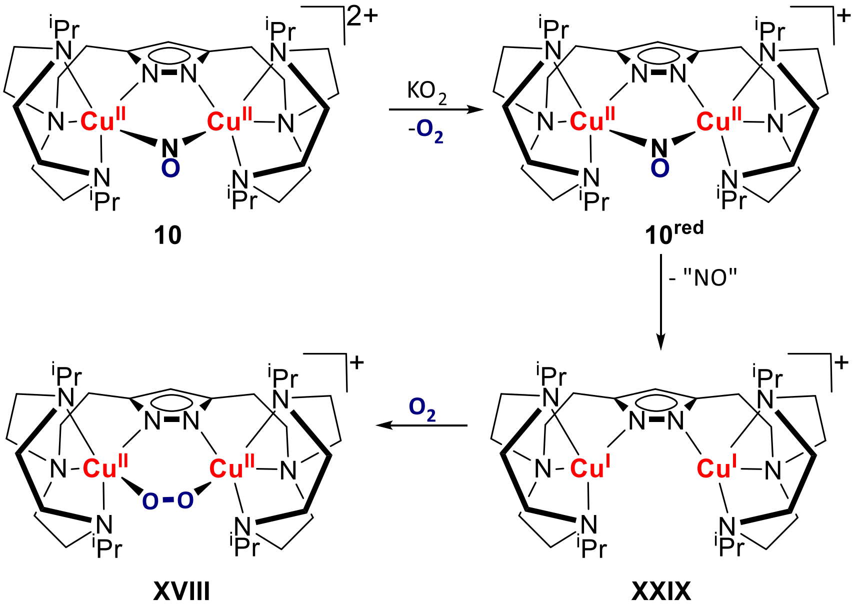

Scheme 34. Putative reaction sequence after addition of potassium superoxide to complex **10** at −40 °C in acetonitrile. Counter ions are omitted.

To further investigate this assumption, UV/Vis titration experiments of nitrosyl complex **10** with cobaltocene at −40 °C in acetonitrile were conducted, whereby the characteristic absorption bands at 354 nm, 394 nm and 525 nm gradually decreased upon substoichiometric addition of $CoCp_2$. After addition of 1.0 equivalents of Cobaltocene no further change of the absorption at 525 nm was observed. Interestingly only a diminished absorption feature at 636 nm was reobserved, which decayed further within minutes, leading to a final spectrum which is reminiscent of the dicopper(I) complex (Figure 96).

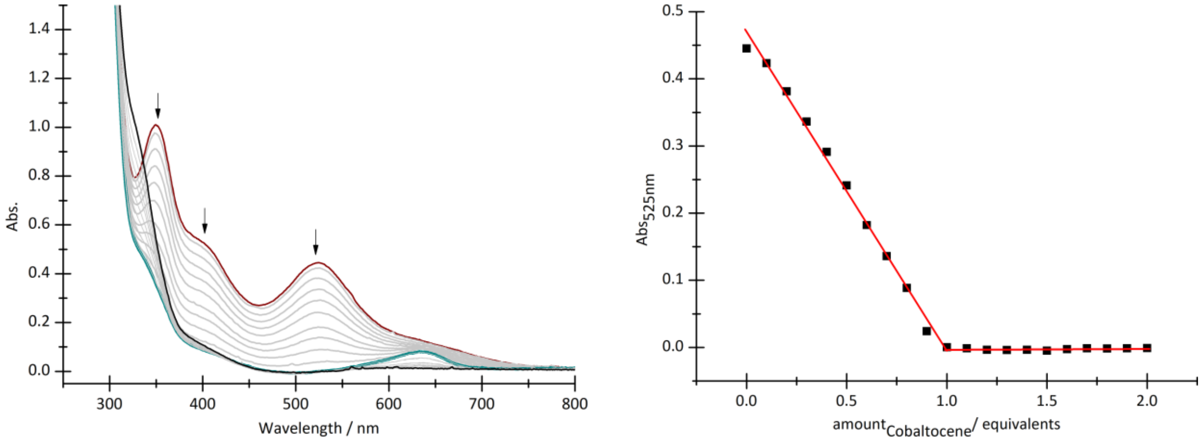

Figure 96. UV/vis Titration of complex **10** with cobaltocene in MeCN at –40 °C. Right: Plot of equivalents of cobaltocene vs. absorbance at 525 nm. Teal colored line represents the spectrum after addition of 1.0 eq. $CoCp_2$, the feature at 636 nm also diminished without further addition of $CoCp_2$ over time.

After addition of molecular oxygen to the solution, the spectroscopical features of the corresponding peroxo complex were obtained, supporting the presence of the dicopper(I) complex. Further UV/Vis titration experiments at −80 °C in propionitrile revealed an increase of the band at 636 nm and a less intense one at 403 nm (Figure 97). Hereby, reduction of complex **10** was complete after addition of one equivalent cobaltocene and the newly formed species **10**^{red} possessed reduced thermal stability even at −100 °C ($t_{1/2}$(−80 °C, EtCN) ≈ 20min). Interestingly, as stated before, the thermodynamic decay of reduced complex **10** leads to a species with no significant absorption features, which is expected for dinuclear Cu^I complexes.

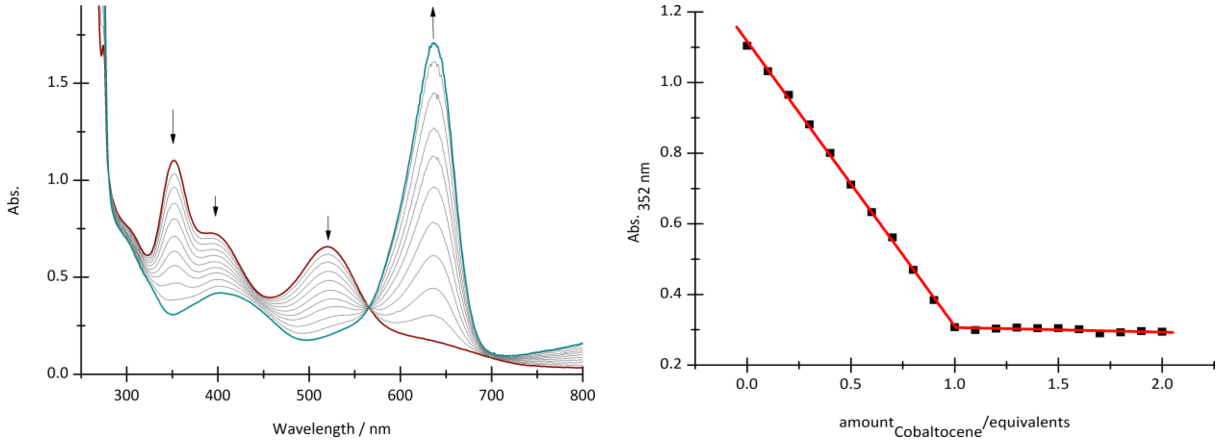

Figure 97. UV/vis Titration of complex **10** with cobaltocene in EtCN at –90 °C. Isosbestic point at 566 nm indicates a clean conversion (left). Plot of equivalents cobaltocene vs. absorbance at 352 nm (right).

Further, it was observed that upon addition of molecular oxygen complex **10**$^{\mathbf{red}}$, prior to decomposition, led to the regain of the spectroscopical features of complex **10** (Figure 98), indicating the simple re-oxidation. The entire process of reduction with cobaltocene and oxidation with molecular oxygen is reversible and can be repeated several times whereby a loss in intensity is observed, attributed to the rapid decomposition of the reduced intermediate.

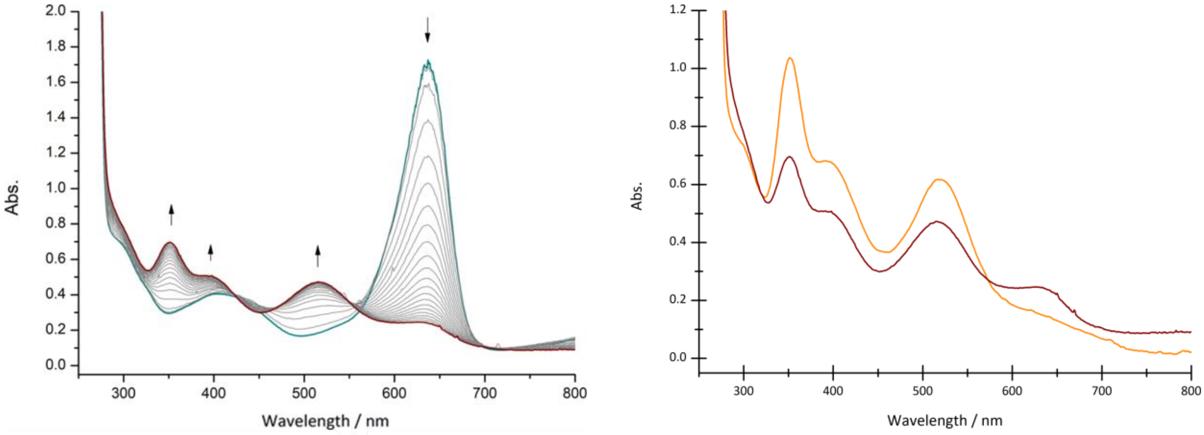

Figure 98. Addition of oxygen to **10**$^{\text{red}}$ in EtCN at −90 °C. Spectra are recorded in a 6 s time interval. Right: Comparison of complex **10** before (orange line) titration with Cobaltocene and after addition and re-oxidation with molecular oxygen (brown line).

5.6.4 Low-Temperature CV Measurements

The electrochemical properties of nitrosyl dicopper(II) complex **10** were investigated by low temperature cyclic voltammetry (CV) measurements in collaboration with NICOLAS LEPOUL from the Université de Bretagne Occidentale in Brest. Therefore, complex **10** was measured at −65 °C in NBu_4PF_6/EtCN solution (Pt WE) within the range of −1.75 V and +0.75 V and revealed a quasi-reversible 1 e^- reduction at −0.97 V vs. Fc/ Fc^+, as well as a second irreversible reduction around -1.32 V. Additionally, irreversible oxidation occurs at −0.25 V and +0.7 V (Figure 99).

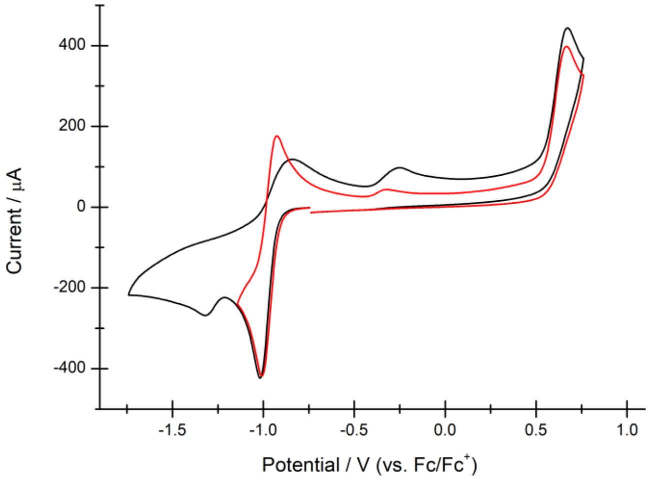

Figure 99. CV of **10** in EtCN/NBu_4PF_6 0.1 M (Pt WE) at −65°C at 20 mV/s. Black Curve: −1.75 V < E < 0.75 V. Red Curve: − 1.14 V < E < 0.75 V.

However, adjustment of the redox window led to simplification of the cyclic voltammogram where the quasi-reversible redox process at −0.97 becomes fully reversible (Figure 100) and the irreversible oxidation around −0.25 V becomes less dominant. Therefore, it was assumed that the second irreversible reduction is attributed to a chemical decomposition reaction, namely the loss of the NO bridging ligand. Hereby, the irreversible oxidation around −0.25 V might originate from the dicopper(I) complex.

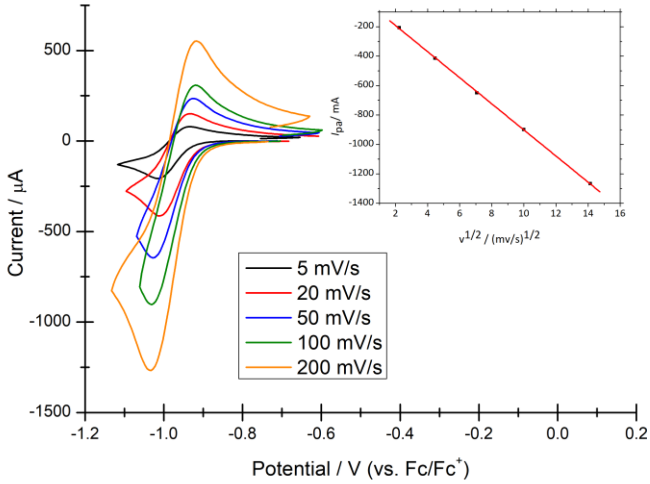

Figure 100. CV of **10** in EtCN/NBu_4PF_6 0.1 M (Pt WE) at −65°C at various scan rates. The inset shows the peak current vs. $v^{1/2}$.

Time-resolved cryo-UV/Vis spectro electrochemistry experiments also revealed the decrease of the characteristic absorption features of complex **10** and the simultaneous increase of a significant absorption feature at 636 nm (Figure 101) attributed to $\mathbf{10}^{\mathbf{red}}$. An isosbestic point at 566 nm indicated clean conversion.

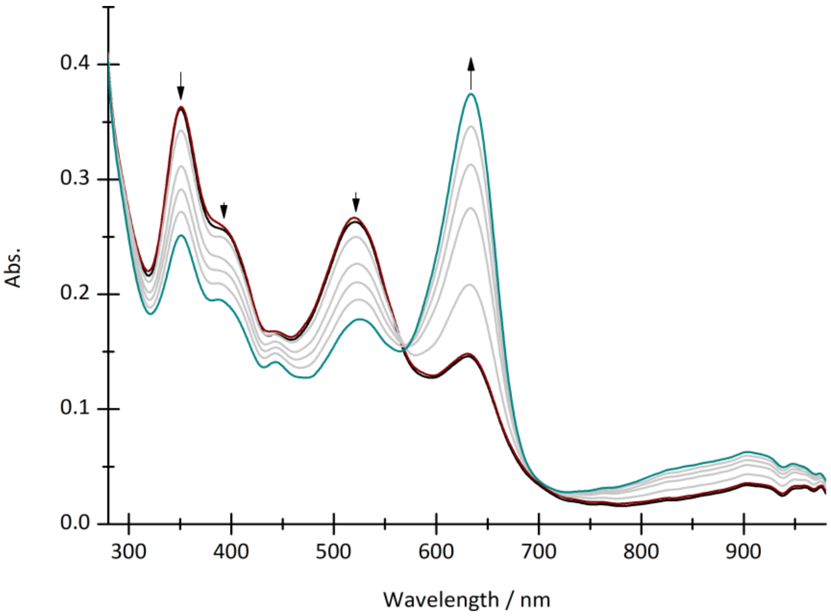

Figure 101. Spectro-electrochemistry of **10** in EtCN/NBu_4PF_6 0.1 M (Pt WE) at −65°C upon electrochemical reduction via controlled potential electrolysis at −1.1 V.

Complex $\mathbf{10}^{\mathbf{red}}$ could be synthesized chemically and electrochemically by reduction of complex **10** and revealed fast decomposition even at −80 °C in solution to the dicopper(I) complex **XXIX** under presumed release of nitric oxide. However, the fast decay of $\mathbf{10}^{\mathbf{red}}$ makes the investigation of its electronic structure (e.g., $Cu^{I}Cu^{I}(NO^{\bullet})$, $Cu^{I}Cu^{II}(NO^{-})$ or $Cu^{II}Cu^{II}(NO^{2-})$) hard and is still ongoing.

5.6.5 DFT calculations

The elusive results of the previous described experiments let to the initiative to conduct DFT calculations (ORCA[155] software, BP86 functional, def2-tzvp basis set[156,157], RI approximation using auxiliary def2/J basis set[220]). Based on the solid-state structure of complex **10**, geometry optimization was performed. TD-DFT calculations of electronic transitions of the reduced nitroxyl complex **10^{red}** could not reproduce the experimentally observed absorption band at 636 nm. Further, according to the calculations, the electron density of the SOMO is mostly located on the nitroxyl unit (Figure 102). The LÖWDIN spin population analysis in Figure 103 indicates that the unpaired spin density is mostly located on the nitrogen (62%), hinting towards a NO-based reduction of complex **10**.

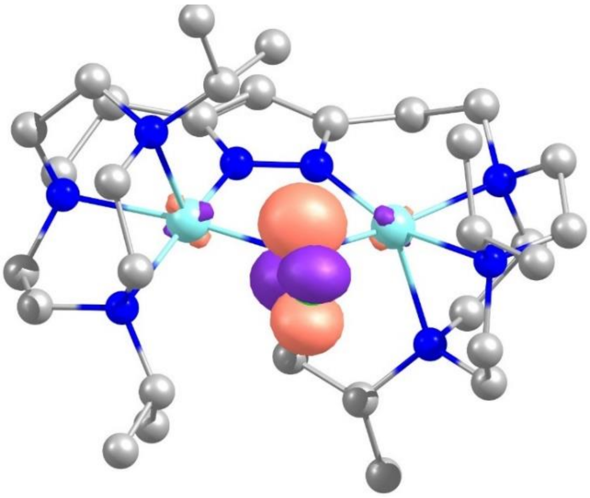

Figure 102. SOMO of **10^{red}** (S = 1/2). Composition (according to LÖWDIN reduced orbital populations per MO): 17% Cu, 72% NO. (isosurface value: 0.08). Copper in teal, oxygen in green, nitrogen in blue, carbon in grey, hydrogen atoms are omitted for clarity.

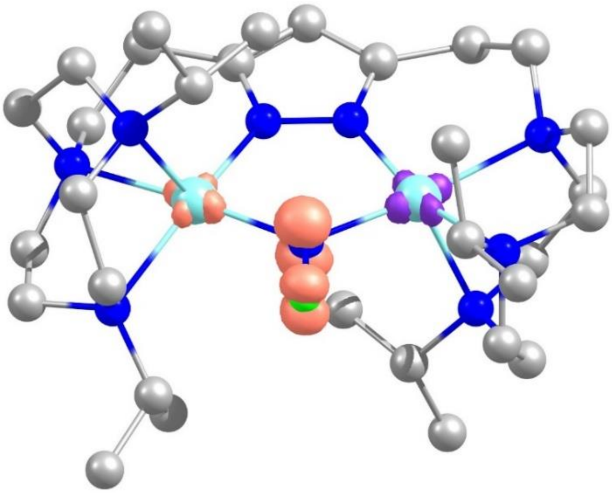

Figure 103. Spin density plot of complex **10^{red}** (S = 1/2). Löwwdin spin population: Cu1 = 0.23, Cu2 = -0.24, N = 0.62, O = 0.38. (isosurface value: 0.04). Copper in teal, oxygen in green, nitrogen in blue, carbon in grey, hydrogen atoms are omitted for clarity.

To further elucidate complex **10^{red}** preliminary EPR experiments were conducted but proved to be rather difficult due to the low temperature preparation setup and rapid decay at temperatures even at −80 °C. Hence, collaborations with NICOLAS LEPOUL from the Univsersite de Occidentale in Brest are still ongoing, to couple low-temperature electrolysis measurements with EPR spectroscopy.

5.6.6 Summary and Conclusion

In this section the synthesis and characterization of a new dicopper(II) nitrosyl complex was presented, extending the scarce examples of such compounds. X-ray diffraction as well as ^{15}N- NMR spectroscopy indicated that the coordinating nitrosyl bridge can be formally regarded as a nitroxyl (NO^-).

Furthermore, electrochemical and chemical reduction of complex **10** at low temperatures led to the formation of a thermal instable intermediate **10^{red}**, which shows rapid decomposition to the corresponding dinuclear copper(I) complex, likely via release of $NO^{\bullet}$. In addition, reaction with potassium superoxide led to the reduction of the nitrosyl complex and conversion to the peroxodicopper(II) complex. Those transformations are particularly important in the context of copper/NO chemistry and should therefore be further elucidated and extended by a variety of substrates. The potential isolation of nitrosyl dicopper(II) complexes with the series of pyrazolate/tacn ligand frameworks (**L^1** and **$L^{1,2}$**) should also be investigated.

6 Summary and Outlook

Dinuclear active centers in which the copper ions are in close proximity to each other are capable of cooperatively activating small molecules such as O_2, e.g., to transport dioxygen or to oxygenate organic substrates. The functionality of cooperativity at multimetallic active sites has inspired bioinorganic chemists in recent years to employ rational ligand design for small molecule activation, aiming at potential bioinspired catalysts.

The previously reported compartmental pyrazolate/tacn ligand scaffolds **L^1** and **L^2** exhibited very versatile copper-oxygen chemistry. Remarkably, even though structural changes of the ligand were comparatively small, electronic properties and reactivities of the resulting copper/oxygen species differed drastically. In order to determine the influence of rational ligand variation on those properties this work utilized the non-symmetric compartmental pyrazolate/TACN ligand scaffold **L^{1,2}** for the isolation of new copper/oxygen adducts.

Based on previous work on pyrazolate/tacn ligands in the MEYER group, the routes for the synthesis of **L^2** and **L^{1,2}** were improved. As a result, the clean isolation of the ligand system **L^{1,2}** allowed the preparation of the corresponding dinuclear Cu^I complex **1**. By optimized crystallization methods, this could be clearly characterized by NMR spectroscopy and X-ray diffraction. The solid-state structure of the Cu^I precursor revealed the combination of structural properties of its two symmetric congeners, thus emphasizing the strength of rational ligand design.

Since the dicppper(I) complex **1** could be obtained in excellent purity for the isolation of reactive copper/oxygen intermediates, the activation of molecular oxygen in solution was investigated by UV/Vis and resonance RAMAN spectroscopy. The formed complex **2** showed almost identical spectroscopic properties to the previous peroxodicopper(II) complexes, indicating the successful synthesis of the same structural motif. Crystalline material of the non-symmetric peroxo complex **2** was obtained and analyzed by X-ray diffraction, which revealed a unique Cu−O−O−Cu torsion angle ϕ of nearly 90°, providing a synthetic model of the initial steps of O_2 activation at type III copper centers suggested by computational studies. Magnetic measurements by SQUID magnetometry revealed a ferromagnetic coupling of the two Cu^{II} ions and thus a triplet (S = 1) ground state. Interestingly, the ferromagnetic coupling turned out to be weaker than expected for the 90° situation and weaker than in the related complex **XVIII** (ϕ = 104°), which is currently still under investigation.

Further, the formation of a hydroperoxo complex **4** was investigated by UV/Vis and resonance RAMAN spectroscopy in solution. The addition of a suitable acid led to a strong change in the electronic absorption bands and an O–O vibration typical for hydroperoxo complexes. Using UV/Vis titration experiments, the reversibility of the protonation as well as the pK_a value of the Cu_2OOH species could be determined. **4** showed a similar acidity as its symmetric congeners. The great stability of the protonated species **4** allowed to obtain crystalline material, revealing a μ-1,1 hydroperoxide binding motif.

In addition, the peroxo species was studied with respect to its chemical and electrochemical oxidation to the superoxo complex **5**. EPR and RAMAN measurements indicated a μ-1,2-superoxo binding mode. Based on the determination of the thermodynamic parameters E^0 and the pK_a value, the BDFE of the OOH bond could be derived (69.5 kcal mol^{-1}). The superoxo complex **5** was evaluated towards its ability to perform HAA reactions with substrates. Reactivity studies with TEMPO–H revealed a reaction rate in between those of the symmetric congeners and impressively demonstrated the steric influence on the kinetics for three systems with essentially identical BDFE. The interconvertible copper/oxygen complexes of the non-symmetric ligand scaffold $\mathbf{L}^{1,2}$ are presented in Scheme 35.

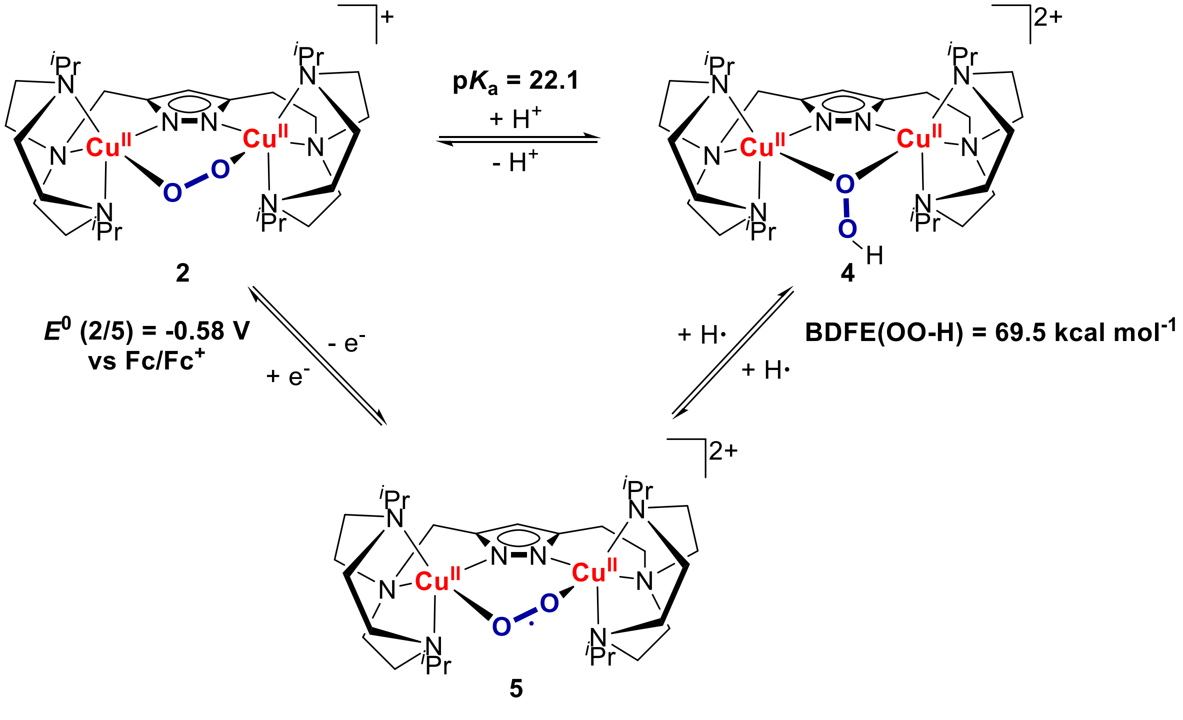

Scheme 35. Interconvertible copper/oxygen complexes **2**, **4** and **5** presented in this work.

Further, the accessibility of the $\{Cu_2O_2\}$ core allowed for interactions with alkali metal ions, which could be studied spectroscopically. Due to the combination of structural properties of the ligand systems $\mathbf{L}^1$ and $\mathbf{L}^2$, the peroxo complex **2** showed interaction properties between those of its congeners. In addition, the non-symmetric peroxodicopper(II) complex revealed significant interactions with protic substrates to an extent, which has not yet been observed (Scheme 36). Thus, adducts of peroxo complex **2** with MeOH, TFE and phenol were studied by UV/Vis spectroscopy. The formed hydrogen bound substrate complexes revealed strong interactions to a point where those could be studied in the solid state. For the MeOH and TFE bound adduct crystalline material was obtained, which could be investigated by X-ray diffraction. In addition, initial UV/Vis spectroscopic studies with TFE and phenol indicated a unique temperature-controlled equilibrium between the μ-1,2-peroxo and the μ-1,1-hydroperoxo species, emphasizing the influence of hydrogen bonding on copper/oxygen complexes and in metalloenzymes.

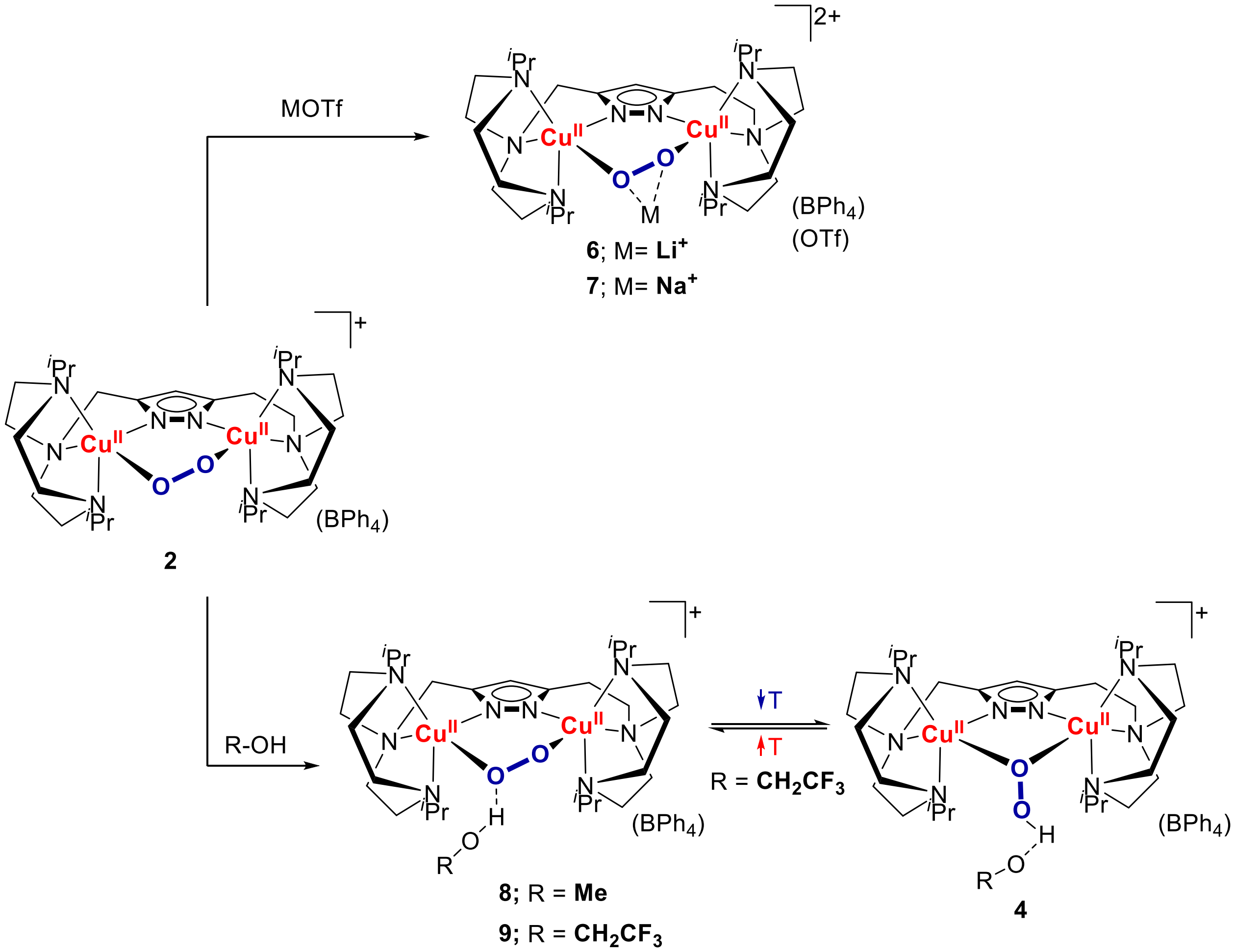

Scheme 36. Alkali metal ion and hydrogen bond donor substrate adducts of peroxodicopper(II) complex **2**.

In addition, the dinuclear copper(I) complex **XXIX**, which exhibited high stability of its copper oxygen intermediates, due to the sterically shielding ligand framework **L**^{2}, was investigated towards the isolation of a dicopper/NO complex. Thus, by adding $NOBF_4$ to complex **XXIX**, a μ-nitroxyl complex could be isolated, which was investigated by NMR and UV/Vis spectroscopy, as well as X-ray diffraction. Furthermore, conversion with KO_2 led to the formation of the corresponding peroxo complex **XVIII**, emphasizing the interplay of NO and O_2 in copper metalloenzymes. Spectroelectrochemical investigations revealed a reversible reduction accompanied with a drastic change of the respective electronic absorption features. The structure of the formed highly unstable intermediate **10**^{red}, which decomposes to the copper(I) complex even at −80°C within minutes, is still a topic of ongoing debate and could not be elucidated in detail so far.

This thesis has demonstrated the variety of copper oxygen complexes, stabilized by compartmental pyrazolate/tacn ligand frameworks. The non-symmetric ligand scaffold $\mathbf{L^{1,2}}$ was employed to isolate several Cu_2/O_2 adducts (e.g., peroxo, superoxo, hydroperoxo complexes) that were investigated in detail by various spectroscopic methods. These complements the series of pyrazolate/tacn copper oxygen complexes with peripheral sterically protecting *iso*-propyl substituents and reveal the effect of ligand design on structural, electronic and reactivity properties. Detailed computational studies have to be conducted to fully elucidate the magnetic and electronic properties of the peroxo complex **2** which favors a Cu−O−O−Cu torsion angle but rather small extent of ferromagnetic coupling.

Furthermore, the unusual temperature-driven equilibrium of the peroxo bound substrate adducts has to be investigated in detail, to elucidate the assumed peroxo/hydroperoxo transformation. In addition, the non-symmetry of the ligand scaffold might also be beneficial to stabilize mixed valent $Cu^{I}Cu^{II}$ species in a sufficient way, which should be definitely researched.

Additionally, to elucidate the structure of the highly unstable intermediate $\mathbf{10^{red}}$ of the reduction of nitroxyl complex **10**, coupled LT-EPR measurements seem to be particular interesting and should be conducted in the future.

7 Experimental Section

7.1 General Information for Synthesis and Materials

The synthesis of water and oxygen sensitive substances was carried out under inert atmosphere (nitrogen or argon) using standard SCHLENK techniques or in a glovebox from MBRAUN. Solvents were either dried by storage over molecular sieves according to literature[221] or dried and distilled under Ar atmosphere from the appropriate drying agents (CaH_2 for MeCN, EtCN, sodium/benzophenone for Et_2O, Mg for MeOH, B_2O_3 for acetone). No significant difference in the amount of residual water was observed for the different drying procedures, as confirmed by KARL-FISCHER Titration. For organic synthesis, the dried solvents were degassed by bubbling with argon. For any other experiment (complex synthesis in the GloveBox or analytics), freeze-pump-thaw degassed solvents were used. If applicable, solvents were stored over molecular sieves (3 Å for MeCN, EtCN, MeOH, TFE and Et_2O) that were activated at 450 °C for 3 hours before use. If not stated otherwise, used chemicals were purchased from suppliers (ABCR, ACROS, SIGMA ALDRICH, VWR) without further purification. Oxygenation of complexes was done by using dioxygen gas which was dried over a P_2O_5 column.

The copper(I) salt $[Cu(MeCN)_4]ClO_4$ for complexation was synthesized according to literature.[222] The acid lutidinium triflate,[223] oxidizing agents $[Fc]BF_4$, $[Fc]SbF_6$, $[Fc]PF_6$, $AgBF_4$, $AgPF_6$ as well as the building block 3,5-bis(hydroxyethyl)pyrazole were provided by the MEYER group. The substrate TEMPO-H was synthesized according to literature and purified by extraction with benzene and subsequent lyophilization.[224] The reagent $NOBF_4$ as well as the isotope labeled $^{15}NOBF_4$ derivative were synthesized according to literature.[225]

7.2 UV/Vis Spectroscopy

UV/Vis measurements were carried out in quartz cuvettes (d = 1cm) which were dried overnight at 60 °C. The spectra were recorded by using an AGILENT Technologies Cary 60 UV/Vis Spectrometer with a cryostat from UNISOKU.

For experiments under exclusion of oxygen, the stock solutions of the respective complexes (c = 0.105 mM) were freshly prepared in the glovebox and used within 2-3 days, whereby the extinction coefficient provided indication of the amount of decay. The cuvettes used for this purpose were sealed in the glovebox with a screw cap with an integrated septum. Reactants were added to the complex solutions using syringes from HAMILTON. Those stock solutions of the reactants were also prepared freshly inside the glovebox.

Solid state UV/Vis spectra were recorded by using an AGILENT Cary 5000 UV/Vis-NIR with a PRAYING MANTIS™ high vacuum sample chamber. Preparation of air sensitive samples was done inside the glovebox with dry KBr as the matrix.

Stopped-flow UV-vis (kinetic) measurements were performed using a TgK Scientific Hi-Tech KinetAsyst™ CSF-61DX2 double mixing cryo-stopped-flow system in single-mixing mode. A xenon lamp was used as the light source and interfaced with a KinetaScan Rapid Scanning CCD (Charge Coupled Device) detector to provide UV-vis spectra in the range of approximately 300-850 nm. To ensure anerobic conditions, all mixing chambers were rinsed with dry, deoxygenated solvent. The sample of complex **2** was anerobically loaded into one of the reagent reservoirs and the KO_2/Kryptofix saturated solution was loaded into the other. The cryo unit allowed for precise temperature control (−40 °C) before mixing the solutions in the optical cell. Data acquisition and processing were performed using the Kinetic Studio software.

7.3 IR Spectroscopy

Infrared Spectra were recorded using a Cary 630 FTIR with a DialPath Diamond ATR spectrometer from AGILENT inside a glovebox from MBraun (argon atmosphere). Measured peaks were reported by ascribing their relative intensity according to: strong (s), medium (m), weak (w).

7.4 NMR Spectroscopy

^{1}H, $^{13}C\{1H\}$ and ^{15}N spectra were recorded on a BRUKER Avance 300 or 500 MHz spectrometer at 298 K if not stated otherwise. Chemical shifts (δ) are reported in parts per million referenced to the corresponding solvent residual proton or carbon signal. Coupling constants *J* are given in Hertz (Hz). Peaks are reported according to their multiplicity (singlet s, doublet d, triplet t, multiplet m).

7.5 RAMAN Spectroscopy

The investigation of substances using RAMAN spectroscopy were carried out by SEBASTIAN DECHERT, using a HORIBA Scientific LabRAM HR 800 spectrometer with an open-electrode CCD detector and a confocal pinhole with user controlled variable aperture, in combination with a free space optical microscope. Sample excitation was achieved by using a He:Ne-laser (λ_{exc} = 633 nm) or a diode-laser (λ_{exc} = 457 nm). When cooling was required, a transparent KryoVac KONTI-Cryostat-Mikro cell cooled with liquid N_2 was used for samples in solution. $^{16}O_2$ and $^{18}O_2$ labeled complex solutions were prepared inside a YOUNG NMR tube by direct addition of the gas. Measurements in the solid state were conducted under air, whereby the sample was mounted on a glass slid. Selected data have been treated with the software LabSpec 5.

7.6 Cyclic Voltammetry

Cyclic voltammetry experiments at room temperature were performed using a Gamry Interface 1010 E and analyzed using the Gamry Framework program. A three electron setup (WE: GC, RE: Ag wire, CE: PT wire) with a MeCN/ NBu_4PF_6 (0.1 M) solution was used. Ferrocene was used as the internal standard.

Low-temperature cyclic voltammetry measurements in collaboration with Nicolas LePoul from the Universite de Occidentale in Brest were performed in EtCN/NBu_4PF_6 (0.1 M) using a potentiostat Metrohm Autolab PGSTAT101 monitored by the NOVA 1.11 software and with a specific home-designed SCHLENK-type cell (WE: Pt, RE: Pt wire, CE: Pt wire). The cell was introduced at room temperature under nitrogen in a liquid nitrogen cryostat (LN2 Oxford Instruments). Temperature was adjusted with a temperature controller (ITC Mercury) connected to the cryostat, still under nitrogen. The exact formal potential values of the complex vs. Fc was determined by addition of ferrocene into the solution. The temperature inside the electrochemical cell was monitored by the ITC and checked by a supplementary thermocouple (Pt1000, VWR, resolution 0.1 K). Thin layer low-temperature UV-Vis-NIR spectroelectrochemistry was performed with a specific home-designed cell in a reflectance mode (WE: Pt, RE: Pt wire, CE: Pt wire). The UV-Vis and Vis-NIR optic fiber probes were purchased from Ocean Optics. Time- resolved UV-Vis detection was performed with QEPro and NIR-Quest spectrometers (Ocean optics, minimum response time 8 ms). Since all cryo-electrochemical and cryo- spectroelectrochemical experiments were carried out under dry atmosphere, we did not observe any problem of fogging or water condensation in the cell.

7.7 Magnetic Measurements

The magnetic measurements were conducted by SERHIY DEMESHKO. For temperature dependent susceptibility measurements, a QUANTUM DESIGN MPMS XL-5 SQUID magnetometer with a 5 T magnet was used. The sample, which was grinded if necessary, was filled in a gelatin capsule and placed in a non-magnetic sample holder. The recorded data were corrected for the magnetic contribution of the capsule.

The magnetic properties of the samples were simulated with the program JulX[226] by applying a fitting procedure to the spin Hamiltonian as stated in the main text or according to the following equation for isotropic exchange coupling and ZEEMAN splitting:

$$\hat{\mathrm{H}} = -2J\hat{S}_1\hat{S}_2 + g\mu_B\vec{B}\,(\vec{S}_1 + \vec{S}_2)$$

Temperature independent paramagnetism (TIP) and paramagnetic impurities (PI, S = 1/2) were included according to $\chi_{\mathrm{calc}} = (1 - \mathrm{PI}) \cdot \chi + \mathrm{PI} \cdot \chi_{\mathrm{mono}} + \mathrm{TIP}$.

7.8 Electron Paramagnetic Resonance Spectroscopy

X-Band EPR spectra were recorded with a BRUKER E500 ELESYS spectrometer, equipped with a standard cavity (ER4102ST, 9.5 GHz). The temperature was controlled by using an OXFORD helium flow cryostat (ESP810) and an OXFORD temperature controller (ITC-4) and was usually set to be around 140 K. Microwave frequency was measured with the built-in frequency counter and the magnetic field was calibrated using an NMR field probe (Bruker ER035M). Measurements at helium temperature were performed on a BRUKER ELESYS E500 T X-band spectrometer. The final spectra were simulated with the software package easyspin[227] or XSophe.

Special care was token for the preparation of superoxo complex **5**, which was generated upon exposure of complex **1** to dioxygen at −40 °C in MeCN at the SCHLENK line, generating the peroxo complex **2**. The sample was freeze-pump-thaw degassed for 5 times, transferred inside the Glovebox and reacted with $AgBF_4$ at approximately −20 °C. The brown solution was filtered through several layers of glass microfiber filter to remove the Ag particles.

7.9 Elemental Analysis

Elemental analyses were carried out by the "Analytic Laboratory of the Institute for Inorganic Chemistry at the University of Göttingen" using a Vario EL III (Co. ELEMENTAR). Oxygen sensitive species were sealed inside a glove box with <0.1 ppm O_2 and H_2O in an aluminum capsule.

7.10 Mass Spectrometry

ESI-MS measurements were performed on a Bruker HCT ultra instrument. Sample preparation was done inside a glovebox under argon atmosphere and directly injected into the instrument via a direct Peek™ tubing connection.

7.11 X-Ray Diffraction

X-ray diffraction experiments were performed by SEBASTIAN DECHERT on a STOE IPDS II diffractometer with an area detector (graphite monochromated Mo-Kα radiation, $\lambda = 0.71073$ Å) by use of ω scans at ca. 130 K. The structures were solved with SHELXT[228] or SHELXS and refined on F^2 with the software package SHELXL-2014 in using all reflections.[229] All non-hydrogen atoms were refined anisotropically. SAME, SADI and ISOR restraints and EADP constraints were applied. Face-indexed absorption corrections were performed numerically with the program X-RED.[230]

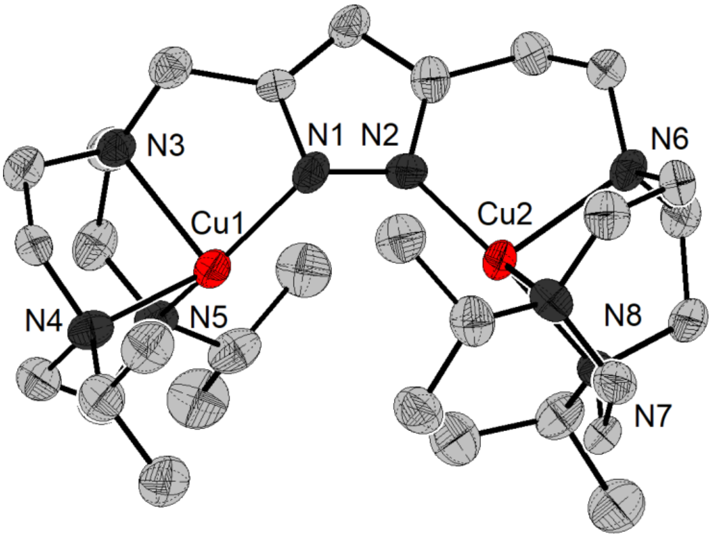

Figure 104. Molecular structure of the cationic part of complex **1**. Thermal displacement ellipsoids given at 50% probability. Hydrogen atoms, solvent molecules and counter ions are omitted for clarity. Selected bond lengths [Å] and angles [°] for **1**: Cu1–N1 1.933(8), Cu1–N4 2.055(9), Cu1–N3 2.233(7), Cu1–N5 2.306(8); N1–Cu1–N4 149.4(4), N1–Cu1–N3 85.2(3), N4–Cu1–N3 85.0(3), N1–Cu1–N5 120.9(3), N4–Cu1–N5 85.4(3), N3–Cu1–N5 79.0(3), C2–N1–Cu1 111.0(6), N2–N1–Cu1 135.5(6), C10–N3–Cu1 105.5(6), C4–N3–Cu1 100.2(5), C5–N3–Cu1 105.2(5), C6–N4–Cu1 101.7(6), C11–N4–Cu1 117.6(6), C7–N4–Cu1 108.2(6), C9–N5–Cu1 108.0(6), C8–N5–Cu1 96.9(6), C14–N5–Cu1 112.8(6). Cu2–N2 1.921(8), Cu2–N8 2.156(8), Cu2–N7 2.159(8), Cu2–N6 2.195(8); N2–Cu2–N8 135.4(3), N2–Cu2–N7 140.5(3), N8–Cu2–N7 84.0(3), N2–Cu2–N6 100.4(3), N8–Cu2–N6 83.2(3), N7–Cu2–N6 83.8(3), N1–N2–Cu2 129.1(6), C3–N2–Cu2 122.3(6), C19–N6–Cu2 99.9(6), C18–N6–Cu2 112.4(6), C24–N6–Cu2 107.7(6), C20–N7–Cu2 106.2(5), C21–N7–Cu2 103.0(5), C25–N7–Cu2 111.3(6), C22–N8–Cu2 106.8(6), C23–N8–Cu2 102.3(6), C28–N8–Cu2 113.2(6).

Table 16. Crystal data and refinement details for complex **1**.

Compound	**1**
Empirical formula	$C_{54} H_{79} B Cu_2 N_8$
Formula weight [g/mol]	978.14
Temperature [K]	133(2)
Wavelength [Å]	0.71073
Crystal system	Orthorhombic
Space group	$Pca2_1$
Unit cell dimensions	a = 31.3337(7) Å, α= 90°
	b = 17.3506(5) Å, β= 90°
	c = 18.5568(5) Å, γ = 90°
Volume [$Å^3$]	10088.6(5)
Z	8
Density (calculated)[mg/m^3]	1.288
Absorption coefficient [mm^{-1}]	0.888
F(000)	4176
Crystal size [mm^3]	0.320 x 0.110 x 0.070
Theta range for data collection [°]	1.174 to 25.767°.
Index ranges	-38<=h<=38, -19<=k<=21, -22<=l<=22
Reflections collected	61627
Independent reflections	18998 [R(int) = 0.1099]
Completeness to theta = 25.242°	100.0%
Absorption correction	Numerical
Max. and min. transmission	0.7615 and 0.4962
Refinement method	Full-matrix least-squares on F^2
Data / restraints / parameters	18998 / 1 / 1187
Goodness-of-fit on F^2	1.024
Final R indices [I>2sigma(I)]	R1 = 0.0650, wR2 = 0.1306
R indices (all data)	R1 = 0.1225, wR2 = 0.1540
Absolute structure parameter	0.002(11)
Extinction coefficient	n/a
Largest diff. peak and hole [e/$Å^3$]	1.166 and -0.442

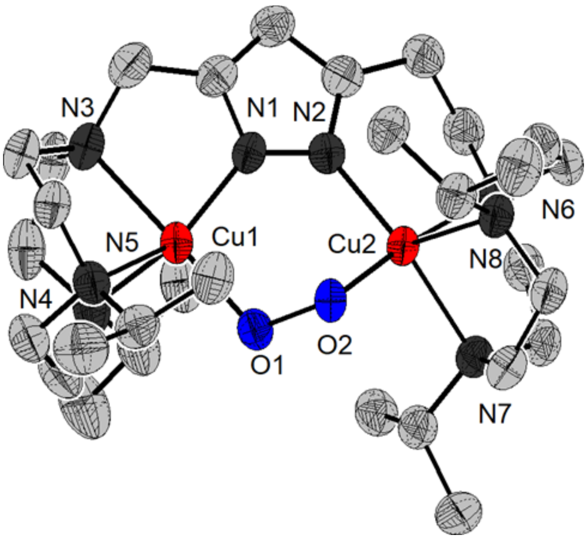

Figure 105. Molecular structure of the cationic part of complex **2**. Thermal displacement ellipsoids given at 50% probability. Hydrogen atoms, solvent molecules and counter ions are omitted for clarity. Selected bond lengths [Å] and angles [°] for **2**: Cu1–O1 1.884(3), Cu1–N1 1.932(4), Cu1–N3 2.131(4), Cu1–N5 2.174(4), Cu1–N4 2.187(4), Cu2–O2 1.897(3), Cu2–N2 1.980(4), Cu2–N6 2.113(4), Cu2–N7 2.135(4), Cu2–N8 2.278(4); O1–Cu1–N1 98.57(13), O1–Cu1–N3 174.73(14), N1–Cu1–N3 80.80(15), O1–Cu1–N5 93.31(15), N1–Cu1–N5 125.83(16), N3–Cu1–N5 82.93(16), O1–Cu1–N4 101.85(14), N1–Cu1–N4 141.93(14), N3–Cu1–N4 81.54(15), N5–Cu1–N4 84.75(14), O2–Cu2–N2 96.45(13), O2–Cu2–N6 172.73(13), N2–Cu2–N6 90.62(14), O2–Cu2–N7 90.22(13), N2–Cu2–N7 160.63(15), N6–Cu2–N7 83.61(14), O2–Cu2–N8 92.34(13), N2–Cu2–N8 113.78(14), N6–Cu2–N8 83.21(14), N7–Cu2–N8 83.96(14).

Table 17. Crystal data and refinement details for complex **2**.

Compound	**2**
Empirical formula	$C_{62} H_{99} B Cu_2 N_8 O_4$
Formula weight [g/mol]	1158.38
Temperature [K]	133(2)
Wavelength [Å]	0.71073
Crystal system	Monoclinic
Space group	$P2_1/n$
Unit cell dimensions	a = 12.4116(3) Å, a= 90°
	b = 26.3561(4) Å, b= 102.930(2)°
	c = 19.3892(4) Å, g = 90°.
Volume [Å^3]	6181.8(2)
Z	4
Density (calculated)[mg/m^3]	1.245
Absorption coefficient [mm^{-1}]	0.739
F(000)	2488
Crystal size [mm^3]	0.500 x 0.480 x 0.430

Theta range for data collection [°]	1.326 to 26.858°
Index ranges	-15<=h<=15, -33<=k<=33, -24<=l<=24
Reflections collected	85935
Independent reflections	13123 [R(int) = 0.0544]
Completeness to theta = 25.242°	99.9%
Absorption correction	Numerical
Max. and min. transmission	0.8746 and 0.7140
Refinement method	Full-matrix least-squares on F^2
Data / restraints / parameters	13123 / 0 / 706
Goodness-of-fit on F^2	1.120
Final R indices [I>2sigma(I)]	R1 = 0.0689, wR2 = 0.1976
R indices (all data)	R1 = 0.0833, wR2 = 0.2086
Extinction coefficient	n/a
Largest diff. peak and hole [e/Å^3]	2.037 and -0.630

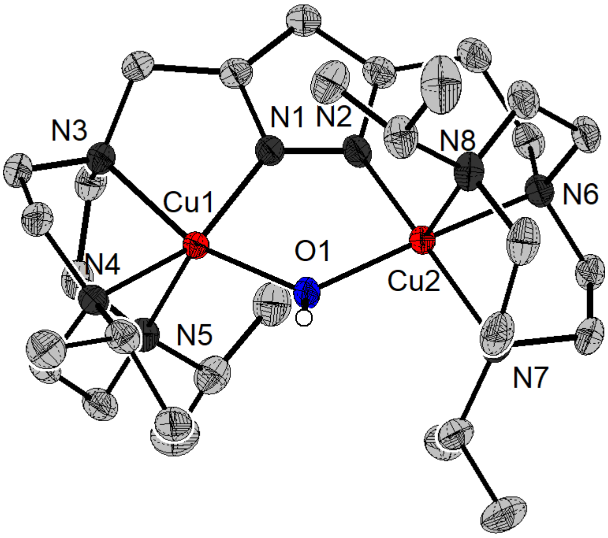

Figure 106. Molecular structure of the cationic part of complex **3**. Thermal displacement ellipsoids given at 50% probability. Hydrogen atoms, solvent molecules and counter ions are omitted for clarity. Selected bond lengths [Å] and angles [°] for **3**: Cu1–N1 1.905(3), Cu1–N2 2.044(4), Cu1–N6 2.088(11), Cu1–N4 2.102(4), Cu1–N5 2.312(4); N1–Cu1–N2 93.14(14), N1–Cu1–N6 86.5(2), N2–Cu1–N6 157.9(2), N1–Cu1–N4 170.73(15), N2–Cu1–N4 85.73(15), N6–Cu1–N4 91.1(3), N1–Cu1–N5 104.14(15), N2–Cu1–N5 83.33(17), N6–Cu1–N5 118.2(2), N4–Cu1–N5 84.88(14), C2–N1–Cu1 128.0(3), N1'–N1–Cu1 120.39(12), C10–N2–Cu1 112.1(3), C5–N2–Cu1 103.0(3), C4–N2–Cu1 111.7(3), C14B–N4–Cu1 121.3(15), C6–N4–Cu1 107.3(3), C7–N4–Cu1 102.3(3), C14A–N4–Cu1 113.3(5), C11B–N5–Cu1 133.1(12), C9–N5–Cu1 99.4(3), C8–N5–Cu1 102.0(3), C11A–N5–Cu1 116.0(6), O1–N6–Cu1 107.0(9). Symmetry transformation used to generate equivalent atoms: (') 2-*x*, 1-*y*, *z*.

Table 18. Crystal data and refinement details for complex **3**.

Compound	**3**
Empirical formula	$C_{81} H_{104} B_2 Cu_2 N_{10} O$
Formula weight [g/mol]	1382.44
Temperature [K]	133(2)
Wavelength [Å]	0.71073
Crystal system	Tetragonal
Space group	$I4_1cd$
Unit cell dimensions	a = 20.3673(3) Å, α=90°
	b = 20.3673(3) Å, β=90°
	c = 35.9270(6) Å, γ=90°
Volume [$Å^3$]	14903.5(5)
Z	8
Density (calculated)[mg/m^3]	1.232
Absorption coefficient [mm^{-1}]	0.623
F(000)	5888
Crystal size [mm^3]	0.500 x 0.490 x 0.420
Theta range for data collection [°]	2.268 to 26.990
Index ranges	-25<=h<=25, -25<=k<=25, -45<=l<=45
Reflections collected	70340
Independent reflections	7934 [R(int) = 0.0293]
Completeness to theta = 25.242°	99.9%
Absorption correction	Numerical
Max. and min. transmission	0.8627 and 0.7407
Refinement method	Full-matrix least-squares on F^2
Data / restraints / parameters	7934 / 114 / 508
Goodness-of-fit on F^2	1.073
Final R indices [I>2sigma(I)]	R1 = 0.0402, wR2 = 0.1096
R indices (all data)	R1 = 0.0449, wR2 = 0.1161
Absolute structure parameter	-0.006(6)
Extinction coefficient	n/a
Largest diff. peak and hole [e/$Å^3$]	0.681 and -0.428

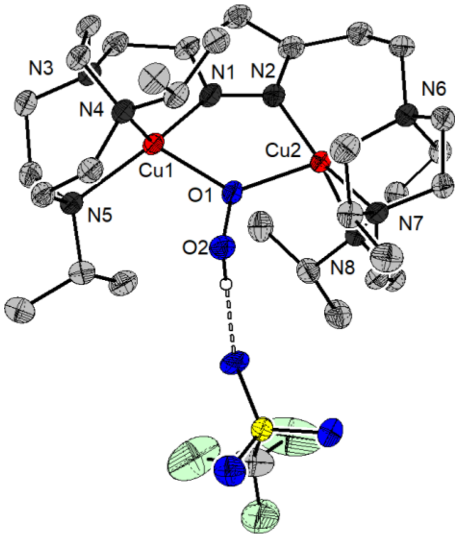

Figure 107. Molecular structure of the cationic part of complex **4** without the second counter ion tetraphenylborate. Thermal displacement ellipsoids given at 50% probability. Hydrogen atoms, solvent molecules and counter ions are omitted for clarity. Selected bond lengths [Å] and angles [°] (sorted) for **4**: Cu1–N1 1.902(2), Cu2–N2 1.959(2), Cu1–O1 1.9849(17), Cu2–O1 2.0452(17), Cu1–N3 2.091(2), Cu2–N7 2.097(2), Cu2–N6 2.110(2), Cu1–N5 2.131(2), Cu1–N4 2.226(2), Cu2–N8 2.303(2); N1–Cu1–N3 81.48(8), N1–Cu1–O1 81.91(8), N3–Cu1–N4 83.12(8), N6–Cu2–N8 83.37(7), N2–Cu2–O1 83.96(8), N7–Cu2–N8 84.21(7), N7–Cu2–N6 84.57(8), N3–Cu1–N5 84.65(8), N5–Cu1–N4 85.14(8), N2–Cu2–N6 89.30(8).

Table 19. Crystal data and refinement details for complex **4**.

Compound	**4**
Empirical formula	$C_{61} H_{89} B Cu_2 F_3 N_{11} O_5 S$
Formula weight [g/mol]	1283.38
Temperature [K]	133(2)
Wavelength [Å]	0.71073
Crystal system	Triclinic
Space group	P-1
Unit cell dimensions	a = 10.9668(5) Å, a= 95.571(4)°
	b = 14.9101(7) Å, b= 105.778(3)°
	c = 20.0052(8) Å, g = 92.191(4)°
Volume [Å^3]	3125.9(2)
Z	2
Density (calculated)[mg/m^3]	1.364
Absorption coefficient [mm^{-1}]	0.780
F(000)	1356
Crystal size [mm^3]	0.492 x 0.487 x 0.274
Theta range for data collection [°]	1.375 to 25.748°.

Index ranges	-13<=h<=13, -18<=k<=18, -24<=l<=24
Reflections collected	30318
Independent reflections	11694 [R(int) = 0.0338]
Completeness to theta = 25.242°	99.7%
Absorption correction	Numerical
Max. and min. transmission	0.9668 and 0.5648
Refinement method	Full-matrix least-squares on F^2
Data / restraints / parameters	11694 / 114 / 845
Goodness-of-fit on F^2	1.068
Final R indices [I>2sigma(I)]	R1 = 0.0372, wR2 = 0.0901
R indices (all data)	R1 = 0.0491, wR2 = 0.0978
Extinction coefficient	n/a
Largest diff. peak and hole [e/Å^3]	0.517 and -0.369 e.Å^{-3}

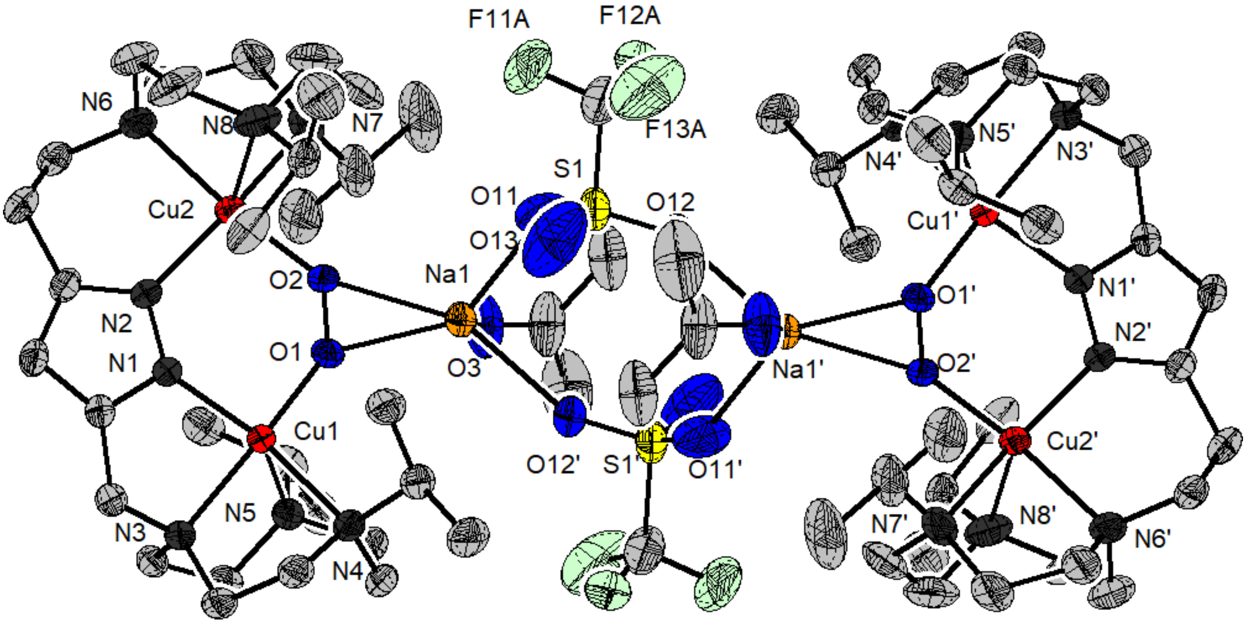

Figure 108. Molecular structure of the dimer of the cationic part of complex **7**. Thermal displacement ellipsoids given at 50% probability. Hydrogen atoms, solvent molecules and counter ions are omitted for clarity. Selected bond lengths [Å] and angles [°] for **7**: Cu1–O1 1.8799(15), Cu1–N1 1.9448(18), Cu1–N3 2.1139(18), Cu1–N5 2.1599(19), Cu1–N4 2.2605(19), Cu2–O2 1.9107(16), Cu2–N2 1.9838(19), Cu2–N6 2.120(2), Cu2–N7 2.144(2), Cu2–N8 2.284(2); O1–Cu1–N1 97.36(7), O1–Cu1–N3 172.99(7), N1–Cu1–N3 82.16(7), O1–Cu1–N5 91.20(7), N1–Cu1–N5 132.87(8), N3–Cu1–N5 84.12(7), O1–Cu1–N4 105.07(7), N1–Cu1–N4 136.96(8), N3–Cu1–N4 79.63(7), N5–Cu1–N4 83.43(7), O2–Cu2–N2 95.72(7), O2–Cu2–N6 173.62(7), N2–Cu2–N6 90.58(8), O2–Cu2–N7 91.72(8), N2–Cu2–N7 162.31(9), N6–Cu2–N7 82.51(9), O2–Cu2–N8 93.96(7), N2–Cu2–N8 113.44(10), N6–Cu2–N8 82.56(8), N7–Cu2–N8 81.91(11), O2–O1–Cu1 113.05(11).

Table 20. Cystal data and refinment details for complex **7**.

Compound	**7**
Empirical formula	$C_{124} H_{190} B_2 Cu_4 F_6 N_{16} Na_2 O_{14} S_2$
Formula weight [g/mol]	2628.79
Temperature [K]	133(2) K
Wavelength [Å]	0.71073 Å
Crystal system	Triclinic
Space group	P-1
Unit cell dimensions	a = 10.1663(3) Å, α= 104.572(2)°
	b = 15.8417(5) Å, β= 98.263(2)°
	c = 22.2299(6) Å, γ = 102.150(3)°
Volume [$Å^3$]	3313.39(18)
Z	1
Density (calculated)[mg/m^3]	1.317
Absorption coefficient [mm^{-1}]	0.744
F(000)	1392
Crystal size [mm^3]	0.500 x 0.370 x 0.280
Theta range for data collection [°]	1.432 to 26.914°.
Index ranges	-12<=h<=12, -20<=k<=19, -28<=l<=28
Reflections collected	38097
Independent reflections	14004 [R(int) = 0.0259]
Completeness to theta = 25.242°	100.0%
Absorption correction	Numerical
Max. and min. transmission	0.8364 and 0.6096
Refinement method	Full-matrix least-squares on F^2
Data / restraints / parameters	14004 / 172 / 859
Goodness-of-fit on F^2	1.023
Final R indices [I>2sigma(I)]	R1 = 0.0403, wR2 = 0.1063
R indices (all data)	R1 = 0.0547, wR2 = 0.1161
Extinction coefficient	n/a
Largest diff. peak and hole [e/$Å^3$]	0.967 and -0.424 e.$Å^{-3}$

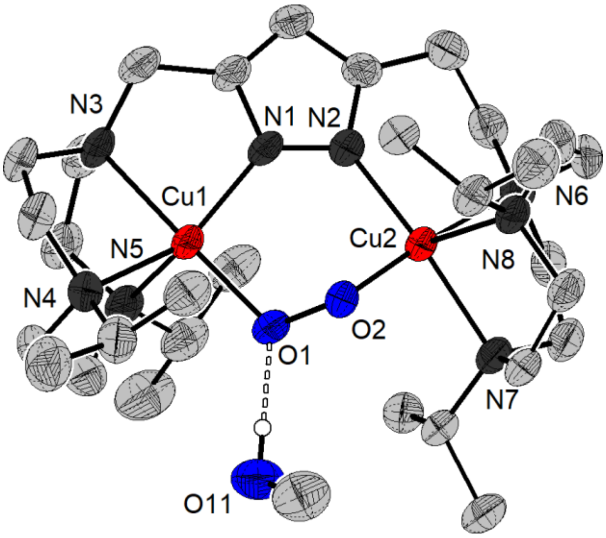

Figure 109. Molecular structure of the cationic portion of complex **8**. Thermal displacement ellipsoids given at 50% probability. Hydrogen atoms, solvent molecules and counter ions are omitted for clarity. Selected bond lengths [Å] and angles [°] for **8**: Cu1–O1 1.907(3), Cu1–N1 1.945(4), Cu1–N3 2.104(4), Cu1–N4 2.184(4), Cu1–N5 2.187(4), Cu2–O2 1.915(3), Cu2–N2 1.974(4), Cu2–N6 2.110(4), Cu2–N7 2.125(4), Cu2–N8 2.300(4); O1–Cu1–N1 96.44(14), O1–Cu1–N3 174.02(15), N1–Cu1–N3 82.31(15), O1–Cu1–N4 102.33(14), N1–Cu1–N4 143.44(16), N3–Cu1–N4 81.85(15), O1–Cu1–N5 92.60(14), N1–Cu1–N5 125.19(16), N3–Cu1–N5 83.44(15), N4–Cu1–N5 85.25(16), O2–Cu2–N2 94.53(14), O2–Cu2–N6 174.58(14), N2–Cu2–N6 90.72(15), O2–Cu2–N7 91.02(14), N2–Cu2–N7 163.73(16), N6–Cu2–N7 84.27(15), O2–Cu2–N8 93.61(13), N2–Cu2–N8 111.19(14), N6–Cu2–N8 83.22(14), N7–Cu2–N8 83.64(14).

Table 21. Cystal data and refinment details for complex **8**.

Compound	**8**
Empirical formula	$C_{57} H_{91} B Cu_2 N_8 O_5$
Formula weight [g/mol]	1106.26
Temperature [K]	133(2)
Wavelength [Å]	0.71073
Crystal system	Triclinic
Space group	P-1
Unit cell dimensions	a = 13.9764(7) Å, α= 86.173(5)°
	b = 13.7584(8) Å, β= 81.622(4)°
	c = 15.1881(8) Å, γ = 83.280(4)°
Volume [Å^3]	2865.9(3)
Z	2
Density (calculated)[mg/m^3]	1.282
Absorption coefficient [mm^{-1}]	0.795
F(000)	1184
Crystal size [mm^3]	0.500 x 0.370 x 0.070
Theta range for data collection [°]	1.357 to 26.900

Index ranges	-17<=h<=17, -17<=k<=17, -19<=l<=19
Reflections collected	40572
Independent reflections	12200 [R(int) = 0.1016]
Completeness to theta = 25.242°	100.0%
Absorption correction	Numerical
Max. and min. transmission	0.9899 and 0.6768
Refinement method	Full-matrix least-squares on F^2
Data / restraints / parameters	12200 / 11 / 684
Goodness-of-fit on F^2	1.021
Final R indices [I>2sigma(I)]	R1 = 0.0703, wR2 = 0.1780
R indices (all data)	R1 = 0.1240, wR2 = 0.2136
Extinction coefficient	n/a
Largest diff. peak and hole [e/Å^3]	1.279 and -1.198

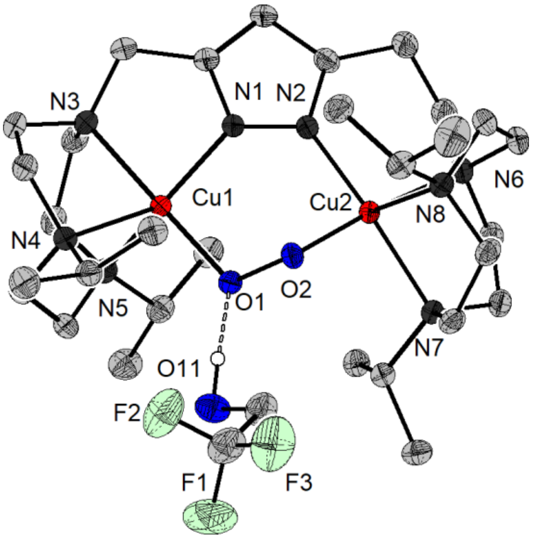

Figure 110. Molecular structure of the cationic part of complex **9**. Thermal displacement ellipsoids given at 50% probability. Hydrogen atoms, solvent molecules and counter ions are omitted for clarity. Selected bond lengths [Å] and angles [°] for **9**: Cu1–O1 1.8936(12), Cu1–N1 1.9499(14), Cu1–N3 2.0999(14), Cu1–N5 2.1776(15), Cu1–N4 2.2045(15), Cu2–O2 1.9011(12), Cu2–N2 1.9803(14), Cu2–N6 2.1035(15), Cu2–N7 2.1282(14), Cu2–N8 2.3006(15); O1–Cu1–N1 97.07(6), O1–Cu1–N3 174.12(6), N1–Cu1–N3 82.35(6), O1–Cu1–N5 92.34(5), N1–Cu1–N5 128.83(6), N3–Cu1–N5 83.56(6), O1–Cu1–N4 102.16(5), N1–Cu1–N4 140.82(6), N3–Cu1–N4 81.68(6), N5–Cu1–N4 84.36(6), O2–Cu2–N2 94.39(6), O2–Cu2–N6 174.55(5), N2–Cu2–N6 90.95(6), O2–Cu2–N7 91.79(5), N2–Cu2–N7 162.06(6), N6–Cu2–N7 83.42(6).

Table 22. Cystal data and refinment details for complex **9**.

Compound	**9**
Empirical formula	$C_{59} H_{88} B Cu_2 F_3 N_8 O_4$

Formula weight [g/mol]	1168.26
Temperature [K]	133(2)
Wavelength [Å]	0.71073
Crystal system	Triclinic
Space group	P-1
Unit cell dimensions	a = 13.5423(4) Å, α= 83.327(2)°
	b = 14.1741(4) Å, β= 87.015(2)°
	c = 15.5475(4) Å, γ = 82.785(2)°
Volume [Å^3]	2938.53(14)
Z	2
Density (calculated)[mg/m^3]	1.320
Absorption coefficient [mm^{-1}]	0.786
F(000)	1240
Crystal size [mm^3]	0.500 x 0.400 x 0.210
Theta range for data collection [°]	1.320 to 26.877°.
Index ranges	-17<=h<=17, -17<=k<=17, -19<=l<=19
Reflections collected	42263
Independent reflections	12447 [R(int) = 0.0306]
Completeness to theta = 25.242°	100.0%
Absorption correction	Numerical
Max. and min. transmission	0.9756 and 0.7873
Refinement method	Full-matrix least-squares on F^2
Data / restraints / parameters	12447 / 0 / 708
Goodness-of-fit on F^2	1.037
Final R indices [I>2sigma(I)]	R1 = 0.0323, wR2 = 0.0818
R indices (all data)	R1 = 0.0427, wR2 = 0.0859
Extinction coefficient	n/a
Largest diff. peak and hole [e/Å^3]	0.622 and -0.339

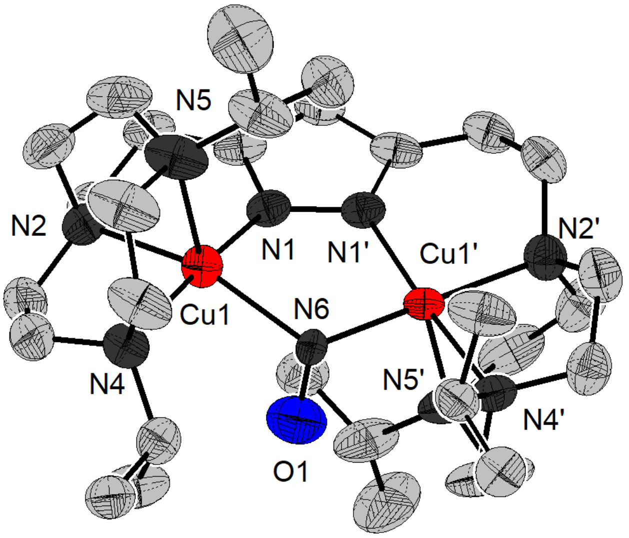

Figure 111. Molecular structure of the cationic part of complex **10**. Thermal displacement ellipsoids given at 50% probability. Hydrogen atoms, solvent molecules and counter ions are omitted for clarity. Selected bond lengths [Å] and angles [°] for **10**: Cu1–N1 1.905(3), Cu1–N2 2.044(4), Cu1–N6 2.088(11), Cu1–N4 2.102(4), Cu1–N5 2.312(4); N1–Cu1–N2 93.14(14), N1–Cu1–N6 86.5(2), N2–Cu1–N6 157.9(2), N1–Cu1–N4 170.73(15), N2–Cu1–N4 85.73(15), N6–Cu1–N4 91.1(3), N1–Cu1–N5 104.14(15), N2–Cu1–N5 83.33(17), N6–Cu1–N5 118.2(2), N4–Cu1–N5 84.88(14), C2–N1–Cu1 128.0(3), N1'–N1–Cu1 120.39(12), C10–N2–Cu1 112.1(3), C5–N2–Cu1 103.0(3), C4–N2–Cu1 111.7(3), C14B–N4–Cu1 121.3(15), C6–N4–Cu1 107.3(3), C7–N4–Cu1 102.3(3), C14A–N4–Cu1 113.3(5), C11B–N5–Cu1 133.1(12), C9–N5–Cu1 99.4(3), C8–N5–Cu1 102.0(3), C11A–N5–Cu1 116.0(6), O1–N6–Cu1 107.0(9). Symmetry transformation used to generate equivalent atoms: (') 2-*x*, 1-*y*, *z*.

Table 23. Cystal data and refinment details for complex **10**.

Compound	**10**
Empirical formula	$C_{81}H_{104}B_2Cu_2N_{10}O$
Formula weight [g/mol]	1382.44
Temperature [K]	133(2)
Wavelength [Å]	0.71073
Crystal system	Tetragonal
Space group	$I4_1cd$
Unit cell dimensions	a = 20.3673(3) Å, α=90°
	b = 20.3673(3) Å, β=90°
	c = 35.9270(6) Å, γ=90°
Volume [Å^3]	14903.5(5)
Z	8
Density (calculated)[mg/m^3]	1.232
Absorption coefficient [mm^{-1}]	0.623
F(000)	5888
Crystal size [mm^3]	0.500 x 0.490 x 0.420

Theta range for data collection [°]	2.268 to 26.990
Index ranges	-25<=h<=25, -25<=k<=25, -45<=l<=45
Reflections collected	70340
Independent reflections	7934 [R(int) = 0.0293]
Completeness to theta = 25.242°	99.9%
Absorption correction	Numerical
Max. and min. transmission	0.8627 and 0.7407
Refinement method	Full-matrix least-squares on F^2
Data / restraints / parameters	7934 / 114 / 508
Goodness-of-fit on F^2	1.073
Final R indices [I>2sigma(I)]	R1 = 0.0402, wR2 = 0.1096
R indices (all data)	R1 = 0.0449, wR2 = 0.1161
Absolute structure parameter	-0.006(6)
Extinction coefficient	n/a
Largest diff. peak and hole [e/Å^3]	0.681 and -0.428

7.12 Ligand Synthesis

7.12.1 Synthesis of 1,4-Diisopropyl-1,4,7-triazacyclononane

***N,N'*-Di-(2-chloracetyl)-*N,N'*-di-*iso*-propylethylenediamine (b)**

Compound **b** has been synthesized according to literature procedures with slight modifications.[138] Di-*iso*-propylethylenediamine (2.11 g, 14.6 mmol, 1.0 eq.) was added to a suspension of potassium carbonate (4.44 g, 32.13 mmol, 2.2 eq.) in DCM (25 mL). After cooling the suspension to 0 °C, chloroacetyl chloride (3.30 g, 29.2 mmol, 2.0 eq.) was added dropwise. Subsequently, the mixture was heated to room temperature, stirred for 30 min, and then stirred at 50 °C for another 12 h. After cooling to RT, H_2O (50 mL) was added and the phases were separated. The organic phase was washed with H_2O (3 x 25 mL), dried over MgSO4, and the solvent was removed. Recrystallization from DCM/hexane at −21 °C afforded the product (2.62 g, 8.8 mmol, 60%) as a white solid.

^{1}H NMR (300 MHz, $CDCl_3$): δ (ppm) = 1.28 (s, 6 H, CH_3), 1.31 (s, 6 H, CH_3), 3.35 (s, 4 H, CH_2) 3.99 (sep, ^3J = 6.5 Hz, 2 H, CH) 4.11 (s, 4 H, CH_2Cl).

^{13}C{^{1}H} NMR (75 MHz, $CDCl_3$): δ (ppm) = 21.0, 39.5, 42.0, 49.8, 166.6.

1,4-Di-*iso*-propyl-7-benzyl-1,4,7-triazacyclononan-2,6-diamid (c)

The compound **c** was synthesized according to literature procedures with slight modifications.[138] Pre-dried Na_2CO_3 (18.5 g, 175 mmol, 5.2 eq.) was suspended in DMF (170 mL) and subsequently compound **b** (10 g, 33.6 mmol, 1.0 eq.) was added. The reaction mixture was heated to 120 °C for 10 min and then cooled to RT. Addition of benzylamine (3.61 g, 33.6 mmol, 1.0 eq.) and stirring at 120 °C for 3 days yielded the curde product, which was purified by column chromatography (silica, 100% EtOAC) to give compound **c** (2.9 g, 9.6 mmol, 28%) as a yellowish oil.

^{1}H NMR (300 MHz, $CDCl_3$): δ (ppm) = 1.09 (s, 6 H, CH_3), 1.12 (s, 6 H, CH_3), 3.48 (s, 4 H, CH_2), 3.59 (s, 4 H, CH_2), 3.87 (s, 2 H, CH_2Ph), 4.92 (sep, ^3J = 6.8 Hz, 2 H, CH), 7.20-7.39 (m, 5 H, Ph).

^{13}C{^{1}H} NMR (75 MHz, $CDCl_3$): δ (ppm) = 20.6, 45.1, 56.6, 59.5, 127.4-137.8, 169.7.

4-Benzyl-1,7-di-*iso*-propyl-1,4,7-triazacyclononane (d)

Compound **d** could be synthesized by two routines according to literature procedures.[138,139] **a)**[138] Compound **c** (1.4 g, 4.27 mmol, 1.0 eq.) was dissolved in dry THF (50 mL) and $LiAlH_4$ (9.4 mmol, 3.9 mL, 2.4 m in THF, 2.2 eq.) slowly added. The mixture was stirred for 1 h at 75 °C and then cooled to RT. A mixture of H_2O/THF (1:1, 50 mL) was added and then filtered. Upon removal of the solvent under vacuum, the residue was dissolved in chloroform (50 mL), washed with water (3 x 50 mL) and dried over $MgSO_4$. Further filtration and evaporation of the solvent in vacuo, the product (1.08 g, 3.54 mmol, 83%) was obtained as a yellowish oil.

b)[139] $NaBH_4$ (84 mg, 2.2 mmol, 2.0 eq.) was added in small portions to a solution of **i** (422 mg, 1.1 mmol, 1.0 eq.) in EtOH (10 mL) at RT. The solution was stirred for 15-25 min and then the solvent was removed in vacuo. The residue was taken up in aqueous NaOH solution (1 M, 20 mL) and extracted with chloroform (3 x 10 mL). The combined organic phases were washed with aqueous NaOH solution (1 M, 3 x 10 mL), dried over Na_2SO_4, and the solvent was removed in vacuo. The product (152 mg, 0.43 mmol, 39%) was obtained as a yellow oil.

^{1}H NMR (300 MHz, $CDCl_3$): δ (ppm) = 0.99 (d, ^3J = 6.7 Hz, 12 H, CH_3), 2.47 (s, 4 H, CH_2), 2.57-2.65 (m, 4 H, CH_2), 2.79-2.91 (m, 6 H, CH_2, CH).

^{13}C{^{1}H} NMR (75 MHz, $CDCl_3$): δ (ppm) = 18.5 (CH_3), 46.7, 54.9(CH_2) 62.3 (CH_2), 126.7-129.0 (Ph).

1,4-Di-*iso*-propyl-1,4,7-triazacyclononane (e)

Compound **e** could be synthesized by two routines according to literature procedures.[138,139]

a)[138] 4-Benzyl-1,7-di-*iso*-propyl-1,4,7-triazacyclononane (**d**) (1.08 g, 3.54 mmol, 1.0 eq.) was dissolved in methanol (30 mL), mixed with ammonium formate (1.12 g, 17.7 mmol, 5.0 eq.) and Pd/C (10%, 1.13 g), and then stirred for 1 h at 80 °C. The reaction mixture was cooled to RT, filtered over Celite, and the residue was washed with methanol (3 x 25 mL). The solvent was removed in vacuo and the residue was redissolved in chloroform (25 mL). Filtration and removal of the solvent afforded the product (514 mg, 2.41 mmol, 68%) as an orange oil.

b)[139] 1-(p-Tosyl)-4,7-(iso-propyl)-1,4,7-triazacyclononane (**n**) (9.75 g, 26.5 mmol, 1.0 eq.) and conc. sulfuric acid (19.5 mL) was refluxed at 120 °C for 24 h. After cooling down to temperature the brown solution was poured on ice and a pH value of 11 was adjusted with concentrated NaOH solution. The reaction mixture was extracted with $CHCl_3$ (5 × 100 mL) and the combined organic layers were washed with brine (50 mL) and dried over $MgSO_4$. The solvent was removed under reduced pressure and the crude product was further purified by distillation under vacuum (90 °C, 5 x 10^{-2} mbar), affording the product as colorless oil (3.05 g, 14.3 mmol, 82%).

^{1}H NMR (300 MHz, $CDCl_3$): δ (ppm) = 0.96 (d, ^3J = 6.6 Hz ,12 H, CH_3), 2.44 (s, 4 H, CH_2), 2.47 (s, 4 H, CH_2), 2.56-2.59 (m, 4 H, CH_2), 2.65-2.69 (m, 4 H, CH_2), 2.87 (sept, ^3J = 6.5 Hz, 2 H, CH), 3.68 (broad s, 1 H, NH).

^{13}C{^{1}H} NMR (75 MHz, $CDCl_3$): δ (ppm) = 18.8 (CH_3), 45.3 (2-C, 9-C), 45.7 (3-C, 8-C), 47.7 (CH), 52.8(5-C, 6-C).

1,7-Di-*iso*-propyl-diethylentriamine (g)

A slightly modified synthetic routine was employed according to literature procedures.[139] To a solution of acetone (9.7 mL, 132 mmol, 2 eq.) in ethanol (500 mL) diethylenetriamine (7.1 mL, 66 mmol, 1 eq.) was added and stirred for 2 h at 50 °C. The reaction mixture was then cooled down to RT and $NaBH_4$ (12.5 g, 330 mmol, 5.0 eq.) was carefully added. The mixture was stirred at 50 °C for

2 h. Subsequently the solvent was removed in vacuo, and the remaining residue resolved in aqueous NaOH (1 M, 200 mL). The aqueous phase was extracted with DCM (3 x 100mL) and the combined organic phases were again washed with aqueous NaOH solution (1 M, 100 mL) and then dried over Na_2SO_4. After removal of the solvent, the product (9.27 g, 49.5 mmol, 75%) was obtained as a colorless oil.

^{1}H NMR (300 MHz, $CDCl_3$): δ (ppm) = 1.02 (s, 6 H, CH_3), 1.04 (s, 6 H, CH_3), 1.39 (s. br., 3 H, NH), 2.60-2.83 (m, 10 H, CH_2/CH).

^{13}C{^{1}H} NMR (75 MHz, $CDCl_3$): δ (ppm) =22.6, 48.3, 54.0, 57.6.

MS (ESI(+)): *m/z* (%) =188.2 (100) $[M+H]^+$, 210.2 (77) $[M+Na]^+$

1,7-Di-*iso*-propyl-octahydroimidazo[1,2-a]pyrazine (h)

The compound **h** was synthesized according to literature procedures with slight modifications.[139] To a suspension of **g** (6.7 g, 36.0 mmol, 1.0 eq.) and K_2CO_3 (9.9 g, 72 mmol, 2.0 eq.) in MeCN (180 mL) chloroacetaldehyde in MeCN (2.8 g, 36 mmol, 1.0 eq.) was added dropwise. The solution was stirred for 4 h at RT and then filtered over Celite. The solvent was removed in vacuo and the residue dissolved in a minimum of DCM (2-5 ml). The solution was dropped into Et_2O (250 mL) and the mixture was filtered through a frit. The solvent of the filtrate was then removed in vacuo, and the product was obtained as brown oil.

^{1}H NMR (300 MHz, $CDCl_3$): δ (ppm) =0.92-1.05 (m, 12 H, CH_3) 2.3-3.1 (m, 13 H, CH_2, CH).

^{13}C{^{1}H} NMR (75 MHz, $CDCl_3$): δ (ppm) =22.0, 46.1, 48.5, 48.7, 74.7.

MS (ESI(+)): *m/z* (%) = 214.2 (100) $[M+3H]^+$, 212.2 (72) $[M+H]^+$.

4-Benzyl-1,7-di-*iso*-propyl-octahydroimidazo[1,2-a]pyrazin-4-iumbromid (i)

The compound **i** was synthesized according to literature procedures with slight modifications.[139] Benzyl bromide (633 mg, 3.7 mmol, 1.0 eq.) was added to a solution of **h** (780 mg, 3.7 mmol, 1.0 eq.) and K_2CO_3 (1.02 g, 7.4 mmol, 2.0 eq.) in MeCN (20 mL) and subsequently stirred for 18 h. The reaction mixture was filtered over Celite and the solvent was removed in vacuo. The residue was dissolved in a minimum DCM and the solution was dropped into Et_2O (40 mL). The resulting residue was filtered off and washed with Et_2O. The product was obtained as a brown oily solid (422 mg, 1.1 mmol, 30%), which was converted directly to give the next product.

MS (ESI(+)): *m/z* (%) = 302.3 (100) $[M+H]^+$.

N, N″,N‴-tritosyl-1,4,7-triazacyclononane (l)

A slightly modified synthetic routine was employed for **l** according to literature procedures.[139] N′, N″, N‴ Tritosyl-dietyhlentriamine (90.4 g, 160 mmol, 1.0 eq.) and Cs_2CO_3 (114 g, 350 mmol, 2.2 eq) were suspended in DMF (950 mL) and stirred for 1 h. Subsequently, a solution of O,O′ ditosyl-etyhlenglycol (60 g, 160 mmol, 1.0 eq) in DMF (400 mL) was added dropwise and the suspension stirred for 48 h. The reaction mixture was carefully transferred into a flask with water (3.5 L) whereby the crude product **l** precipitated. After stirring for 1 h and filtration, the solid was stirred in a solution of DMF/H_2O (1:1, 1 L). The solvent was decantated and EtOH (500 mL) added to the solid and the suspension again stirred for 1 h. Subsequent filtration and drying of the solid in vacuum over several days yielded the product as a clean white solid (78 g, 130 mmol, 83%).

^{1}H-NMR (300 MHz, $CDCl_3$): δ [ppm] = 2.43 (s, 9 H, CH_3), 3.42 (s, 12 H, CH_2), 7.32 (d, ^3J = 8.0 Hz, 6 H, ^{Ar}C-H), 7.68-7.72 (m, 6 H, ^{Ar}C-H),

^{13}C{^{1}H}-NMR (75 MHz, $CDCl_3$): δ [ppm] = 21.6, 52.0, 127.6, 130.0, 134.8, 144.0.

1-(p-Tosyl)-1,4,7-triazacyclononane (m)

A slightly modified synthetic routine was employed for **m** according to literature procedures.[139] To N, N″, N‴-tritosyl-1,4,7-triazacyclononane (50g, 84.4 mmol, 1.0 eq) and phenol (62 g, 660 mmol, 7.8 eq) HBr/EtOAc (33%, 500ml) was added. The reaction mixture was stirred for 48 h at 80 °C whereby large quantities of HBr evolved (caution!). Therefore, three gas washing bottles were connected to the reaction setup (an empty one, one with water and one with a sodium thiosulfate solution). After cooling to room temperature, the orange precipitate was filtered off and washed thoroughly with diethyl ether (5 x 200 mL). The solid was taken up in aqueous NaOH solution (1 M, 500 mL) and extracted with $HCCl_3$ (3 x 200 mL). Combination of the organic phases, drying over $MgSO_4$ and removal of solvent under vacuum led to the isolation of an off-white solid (20.1 g, 71 mmol, 84%).

It should be noted that the isolated product showed decomposition over time, even at temperatures around – 30°C. Therefore, the crude HBr of compound salt was usually stored as an intermediate compound which showed no significant decay.

^{1}H-NMR (300 MHz, $CDCl_3$): δ [ppm] = 2.43 (s, 3 H, CH_3), 2.97 (s, 4 H, CH_2), 3.06-3.09 (m, 4 H, CH_2), 3.16-3.19 (m, 4 H, CH_2), 7.31 (d, ^3J = 8.3 Hz, 2 H, ^{Ar}C-H), 7.68 (d, ^3J = 8.3 Hz, 2 H, ^{Ar}C-H),

^{13}C{^{1}H}-NMR (75 MHz, $CDCl_3$): δ [ppm] = 21.6, 49.6, 49.7, 54.1, 127.3, 129.8, 135.6, 143.4

1-(p-Tosyl)-4,7-(iso-propyl)-1,4,7-triazacyclononane (n)

The compound **n** was synthesized according to literature procedures with slight modifications.[139]

1-(p-Tosyl)-1,4,7-triazacyclononane (8.31 g, 29.3 mmol, 1.0 eq), 2-bromopropane (11 mL, 117 mmol, 4.0 eq.), Na_2CO_3 (12.42 g, 29.3 mmol, 4.0 eq) and tetrabutylammonium bromide (94 mg, 0.29 mmol, 1 mol%) were heated under reflux in acetonitrile for 16 h. Subsequently the reaction mixture was filtered and the remaining residue washed with $CHCl_3$ (120 mL). The combined filtrate was washed with aqueous NaOH solution (1 M ,70 mL). The aqueous phase was extracted with $HCCl_3$ (3 x 100 mL) and all organic phases combined and dried over $MgSO_4$. The solvent was removed under vacuum and the product obtained as a yellowish solid (9.75 g, 26.5 mmol, 91%)

^{1}H-NMR (300 MHz, $CDCl_3$): δ [ppm] = 0.93 (d, ^3J = 6.6 Hz ,12 H, CH_3), 2.41 (s, 3 H, CH_3), 2.47 (s, 4 H, CH_2), 2.79 (sept, ^3J = 6.5 Hz, 2 H, CH), 2.84-2.87 (m, 4 H, CH_2), 3.28-3.31 (m, 4 H, CH_2), 7.29 (d, ^3J = 8.2 Hz, 2 H, ^{Ar}C-H), 7.69 (d, ^3J = 8.2 Hz, 2 H, ^{Ar}C-H).

^{13}C{^{1}H}-NMR (75 MHz, $CDCl_3$): δ [ppm] = 18.0, 21.2, 50.1, 52.0, 53.4, 126.9, 129.2, 136.3, 142.4.

7.12.2 Synthesis of Pyrazole Building Blocks

3,5-bis(chloroethyl)pyrazole (p)

Thionyl chloride (100 mL) was added dropwise to 3,5-bis(hydroxyethyl)pyrazole (4.84 g, 30.9 mmol, 1.0 eq.) at 0 °C. After complete addition, the reaction mixture was heated under reflux for 1 h and then the solvent was removed in vacuo. The remaining oil was dissolved in EtOH (50 mL) and the volume was then divided in half. After addition of Et_2O and storage at −30°C, compound **k** (4.69 g, 20.43 mmol, 66%) was obtained as a white solid.

^{1}H NMR (300 MHz, MeCN-d_3): *δ* (ppm) = 3.12 (t, ^3J= 6.7 Hz, 4 H, CH_2), 3.91 (t, ^3J= 6.7 Hz, 4 H, CH_2Cl), 6.42 (s, 1 H, CH^{pz}).

^{13}C{^{1}H} NMR (75 MHz, MeCN-d_3): *δ* (ppm) = 29.6 (CH_2), 43.0 (CH_2Cl), 107.5 (4-C^{pz}), 146.9 (3,5-C^{pz}).

Synthesis of 3-(β-chloroethyl)-5-(chloromethyl)pyrazole

3-(β -Hydroxyethyl)-5-hydroxymethylpyrazole hydrochloride (r)

A solution of 1,6-dihydroxy-2,4-hexadiyne (2.5 g, 22.7 mmol, 1.0 eq.) and H_2N-NH_2 H_2O (3.41 g, 68.11 mmol, 3.0 eq.) in EtOH (130 mL) was heated to 85 °C for 24 hours. The solvent and excess hydrazine was then removed under vacuum by using a cold trap and after drying the yellow oil overnight, ethanolic HCl is added and subsequently diethyl ether, yielding a brown oil or solid (depending on the quality of the educt). The excess solvent is decanted the product dried in vacuum over night yielding a brown oil (3.36, 18.8 mmol, 83%).

^{1}H-NMR (300 MHz, D_2O): δ [ppm] = 6.24 (s, 1 H, ^{Py}C-H), 4.58 (s, 2 H, $^{Me}CH_2$), 3.78 (t, ^3J = 6.3 Hz, 2 H, $^{Et}CH_2$), 2.83 (t, ^3J = 6.3 Hz, 2 H, $^{Et}CH_2$).

^{13}C{^{1}H}-NMR (75 MHz, D_2O): δ [ppm] = 149.12 (^{Ar}C), 146.07 (^{Ar}C), 103.27 (^{Ar}C-H), 60.28 ($^{Et}CH_2OH$), 55.85 ($^{Me}CH_2OH$), 28.59 (CH_2).

MS (ESI$^+$): *m/z* (%) = 143.1 (39) $[M+H]^+$, 125.1 (100) $[M-OH]^+$.

3-(β -chloroethyl)-5-chloromethylpyrazole hydrochloride (s)

To compound **r** (3.26 g, 18.3 mmol, 1.0 eq.) Thionyl chloride (80 mL) was added slowly at 0 °C. The solution was then heated to 65 °C for one hour, cooled to RT and excess thionyl chloride removed under vacuum by using a cold trap. The resulting brown oil was dried under vacuum over night (Important). Addition of diethyl ether and strong stirring for 24 h led to the formation of a brown powder. Excess solvent was decanted, the solid dried under vacuum and the product obtained as a beige powder (3.50 g, 16.2 mmol, 89%).

^{1}H-NMR (300 MHz, D_2O): δ [ppm] = 6.57 (s, 1 H, ^{pz}CH), 4.72 (s, 2 H, CH_2), 3.85 (t, ^3J = 6.2 Hz, 2 H, CH_2), 3.20 (t, ^3J = 6.3 Hz, 2 H, CH_2).

^{13}C-NMR (75 MHz, D2O): δ [ppm] = 146.32 (^{Ar}C), 145.49(^{Ar}C), 106.22 (^{Ar}C), 42.22 ($^{Et}CH_2Cl$), 34.31 ($^{Me}CH_2Cl$), 28.36 ($^{Et}CH_2$).

MS(ESI+): *m/z* (%) = 179.0 (100) $[M+H]^+$, 143.0 (31) $[M-Cl]^+$.

7.12.3 Synthesis of pyrazolate/tacn Ligands

While the symmetrical ligand **$HL^2 \cdot 7\ HClO_4$** was synthesized according to the literature known procedure,[112] the non-symmetric Ligand **$HL^{1,2} \cdot 7\ HClO_4$** was obtained via a modified synthetic route reported by SILKE BUCHLER,[135]described in the following sections.

$HL^2 \cdot 7\ HClO_4$

1,4-Diisopropyl-1,4,7-triazacyclononane (800mg, 3.75 mmol, 2.0 eq.) was added dropwise to a suspension of dry Na_2CO_3 (2.25 g, 21.2 mmol, 11.3 eq.), tetrabutylammonium bromide (226 mg, 0.7 mmol) and 3,5-bis(chloroethyl)pyrazole (432 mg, 1.88 mmol, 1.0 eq.) in MeCN (40 mL) and subsequently heated to 120 °C for 24 h. After cooling the reaction mixture to room temperature, filtration and removal of the solvent in vacuo a brown oil was obtained, which was dissolved in DCM (35 mL). The brown solution was washed with an aqueous NaOH solution (1 M, 15 mL). The aqueous phase was extracted with DCM (2 x 35 mL) and the combined organic phases dried over $MgSO_4$. The solvent was removed in vacuo and the remaining oil dissolved in dimethoxyethane (5 mL). Concentrated perchloric acid was added until the formed precipitate started to dissolve again. Addition of an ethanol/diethyl ether mixture (1:1, 25mL) led to the precipitation of a beige solid. The liquid was decantated and the solid washed with EtOH (25 mL) and Et_2O (25 mL), yielding the ligand **$HL^2 \cdot 7\ HClO_4$** (740 mg, 0.58 mmol, 31%). as an off-white solid upon drying under vacuum. The amount of $HClO_4$ molecules per molecule ligand was determined via ^{1}H NMR spectroscopy, using sodium benzoate as an internal standard.

^{1}H NMR (300 MHz, CD_3CN): *δ* (ppm) = 1.31-1.40 (m, 24 H, CH_3), 2.98-3.27 (m, 12 H, CH_2), 3.07 (s, 8 H, CH_2) 3.42-3.66 (m, 8 H, CH_2), 3.80 (sept. ^3J = 6.6 Hz, 4 H, CH), 6.59 (s, 1 H, ^{pz}CH).

^{13}C-NMR (75 MHz, CD3CN): δ [ppm] =14.5 (CH_3), 17.0 (CH_3), 45.1 (CH_2), 46.5 (CH_2), 47.5(CH_2), 51.5 (CH_2)), 57.6 (CH_2), 60.2 (CH), 106.3, 147.4

$HL^{1,2}$ · 7 $HClO_4$

Compound **s** (1.16 g, 5.39 mmol, 1.0 eq.), [TBA]Br (643 mg. 1.99 mmol, 0.37 eq.), Na_2CO_3 (6.46 g, 60.9 mmol, 11.3 eq.) were dried overnight under vacuum in a SCHLENK flask. Subsequently the solids were suspended in acetonitrile (110ml) and 1,4-di(iso-propyl)-1,4,7-triazacyclononane (2.5 g, 11.7 mmol, 2.2 eq.) was added via a syringe. The reaction mixture was then heated under reflux for 24 h at 100 °C and afterwards cooled to RT and filtered. The residue was washed with MeCN (30-50 ml) and volatiles were removed under vacuum. The resulting brown oil was dissolved in DCM (100 ml) and washed with 1 M NaOH (40 ml). The aqueous phase was extracted with DCM (3 x 80 ml) and the combined organic phases are dried with $MgSO_4$. The solvent was removed and the brown oil dried overnight under vacuum (important).

The dried oil was then dissolved in DME (16 ml) and drops of perchloric acid were added until the resulting precipitate began to dissolve again. A 1:1 solution of ethanol/diethyl ether (100 ml) was added to form a brown viscous mass which is stirred for 1-2 hours. The liquid yellow phase was decanted and EtOH (100 ml) added. A beige-colored solid formed while stirring vigorously for 24-72 h. The liquid yellow phase was decanted and Et_2O (100 mL) added to the beige solid and stirred again for 1-2 h. The liquid phase is then decanted and the light yellow/beige solid is dried in a vacuum. (3.02 g, 2.43 mmol, 45%). The amount of $HClO_4$ molecules per molecule ligand was determined via ^{1}H NMR spectroscopy, using sodium benzoate as an internal standard.

^{1}H-NMR (300 MHz, CD_3CN): δ [ppm] = 6.33 (s, 1 H, ^{Ar}CH), 3.98 (s, 2 H, $^{Me}CH_2$), 3.86-3.71 (m, 4 H), 3.66-3.57 (m, 4 H), 3.44-3.34 (m, 4 H), 3.26-3.07 (m, 2 H), 3.07-3.00 (m, 2 H), 2.98-2.85 (m, 4 H), 1.60-0.80 (m, 24 H, CH_3). Full assignment of 1H-NMR-Signals tend to be difficult due to different protonation states of the ligand.

^{13}C-NMR (75 MHz, CD3CN): δ [ppm] = 60.03 (^{iPr}CH), 48.52 (CH_2), 47.77 (CH_2), 46.95 (CH_2), 45.70 (CH_2), 44.97 (CH_2), 17.50 (CH_2), 17.21 (CH_2), 15.07 (CH_3), 14.86 (CH_3).

MS(ESI$^+$): m/z (%) = 633.5 (24) [M·$HClO_4$ + H]+, 533 (9) [M+H]+, 356,3 (34) [M-^{iPr}tacn+Cl]+, 320.3 (21) [M-^{iPr}tacn+H]+, 267.3 (100) [M+2H]$^{2+}$.

7.13 Complex Synthesis

7.13.1 $[L^2Cu_2](BPh_4)$ (**XXIX**)

The ligand **$HL^2 \cdot 7\ HClO_4$** (1.02 g, 0.81 mmol, 1.00 eq.). was suspended with KO*t*Bu (732 mg, 6.52 mmol, 8.15 eq.) in dry methanol (15 mL). A suspension of $[Cu(MeCN)_4](ClO_4)$ (531 mg, 1.6 mmol, 2.00 eq.) in methanol (2.5 mL) was then added and the yellowish reaction solution stirred for 4 h. and then passed through a WHATMAN glass microfiber filter. Addition of $NaBPh_4$ in methanol to the yellow filtrate led to the formation of a white precipitate. The supernatant solution was decanted and the white solid dissolved in acetone. Subsequent diffusion of diethyl ether at room temperature resulted in pale yellow crystals of $[LCu_2](BPh_4)$ (504 mg, 0.50 mmol, 62%).

^{1}H-NMR (300 MHz, CD_3CN): δ [ppm] = 1.23 (d, ^3J = 6.6 Hz, 12 H, CH_3), 1.24 (d, ^3J = 6.6 Hz, 12 H, CH_3), 2.46-2.64 (m, 4 H, $^{pz}CCH_2$), 2.64-2.90 (m, 28 H, CH_2), 3.14 (sept, ^3J = 6.6 Hz, 4 H, CH), 5.69 (s, 1 H, ^{pz}CH), 6.82-6.88 (m, 4H, ^{Ar}CH), 6.99-7.05 (m, 8 H, ^{Ar}CH), 7.26-7.33 (m, 8 H, ^{Ar}CH).

^{13}C-NMR (75 MHz, CD3CN): δ [ppm] = 17.5 (CH_3), 20.1 (CH_3), 25.9 ($^{pz}CCH_2$). 47.8 (CH_2), 50.9 (CH_2), 53.2 (CH_2), 57.1 (CH_2), 58.4 (CH), 102.3 (4-^{pz}C), 121.3 (^{Ar}CH), 125.2 (^{Ar}CH), 135.2 (^{Ar}CH), 149.3 (3,5-^{pz}C).

7.13.2 $[L^2Cu_2(O_2)](BPh_4)$ (**XVIII**)

Complex **XXIX** (20 mg, 20 μmol, 1.0 eq.) was dissolved in acetone (1.0 – 1.5 ml) and Et_2O (3.0 ml) was subsequently added. The solution was then transferred in a test tube which was placed in a SCHLENK tube containing Et_2O. The complex solution was then cooled down to –30 °C and the atmosphere in the SCHLENK tube was replaced by dry oxygen. Thereupon the solution was left for ET_2O diffusion at –26 °C, causing the formatting of crystalline material (15.4 mg, 15 μmol, 75%).

UV/Vis (MeCN, T=–40°C): λ_{max}[nm] (ε[$M^{-1}cm^{-1}$])= 506 (4800), 607 (sh, 3000), 800 (1140).

rR (solution, λ_{exc}=633 nm): $\tilde{\nu}_{O-O}$[cm^{-1}] = 803 ($\Delta^{16}O_2-^{18}O_2$ =54).

rR (solid, λ_{exc}=633 nm): $\tilde{\nu}_{O-O}$[cm^{-1}] = 798 ($\Delta^{16}O_2-^{18}O_2$ =49).

7.13.3 $[L^2Cu_2(NO)](BPh_4)_2$ (**10**)

$[LCu_2](BPh_4)$ (**XXIX**) (25 mg, 26 μmol, 1.0 eq.) was dissolved in MeCN (2-3 ml) and added to $NOBF_4$ (2.95 mg, 25.7 μmol, 0.99 eq.) at RT, resulting in an intense red coloring. The solution was stirred for 10-15 min and then sodium tetraphenylborate(10.6 mg, 31.2 μmol, 1.2 eq.) was added. Subsequent addition of Et_2O (8 ml) lead to the formation of a precipitate that was separated by filtration. The precipitate was washed with Et_2O (3 x 3 ml) and dissolved in as less MeCN as possible (approx. 1-2 ml). The dark red solution was left for Et_2O diffusion at −20 °C to yield crystalline material of complex **2** (yield: 4.3 mg, 3.2 μmol, 12%) after several weeks.

^{1}H-NMR (500 MHz, CD_3CN): δ (ppm) = 1.14 (d, ^3J =6.6 Hz, 12 H, CH_3), 1.36 (d, ^3J =6.6 Hz, 12 H, CH_3), 2.47 – 2.56 (m, 8 H, $^{tacn}CH_2$), 2.70 (t, ^3J =5.5 Hz, 4 H, $^{Et}CH_2$), 2.76 - 2.83 (m, 8 H, $^{tacn}CH_2$), 2.89 - 3.01(m, 12 H, ^{iPr}CH, $^{tacn}CH_2$), 3.15 (t, ^3J =5.5 Hz ,4 H, $^{Et}CH_2$), 6.24 (s, 1 H , CH^{pz}), 6.83 (t, ^3J = 7.3 Hz, 8 H, CH^{Ar}), 6.99 (t, ^3J = 7.3 Hz, 8 H, CH^{Ar}) 7.23-7.27 (m, 8H, CH^{Ar}).

^{13}C-NMR (125 MHz, CD_3CN): δ (ppm) = 15.2 (CH_3), 15.6 (CH_3), 24.2 ($^{Et}CH_2$), 45.7 ($^{tacn}CH_2$), 56.1 (^{tacn}CH), 56.3 ($^{tacn}CH_2$) , 58.7($^{tacn}CH_2$), 66.3 ($^{Et}CH_2$), 110.5(4-C^{pz}).

^{15}N-NMR (50 MHz, CD_3CN): δ (ppm) = 228 (s, ^{15}NO).

UV/Vis (EtCN, T=-90°C): λ_{max}[nm] (ε[$M^{-1}cm^{-1}$]) = 352 (9600), 392 (6400), 521 (5900).

MS(ESI^+): m/z (%) = 335.7 $[M-NO]^{2+}$ (100), 350.2 $[M]^{2+}$ (17.2), 671.4 $[M-NO]^+$ (4.3).

7.13.4 $[L^{1,2}Cu_2](BPh_4)$ (**1**)

Complex **1** was prepared according to a slightly modified routine of the symmetrical ligand systems. Therefore **$HL^{1,2}\cdot 7\ HClO_4$** (250 mg, 0.203 mmol, 1.0 eq.) was suspended together with KO^tBu (185 mg, 1.65 mmol, 8.15 eq.) in MeOH (2.0 ml). Then a suspension of $[Cu(MeCN)_4](ClO_4)$ (133 mg, 0.41 mmol, 2.00 eq.) in methanol (2.0 mL) was added. The yellow-brown reaction mixture was stirred for 2-4 h and then filtered through a Whatman filter. A solution of $NaBPh_4$(104 mg, 0,304 mmol, 1.5 eq.) in MeOH (0.5 mL) was added to the filtrate, forming a beige precipitate which was further stirred for 30 min and then filtered off. The residue was dissolved in a minimum of acetone (~0.5 mL) to form a golden-brown solution. Subsequent ether diffusion over 2-3 days led to the formation of a dark brown oil and a near colorless solution. The clear solution was collected and further diffusion of diethyl ether provided crystalline material (40 mg, 41 μmol, 20%) after 1-2 weeks.

^{1}H-NMR (300 MHz, CD_3CN): δ [ppm] = 1.10-1.15 (m, 6 H, CH_3), 1.18-1.24(m, 6 H, CH_3) ,1.33 (d, ^3J=6.6 Hz, 6 H, CH_3), 2.47-2.96 (m, 28 H, CH_2), 3.05 (sept, ^3J=6.6 Hz, 4 H, CH), 3.77 (s, 2 H, $^{pz}CH_2$), 5.72 (s, 1 H, ^{pz}CH), 6.81-6.88 (m. 4 H ^{Ar}CH), 6.96-7.03 (m, 8 H, ^{Ar}CH), 7.25-7.32 (m, 8H, ^{Ar}CH).

$^{13}C\{^1H\}$-NMR (75 MHz, CD3CN): δ [ppm] = 19.9 (CH_3), 20.6 (CH_3), 21.6 (CH_3) 26.9 ($^{Et\text{-}pz}CH_2$), 50.9 (CH_2), 51.1 (CH_2), 51.3 (CH_2), 51.8 (CH2), 52.3 (CH_2), 53.2 (CH_2), 55.3 ($^{Me\text{-}pz}CH_2$) 58.6 (CH), 58.7 (CH_2), 101.5 (4-C^{pz}), 122.7 (^{Ar}CH), 126.6 (^{Ar}CH), 136.7 (^{Ar}CH), 149.3 (C^{pz}), 150.1 (C^{pz}).

7.13.5 $[L^{1,2}Cu_2(O_2)](BPh_4)$ (**2**)

Complex **1** (30 mg, 31 μmol) was dissolved in acetone (1.0 ml) and Et_2O (1.0 ml) subsequently added. The solution was then transferred in a test tube which was placed in a SCHLENK tube containing Et_2O. The complex solution was then cooled to −30 °C and the atmosphere in the SCHLENK tube was replaced by dry oxygen. Then the solution was left for Et_2O diffusion at −26 °C for several weeks, causing the formation of crystalline material (20 mg, 19.8 μmol, 64%) suitable for X-ray diffraction analysis.

UV/Vis (MeCN, T = –40°C): λ_{max}[nm] (ε[$M^{-1}cm^{-1}$])= 437 (2000), 520 (5500), 617 (sh, 3300).

rR (solution, λ_{exc}=633 nm): $\tilde{\nu}_{O-O}$[cm^{-1}] = 804 ($\Delta^{16}O_2-^{18}O_2$ = 57).

rR (solid, λ_{exc}=633 nm): $\tilde{\nu}_{O-O}$[cm^{-1}] = 807 ($\Delta^{16}O_2-^{18}O_2$ =50).

EA: Found: C: 62.87, H: 7.88, N: 10.53. Calculated for $C_{54}H_{79}BCu_2N_8O_2\cdot H_2O$ C: 63.08, H: 7.94, N: 10.90. Complex **2** tends to be hygroscopic under aerobic conditions, therefore H_2O was taken into account.

7.13.6 [$L^{1,2}Cu_2(OH)](BPh_4)_2$ (**3**)

a) Ligand **HL**^{3} **7ClO**$_4$ (250 mg, 0.203 mmol, 1.0 eq.) was dissolved together with KO^{t}Bu (185 mg, 1.65 mmol, 8.15 eq.) in MeOH (2.0 ml). Then $Cu(ClO_4)_2\cdot 6H_2O$ (150 mg, 0.406 mmol, 2.0 eq.) in MeOH (2.5 ml) was added, whereby the golden brown solution suddenly turned dark green. The reaction solution was stirred overnight and then filtered through a Whatman filter. NaPh4 (139 mg, 0.41 mmol, 2.0 eq.) in MeOH (1 ml) was added to form a precipitate which was stirred for 1 hour. Afterwards the residue was filtered and washed with methanol (10 mL) and then dissolved in as little EtCN as necessary. Et_2O-diffusion into this solution made it possible to obtain crystalline material (150 mg, 0.11 mmol, 55%) of complex **3** suitable for X-ray structure analysis.

b) Complex **2** (20 mg, 19.8 μmol, 1.0 eq.) and $NaBPh_4$ (10mg, 29.7 μmol, 1.5 eq) was dissolved in EtCN (2 ml) at room temperature in a test tube. Diethyl ether diffusion into this solution over several days led to the isolation of dark green crystals (23 mg, 16.9 μmol, 85%) of complex **3,** also suitable for X-ray analysis.

MS (ESI(+), MeCN): m/z (%) = 337.2 (100) $[M]^{2+}$.

UV/Vis (MeCN, T=25 °C): λ_{max}[nm] (ε[$M^{-1}cm^{-1}$]) = 374.6 (4600), 630 (240).

IR (ATR): $\tilde{\nu}$[cm^{-1}] = 457 m, 602 m, 706 s, 726 s, 747 s, 1047 m, 1136 m, 1264 m, 1316 m, 1389 m, 1415 m, 1482 m, 1575 m, 2962 m, 3035 m, 3056 m, 3695 w.

EA: Found: 71.14, H: 7.77, N: 8.58. Calculated for $C_{78}H_{100}B_2Cu_2N_8O$: C: 71.37, H: 7.81, N: 8.43.

7.13.7 [$L^{1,2}Cu_2(OOH)](BPh_4)(OTf)$ (**4**)

Complex 2 (30 mg, 31 μmol, 1.0 Eq.) was dissolved in MeCN (1.5 ml) at –30 °C in a SCHLENK tube and afterwards a solution of HLutOTf (8.7 mg,34 μmol, 1.1 Eq.) in MeCN (0.5 ml) was added. A color change to intense green was observed. Layering of the solution with Et_2O (4 ml) and keeping it at -26°C for several days yielded dark green crystals of complex **4** (23.2 mg, 19.98 μmol, 64%).

UV/Vis (MeCN, T = –40°C): λ_{max}[nm] (ε[$M^{-1}cm^{-1}$])= 374 (4440), 424 (6300), 612 (610).

rR (solution, λ_{exc} = 633 nm): $\tilde{\nu}_{O-O}$[cm^{-1}] = 853 ($\Delta^{16}O_2-^{18}O_2$ = 46).

EA: Found: 56.96, H: 6.90, N: 9.60. Calculated for $C_{55}H_{80}BCu_2F_3N_8O_5S$ C: 56.94, H: 6.95, N: 9.66.

7.13.8 $[L^{1,2}Cu_2(O_2)](BPh_4)(BF_4)$ (**5**)

Crystalline material of complex **2** (10 mg, 10 µmol, 1.0 eq.) was dissolved in acetone/Et_2O (2 mL, 1:2) at −40 °C. Then a solution of $AgBF_4$ in MeCN (2.0 mg, 10.3 µmol, 1.03 eq.) was added dropwise to the solution, whereby the color changed from deep purple to intense brown.

UV/Vis (MeCN, T = −40 °C): λ_{max}[nm] (ε[$M^{-1}cm^{-1}$]) = 444 (10300),535 nm (1700 M^{-1} cm^{-1}).

rR (solution, λ_{exc} = 457 nm): $\tilde{\nu}_{O-O}$[cm^{-1}] = 1074 cm^{-1} ($\Delta^{16}O_2$–$^{18}O_2$ =58 cm^{-1}).

7.13.9 $[L^1Cu_2(O_2)(Li^+)](BPh_4)(OTf)$ (**6**)

Crystalline material of complex **2** (30 mg, 31 μmol, 1.0 eq.) was dissolved under cooling at –40 °C in acetone/Et_2O (2 ml, 1:1) inside a test tube surrounded by Et_2O. Subsequently a solution of LiOTf (9.7 mg, 62 μmol, 2.0 eq.) in acetone (0.5 – 1.0 ml) was slowly added. Diffusion of Et_2O at –26°C into this solution led to the isolation of crystalline materials within several weeks.

UV/Vis (MeCN, T = −40 °C): λ_{max}[nm] (ε[$M^{-1}cm^{-1}$])= 367 (2200 M^{-1}), 434 (4000).

7.13.10 $[L^1Cu_2(O_2)((CH_3)_2CO)(NaOTf)]_2(BPh_4)_2$ (**7**)

Crystalline material of complex **2** (30 mg, 31 μmol, 1.0 eq.) was dissolved under cooling at –40 °C in acetone/Et_2O (2 ml, 1:1) inside a test tube surrounded by Et_2O. Subsequently a solution of NaOTf (10.7 mg, 62 μmol, 2.0 eq.) in acetone (0.5 – 1.0 ml) was slowly added. Diffusion of Et_2O at –26°C into this solution led to the isolation of crystalline material suitable for X-ray analysis within several weeks.

7.13.11 $[L^{1,2}Cu_2(O_2)(MeOH](BPh_4)$ (**8**)

Complex **1** (30 mg, 31 μmol) was dissolved in acetone (0.5 ml) and MeOH (2 ml) and put in a SCHLENK tube and cooled to approximately −40 °C. Then the atmosphere was exchanged by oxygen, whereas the colorless solution turned intense purple/brown. Crystallization proceeded at –26 °C over several days, yielding dark crystalline material (25 mg, 23 μmol, 74%).

UV/Vis (MeCN, T = −40 °C): λ_{max}[nm] (ε[$M^{-1}cm^{-1}$])= 400 (2500), 490 (5600).

rR (solid, λ_{exc}=633 nm): $\tilde{\nu}_{O-O}$[cm^{-1}] = 808 ($\Delta^{16}O_2$–$^{18}O_2$ = 51).

7.13.12 $[L^{1,2}Cu_2(O_2)(TFE)](BPh_4)$ (**9**)

Complex **1** (30 mg, 31 μmol) was dissolved in acetone (0.9 ml), put in a SCHLENK tube and cooled to approximately −40 °C. Then the atmosphere was exchanged by oxygen, whereas the colourless solution turned intense purple. Subsequently 2,2,2-trifluorethanol (0.1 ml) was added and the solution left for Et_2O diffusion at –26 °C over several weeks, yielding dark crystalline material.

UV/Vis (MeCN, T = –40°C): λ_{max}[nm] (ε[$M^{-1}cm^{-1}$])= 404 (2100), 495 (5800).

rR (solid, λ_{exc}=633 nm): $\tilde{\nu}_{0-0}$[cm^{-1}] = 808 .

8 References

(1) Kaim, W.; Schwederski, B.; Klein, A. *Bioinorganic Chemistry: Inorganic Elements in the Chemstry of Life*, 2nd ed.; Wiley, 2013.

(2) Karlin, K. D.; Lippard, S. J.; Valentine, J. S.; Burrows, C. J. Solving 21st Century Problems in Biological Inorganic Chemistry Using Synthetic Models. *Acc. Chem. Res.* **2015**, *48*, 2659–2660.

(3) Lippard, S. J.; Berg, J. M. *Principles of Bioinorganic Chemistry*; University Science Books, 2009.

(4) Yannone, S. M.; Hartung, S.; Menon, A. L.; Adams, M. W. W.; Tainer, J. A. Metals in Biology: Defining Metalloproteomes. *Curr. Opin. Biotechnol.* **2012**, *23*, 89–95.

(5) Waldron, K. J.; Rutherford, J. C.; Ford, D.; Robinson, N. J. Metalloproteins and Metal Sensing. *Nature* **2009**, *460*, 823–830.

(6) Lu, Y.; Yeung, N.; Sieracki, N.; Marshall, N. M. Design of Functional Metalloproteins. *Nature* **2009**, *460*, 855–862.

(7) Murakami, Y.; Kikuchi, J.; Hisaeda, Y.; Hayashida, O. Artificial Enzymes. *Chem. Rev.* **1996**, *96*, 721–758.

(8) Rihel, J. Copper on the Brain. *Nat. Chem. Biol.* **2018**, *14*, 638–639.

(9) Giacovazzi, R.; Ciofini, I.; Rao, L.; Amatore, C.; Adamo, C. Copper-Amyloid-β Complex May Catalyze Peroxynitrite Production in Brain: Evidence from Molecular Modeling. *Phys. Chem. Chem. Phys.* **2014**, *16*, 10169–10174.

(10) Bandara, N.; Sharma, A. K.; Krieger, S.; Schultz, J. W.; Han, B. H.; Rogers, B. E.; Mirica, L. M. Evaluation of ^{64}Cu-Based Radiopharmaceuticals That Target Aβ Peptide Aggregates as Diagnostic Tools for Alzheimer's Disease. *J. Am. Chem. Soc.* **2017**, *139*, 12550–12558.

(11) Desoize, B. Metals and Metal Compounds in Cancer Treatment. *Anticancer Res.* **2004**, *24*, 1529–1544.

(12) Frezza, M.; Hindo, S.; Chen, D.; Davenport, A.; Schmitt, S.; Tomco, D.; Ping Dou, Q. Novel Metals and Metal Complexes as Platforms for Cancer Therapy. *Curr. Pharm. Des.* **2010**, *16*, 1813–1825.

(13) Englinger, B.; Pirker, C.; Heffeter, P.; Terenzi, A.; Kowol, C. R.; Keppler, B. K.; Berger, W. Metal Drugs and the Anticancer Immune Response. *Chem. Rev.* **2019**, *119*, 1519–1624.

(14) Solomon, E. I.; Heppner, D. E.; Johnston, E. M.; Ginsbach, J. W.; Cirera, J.; Qayyum, M.; Kieber-Emmons, M. T.; Kjaergaard, C. H.; Hadt, R. G.; Tian, L. Copper Active Sites in Biology. *Chem. Rev.* **2014**, *114*, 3659–3853.

(15) Elwell, C. E.; Gagnon, N. L.; Neisen, B. D.; Dhar, D.; Spaeth, A. D.; Yee, G. M.; Tolman, W. B. Copper-Oxygen Complexes Revisited: Structures, Spectroscopy, and Reactivity. *Chem. Rev.* **2017**, *117*, 2059–2107.

(16) Dupont, C. L.; Butcher, A.; Valas, R. E.; Bourne, P. E.; Caetano-Anollés, G. History of Biological Metal Utilization Inferred through Phylogenomic Analysis of Protein Structures. *Proc. Natl. Acad. Sci. U. S. A.* **2010**, *107*, 10567–10572.

(17) Ochiai, E. Copper and the Biological Evolution. *BioSystems* **1983**, *16*, 81–86.

(18) Festa, R. A.; Thiele, D. J. Copper: An Essential Metal in Biology. *Curr. Biol.* **2011**, *21*, 877–883.

(19) Tishchenko, K. I.; Beloglazkina, E. K.; Mazhuga, A. G.; Zyk, N. V. Copper-Containing Enzymes: Site Types and Low-Molecular-Weight Model Compounds. *Rev. J. Chem.* **2016**, *6*, 49–82.

(20) Koval, I. A.; Gamez, P.; Belle, C.; Selmeczi, K.; Reedijk, J. Synthetic Models of the Active Site of Catechol Oxidase: Mechanistic Studies. *Chem. Soc. Rev.* **2006**, *35*, 814–840.

(21) Solomon, E. I. Spectroscopic Methods in Bioinorganic Chemistry: Blue to Green to Red Copper Sites. *Inorg. Chem.* **2006**, *45*, 8012–8025.

(22) Dennison, C. Investigating the Structure and Function of Cupredoxins. *Coord. Chem. Rev.* **2005**, *249*, 3025–3054.

(23) Zong, C.; Wilson, C. J.; Shen, T.; Wittung-Stafshede, P.; Mayo, S. L.; Wolynes, P. G. Establishing the Entatic State in Folding Metallated Pseudomonas Aeruginosa Azurin. *Proc. Natl. Acad. Sci. U. S. A.* **2007**, *104*, 3159–3164.

(24) Solomon, E. I.; Hadt, R. G. Recent Advances in Understanding Blue Copper Proteins. *Coord. Chem. Rev.* **2011**, *255*, 774–789.

(25) Cattani, G.; Vogeley, L.; Crowley, P. B. Structure of a PEGylated Protein Reveals a Highly Porous Double-Helical Assembly. *Nat. Chem.* **2015**, *7*, 823–828.

(26) Solomon, E. I.; Baldwin, M. J.; Lowery, M. D. Electronic Structures of Active Sites in Copper Proteins: Contributions to Reactivity. *Chem. Rev.* **1992**, *92*, 521–542.

(27) Colman, P. M.; Freeman, H. C.; Guss, J. M.; Murata, M.; Norris, V. A.; Ramshaw, J. A. M.; Venkatappat, M. P. X-Ray Crystal Structure Analysis of Plastocyanin at 2.7 Å Resolution. *Nature* **1978**, *272*, 319–324.

(28) Gray, H. B.; Malmström, B. G.; Williams, R. J. P. Copper Coordination in Blue Proteins. *J. Biol. Inorg. Chem.* **2000**, *5*, 551–559.

(29) Que Jr, L.; Tolman, W. B. Biologically Inspired Oxidation Catalysis. *Nature* **2008**, *455*, 333–340.

(30) Ito, N.; Phillips, S. E. V.; Stevens, C.; Ogel, Z. B.; McPherson, M. J.; Keen, J. N.; Yadav, K. D. S.; Knowles, P. F. Novel Thioether Bond Revealed by a 1.7 Å Crystal Structure of Galactose Oxidase. *Nature* **1991**, *350*, 87–90.

(31) Humphreys, K. J.; Mirica, L. M.; Wang, Y.; Klinman, J. P. Galactose Oxidase as a Model for Reactivity at a Copper Superoxide Center. *J. Am. Chem. Soc.* **2009**, *131*, 4657–4663.

(32) Chen, P.; Solomon, E. I. Oxygen Activation by the Noncoupled Binuclear Copper Site in Peptidylglycine α-Hydroxylating Monooxygenase. Reaction Mechanism and Role of the

Noncoupled Nature of the Active Site. *J. Am. Chem. Soc.* **2004**, *126*, 4991–5000.

(33) Prigge, S. T.; Eipper, B. A.; Mains, R. E.; Amzel, L. M. Dioxygen Binds End-On to Mononuclear Copper in a Precatalytic Enzyme Complex. *Science* **2004**, *304*, 864–867.

(34) Rogers, M. S.; Tyler, E. M.; Akyumani, N.; Kurtis, C. R.; Spooner, R. K.; Deacon, S. E.; Tamber, S.; Firbank, S. J.; Mahmoud, K.; Knowles, P. F.; Phillips, S. E. V.; McPherson, M. J.; Dooley, D. M. The Stacking Tryptophan of Galactose Oxidase: A Second-Coordination Sphere Residue That Has Profound Effects on Tyrosyl Radical Behavior and Enzyme Catalysis. *Biochemistry* **2007**, *46*, 4606–4618.

(35) Yin, D. T.; Urresti, S.; Lafond, M.; Johnston, E. M.; Derikvand, F.; Ciano, L.; Berrin, J.-G.; Henrissat, B.; Walton, P. H.; Davies, G. J.; Brumer, H. Structure-Function Characterization Reveals New Catalytic Diversity in the Galactose Oxidase and Glyoxal Oxidase Family. *Nat. Commun.* **2015**, *6*, 10197.

(36) Zumft, W. G. Cell Biology and Molecular Basis of Denitrification. *Microbiol. Mol. Biol. Rev.* **1997**, *61*, 533–616.

(37) Knowles, R. Denitrification. *Microbiol. Rev.* **1982**, *46*, 43–70.

(38) Horrell, S.; Kekilli, D.; Strange, R. W.; Hough, M. A. Recent Structural Insights into the Function of Copper Nitrite Reductases. *Metallomics* **2017**, *9*, 1470–1482.

(39) Tocheva, E. I.; Rosell, F. I.; Mauk, A. G.; Murphy, M. E. P. Side-On Copper-Nitrosyl Coordination by Nitrite Reductase. *Science* **2004**, *304*, 867–870.

(40) Ghosh, S.; Dey, A.; Sun, Y.; Scholes, C. P.; Solomon, E. I. Spectroscopic and Computational Studies of Nitrite Reductase: Proton Induced Electron Transfer and Backbonding Contributions to Reactivity. *J. Am. Chem. Soc.* **2009**, *131*, 277–288.

(41) Lintuluoto, M.; Lintuluoto, J. M. DFT Study on Nitrite Reduction Mechanism in Copper-Containing Nitrite Reductase. *Biochemistry* **2016**, *55*, 210–223.

(42) Merkle, A. C.; Lehnert, N. Binding and Activation of Nitrite and Nitric Oxide by Copper Nitrite Reductase and Corresponding Model Complexes. *Dalton Trans.* **2012**, *41*, 3355–3368.

(43) Li, Y.; Hodak, M.; Bernholc, J. Enzymatic Mechanism of Copper-Containing Nitrite Reductase. *Biochemistry* **2015**, *54*, 1233–1242.

(44) Decker, H.; Schweikardt, T.; Tuczek, F. The First Crystal Structure of Tyrosinase: All Questions Answered? *Angew. Chem. Int. Ed.* **2006**, *45*, 4546–4550.

(45) Matoba, Y.; Kumagai, T.; Yamamoto, A.; Yoshitsu, H.; Sugiyama, M. Crystallographic Evidence That the Dinuclear Copper Center of Tyrosinase Is Flexible during Catalysis. *J. Biol. Chem.* **2006**, *281*, 8981–8990.

(46) Van Holde, K. E.; Miller, K. I.; Decker, H. Hemocyanins and Invertebrate Evolution. *J. Biol. Chem.* **2001**, *276*, 15563–15566.

(47) Quist, D. A.; Diaz, D. E.; Liu, J. J.; Karlin, K. D. Activation of Dioxygen by Copper Metalloproteins and Insights from Model Complexes. *J. Biol. Inorg. Chem.* **2016**, *22*, 253–288.

(48) Magnus, K. A.; Hazes, B.; Ton-That, H.; Bonaventura, C.; Bonaventura, J.; Hol, W. G. J. Crystallographic Analysis of Oxygenated and Deoxygenated States of Arthropod Hemocyanin Shows Unusual Differences. *Proteins Struct. Funct. Bioinforma.* **1994**, *19*, 302–309.

(49) Solomon, E. I.; Chen, P.; Metz, M.; Lee, S. K.; Palmer, A. E. Oxygen Binding, Activation, and Reduction to Water by Copper Proteins. *Angew. Chem. Int. Ed.* **2001**, *40*, 4570–4590.

(50) Metz, M.; Solomon, E. I. Dioxygen Binding to Deoxyhemocyanin: Electronic Structure and Mechanism of the Spin-Forbidden Two-Electron Reduction of O_2. *J. Am. Chem. Soc.* **2001**, *123*, 4938–4950.

(51) Solomon, E. I. Dioxygen Binding, Activation, and Reduction to H_2O by Cu Enzymes. *Inorg. Chem.* **2016**, *55*, 6364–6375.

(52) Dalle, K. E.; Gruene, T.; Dechert, S.; Demeshko, S.; Meyer, F. Weakly Coupled Biologically Relevant $Cu^{II}_2(\mu\text{-}\eta^1\text{:}\eta^1\text{-}O_2)$ Cis -Peroxo Adduct That Binds Side-on to Additional Metal Ions. *J. Am. Chem. Soc.* **2014**, *136*, 7428–7434.

(53) Solomon, E. I.; Sundaram, U. M.; Machonkin, T. E. Multicopper Oxidases and Oxygenases. *Chem. Rev.* **1996**, *96*, 2563–2605.

(54) Rubino, J. T.; Franz, K. J. Coordination Chemistry of Copper Proteins: How Nature Handles a Toxic Cargo for Essential Function. *J. Inorg. Biochem.* **2012**, *107*, 129–143.

(55) Bertrand, T.; Jolivalt, C.; Briozzo, P.; Caminade, E.; Joly, N.; Madzak, C.; Mougin, C. Crystal Structure of a Four-Copper Laccase Complexed with an Arylamine: Insights into Substrate Recognition and Correlation with Kinetics. *Biochemistry* **2002**, *41*, 7325–7333.

(56) Enguita, F. J.; Marçal, D.; Martins, L. O.; Grenha, R.; Henriques, A. O.; Lindley, P. F.; Carrondo, M. A. Substrate and Dioxygen Binding to the Endospore Coat Laccase from Bacillus Subtilis. *J. Biol. Chem.* **2004**, *279*, 23472–23476.

(57) Taylor, A. B.; Stoj, C. S.; Ziegler, L.; Kosman, D. J.; Hart, P. J. The Copper-Iron Connection in Biology: Structure of the Metallo-Oxidase Fet3p. *Proc. Natl. Acad. Sci. U. S. A.* **2005**, *102*, 15459–15464.

(58) Enguita, F. J.; Martins, L. O.; Henriques, A. O.; Carrondo, M. A. Crystal Structure of a Bacterial Endospore Coat Component: A Laccase with Enhanced Thermostability Properties. *J. Biol. Chem.* **2003**, *278*, 19416–19425.

(59) Solomon, E. I.; Ginsbach, J. W.; Heppner, D. E.; Kieber-Emmons, M. T.; Kjaergaard, C. H.; Smeets, P. J.; Tian, L.; Woertink, J. S. Copper Dioxygen (Bio)Inorganic Chemistry. *Farrad. Discuss.* **2011**, *148*, 11–39.

(60) Sekretaryova, A.; Jones, S. M.; Solomon, E. I. O_2 Reduction to Water by High Potential Multicopper Oxidases: Contributions of the T1 Copper Site Potential and the Local

Environment of the Trinuclear Copper Cluster. *J. Am. Chem. Soc.* **2019**, *141*, 11304–11314.

(61) Cole, J. L.; Solomon, E. I.; Ballou, D. P. Spectroscopic Characterization of the Peroxide Intermediate in the Reduction of Dioxygen Catalyzed by the Multicopper Oxidases. *J. Am. Chem. Soc.* **1991**, *113*, 8544–8546.

(62) Shin, W.; Sundaram, U. M.; Cole, J. L.; Zhang, H. H.; Hedman, B.; Hodgson, K. O.; Solomon, E. I. Chemical and Spectroscopic Definition of the Peroxide-Level Intermediate in the Multicopper Oxidases: Relevance to the Catalytic Mechanism of Dioxygen Reduction to Water. *J. Am. Chem. Soc.* **1996**, *118*, 3202–3215.

(63) Lee, S. K.; George, S. D. B.; Antholine, W. E.; Hedman, B.; Hodgson, K. O.; Solomon, E. I. Nature of the Intermediate Formed in the Reduction of O_2 to H_2O at the Trinuclear Copper Cluster Active Site in Native Laccase. *J. Am. Chem. Soc.* **2002**, *124*, 6180–6193.

(64) Heppner, D. E.; Kjaergaard, C. H.; Solomon, E. I. Molecular Origin of Rapid versus Slow Intramolecular Electron Transfer in the Catalytic Cycle of the Multicopper Oxidases. *J. Am. Chem. Soc.* **2013**, *135*, 12212–12215.

(65) Heppner, D. E.; Kjaergaard, C. H.; Solomon, E. I. Mechanism of the Reduction of the Native Intermediate in the Multicopper Oxidases: Insights into Rapid Intramolecular Electron Transfer in Turnover. *J. Am. Chem. Soc.* **2014**, *136*, 17788–17801.

(66) Solomon, E. I.; Augustine, A. J.; Yoon, J. O_2 Reduction to H_2O by the Multicopper Oxidases. *Dalton Trans.* **2008**, *9226*, 3921–3932.

(67) Schaefer, A. W.; Roveda, A. C.; Jose, A.; Solomon, E. I. Geometric and Electronic Structure Contributions to O-O Cleavage and the Resultant Intermediate Generated in Heme-Copper Oxidases. *J. Am. Chem. Soc.* **2019**, *141*, 10068–10081.

(68) Schaefer, A. W.; Kieber-Emmons, M. T.; Adam, S. M.; Karlin, K. D.; Solomon, E. I. Phenol-Induced O-O Bond Cleavage in a Low-Spin Heme-Peroxo-Copper Complex: Implications for O2 Reduction in Heme-Copper Oxidases. *J. Am. Chem. Soc.* **2017**, *139*, 7958–7973.

(69) Schaefer, A. W.; Ehudin, M. A.; Quist, D. A.; Tang, J. A.; Karlin, K. D.; Solomon, E. I. Spin Interconversion of Heme-Peroxo-Copper Complexes Facilitated by Intramolecular Hydrogen-Bonding Interactions. *J. Am. Chem. Soc.* **2019**, *141*, 4936–4951.

(70) Poiana, F.; Von Ballmoos, C.; Gonska, N.; Blomberg, M. R. A.; Ädelroth, P.; Brzezinski, P. Splitting of the O–O Bond at the Heme-Copper Catalytic Site of Respiratory Oxidases. *Sci. Adv.* **2017**, *3*, 1–9.

(71) Iwata, S.; Ostermeier, C.; Ludwig, B.; Michel, H. Structure at 2.8 Å Resolution of Cytochrome c Oxidase from Paracoccus Denitrificans. *Nature* **1995**, *376*, 660–669.

(72) Tsukihara, T.; Aoyama, H.; Yamashita, E.; Tomizaki, T.; Yamaguchi, H.; Shinzawa-Itoh, K.; Nakashima, R.; Yaono, R.; Yoshikawa, S. Structures of Metal Sites of Oxidized Bovine Heart Cytochrome c Oxidase at 2.8 Å. *Science* **1995**, *269*, 1069–1074.

(73) Savelieff, M. G.; Lu, Y. CuA Centers and Their Biosynthetic Models in Azurin. *J. Biol. Inorg. Chem.* **2010**, *15*, 461–483.

(74) Zhang, S.; Warren, T. H. Three Coordinate Models for the Binuclear CuA Electron-Transfer Site. *Chem. Sci.* **2013**, *4*, 1786–1792.

(75) Pomowski, A.; Zumft, W. G.; Kroneck, P. M. H.; Einsle, O. N_2O Binding at a [4Cu:2S] Copper-Sulphur Cluster in Nitrous Oxide Reductase. *Nature* **2011**, *477*, 234–237.

(76) Dell'Acqua, S.; Pauleta, S. R.; Moura, I.; Moura, J. J. G. The Tetranuclear Copper Active Site of Nitrous Oxide Reductase: The CuZ Center. *J. Biol. Inorg. Chem.* **2011**, *16*, 183–194.

(77) Tavares, P.; Pereira, A. S.; Moura, J. J. G.; Moura, I. Metalloenzymes of the Denitrification Pathway. *J. Inorg. Biochem.* **2006**, *100*, 2087–2100.

(78) Dell'Acqua, S.; Pauleta, S. R.; De Sousa, P. M. P.; Monzani, E.; Casella, L.; Moura, J. J. G.; Moura, I. A New CuZ Active Form in the Catalytic Reduction of N_2O by Nitrous Oxide Reductase from Pseudomonas Nautica. *J. Biol. Inorg. Chem.* **2010**, *15*, 967–976.

(79) Johnston, E. M.; Carreira, C.; Dell'Acqua, S.; Dey, S. G.; Pauleta, S. R.; Moura, I.; Solomon, E. I. Spectroscopic Definition of the CuZ° Intermediate in Turnover of Nitrous Oxide Reductase and Molecular Insight into the Catalytic Mechanism. *J. Am. Chem. Soc.* **2017**, *139*, 4462–4476.

(80) Rathnayaka, S. C.; Mankad, N. P. Coordination Chemistry of the CuZ Site in Nitrous Oxide Reductase and Its Synthetic Mimics. *Coord. Chem. Rev.* **2021**, *429*, 213718.

(81) Rasmussen, T.; Berks, B. C.; Butt, J. N.; Thomson, A. J. Multiple Forms of the Catalytic Centre, Cuz, in the Enzyme Nitrous Oxide Reductase from Paracoccus Pantotrophus. *Biochem. J.* **2002**, *364*, 807–815.

(82) Alvarez, M. L.; Ai, J.; Zumft, W.; Sanders-Loehr, J.; Dooley, D. M. Characterization of the Copper-Sulfur Chromophores in Nitrous Oxide Reductase by Resonance Raman Spectroscopy: Evidence for Sulfur Coordination in the Catalytic Cluster. *J. Am. Chem. Soc.* **2001**, *123*, 576–587.

(83) Walton, P. H.; Davies, G. J. On the Catalytic Mechanisms of Lytic Polysaccharide Monooxygenases. *Curr. Opin. Chem. Biol.* **2016**, *31*, 195–207.

(84) Simmons, T. J.; Frandsen, K. E. H.; Ciano, L.; Tryfona, T.; Lenfant, N.; Poulsen, J. C.; Wilson, L. F. L.; Tandrup, T.; Tovborg, M.; Schnorr, K.; Johansen, K. S.; Henrissat, B.; Walton, P. H.; Lo Leggio, L.; Dupree, P. Structural and Electronic Determinants of Lytic Polysaccharide Monooxygenase Reactivity on Polysaccharide Substrates. *Nat. Commun.* **2017**, *8*, 1–12.

(85) Paradisi, A.; Johnston, E. M.; Tovborg, M.; Nicoll, C. R.; Ciano, L.; Dowle, A.; Mcmaster, J.; Hancock, Y.; Davies, G. J.; Walton, P. H. Formation of a Copper(II)-Tyrosyl Complex at the Active Site of Lytic Polysaccharide Monooxygenases Following Oxidation by H_2O_2. *J. Am. Chem. Soc.* **2019**, *141*, 18585–18599.

(86) Lieberman, R. L.; Kondapalli, K. C.; Shrestha, D. B.; Hakemian, A. S.; Smith, S. M.; Telser, J.;

Kuzelka, J.; Gupta, R.; Borovik, A. S.; Lippard, S. J.; Hoffman, B. M.; Rosenzweig, A. C.; Stemmler, T. L. Characterization of the Particulate Methane Monooxygenase Metal Centers in Multiple Redox States by X-Ray Absorption Spectroscopy. *Inorg. Chem.* **2006**, *45*, 8372–8381.

(87) Balasubramanian, R.; Smith, S. M.; Rawat, S.; Yatsunyk, L. A.; Stemmler, T. L.; Rosenzweig, A. C. Oxidation of Methane by a Biological Dicopper Centre. *Nature* **2010**, *465*, 115–119.

(88) Koo, C. W.; Rosenzweig, A. C. Biochemistry of Aerobic Biological Methane Oxidation. *Chem. Soc. Rev.* **2021**, *50*, 3424–3436.

(89) Wang, B.; Walton, P. H.; Rovira, C. Molecular Mechanisms of Oxygen Activation and Hydrogen Peroxide Formation in Lytic Polysaccharide Monooxygenases. *ACS Catal.* **2019**, *9*, 4958–4969.

(90) VanNatta, P. E.; Ramirez, D. A.; Velarde, A. R.; Ali, G.; Kieber-Emmons, M. T. Exceptionally High O-H Bond Dissociation Free Energy of a Dicopper(II) μ-Hydroxo Complex and Insights into the Geometric and Electronic Structure Origins Thereof. *J. Am. Chem. Soc.* **2020**, *142*, 16292–16312.

(91) Klinman, J. P. The Copper-Enzyme Family of Dopamine β-Monooxygenase and Peptidylglycine α-Hydroxylating Monooxygenase: Resolving the Chemical Pathway for Substrate Hydroxylation. *J. Biol. Chem.* **2006**, *281*, 3013–3016.

(92) Itoh, S. Developing Mononuclear Copper-Active-Oxygen Complexes Relevant to Reactive Intermediates of Biological Oxidation Reactions. *Acc. Chem. Res.* **2015**, *48*, 2066–2074.

(93) Solomon, E. I.; Tuczek, F.; Root, D. E.; Brown, C. A. Spectroscopy of Binuclear Dioxygen Complexes. *Chem. Rev.* **1994**, *94*, 827–856.

(94) Lewis, E. A.; Tolman, W. B. Reactivity of Dioxygen − Copper Systems. *Chem. Rev.* **2004**, *104*, 1047–1076.

(95) Lee, J. Y.; Karlin, K. D. Elaboration of Copper-Oxygen Mediated CH Activation Chemistry in Consideration of Future Fuel and Feedstock Generation. *Curr. Opin. Chem. Biol.* **2015**, *25*, 184–193.

(96) Mann, S. I.; Heinisch, T.; Ward, T. R.; Borovik, A. S. Peroxide Activation Regulated by Hydrogen Bonds within Artificial Cu Proteins. *J. Am. Chem. Soc.* **2017**, *139*, 17289–17292.

(97) Bhadra, M.; Lee, J. Y. C.; Cowley, R. E.; Kim, S.; Siegler, M. A.; Solomon, E. I.; Karlin, K. D. Intramolecular Hydrogen Bonding Enhances Stability and Reactivity of Mononuclear Cupric Superoxide Complexes. *J. Am. Chem. Soc.* **2018**, *140*, 9042–9045.

(98) Chen, P.; Root, D. E.; Campochiaro, C.; Fujisawa, K.; Solomon, E. I. Spectroscopic and Electronic Structure Studies of the Diamagnetic Side-on Cu^{II}-Superoxo Complex $Cu(O_2)[HB(3\text{-}R\text{-}5\text{-}{}^{i}Prpz)_3]$: Antiferromagnetic Coupling versus Covalent Delocalization. *J. Am. Chem. Soc.* **2003**, *125*, 466–474.

(99) Würtele, C.; Gaoutchenova, E.; Harms, K.; Holthausen, M. C.; Sundermeyer, J.; Schindler, S. Crystallographic Characterization of a Synthetic 1:1 End-on Copper Dioxygen Adduct

Complex. *Angew. Chem. Int. Ed.* **2006**, *45*, 3867–3869.

(100) Woertink, J. S.; Tian, L.; Maiti, D.; Lucas, H. R.; Himes, R. A.; Karlin, K. D.; Neese, F.; Würtele, C.; Holthausen, M. C.; Bill, E.; Sundermeyer, J.; Schindler, S.; Solomon, E. I. Spectroscopic and Computational Studies of an End-on Bound Superoxo-Cu(II) Complex: Geometric and Electronic Factors That Determine the Ground State. *Inorg. Chem.* **2010**, *49*, 9450–9459.

(101) Peterson, R. L.; Ginsbach, J. W.; Cowley, R. E.; Qayyum, M. F.; Himes, R. A.; Siegler, M. A.; Moore, C. D.; Hedman, B.; Hodgson, K. O.; Fukuzumi, S.; Solomon, E. I.; Karlin, K. D. Stepwise Protonation and Electron-Transfer Reduction of a Primary Copper-Dioxygen Adduct. *J. Am. Chem. Soc.* **2013**, *135*, 16454–16467.

(102) Peterson, R. L.; Himes, R. A.; Kotani, H.; Suenobu, T.; Tian, L.; Siegler, M. A.; Solomon, E. I.; Fukuzumi, S.; Karlin, K. D. Cupric Superoxo-Mediated Intermolecular C-H Activation Chemistry. *J. Am. Chem. Soc.* **2011**, *133*, 1702–1705.

(103) Dhar, D.; Tolman, W. B. Hydrogen Atom Abstraction from Hydrocarbons by a Copper(III)-Hydroxide Complex. *J. Am. Chem. Soc.* **2015**, *137*, 1322–1329.

(104) Jacobson, R. R.; Tyeklar, Z.; Farooq, A.; Karlin, K. D.; Liu, S.; Zubieta, J. A Cu_2-O_2 Complex. Crystal Structure and Characterization of a Reversible Dioxygen Binding System. *J. Am. Chem. Soc.* **1988**, *110*, 3690–3692.

(105) Kitajima, N.; Fujisawa, K.; Fujimoto, C.; Moro-oka, Y.; Hashimoto, S.; Kitagawa, T.; Toriumi, K.; Tatsumi, K.; Nakamura, A. A New Model for Dioxygen Binding in Hemocyanin. Synthesis, Characterization, and Molecular Structure of the μ-η^2:η^2 Peroxo Dinuclear Copper(II) Complexes, $[Cu(HB(3,5\text{-}R_2Pz)_3)]_2(O_2)$ (R = i-Pr. *J. Am. Chem. Soc.* **1992**, *114*, 1277–1291.

(106) Henson, M. J.; Mahadevan, V.; Stack, T. D. P.; Solomon, E. I. A New Cu(II) Side-on Peroxo Model Clarifies the Assignment of the Oxyhemocyanin Raman Spectrum. *Inorg. Chem.* **2001**, *40*, 5068–5069.

(107) Mirica, L. M.; Ottenwaelder, X.; Stack, T. D. P. Structure and Spectroscopy of Copper – Dioxygen Complexes. *Chem. Rev.* **2004**, *104*, 1013–1045.

(108) Halfen, J. A.; Mahapatra, S.; Wilkinson, E. C.; Kaderli, S.; Young, V. G.; Que, L.; Zuberbühler, A. D.; Tolman, W. B. Reversible Cleavage and Formation of the Dioxygen O-O Bond within a Dicopper Complex. *Science* **1996**, *271*, 1397–1400.

(109) Holland, P. L.; Cramer, C. J.; Wilkinson, E. C.; Mahapatra, S.; Rodgers, K. R.; Itoh, S.; Taki, M.; Fukuzumi, S.; Que, L.; Tolman, W. B.; Chemistry, A.; V, O. U. Resonance Raman Spectroscopy as a Probe of the Bis (μ-Oxo) Dicopper Core. *J. Am. Chem. Soc.* **2000**, *122*, 792–802.

(110) Ross, M. O.; Rosenzweig, A. C. A Tale of Two Methane Monooxygenases. *J. Biol. Inorg. Chem.* **2016**, *22*, 307–319.

(111) Miyanishi, M.; Abe, T.; Hori, Y.; Shiota, Y.; Yoshizawa, K. Role of Amino Acid Residues for Dioxygen Activation in the Second Coordination Sphere of the Dicopper Site of PMMO. *Inorg.*

Chem. **2019**, *58*, 12280–12288.

(112) Kindermann, N.; Bill, E.; Dechert, S.; Demeshko, S.; Reijerse, E. J.; Meyer, F. A Ferromagnetically Coupled (S = 1) Peroxodicopper(II) Complex. *Angew. Chem. Int. Ed.* **2015**, *54*, 1738–1743.

(113) Brinkmeier, A. Bimetallic Copper Complexes for Bioinspired Dioxygen Activation and Catalytic Water Oxidation, *Dissertation*, Georg-August-Universität Göttingen, **2017**.

(114) Vargo, N. P.; Harland, J. B.; Musselman, B. W.; Lehnert, N.; Ertem, M. Z.; Robinson, J. R. Calcium-ion Binding Mediates the Reversible Interconversion of Cis and Trans Peroxido Dicopper Cores. *Angew. Chem. Int. Ed.* **2021**.

(115) Garcia-Bosch, I.; Cowley, R. E.; Diaz, D. E.; Peterson, R. L.; Solomon, E. I.; Karlin, K. D. Substrate and Lewis Acid Coordination Promote O–O Bond Cleavage of an Unreactive $L_2Cu^{II}_2(O_2^{2-})$ Species to Form $L_2Cu^{III}_2(O)_2$ Cores with Enhanced Oxidative R. *J. Am. Chem. Soc.* **2017**, *139*, 3186–3195.

(116) Dahl, E. W.; Dong, H. T.; Szymczak, N. K. Phenylamino Derivatives of Tris(2-Pyridylmethyl)Amine: Hydrogen-Bonded Peroxodicopper Complexes. *Chem. Commun.* **2018**, *54*, 892–895.

(117) Kindermann, N.; Günes, C. J.; Dechert, S.; Meyer, F. Hydrogen Atom Abstraction Thermodynamics of a μ-1,2-Superoxo Dicopper(II) Complex. *J. Am. Chem. Soc.* **2017**, *139*, 9831–9834.

(118) Cao, R.; Saracini, C.; Ginsbach, J. W.; Kieber-Emmons, M. T.; Siegler, M. A.; Solomon, E. I.; Fukuzumi, S.; Karlin, K. D. Peroxo and Superoxo Moieties Bound to Copper Ion: Electron-Transfer Equilibrium with a Small Reorganization Energy. *J. Am. Chem. Soc.* **2016**, *138*, 7055–7066.

(119) Quist, D. A.; Ehudin, M. A.; Schaefer, A. W.; Schneider, G. L.; Solomon, E. I.; Karlin, K. D. Ligand Identity-Induced Generation of Enhanced Oxidative Hydrogen Atom Transfer Reactivity for a $Cu^{II}_2(O_2^{\bullet-})$ Complex Driven by Formation of a Cu^{II}_2(-OOH) Compound with a Strong O-H Bond. *J. Am. Chem. Soc.* **2019**, *141*, 12682–12696.

(120) Mahroof-Tahir, M.; Karlin, K. D. A Dinuclear Mixed-Valence Cu(I)/Cu(II) Complex and Its Reversible Reactions with Dioxygen: Generation of a Superoxodicopper(II) Species. *J. Am. Chem. Soc.* **1992**, *114*, 7599–7601.

(121) Brinkmeier, A.; Schulz, R. A.; Buchhorn, M.; Spyra, C. J.; Demeshko, S.; Krewald, V.; Meyer, F. Structurally Characterized M-1, 2-Peroxo / Superoxo Dicopper(II) Pair. *J. Am. Chem. Soc.* **2021**, *143*, 10361–10366.

(122) Trammell, R.; Rajabimoghadam, K.; Garcia-Bosch, I. Copper-Promoted Functionalization of Organic Molecules: From Biologically Relevant Cu/O_2 Model Systems to Organometallic Transformations. *Chem. Rev.* **2019**, *119*, 2954–3031.

(123) Itoh, K.; Hayashi, H.; Furutachi, H.; Matsumoto, T.; Nagatomo, S.; Tosha, T.; Terada, S.;

Fujinami, S.; Suzuki, M.; Kitagawa, T. Synthesis and Reactivity of a (μ-1,1-Hydroperoxo)(μ-Hydroxo) Dicopper(II) Complex: Ligand Hydroxylation by a Bridging Hydroperoxo Ligand. *J. Am. Chem. Soc.* **2005**, *127*, 5212–5223.

(124) Kindermann, N.; Dechert, S.; Demeshko, S.; Meyer, F. Proton-Induced, Reversible Interconversion of a μ-1,2-Peroxo and a μ-1,1-Hydroperoxo Dicopper(II) Complex. *J. Am. Chem. Soc.* **2015**, *137*, 8002–8005.

(125) Bordwell, F. G.; Cheng, J.-P.; Harrelson Jr, J. A. Homolytic Bond Dissociation Energies in Solution from Equilibrium Acidity and Electrochemical Data. *J. Am. Chem. Soc.* **1988**, *110*, 1229–1231.

(126) Warren, J. J.; Tronic, T. A.; Mayer, J. M. Thermochemistry of Proton-Coupled Electron Transfer Reagents and Its Implications. *Chem. Rev.* **2010**, *110*, 6961–7001.

(127) Wise, C. F.; Agarwal, R. G.; Mayer, J. M. Determining Proton-Coupled Standard Potentials and X-H Bond Dissociation Free Energies in Nonaqueous Solvents Using Open-Circuit Potential Measurements. *J. Am. Chem. Soc.* **2020**, *142*, 10681–10691.

(128) Hayton, T. W.; Legzdins, P.; Sharp, W. B. Coordination and Organometallic Chemistry of Metal-NO Complexes. *Chem. Rev.* **2002**, *102*, 935–991.

(129) Ruggiero, C. E.; Carrier, S. M.; Cramer, C. J.; Tolman, W. B.; Antholine, W. E.; Whittaker, J. W. Synthesis and Structural and Spectroscopic Characterization of Mononuclear Copper Nitrosyl Complexes: Models for Nitric Oxide Adducts of Copper Proteins and Copper-Exchanged Zeolites. *J. Am. Chem. Soc.* **1993**, *115*, 11285–11298.

(130) Wright, A. M.; Wu, G.; Hayton, T. W. Structural Characterization of a Copper Nitrosyl Complex with a $\{CuNO\}^{10}$ Configuration. *J. Am. Chem. Soc.* **2010**, *132*, 14336–14337.

(131) Paul, P. P.; Tyeklár, Z.; Farooq, A.; Karlin, K. D.; Liu, S.; Zubieta, J.; Karlin, K. D. Isolation and X-Ray Structure of a Dinuclear Copper-Nitrosyl Complex. *J. Am. Chem. Soc.* **1990**, *112*, 2430–2432.

(132) Cao, R.; Elrod, L. T.; Lehane, R. L.; Kim, E.; Karlin, K. D. A Peroxynitrite Dicopper Complex: Formation via Cu-NO and Cu-O_2 Intermediates and Reactivity via O-O Cleavage Chemistry. *J. Am. Chem. Soc.* **2016**, *138*, 16148–16158.

(133) Tao, W.; Bower, J. K.; Moore, C. E.; Zhang, S. Dicopper μ-Oxo, μ-Nitrosyl Complex from the Activation of NO or Nitrite at a Dicopper Center. *J. Am. Chem. Soc.* **2019**, *141*, 10159–10164.

(134) Tao, W.; Moore, C. E.; Zhang, S. Redox-Neutral S -Nitrosation Mediated by a Dicopper Center. *Angew. Chem. Int. Ed.* **2021**, *133*, 2–10.

(135) Buchler, S.; Meyer, F.; Kaifer, E.; Pritzkow, H. Tunable TACN/Pyrazolate Hybrid Ligands as Dinucleating Scaffolds for Metallobiosite Modeling - Dinickel(II) Complexes Relevant to the Urease Active Site. *Inorg. Chim. Acta* **2002**, *337*, 371–386.

(136) Lücken, J.; Auth, T.; Mozzi, S. I.; Meyer, F. Hexanuclear Copper(I) Hydride from the Reduction-

Induced Decarboxylation of a Dicopper(II) Formate. *Inorg. Chem.* **2020**, *59*, 14347–14354.

(137) Kindermann, N. Diiron and Dicopper Complexes with Pyrazolate/Tacn Hybrid Ligands for Small Molecule Activation, *Dissertation*, Georg-August-Universität Göttingen, **2015**.

(138) Thangavel, A.; Wieliczko, M.; Bacsa, J.; Scarborough, C. C. 1,4,7-Triazacyclononane Ligands Bearing Tertiary Alkyl Nitrogen Substituents. *Inorg. Chem.* **2013**, *52*, 13282–13287.

(139) Gros, G.; Hasserodt, J. Multigram Four-Step Synthesis of 1,4,7-Triazacyclononanes with $2R_a/R_b$ N-Functionalization Pattern by Starting from Diethylenetriamine. *Eur. J. Org. Chem.* **2015**, *2015*, 183–187.

(140) Halfen, J. A.; Jazdzewski, B. A.; Mahapatra, S.; Berreau, L. M.; Wilkinson, E. C.; Que, L.; Tolman, W. B. Synthetic Models of the Inactive Copper(II)-Tyrosinate and Active Copper(II)-Tyrosyl Radical Forms of Galactose and Glyoxal Oxidases. *J. Am. Chem. Soc.* **1997**, *119*, 8217–8227.

(141) Richman, J. E.; Atkins, T. J. Nitrogen Analogs of Crown Ethers. *J. Am. Chem. Soc.* **1974**, *96*, 2268–2270.

(142) Gondoh, A.; Koike, T.; Akita, M. 3,5-Bis(Diphenylphosphinoethyl)Pyrazolate Ligand ($PNNP^{C2}$) and Its Dirhodium Complexes: Comparison with Related Quadridentate Dinucleating Diphenylphosphinomethyl ($PNNP^{Py}$) and Phthalazine Derivatives ($PNNP^{Ph}$). *Inorg. Chim. Acta* **2011**, *374*, 489–498.

(143) Bendrath, F.; Specowius, V.; Michalik, D.; Langer, P. 3,5-Dioxopimelates as New Synthetic Building Blocks. Cyclocondensation with 1,2-, 1,3- and 1,4-Dinucleophiles. *Tetrahedron* **2012**, *68*, 6456–6462.

(144) Paudler, W. W.; Zeiler, A. G. 1,3-Butadiynes in the Synthesis of Heterocyclic Compounds. I. 2,3-Dihydro-1,4-Diazepine, Pyrazole, and Isoxazole Derivatives. *J. Org. Chem.* **1969**, *34*, 999–1001.

(145) Yang, L.; Powell, D. R.; Houser, R. P. Structural Variation in Copper(I) Complexes with Pyridylmethylamide Ligands: Structural Analysis with a New Four-Coordinate Geometry Index, τ_4. *J. Chem. Soc. Dalt. Trans.* **2007**, *9*, 955–964.

(146) Weitzer, M.; Schindler, S.; Brehm, G.; Schneider, S.; Hörmann, E.; Jung, B.; Kaderli, S.; Zuberbuehler, A. D. Reversible Binding of Dioxygen by the Copper(I) Complex with Tris(2-Dimethylaminoethyl)Amine (Me_6Tren) Ligand. *Inorg. Chem.* **2003**, *42*, 1800–1806.

(147) Aboelella, N. W.; Gherman, B. F.; Hill, L. M. R.; York, J. T.; Holm, N.; Young, V. G.; Cramer, C. J.; Tolman, W. B. Effects of Thioether Substituents on the O_2 Reactivity of β-Diketiminate-Cu(I) Complexes: Probing the Role of the Methionine Ligand in Copper Monooxygenases. *J. Am. Chem. Soc.* **2006**, *128*, 3445–3458.

(148) Comba, P.; Haaf, C.; Helmle, S.; Karlin, K. D.; Pandian, S.; Waleska, A. Dioxygen Reactivity of New Bispidine-Copper Complexes. *Inorg. Chem.* **2012**, *51*, 2841–2851.

(149) Kahn, O. Dinuclear Complexes with Predictable Magnetic Properties. *Angew. Chem. Int. Ed.*

1985, *24*, 834–850.

(150) Girerd, J. J.; Journaux, Y.; Kahn, O. Natural or Orthogonalized Magnetic Orbitals: Two Alternative Ways to Describe the Exchange Interaction. *Chem. Phys. Lett.* **1981**, *82*, 534–538.

(151) Driessen, W. L.; Chang, L.; Finazzo, C.; Gorter, S.; Reedijk, J.; Lutz, M.; Spek, A. L. Two Pyrazolato-Bridged , Linear Trinuclear Cu (II) Complexes . Crystal Structures and Magnetic Properties. **2003**, *350*.

(152) Prokofieva, A.; Prikhod, A. I.; Enyedy, E. A.; Farkas, E.; Maringgele, W.; Demeshko, S.; Dechert, S.; Meyer, F. Oligonuclear Copper Complexes of a Bioinspired Pyrazolate-Bridging Ligand : Synthesis , Structures , and Equilibria in Solution. **2007**, *46*, 3703–3711.

(153) Dalle, K. E. Bioinspired Activation of Oxygen with Pyrazole-Supported Dinuclear Copper Complexes, *Dissertation*, Georg-August-Universität Göttingen, **2014**.

(154) Girerd, J. J.; Charlot, M. F.; Kahn, O. Orbital Interaction in One-Dimensional Magnetic Compounds. *Mol. Phys.* **1977**, *34*, 1063–1076.

(155) Neese, F. The ORCA Program System. *Wiley Interdiscip. Rev. Comput. Mol. Sci.* **2012**, *2*, 73–78.

(156) Schäfer, A.; Horn, H.; Ahlrichs, R. Fully Optimized Contracted Gaussian Basis Sets for Atoms Li to Kr. *J. Chem. Phys.* **1992**, *97*, 2571–2577.

(157) Weigend, F.; Ahlrichs, R. Balanced Basis Sets of Split Valence, Triple Zeta Valence and Quadruple Zeta Valence Quality for H to Rn: Design and Assessment of Accuracy. *Phys. Chem. Chem. Phys.* **2005**, *7*, 3297–3305.

(158) Ginsberg, A. P. Magnetic Exchange in Transition Metal Complexes. 12.1 Calculation of Cluster Exchange Coupling Constants with the Xα-Scattered Wave Method. *J. Am. Chem. Soc.* **1980**, *102*, 111–117.

(159) Noodleman, L. Valence Bond Description of Antiferromagnetic Coupling in Transition Metal Dimers. *J. Chem. Phys.* **1981**, *74*, 5737–5743.

(160) Noodleman, L.; Davidson, E. R. Ligand Spin Polarization and Antiferromagnetic Coupling in Transition Metal Dimers. *Chem. Phys.* **1986**, *109*, 131–143.

(161) Bencini, A.; Gatteschi, D. Xα-SW Calculations of the Electronic Structure and Magnetic Properties of Weakly Coupled Transition-Metal Clusters. The $[Cu_2Cl_6]^{2-}$Dimers. *J. Am. Chem. Soc.* **1986**, *108*, 5763–5771.

(162) Soda, T.; Kitagawa, Y.; Onishi, T.; Takano, Y.; Shigeta, Y.; Nagao, H.; Yoshioka, Y.; Yamaguchi, K. Ab Initio Computations of Effective Exchange Integrals for H-H, H-He-H and Mn_2O_2 Complex: Comparison of Broken-Symmetry Approaches. *Chem. Phys. Lett.* **2000**, *319*, 223–230.

(163) Singh, A. K.; Van Vlugt, J. I. Der; Demeshko, S.; Dechert, S.; Meyer, F. Bis(Terdentate) Pyrazole/Pyridine Ligands: Synthesis, Crystal Structures and Magnetic Properties of Bridged Binuclear and Tetranuclear Copper(II) Complexes. *Eur. J. Inorg. Chem.* **2009**, *23*, 3431–3439.

(164) Van Crawford, H.; Richardson, H. W.; Wasson, J. R.; Hodgson, D. J.; Hatfield, W. E. Relation Between the Singlet-Triplet Splitting and the Cu-O-Cu Bridge Angle in Hydroxo-Bridged Copper Dimers. *Inorg. Chem.* **1976**, *15*, 2107–2110.

(165) Ruiz, E.; Alemany, P.; Alvarez, S.; Cano, J. Structural Modeling and Magneto-Structural Correlations for Hydroxo-Bridged Copper(II) Binuclear Complexes. *Inorg. Chem.* **1997**, *36*, 3683–3688.

(166) Ruiz, E.; Alemany, P.; Alvarez, S.; Cano, J. Toward the Prediction of Magnetic Coupling in Molecular Systems: Hydroxo- and Alkoxo-Bridged Cu(II) Binuclear Complexes. *J. Am. Chem. Soc.* **1997**, *119*, 1297–1303.

(167) Connelly, N. G.; Geiger, W. E. Chemical Redox Agents for Organometallic Chemistry. *Chem. Rev.* **1996**, *96*, 877–910.

(168) Citek, C.; Herres-Pawlis, S.; Stack, T. D. P. Low Temperature Syntheses and Reactivity of Cu_2O_2 Active-Site Models. *Acc. Chem. Res.* **2015**, *48*, 2424–2433.

(169) Haack, P.; Limberg, C. Molecular Cu^{II}-O-Cu^{II} Complexes: Still Waters Run Deep. *Angew. Chem. Int. Ed.* **2014**, *53*, 4282–4293.

(170) Bailey, W. D.; Gagnon, N. L.; Elwell, C. E.; Cramblitt, A. C.; Bouchey, C. J.; Tolman, W. B. Revisiting the Synthesis and Nucleophilic Reactivity of an Anionic Copper Superoxide Complex. *Inorg. Chem.* **2019**, *58*, 4706–4711.

(171) Kaljurand, I.; Kütt, A.; Sooväli, L.; Rodima, T.; Mäemets, V.; Leito, I.; Koppel, I. A. Extension of the Self-Consistent Spectrophotometric Basicity Scale in Acetonitrile to a Full Span of 28 PKa Units: Unification of Different Basicity Scales. *J. Org. Chem.* **2005**, *70*, 1019–1028.

(172) Giguère, P. A. The Infra-Red Spectrum of Hydrogen Peroxide. *J. Chem. Phys.* **1950**, *18*, 88–92.

(173) Un, C.; Root, D. E.; Mahroof-tahir, M.; Karlin, K. D.; Solomon, E. I. Effect of Protonation on Peroxo - Copper Bonding : Spectroscopic and Electronic Structure. *Inorg. Chem.* **1998**, *37*, 4838–4848.

(174) Brunold, T. C.; Tamura, N.; Kitajima, N.; Moro-oka, Y.; Solomon, E. I. Spectroscopic Study of $[Fe_2(O_2)(OBz)_2\{HB(Pz')_3\}_2]$: Nature of the μ-1 ,2 Peroxide-Fe(III) Bond and Its Possible Relevance to O_2 Activation by Non-Heme Iron Enzymes. *J. Am. Chem. Soc.* **1998**, *2*, 5674–5690.

(175) Chen, P.; Fujisawa, K.; Solomon, E. I. Spectroscopic and Theoretical Studies of Mononuclear Copper (II) Alkyl- and Hydroperoxo Complexes : Electronic Structure Contributions to Reactivity. *J. Am. Chem. Soc.* **2000**, *122*, 10177–10193.

(176) Tshepelevitsh, S.; Kütt, A.; Lõkov, M.; Kaljurand, I.; Saame, J.; Heering, A.; Plieger, P. G.; Vianello, R.; Leito, I. On the Basicity of Organic Bases in Different Media. *Eur. J. Org. Chem.* **2019**, 6735–6748.

(177) Kovačević, B.; Barić, D.; Maksić, Z. B. Basicity of Exceedingly Strong Non-Ionic Organic Bases in Acetonitrile - Verkade's Superbase and Some Related Phosphazenes. *New J. Chem.* **2004**,

28, 284–288.

(178) Abe, T.; Hori, Y.; Shiota, Y.; Ohta, T.; Morimoto, Y.; Sugimoto, H.; Ogura, T.; Yoshizawa, K.; Itoh, S. Cupric-Superoxide Complex That Induces a Catalytic Aldol Reaction-Type C–C Bond Formation. *Commun. Chem.* **2019**, *2*, 6–12.

(179) Piechota, E. J.; Meyer, G. J. Introduction to Electron Transfer: Theoretical Foundations and Pedagogical Examples. *J. Chem. Educ.* **2019**, *96*, 2450–2466.

(180) Laborda, E.; Henstridge, M. C.; Batchelor-McAuley, C.; Compton, R. G.; Batchelor-Mc Auley, C.; Compton, R. G. Asymmetric Marcus–Hush Theory for Voltammetry. *Chem. Soc. Rev.* **2013**, *42*, 4894–4905.

(181) Mayer, J. M. Proton-Coupled Electron Transfer: A Reaction Chemist's View. *Annu. Rev. Phys. Chem.* **2004**, *55*, 363–390.

(182) Mayer, J. M. Understanding Hydrogen Atom Transfer: From Bond Strengths to Marcus Theory. *Acc. Chem. Res.* **2011**, *44*, 36–46.

(183) Mayer, J. M. Simple Marcus-Theory-Type Model for Hydrogen-Atom Transfer/Proton-Coupled Electron Transfer. *J. Phys. Chem. Lett.* **2011**, *2*, 1481–1489.

(184) Lin, C. Y.; Peh, J.; Coote, M. L. Effects of Chemical Structure on the Thermodynamic Efficiency of Radical Chain Carriers for Organic Synthesis. *J. Org. Chem.* **2011**, *76*, 1715–1726.

(185) Thordarson, P. Determining Association Constants from Titration Experiments in Supramolecular Chemistry. *Chem. Soc. Rev.* **2011**, *40*, 1305–1323.

(186) Borovik, A. S. Bioinspired Hydrogen Bond Motifs in Ligand Design: The Role of Noncovalent Interactions in Metal Ion Mediated Activation of Dioxygen. *Acc. Chem. Res.* **2005**, *38*, 54–61.

(187) Yamaguchi, S.; Kumagai, A.; Nagatomo, S.; Kitagawa, T.; Funahashi, Y.; Ozawa, T.; Jitsukawa, K.; Masuda, H. Synthesis , Characterization , and Thermal Stability of New Mononuclear Hydrogenperoxocopper (II) Complexes with N_3O-Type Tripodal Ligands Bearing Hydrogen-Bonding Interaction Sites. *Bull. Chem. Soc. Jpn.* **2005**, *78*, 116–124.

(188) Wada, A.; Honda, Y.; Yamaguchi, S.; Nagatomo, S.; Kitagawa, T. Steric and Hydrogen-Bonding Effects on the Stability of Copper Complexes with Small Molecules. *Inorg. Chem.* **2004**, *43*, 5725–5735.

(189) Wada, A.; Harata, M.; Hasegawa, K.; Jitsukawa, K.; Masuda, H. Structural and Spectroscopic Characterization of a Mononuclear Hydroperoxo-Copper(II) Complex with Tripodal Pyridylamine. *Angew. Chem. Int. Ed.* **1998**, *37*, 798–799.

(190) Leo, A. J. Evaluating Hydrogen-Bond Donor Strength. *J. Pharm. Sci.* **2000**, *89*, 1567–1578.

(191) Zheng, S.; Xu, S.; Wang, G.; Tang, Q.; Jiang, X.; Li, Z.; Xu, Y.; Wang, R.; Lin, F. Proposed Hydrogen-Bonding Index of Donor or Acceptor Reflecting Its Intrinsic Contribution to Hydrogen-Bonding Strength. *J. Chem. Inf. Model.* **2017**, *57*, 1535–1547.

(192) Kütt, A.; Selberg, S.; Kaljurand, I.; Tshepelevitsh, S.; Heering, A.; Darnell, A.; Kaupmees, K.; Piirsalu, M.; Leito, I. PK$_a$ Values in Organic Chemistry – Making Maximum Use of the Available Data. *Tetrahedron Lett.* **2018**, *59*, 3738–3748.

(193) Rossini, E.; Bochevarov, A. D.; Knapp, E. W. Empirical Conversion of PKa Values between Different Solvents and Interpretation of the Parameters: Application to Water, Acetonitrile, Dimethyl Sulfoxide, and Methanol. *ACS Omega* **2018**, *3*, 1653–1662.

(194) Kütt, A.; Tshepelevitsh, S.; Saame, J.; Lõkov, M.; Kaljurand, I.; Selberg, S.; Leito, I. Strengths of Acids in Acetonitrile. *Eur. J. Inorg. Chem.* **2021**, 1407–1419.

(195) Kida, T.; Sato, S. I.; Yoshida, H.; Teragaki, A.; Akashi, M. 1,1,1,3,3,3-Hexafluoro-2-Propanol (HFIP) as a Novel and Effective Solvent to Facilely Prepare Cyclodextrin-Assembled Materials. *Chem. Commun.* **2014**, *50*, 14245–14248.

(196) Lam, Y. C.; Nielsen, R. J.; Gray, H. B.; Goddard, W. A. A Mn Bipyrimidine Catalyst Predicted to Reduce CO_2 at Lower Overpotential. *ACS Catal.* **2015**, *5*, 2521–2528.

(197) McCarthy, B. D.; Martin, D. J.; Rountree, E. S.; Ullman, A. C.; Dempsey, J. L. Electrochemical Reduction of Brønsted Acids by Glassy Carbon in Acetonitrile-Implications for Electrocatalytic Hydrogen Evolution. *Inorg. Chem.* **2014**, *53*, 8350–8361.

(198) Venkateswarlu, P.; Gordy, W. Methyl Alcohol. II. Molecular Structure. *J. Chem. Phys* **1955**, *23*, 1200–1202.

(199) Herschlag, D.; Pinney, M. M. Hydrogen Bonds: Simple after All? *Biochemistry* **2018**, *57*, 3338–3352.

(200) Grabowski, S. J. Chapter 1: Hydrogen Bond - Definitions, Criteria of Existence and Various Types. *RSC Theor. Comput. Chem. Ser.* **2021**, *19*, 1–40.

(201) Roy, K.; Popelier, P. L. A. Predictive QSPR Modeling of the Acidic Dissociation Constant (PK$_a$) of Phenols in Different Solvents. *J. Phys. Org. Chem.* **2009**, *22*, 186–196.

(202) Campbell, R.; Fisher, J. P.; Sharman, J. E.; McDonnell, B. J.; Frenneaux, M. P. Contribution of Nitric Oxide to the Blood Pressure and Arterial Responses to Exercise in Humans. *J. Hum. Hypertens.* **2011**, *25*, 262–270.

(203) Houston, M.; Hays, L. Acute Effects of an Oral Nitric Oxide Supplement on Blood Pressure, Endothelial Function, and Vascular Compliance in Hypertensive Patients. *J. Clin. Hypertens.* **2014**, *16*, 524–529.

(204) Page, A. J.; O'Donnell, T. A.; Cooper, N. J.; Young, R. L.; Blackshaw, L. A. Nitric Oxide as an Endogenous Peripheral Modulator of Visceral Sensory Neuronal Function. *J. Neurosci.* **2009**, *29*, 7245–7255.

(205) Bogdan, C. Nitric Oxide and the Immune Response. *Nat. Immunol.* **2001**, *2*, 907–916.

(206) Wink, D. A.; Hines, H. B.; Cheng, R. Y. S.; Switzer, C. H.; Flores-Santana, W.; Vitek, M. P.; Ridnour, L. A.; Colton, C. A. Nitric Oxide and Redox Mechanisms in the Immune Response. *J. Leukoc. Biol.*

2011, *89*, 873–891.

(207) Sarti, P.; Forte, E.; Mastronicola, D.; Giuffrè, A.; Arese, M. Cytochrome c Oxidase and Nitric Oxide in Action: Molecular Mechanisms and Pathophysiological Implications. *Biochim. Biophys. Acta - Bioenerg.* **2012**, *1817*, 610–619.

(208) Sarti, P.; Giuffré, A.; Forte, E.; Mastronicola, D.; Barone, M. C.; Brunori, M. Nitric Oxide and Cytochrome c Oxidase: Mechanisms of Inhibition and NO Degradation. *Biochem. Biophys. Res. Commun.* **2000**, *274*, 183–187.

(209) Collman, J. P.; Dey, A.; Decreau, R. A.; Yang, Y.; Hosseini, A.; Solomon, E. I.; Eberspacher, T. A. Interaction of Nitric Oxide with a Functional Model of Cytochrome c Oxidase. *Proc. Natl. Acad. Sci. U. S. A.* **2008**, *105*, 9892–9896.

(210) Palacios-Callender, M.; Hollis, V.; Frakich, N.; Mateo, J.; Moncada, S. Cytochrome c Oxidase Maintains Mitochondrial Respiration during Partial Inhibition by Nitric Oxide. *J. Cell Sci.* **2007**, *120*, 160–165.

(211) Hematian, S.; Garcia-Bosch, I.; Karlin, K. D. Synthetic Heme/Copper Assemblies: Toward an Understanding of Cytochrome c Oxidase Interactions with Dioxygen and Nitrogen Oxides. *Acc. Chem. Res.* **2015**, *48*, 2462–2474.

(212) Adam, S. M.; Wijeratne, G. B.; Rogler, P. J.; Diaz, D. E.; Quist, D. A.; Liu, J. J.; Karlin, K. D. Synthetic Fe/Cu Complexes: Toward Understanding Heme-Copper Oxidase Structure and Function. *Chem. Rev.* **2018**, *118*, 10840–11022.

(213) Beckman, J. S.; Koppenol, W. H. Nitric Oxide, Superoxide, and Peroxynitrite: The Good, the Bad, and the Ugly. *Am. Physiol. Soc.* **1996**, No. 271, 1424–1437.

(214) Van Dyke, K. The Possible Role of Peroxynitrite in Alzheimer's Disease: A Simple Hypothesis That Could Be Tested More Thoroughly. *Med. Hypotheses* **1997**, *48*, 375–380.

(215) Stamler, J. S.; Singel, D. J.; Loscalzo, J. Biochemistry Nitric Oxide and Redox-Activated Forms. *Science* **1992**, *258*, 1898–1902.

(216) Yeh, S. W.; Tsou, C. C.; Liaw, W. F. The Dinitrosyliron Complex $[Fe_4(\mu_3\text{-}S)_2(\mu_2\text{-}NO)_2(NO)_6]^{2-}$ Containing Bridging Nitroxyls: ^{15}N (NO) NMR Analysis of the Bridging and Terminal NO-Coordinate Ligands. *Dalton Trans.* **2014**, *43*, 9022–9025.

(217) Mason, J.; Larkworthy, L. F.; Moore, E. A. Nitrogen NMR Spectroscopy of Metal Nitrosyls and Related Compounds. *Chem. Rev.* **2002**, *102*, 913–934.

(218) Bell, L. K.; Mason, J.; Mingos, D. M. P.; Tew, D. G. 15NMR Studies of Nitrosyl (Bent and Linear), Nitro, and Nitrito Ligands in 4-, 5-, and 6-Coordinate Complexes of the Platinum Metals. *Inorg. Chem.* **1983**, *22*, 3497–3502.

(219) Michael, D.; Mingos, P.; Sherman, D. J. Transition Metal Nitrosyl Complexes. *Adv. Inorg. Chem.* **1989**, *34*, 293–377.

(220) Grimme, S.; Antony, J.; Ehrlich, S.; Krieg, H. A Consistent and Accurate Ab Initio

Parametrization of Density Functional Dispersion Correction (DFT-D) for the 94 Elements H-Pu. *J. Chem. Phys.* **2010**, *132*.

(221) Williams, D. B. G.; Lawton, M. Drying of Organic Solvents: Quantitative Evaluation of the Efficiency of Several Desiccants. *J. Org. Chem.* **2010**, *75*, 8351–8354.

(222) Liang, H. C.; Karlin, K. D.; Dyson, R.; Kaderli, S.; Jung, B.; Zuberbühler, A. D. Dioxygen-Binding Kinetics and Thermodynamics of a Series of Dicopper(I) Complexes with Bis[2-(2-Pyridyl)Ethyl]Amine Tridendate Chelators Forming Side-on Peroxo-Bridged Dicopper(II) Adducts. *Inorg. Chem.* **2000**, *39*, 5884–5894.

(223) Curley, J. J.; Bergman, R. G.; Tilley, T. D. Preparation and Physical Properties of Early-Late Heterobimetallic Compounds Featuring Ir-M Bonds (M = Ti, Zr, Hf). *Dalton Trans.* **2012**, *41*, 192–200.

(224) Ozinskas, A. J.; Bobst, A. M. Formation OfN-Hydroxy-Amines of Spin Labeled Nucleosides For1H-NMR. Analysis. *Helv. Chim. Acta* **1980**, *63*, 1407–1411.

(225) Connelly, N. G.; Draggett, M. G.; Kuc, T. A. Synthesis and Reactivity of the Tetrakis(Acetonitrile)Nitrosylrhodium Dication. *Dalton Trans.* **1977**, 70–73.

(226) Bill, E. Max-Planck Institute for Chemical Energy Conversion, Mülheim/Ruhr, Germany. **2008**.

(227) Stoll, S.; Schweiger, A. ESR Simulation Mit Easyspin. *J. Magn. Reson* **2006**, *178*, 42–55.

(228) Sheldrick, G. M. *Acta Cryst.* **2015**, *A71*, 3–8.

(229) Sheldrick, G. M. *Acta Cryst.* **2015**, *C71*, 3–8.

(230) X-RED; STOE & CIE GmbH: Darmstadt, Germany, 2002.

9 Overview of Ligands and Complexes

9.1 Ligands

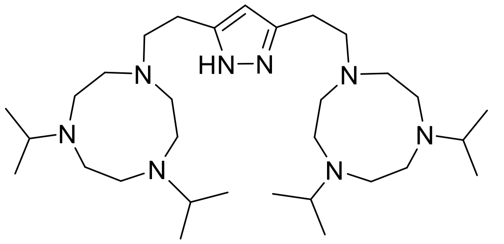

HL^2

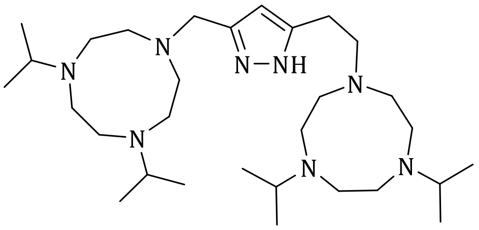

$HL^{1,2}$

9.2 Complexes

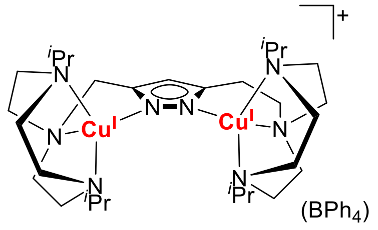

1

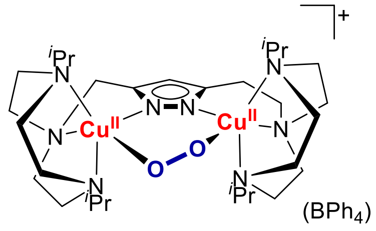

2

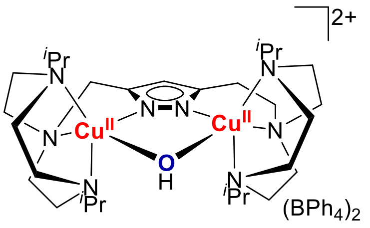

3

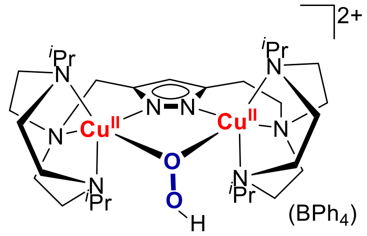

4 (OTf)

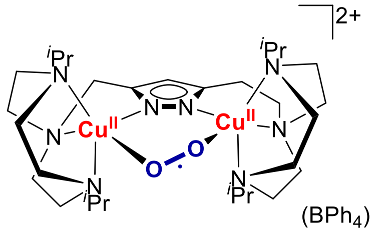

5 (BF_4)

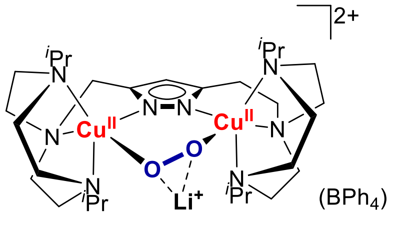

6 [2+Li$^+$] (OTf)

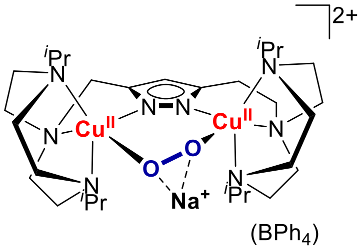

7 [2+Na$^+$] (OTf)

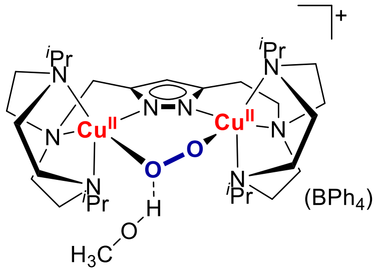

8

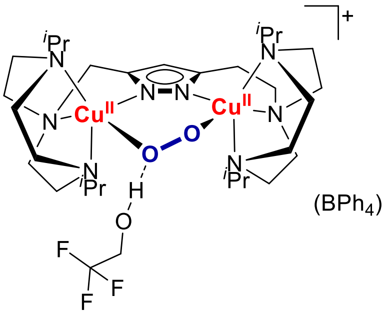

9

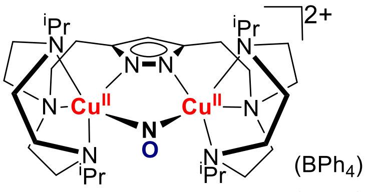

10 (BPh_4)

10 Abbreviations

ATR	Attenuated Total Reflection
BDFE	Bond dissociation free energy
BS	Broken-symmetry
CHD	cyclohexadiene
CT	Charge transfer
$CoCp_2$	cobaltocene
Cu	Copper
CV	Cyclic voltammetry
δ	chemical shift
DCM	Dichlormethane
DFT	Density functional theory
EPR	Electron Paramagnetic Resonance
ESI-MS	Electro Spray Ionization Mass Spectrometry
Et	ethyl
EtCN	Propionitrile
Et_2O	Diethyl ether
eq.	equivalent
Fc	ferrocene
Fe	Iron
HAA	Hydrogen Atom Abstraction
HAT	Hydrogen Atom Transfer
HBr	Hydrogen bromide
HSAB	principle of Hard and Soft Acids and Bases
Hz	Hertz
HOMO	Highest occupied molecular orbital
IR	Infrared
ISC	Intersystem crossing
IUPAC	International union of pure and applied chemistry
K	Kelvin
KBr	Potassium bromide
KO^tBu	Potassium *tert*-butoxide
Li	Lithium

LMCT	Ligand to Metal Charge Transfer
Lut	2,6-lutidine
Me	methyl
MeCN	acetonitrile
MeOH	methanol
MS	Mass spectrometry
Na	Sodium
NaO^{t}Bu	Sodium *tert*-butoxide
NMR	Nuclear Magnetic Resonance
OTf	Triflate
PCET	Proton Coupled Electron Transfer
PDB	Protein Data Bank
Ppm	Parts per million
rR	Resonance RAMAN
RT	Room temperature
SQUID	Superconducting Quantum Interference Device
tacn	1,4,7-Triazacyclononane
TFE	2,2,2-Trifluoroethanole
THF	Tetrahydrofuran
TMG	1,1,3,3-Tetramethylguanidine
Ts	Tosyl
tpa	tris(2-pyridyl-methyl)amine
UV/vis	Ultraviolet/visible
VTVH	Variable temperature variable field
ZFS	Zero field splitting

11 Acknowledgements

First of all, I want to thank my advisor Prof. Dr. Franc Meyer for giving me the opportunity to work on this fascinating topic, great scientific freedom to pursue my research and for his expertise and highly-engaging motivation. I also want to thank Prof. Dr. Inke Siewert for co-supervising this thesis and for her inspirational and constructive ideas for my research projects.

Special thanks also to Nicolas LePoul for the opportunity for my research visit in Brest and the highly appreciated scientific discussions about low-temperature CV measurements as well as the introduction into french cuisine.

Further I would like to thank Dr. Sebastian Dechert for performing all the X-ray diffraction and Raman measurements as well as DFT calculations. I am also thanking Dr. Serhiy Demeshko for conducting magnetic measurements of my samples and to the related scientific discussions. Also, I would like to thank Dr. Claudia Stückl for conducting EPR measurements and for taking care of all the administrative issues. In the context of administrative questions, I would also like to thank Britta Müller. Special thanks also to Andreas Schwarz and Jörg Teichgräber for providing me with pyrazolate building blocks for my ligands and their advanced technical experience. I am also thankful to Eckhard Bill for his helping manner regarding all EPR related questions and for conducting EPR measurements. I would also like to thank my lab mate Martin Dzemski for the great atmosphere in the lab and, together with Roland Schulz and Thomas Kothe, for their supportive help. Further, I would like to thank Anna Kölpin, Jana Lücken, Hendrik Stevens, Massimiliano Morganti, Munmun Ghosh, Ting-Yi Chen, Guillermo Duran-Solares, Giuseppe Lococciolo, Manuel Oelschlegel, Alexander Brinkmeier and all other group members for their nice company and scientific suggestions during the last years. Special thanks also to Roland Schulz, Giuseppe Lococciolo, Guillermo Duran-Solares, Manuel Oelschlegel and Martin Dzemski for proofreading this thesis. I would also like to thank my bachelor students Dorothea Dönges and Maximilian Winkler as well as my research student Hendrik Flegel for supporting this thesis with their experimental work.

Special thanks to my friends Marcus Thater, Valentin Müller and Mike Groth who started the journey of studying chemistry with me 10 years ago and made it through.

Finally, I want to thank my family and friends for their love and support during the last couple of years and last but not least my wife Katrin for her everlasting belief in me that always motivates me and keeps me going.